Dynamic Modelling, Measurement and Control of Co-rotating Twin-Screw Extruders

Justin Rae Elsey, B.E.(Chem)

A thesis submitted in fulfillment of the
requirements for the degree of
Doctor of Philosophy

Department of Chemical Engineering
University of Sydney, Australia
August, 2002

Declaration

I hereby declare that the work presented in this thesis is solely my own work. To the best of my knowledge the work presented is original except where otherwise indicated by reference to other authors. No part of this work has been submitted for any other degree.

(Justin Rae Elsey)
25 August, 2002

Summary

Co-rotating twin-screw extruders are unique and versatile machines that are used widely in the plastics and food processing industries. Due to the large number of operating variables and design parameters available for manipulation and the complex interactions between them, it cannot be claimed that these extruders are currently being optimally utilised. The most significant improvement to the field of twin-screw extrusion would be through the provision of a generally applicable dynamic process model that is both computationally inexpensive and accurate. This would enable product design, process optimisation and process controller design to be performed cheaply and more thoroughly on a computer than can currently be achieved through experimental trials.

This thesis is divided into three parts: dynamic modelling, measurement and control. The first part outlines the development of a dynamic model of the extrusion process which satisfies the above mentioned criteria. The dynamic model predicts quasi-3D spatial profiles of the degree of fill, pressure, temperature, specific mechanical energy input and concentrations of inert and reacting species in the extruder. The individual material transport models which constitute the dynamic model are examined closely for their accuracy and computational efficiency by comparing candidate models amongst themselves and against full 3D finite volume flow models. Several new modelling approaches are proposed in the course of this investigation. The dynamic model achieves a high degree of simplicity and flexibility by assuming a slight compressibility in the process material, allowing the pressure to be calculated directly from the degree of over-fill in each model element using an equation of state. Comparison of the model predictions with dynamic temperature, pressure and residence time distribution data from an extrusion cooking process indicates a good predictive capability. The model can perform dynamic step-change calculations for typical screw configurations in approximately 30 seconds on a 600 MHz Pentium 3 personal computer.

The second part of this thesis relates to the measurement of product quality attributes of extruded materials. A digital image processing technique for measuring the bubble size distribution in extruded foams from cross sectional images is presented. It is recognised that this is an important product quality attribute, though difficult to measure accurately with existing techniques. The present technique is demonstrated on several different products. A simulation study of the formation mechanism of polymer foams is also performed. The

measurement of product quality attributes such as bulk density and hardness in a manner suitable for automatic control is also addressed. This is achieved through the development of an acoustic sensor for inferring product attributes using the sounds emanating from the product as it leaves the extruder. This method is found to have good prediction ability on unseen data.

The third and final part of this thesis relates to the automatic control of product quality attributes using multivariable model predictive controllers based on both direct and indirect control strategies. In the given case study, indirect control strategies, which seek to regulate the product quality attributes through the control of secondary process indicators such as temperature and pressure, are found to cause greater deviations in product quality than taking no corrective control action at all. Conversely, direct control strategies are shown to give tight control over the product quality attributes, provided that appropriate product quality sensors or inferential estimation techniques are available.

Original Work and Publications

The conditions of candidature for the degree of Doctor of Philosophy at The University of Sydney require the candidate to state the sources from which they have derived their information, the extent to which they have availed themselves of the work of others, and the portions of the work they claim as original. The following papers are associated with the work presented in this thesis, while the table below summarises the work in this thesis that is claimed to be original.

J. Elsey, J. Riepenhausen, B. McKay, G.W. Barton, and M. Willis. Modelling and control of a food extrusion process. *Computers in Chemical Engineering Supplementary Series*, 21:S361–S366, 1997

J. Elsey, G.W. Barton, S. Jungk, G. Francis, J. Sellahewa, and C. Chessari. Acoustics based on-line quality estimation. *Computers in Chemical Engineering Supplementary Series*, 22: S925–S928, 1998

J. Elsey, B. McKay, M. Willis, and G.W. Barton. Extruder modelling using genetic programming. *MODSIM 95, Newcastle, Australia, 27-30 November*, 1:276–283, 1995

B. McKay, J. Elsey, M.J. Willis, and G.W. Barton. Evolving input-output models of chemical process systems using genetic programming. *13th World Congress, International Federation of Automatic Control (IFAC'96), San Francisco, 30 June - 5 July*, M:277–282, 1996

J. Elsey, J. Riepenhausen, B. McKay, G.W. Barton, and M. Willis. Dynamic modelling of a cooking extruder. *CHEMECA'96 Sydney, Australia, 30 September - 2 October*, 2:43–48, 1996

G.W. Barton, J. Elsey, B. McKay, and M. Willis. Modelling extrusion cooking: A comparison of neural networks and genetic programming. *7th International Congress on Engineering and Food, Part 2, Brighton, England, 13-17 April*, pages N9–N12, 1997

G.W. Barton, J. Elsey, B. McKay, and C. Sanderson. AI based hybrid modelling. *Australasia-Pacific Forum on Intelligent Processing and Manufacturing of Materials, Gold Coast, 14-17 July*, 1:356–362, 1997

G.W. Barton, J. Elsey, S. Jungk, G. Francis, J. Sellahewa, and C. Chessari. Acoustics based on-line quality estimation. *Australian MATLAB Conference, Sydney, 23-24 October*, 1997

G.W. Barton, J. Elsey, C. Chessari, G. Francis, and J. Sellahewa. The application of genetic programming in extruder modelling and control. *Automatic Control of Food and Biological Processes, Goteborg, Sweden, 21-23 September*, 2:557–562, 1998

J. Elsey and G.W. Barton. Measurement of bubble size distributions in extruded food products. *CHEMECA'99, Newcastle, Australia, 26-29 September, Proceedings on CD-ROM*, 1999. Paper 122

D. Pomerleau, J. Elsey, and G.W. Barton. Model-predictive control of an extrusion cooking process. *APCChE/CHEMECA 2002, 29 September – 3 October 2002, Christchurch, New Zealand*, 2002. In press

Table 1: Original work performed in this thesis.

Chapter	*Description*	*Other similar published work*
2	Expression for the surface area of trapezoidal flight screws.	Booy (1980) derived an expression for the surface area of self-wiping screws.
2	Analysis of the leakage gap geometries in co-rotating screw pairs.	Janssen (1978) analysed leakage gap geometries in counter-rotating screw pairs.
3	Analysis of flow in co-rotating screw pairs using a flow structure based on a repeating sequence of six elements to represent the geometry.	None to author's knowledge.
3	Simplified 1D mesh approach for calculating forward and reverse flow rates of a non-Newtonian fluid in a 2D conduit.	None to author's knowledge.
3	Calculation of 3D non-Newtonian isothermal flow in co-rotating screw pairs using correct boundary conditions.	None to author's knowledge.
4	Direct comparison of 1D, 2D and 3D models for calculating flow in kneading discs.	None to author's knowledge.
4	Prediction of reversing net flow direction in kneading discs at high stagger angles.	None to author's knowledge.
6	Dynamic simulation of the co-rotating twin-screw extrusion process using fixed model elements and an equation of state to calculate the pressure directly from the degree of over-fill in each model element.	None to author's knowledge.
6	Inclusion of starch gelatinisation kinetics and product bubble growth dynamics in a dynamic model of the extrusion cooking process.	None to author's knowledge.
6	Dynamic simulation of non-isothermal start-up of a co-rotating twin-screw extruder.	Kim and White (2000) modelled isothermal start-up.
6	The modelling of uneven fill across the screws in the partially filled zone of a co-rotating twin-screw extruder.	None to author's knowledge.
6	Calculation of residence time distributions using a first principles dynamic process model.	None to author's knowledge.
7	Analysis of the pore size distribution in extruded products using a digital image processing algorithm.	Campbell et al. (1991) used a manual measurement technique for measuring bubbles in bread doughs
8	Simulation of bubble nucleation, growth and coalescence during puffing.	None to author's knowledge.
9	Estimation of bulk density and hardness of extruded products using an acoustic sensor.	None to author's knowledge.
10	Simulation of model predictive controller performance to compare the effect on product quality attributes when both indirect and direct control strategies are used.	None to author's knowledge.

Acknowledgements

I have been fortunate in working with many talented people while undertaking this thesis. Special thanks must first go to my thesis supervisor Geoff Barton, whose guidance, patience and support made this thesis possible. My associate supervisor Tim Langrish also provided constant encouragement and technical advice on many occasions. My thanks also to David Fletcher for scrutinising my fluid modelling work and making himself available to answer my many questions on the subject. Dominique Pomerleau has been extremely generous in tutoring me on model predictive control and testing my software for bugs. Hans Musch deserves special thanks for his guidance with the early modelling work. Chris Durrant of the Mathematics Department went beyond the call of duty in helping me to understand the helical coordinate system used in this thesis. Thanks also to Jörg Riepenhausen, an early collaborator on this project and still a good friend.

All of the experimental extrusion data and product samples used in this thesis were provided by Food Science Australia, so I thank Jay Sellahewa and Charlie Chessari for their frequent assistance. I would especially like to thank Geoff Francis, a creative thinker who was always very helpful and who originally suggested that acoustics might be used to infer various product attributes.

I spent four months working on projects related to this thesis at the University of Newcastle Upon Tyne under the supervision of Mark Willis. Mark was very generous in inviting me to stay at his home when I first arrived, and I would like to thank him and Ming Tham for their friendly supervision during my stay.

Of my past and present postgraduate friends I would particularly like to thank Tim Dun, Geoff Henry, Ben McKay, Dennis McNevin and Chiew Hiet Wong for their helpful discussions over the years. Tim Dun deserves special thanks for proof-reading this entire manuscript, making valuable suggestions and keeping me in high spirits during the write-up process. However, this is almost completely offset by all the speed chess distractions that he provided during our studies.

My current employer Susan Law at the Optical Fibre Technology Centre has been very accommodating during the final and most demanding months of writing this thesis. Without her support this thesis would have taken far longer to complete.

For their financial support I would like to thank the Australian Postgraduate Award Scheme, Geoff Barton, The British Council Postgraduate Bursaries Scheme, the James Kentley Memorial Scholarship, and my parents.

Contents

List of Figures

List of Tables

Chapter 1

Introduction

Abstract: This thesis is concerned with the dynamic modelling, sensing and control of co-rotating twin-screw extruders. The purpose of this chapter is to give a general overview of the present state of screw extrusion, to discuss the developments required to improve the utilisation of these machines, and to outline the format of this thesis.

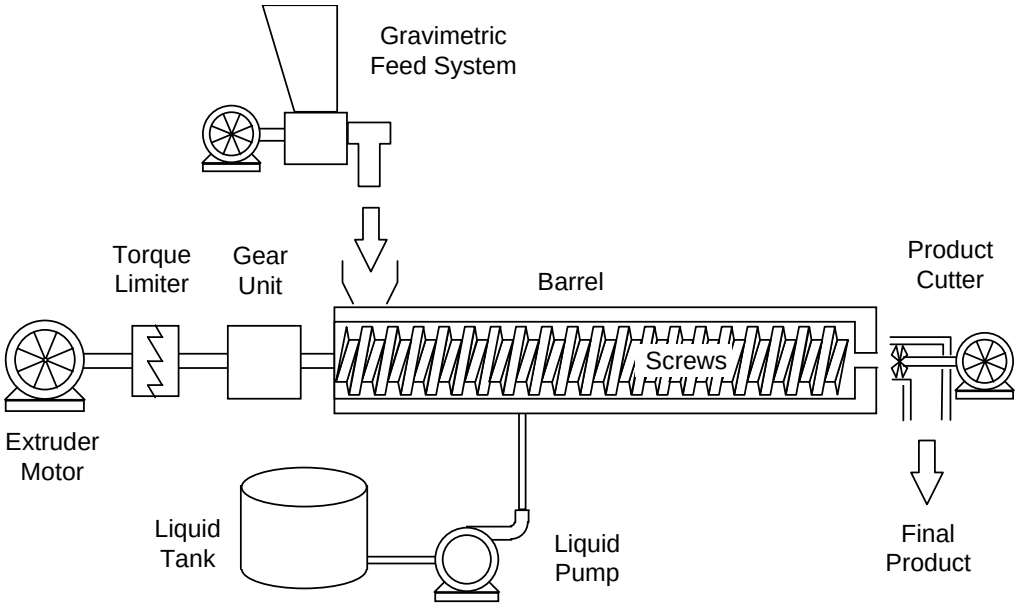

Figure 1.1: Extrusion cooking process diagram.

1.1 A General Overview of Screw Extrusion Technology

Screw extrusion is a unique continuous process that accepts feed material, performs mixing, shearing, heating and pressurisation upon it, and then shapes it by forcing it through a die. Screw extruders are common in the polymer processing industries where they are used, for example, in blending polymers, extruding tubes and beams, plastic coating wires, and thin film production. Almost all the plastic in the world has passed through an extruder at least once during its lifetime. Screw extruders are also being increasingly applied in other areas such as paper pulping, the manufacture of nitrocellulose propellants and pharmaceutical additives. Food production is another field where screw extruders are widely applied, where they are used for making diverse products such as pastas, textured soy proteins, puffed cereals and snack foods, and animal feed pellets. Because screw extruders combine processes such as mixing, cooking and shape forming in a single unit, they enable process simplification and rationalisation over traditional production methods.

Screw extruders consist of a barrel inside which one or more helical screws rotate to propel feed material towards a die at the discharge end of the machine. A typical food extrusion process is shown in Figure 1.1. Of the two basic design variants, single screw and twin-screw extruders, the latter are the more versatile as they allow a wider range of feed materials and processing conditions. In particular, co-rotating twin-screw extruders uniquely allow self-wiping screw geometries that prevent build-up of material on the screws that can result in material degradation and surging. Due to their industrial importance and operational challenges, this thesis is concerned only with co-rotating twin-screw extruders.

An example of the screw shafts and barrel of a co-rotating twin-screw extruder is illus-

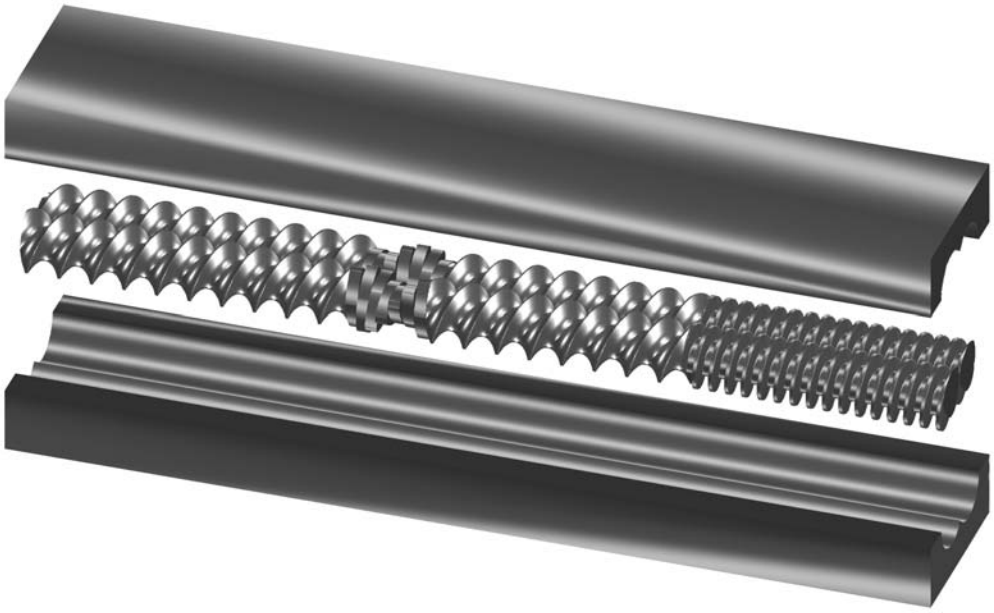

Figure 1.2: Exploded view of shaft and barrel of a co-rotating twin-screw extruder.

trated in Figure 1.2. It can be seen that the screw shaft consists of several different types of screw components. This is typical of modern extruder designs, which have a modular construction allowing the screw shaft to be built up and modified using a variety of components that perform different processing tasks. This allows a high degree of customisation and flexibility in these machines. The mechanical action of the screws on the process material usually results in significant heat generation from friction and viscous heat dissipation. It is common to have heat exchangers built into the barrel to allow additional heating or cooling to be applied to the process material.

Although co-rotating twin-screw extruders have been used commercially for many years, there is still a great deal of art and operator experience involved in their successful application. This is because the process operating characteristics depend on a large number of interacting factors. These include material properties such as rheology, thermal conductivity and chemical transformations; geometrical factors such as screw design, leakage gap flows and screw wear; and operating conditions such as screw speeds, feed rates, and barrel temperature profiles. From a process and material transport modelling point of view there are several significant challenges. These include mobile flow boundaries due to the rotation of the screws; mobile interfaces between solid, liquid and gas phases; and a detailed complex geometry that cannot be greatly simplified without eliminating some of the important features that characterise the extrusion process. As a result, twin-screw extruders defy simplistic modelling attempts. At the other end of the modelling spectrum, highly detailed computational fluid dynamics approaches suitable for the twin-screw extrusion process are prohibitively computationally intensive.

Despite these challenges, the value of a generally applicable extrusion process model is evident. New product design or optimisation of existing processes requires extensive experimental trials that are time consuming and costly. This is necessary to understand the effect of the multitude of different operating conditions and possible screw configurations on the process at hand. If these experiments could be replaced in whole or part with computer simulations then the product design cycle would be faster and cheaper.

Extrusion modelling has been addressed in the literature on two different levels: screw component modelling and whole process modelling. Screw component models generally employ detailed finite element fluid modelling techniques that are quite accurate when the boundary conditions can be precisely specified. Such methods are computationally intensive and may require many hours or days of calculation time on a dedicated computer. For this reason they are only applied to short lengths of a particular screw type to analyse the local fluid flow around it. Process models, which consider the entire process from feed hopper to die, need to employ greater process simplifications in order to arrive at a solution in an acceptable time-frame, which is preferably minutes or hours rather than days or weeks. The challenge lies not only in developing computationally cheap models for describing the material transport in the screws, but also in devising a suitable model mechanism which gives a true representation of the boundary conditions and process characteristics while offering a tractable solution. Some existing steady-state process modelling approaches are reasonably advanced, although the prediction capability in general could be improved by representing the boundary conditions more accurately. Dynamic process models, which are necessary to perform process control and residence time distribution simulations, have received little attention in the literature because of the difficulty in representing the moving phase boundaries during transients. There is currently no generally applicable dynamic model that provides an accurate representation of the extrusion process.

The boon of process modelling becomes more significant when some of the newer extruder applications are considered. Extruders are being increasingly applied in specialty areas where they are used as chemical reactors for making plastics and pharmaceutical additives. Chemical reactions contribute an additional dimension of complexity to the process that can be extremely difficult to optimise without a reliable process model. However, models capable of tracking reactions occurring within the extruder need to consider mixing and residence time distribution effects that are not well characterised in existing process models.

Another topic of growing concern in recent years is the reduction of product variability through improved process control. This is particularly an issue in food extrusion processes, which are highly sensitive to process disturbances. This is because the product properties of interest, typically chemical or physical properties such as the degree of cook or extent of puffing, depend on the entire processing history and not just the final temperature at which the product leaves the extruder. Cooking extruders are regularly subjected to

significant disturbances in the feed material properties, as the rheological properties of biological materials can vary seasonally or with storage conditions. By contrast, polymer extrusion processes experience far less variation in their plastic feed materials, and chemical reactions, unless specifically encouraged, do not greatly influence product quality. Good control schemes need to incorporate an understanding of the process to be controlled in order to determine the impact of disturbances on product quality, the best choice of controlled and manipulated variables, and the required degree of controller sophistication. The most cost effective way to carry out such investigations and assess the performance of different control strategies is via simulation studies based on a realistic dynamic process model. Again, this reduces the need for trial-and-error experimentation with candidate control schemes.

A second issue related to process control is the automatic on-line measurement of product quality attributes (PQAs) in a manner suitable for feedback control. Current extruder control systems, where present, usually seek to regulate the process by controlling easily measured process variables such as die temperature and pressure. However, the control of these variables does not necessarily guarantee that the PQAs of interest are also tightly regulated. Novel sensing techniques are becoming increasingly sought after in order to measure or infer the values of PQAs so that they can be regulated using automatic control.

1.2 Scope For Process Improvement

In summary, screw extrusion is a mature process that is unique and widely used, though the exact mechanisms of operation are not entirely understood. In order to utilise extruders optimally and accelerate product development cycles, particularly when a large number of operating parameters can be varied, an accurate and generally applicable process model that is computationally inexpensive would be extremely useful. To enable process control strategies to be investigated, a dynamic process model is required. In order to control PQAs directly rather than indirectly through secondary process variables, new sensing and inferential measurement techniques are required. Each of these issues is addressed by this thesis.

1.3 Thesis Aims and Organisation

The general aim of this thesis is to develop tools that will enable the utilisation of extruders to be improved. The specific goals are to develop a dynamic model of the co-rotating twin-screw extrusion process, to develop a product quality sensor suitable for control purposes, and to evaluate the performance of direct and indirect control strategies on the regulatory control of PQAs. The generic approaches developed in this thesis will be demonstrated predominantly with case studies in food extrusion, although the techniques are completely

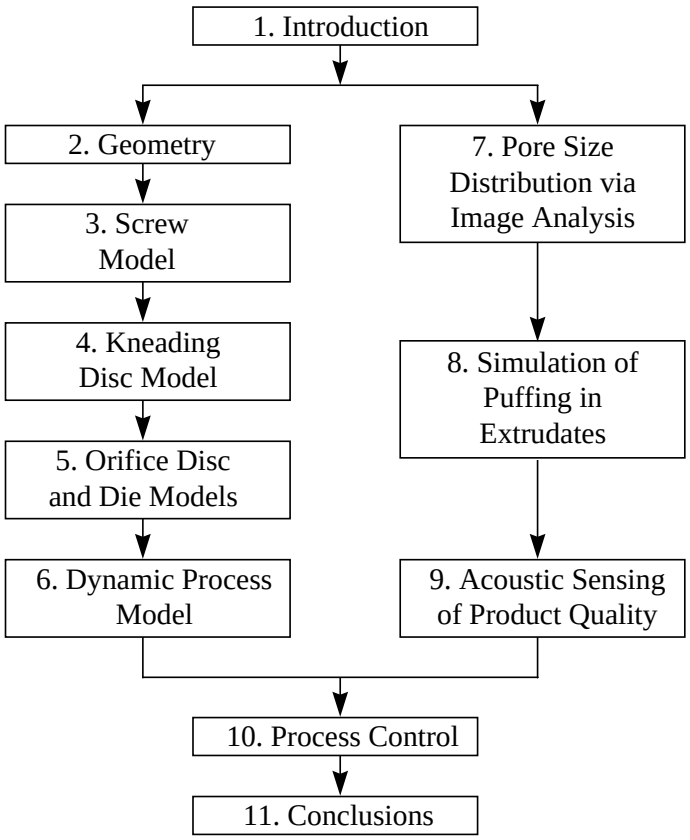

Figure 1.3: Organisation of thesis.

general and can be applied to any co-rotating twin-screw extrusion process. This thesis is organised as shown in Figure 1.3.

Chapters 2–6 of this thesis relate to the development of a dynamic model of the co-rotating twin-screw extrusion process. Chapter 2 considers the geometry of the barrel, die and common screw types that comprise co-rotating twin-screw extruders. The relevant expressions for volume, surface area and cross-sectional geometry of the leakage gaps are sourced from the literature or derived where necessary. Chapter 3 presents a new computationally inexpensive approach for modelling non-Newtonian fluid transport in co-rotating intermeshing screw pairs. The accuracy of the model is assessed by comparing its flow rate predictions with a 3D finite volume solution of the flow equations. Chapter 4 aims to determine which of the published simplified approaches for calculating the flow rate in the kneading discs section of an extruder offer the best accuracy for their computational effort. A simple 1D model and a 2D flow analysis network (FAN) model are compared with a 3D finite volume approach. Chapter 5 is a brief chapter which considers fluid transport in orifice discs and simple circular die elements. Chapter 6 describes how the models for the screw components presented in Chapters 3–5 are combined to simulate the dynamic behaviour of a complete co-rotating twin-screw extrusion process. The basic dynamic model

is extended to include models for gelatinisation kinetics and product bubble growth dynamics to enable product quality attributes to be estimated.

Chapters 7 – 9 relate to automatic metrology and sensing of PQAs of extruded products. Chapter 7 describes a digital image processing technique for analysing cross-sectional images of puffed extruded products that automatically measures the pore size distribution of the sample. Chapter 8 confirms the experimentally observed distributions in Chapter 7 using a simple simulation model for bubble nucleation, growth and coalescence in a puffing medium. Chapter 9 presents an acoustic sensing technique that allows the product bulk density to be measured rapidly and accurately using only the sounds emanating from the extruder.

Chapter 10 considers the model predictive control of an extrusion cooking process. Using the dynamic model of Chapter 6 as a virtual process, both direct and indirect control strategies are examined for regulating the PQAa in the face of process disturbances. Finally, Chapter 11 presents the conclusions from this thesis.

Each chapter is written as much as possible in a self-contained style that introduces the relevant background material, develops or references the necessary theory, presents results and draws conclusions based on those results. This leads to the repetition of some supporting material, but the improvement in the readability of each chapter as a separate piece of work is believed to be worthwhile.

Chapter 2

Geometry of Co-rotating Twin-Screw Extrusion Equipment

Abstract: In this chapter the geometrical information required to model fluid transport and heat transfer in co-rotating twin-screw extrusion equipment is presented. The screw components analysed include trapezoidal flight screws, self-wiping screws, kneading discs, orifice discs, reverse screw elements, the barrel and the die. Expressions are presented for the cross-sectional geometry, surface area and volume of each component as functions of their defining parameters. The geometry of the flow channels is also considered, and two-dimensional cross-sections representative of the shape of the flow channel and leakage gaps are described. These expressions will be used extensively in the subsequent chapters for the development of fluid transport and heat transfer models for co-rotating twin-screw extruders.

2.1 Introduction

The analysis of material transport and heat transfer in screw extruders requires a complete geometrical description of the screws, barrel and die which comprise the machine. In this chapter the geometry of each of these components is reviewed, and expressions for the cross-sectional geometry, surface area and flow volume are presented. The geometries of several common screw types are described, including trapezoidal flight screws, self-wiping screws, kneading discs, orifice discs and reverse screw elements.

The geometry of self-wiping screws and kneading discs has already been investigated in detail by Booy (1978). Trapezoidal flight screws have a simpler geometrical description, though no equations for their surface area have been noted in the literature, so one such expression is derived here. The remaining equipment have trivial geometric descriptions.

One aspect of this thesis involves the development of a new approach for analysing flow in co-rotating intermeshing screw pairs. This analysis requires a description of the screw's leakage gap geometry, which is not available in the literature. Although Janssen (1978) has studied the geometry of leakage gaps in closely intermeshing counter-rotating extruders, the same analysis cannot be applied to co-rotating equipment. Consequently, expressions are derived here for the geometry of the relevant leakage gaps in trapezoidal flight and self-wiping screw pairs.

2.2 Cross-Section Geometry, Surface Area and Volume

2.2.1 The Barrel

The screw shafts rotate within a tightly fitting figure-eight shaped barrel as illustrated in Figure 2.1(a). Only the bore of the barrel is considered here, the geometry being defined by two parameters:

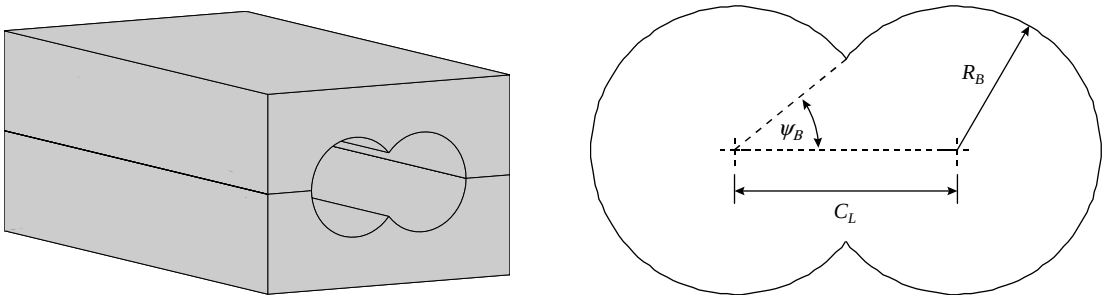

(a) (b)

Figure 2.1: (a) The extruder barrel; (b) geometrical parameters of the bores.

R_B : The bore radius.

C_L : The distance between the screw axes.

The angle ψ_B shown in Figure 2.1(b) is given by:

$$\psi_B = \cos^{-1}\left(\frac{C_L}{2R_B}\right) \tag{2.1}$$

The bore cross-sectional area is equal to

$$A_{BX} = 2(\pi - \psi_B)R_B^2 + C_L R_B \sin\psi_B \tag{2.2}$$

so the volume V_B of a length L of barrel is

$$V_B = A_{BX} L \tag{2.3}$$

The perimeter of the barrel cross-section has a length P_B given by

$$P_B = 4(\pi - \psi_B)R_B \tag{2.4}$$

The internal surface area A_B of a length L of the bore is therefore given by

$$A_B = 4(\pi - \psi_B)R_B L \tag{2.5}$$

2.2.2 Trapeziodal-Flight Screws

Intermeshing pairs of trapezoidal flight screws are shown from different perspectives in Figures 2.2(a)–(c). A cross-section through a trapezoidal flight screw is shown in Figure 2.2(d), revealing the salient geometrical features of this screw type. The screw flight's cross-section is trapeziodal and symmetrical in shape, and the screw geometry is completely specified by 5 parameters:

R_r : The radius of the screw root.

R_s : The radius of the screw tip.

w_c : The channel width.

t_f : The flight tip width.

L_p : The screw pitch length.

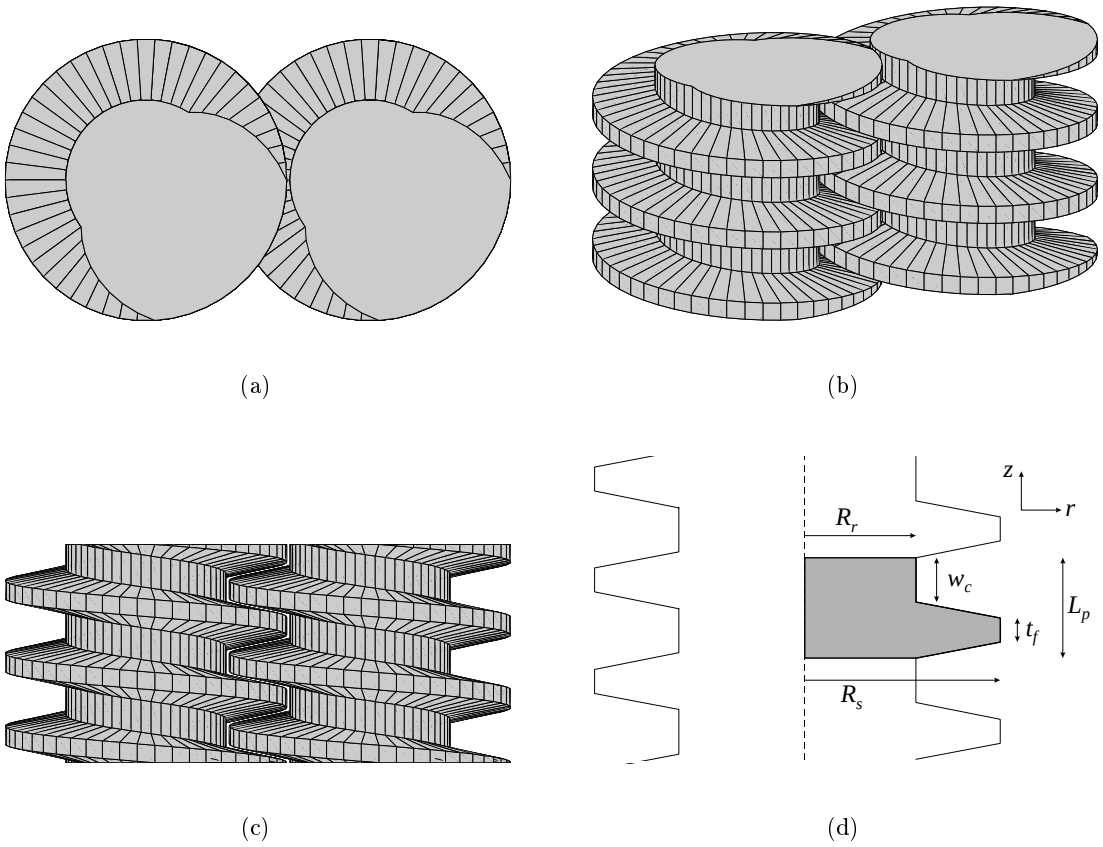

Figure 2.2: The trapezoidal flight screw from (a) plan; (b) orthographic; and (c) elevation perspectives. (d) Screw defining parameters.

The full screw is generated by sweeping the shaded portion in Figure 2.2(d) about the z-axis along a helical path of pitch L_p. Trapezoidal flight screws can be designed to closely intermesh so that the flights of neighbouring screws block each other's flow channel. They can consequently generate steep pressure gradients, and are commonly placed prior to the die and other shaft components which produce a flow constriction.

The radius of the screw surface as a function of the z-coordinate shown in Figure 2.2(d) is given by:

$$r(z) = \begin{cases} R_r + \frac{2(R_s - R_r)}{(L_p - w_c - t_f)} z & \text{for } 0 \leq z < \frac{L_p - w_c - t_f}{2} \\ R_s & \text{for } \frac{L_p - w_c - t_f}{2} \leq z < \frac{L_p - w_c - t_f}{2} + t_f \\ R_r + \frac{2(L_p - z - w_c)(R_s - R_r)}{(L_p - w_c - t_f)} & \text{for } \frac{L_p - w_c - t_f}{2} + t_f \leq z < L_p - w_c \\ R_s & \text{for } L_p - w_c \leq z \leq L_p \end{cases} \tag{2.6}$$

The axial coordinate z is related to the angle of rotation θ about the z-axis by

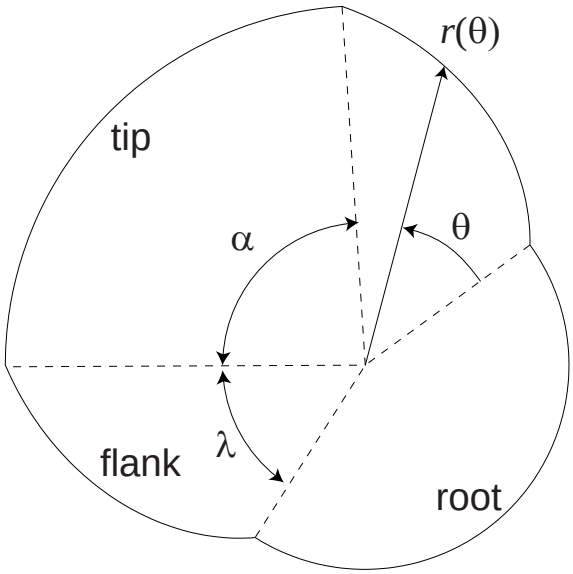

Figure 2.3: Cross-section geometry of the trapezoidal flight screw.

$$z = \frac{L_p \theta}{2\pi} \tag{2.7}$$

Making this substitution into Equation 2.6 provides a definition for the screw cross-section's radius as a function of θ. The cross-section geometry is shown in Figure 2.3. The equation for the radial distance $r(\theta)$ to the flight flank is then

$$r(\theta) = R_r + \frac{L_p \theta (R_s - R_r)}{\pi (L_p - w_c - t_f)} \tag{2.8}$$

The tip angle α is given by the expression

$$\alpha = \frac{t_f}{L_p} 2\pi \tag{2.9}$$

and the angle of the flight flanks λ is

$$\lambda = \frac{L_p - w_c - t_f}{L_p} \pi \tag{2.10}$$

The cross-sectional area of the screw is equal to the contributions from the root, tip and both flanks:

$$A_{SX} = \frac{\alpha}{2} R_s^2 + \frac{2\pi - \alpha - 2\lambda}{2} R_r^2 + 2 \int_0^{\lambda} \frac{r(\theta)^2}{2} \mathrm{d}\theta \tag{2.11}$$

Evaluating the integral using the expression for $r(\theta)$ in Equation 2.8 and simplifying using Equations 2.9 and 2.10 leads to

$$A_{SX} = \frac{\pi}{L_p}\left[t_f R_s^2 + w_c R_r^2 + (L_p - w_c - t_f)\left(R_s R_r + \frac{(R_s - R_r)^2}{3}\right)\right] \tag{2.12}$$

The volume of a trapezoidal flight screw of length L is therefore given by

$$V_S = A_{SX} L \tag{2.13}$$

An expression for the screw surface area is derived using an approach identical to that taken in Booy (1978) who studied the geometry of self-wiping co-rotating screws. The surface area of a trapezoidal flight screw consists of three types of surface: one generated by the tip, the second generated by the root, and the third generated by the flanks. The surface area generated by the tip is:

$$A_{tip} = \alpha R_s L = \frac{t_f}{L_p} 2\pi R_s L \tag{2.14}$$

Similarly, the root curve generates the area:

$$A_{root} = \frac{w_c}{L_p} 2\pi R_r L \tag{2.15}$$

To determine the area A_{flank} generated by one flank curve over an axial length L, consider the screw surface geometry in the proximity of point P on the screw cross-section shown in Figure 2.4(a). Q is a neighbouring point on the flank curve, so PQ lies on the screw surface. S lies on the indicated arc such that $SO = PO = r$. The area of a helical strip through SP (which would lie on a cylinder of radius r) is

$$\mathrm{d}A_{cyl} = L r(\theta)\,\mathrm{d}\theta \tag{2.16}$$

Through S a line can be drawn parallel to the screw axis. That line is perpendicular to the plane of the screw cross-section and perpendicular to SP. The helical curve drawn through P intersects this line at T when $\mathrm{d}\theta$ is appropriately small. The triangle QTP is now an element of the screw surface, while triangle STP is part of $\mathrm{d}A_{cyl}$. Figure 2.4(b) shows the angle γ between the lines SG and QG, which are in a plane normal to PT. Angle $\angle SPT$ is equal to the local helix angle ϕ, which is a function of r given by

$$\phi(r(\theta)) = \tan^{-1}\left(\frac{L_p}{2\pi r(\theta)}\right) \tag{2.17}$$

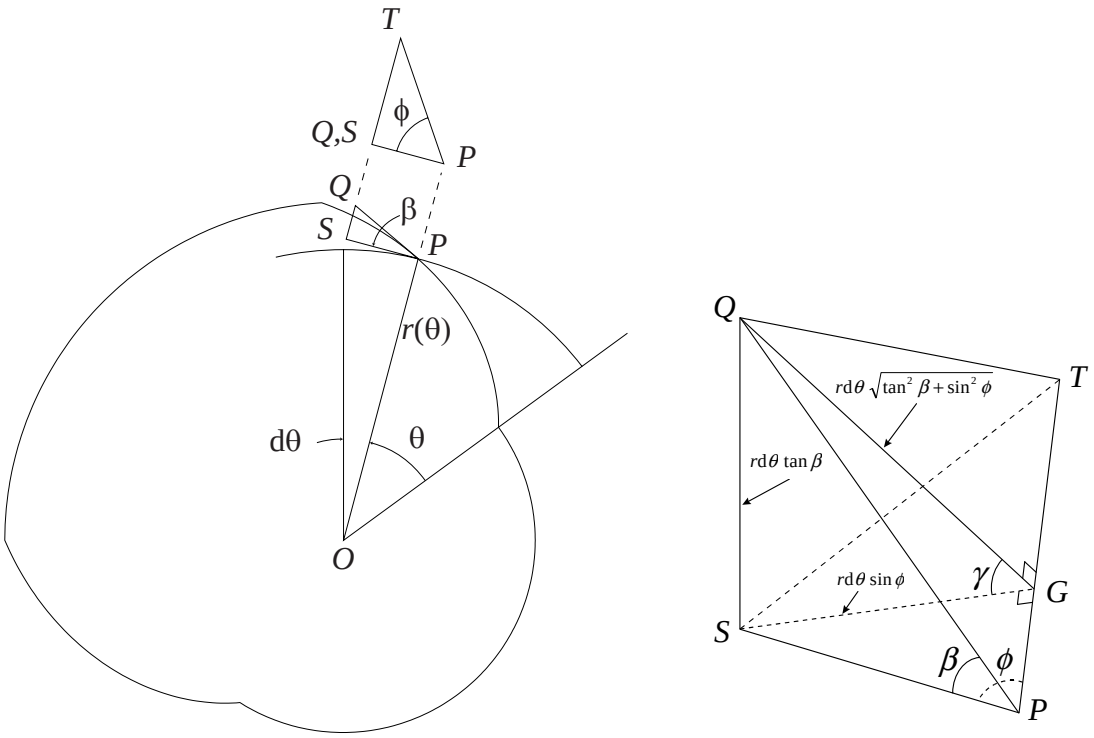

(a) (b)

Figure 2.4: (a) Trapezoidal flight screw surface area element with (b) enlarged perspective of the element.

From Figure 2.4(b) it can be seen that

$$\cos\gamma = \frac{SG}{QG} = \frac{\sin\phi(r(\theta))}{\sqrt{\sin^2\phi(r(\theta)) + \tan^2\beta}} \tag{2.18}$$

From Figure 2.4(a) showing the angle β it can also be seen that

$$\tan\beta = \frac{r(\theta + \mathrm{d}\theta) - r(\theta)}{r(\theta)\mathrm{d}\theta} \tag{2.19}$$

Recognising the definition of the derivative, Equation 2.19 becomes:

$$\tan\beta = \frac{1}{r}\frac{\mathrm{d}r}{\mathrm{d}\theta} \tag{2.20}$$

The radius $r(\theta)$ of the flank surface can be expressed in terms of the known dimensions as per Equation 2.8, resulting in:

$$\tan\beta = \frac{1}{\frac{R_r\pi(L_p - w_c - t_f)}{L_p(R_s - R_r)} + \theta} \tag{2.21}$$

The surface generated by one flank curve becomes:

$$A_{flank} = \int_0^{\frac{\pi(L_p - w_c - t_f)}{L_p}} \frac{Lr(\theta)}{\cos\gamma} \mathrm{d}\theta \tag{2.22}$$

All the variables in Equation 2.22 can be expressed in terms of the defining screw dimensions. This equation can be numerically integrated to determine A_{flank} for a given screw. The total surface area then becomes:

$$A_S = A_{tip} + A_{root} + 2A_{flank} \tag{2.23}$$

One final important note on the geometry of trapezoidal flight screws is that adjacent screws are *in phase* with each other, meaning that the lobes of adjacent screws have the same angular orientation, which can be seen in Figure 2.2(a).

Only single tipped trapezoidal flight screws were relevant to this thesis, although corresponding expressions for multi-tipped trapezoidal flight screws can be easily derived by using a similar analysis to that shown here.

2.2.3 Self-Wiping Screws

Self-wiping screws, by definition, wipe their mate at all rotational positions. This property makes them useful for food and polymer processing as they prevent the build-up of ingredients on the screw surfaces that can cause surging or lead to the degradation of heat and shear sensitive materials. A self-wiping screw is uniquely defined by four parameters:

R_s : The screw radius.

C_L : The distance between the screw axes.

n_t : The number of tips.

L_p : The pitch length.

Figure 2.5 shows examples of both two and three tipped self-wiping screws. In practice, the screws should not physically touch each other, so a clearance gap g_s is provided for. The clearance gap might also be indirectly specified by including the screw root radius R_r, as $g_s = C_L - R_s - R_r$. The analysis presented here will ignore this clearance for the time being, which can easily be accounted for by using a smaller axial spacing $C_L^* = C_L - g_s$ in the calculations.

The self-wiping nature of these so-named screws is demonstrated in Figure 2.6, which shows cross-sections through a pair of self-wiping screws at several stages of rotation. The geometry of self-wiping screws has been investigated in detail by Booy (1978), so this section is essentially a summary of the relevant geometrical expressions reported there. It

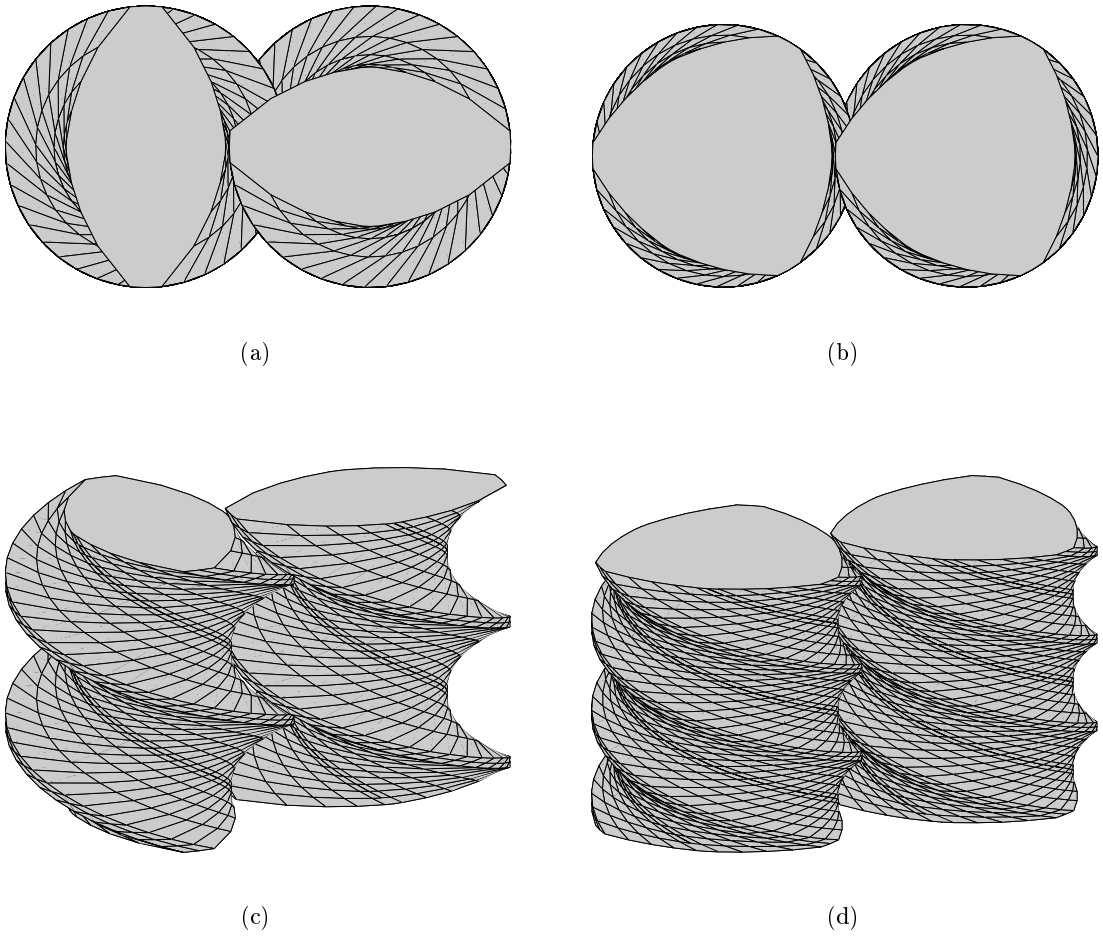

Figure 2.5: Plan and perspective views of self-wiping screws with two and three tips.

is assumed that the screws have equal diameters, rotate in the same direction at identical speeds, and have identical tip and root angles α. If the angle ψ_S is defined in a similar manner to Equation 2.1 as

$$\psi_S = \cos^{-1}\left(\frac{C_L}{2R_s}\right) \tag{2.24}$$

then the tip and root angles α as shown in Figure 2.7 are given by

$$\alpha = \frac{\pi}{n_t} - 2\psi_S \tag{2.25}$$

The root has a constant radius of $C_L - R_s$. The radius of the flank curve at an angle θ as shown in Figure 2.7 is given by:

$$r(\theta) = \sqrt{C_L^2 - R_s^2 \sin^2\theta} - R_s \cos\theta \tag{2.26}$$

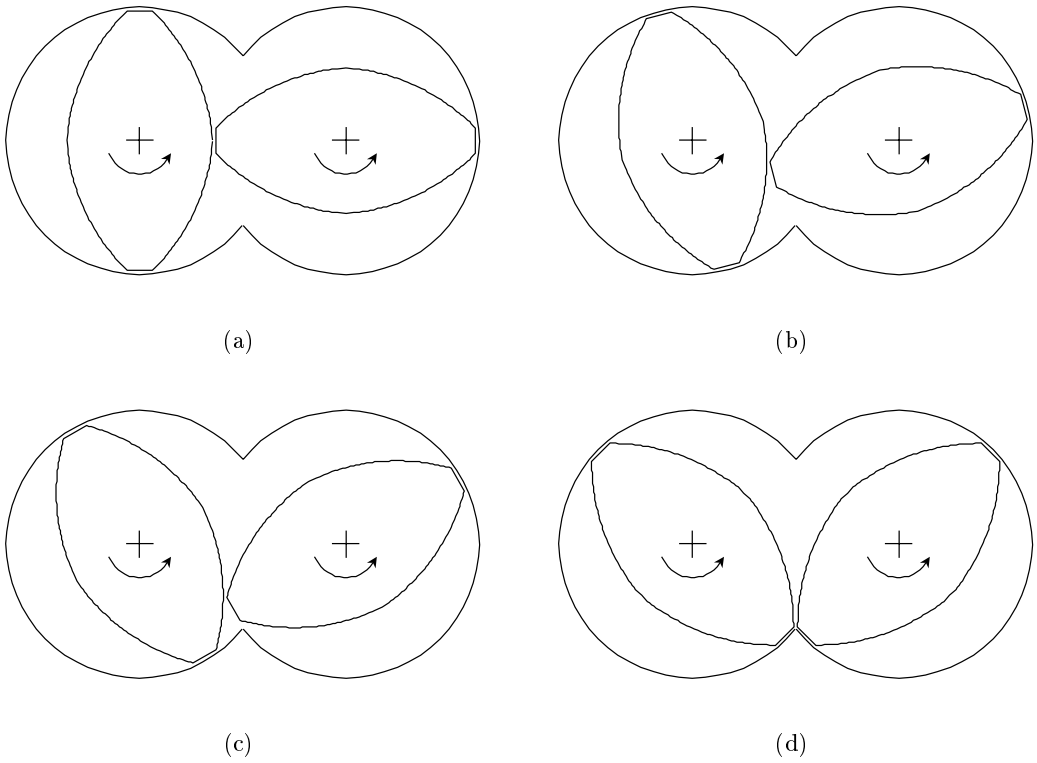

Figure 2.6: Self-wiping screws in various stages of rotation.

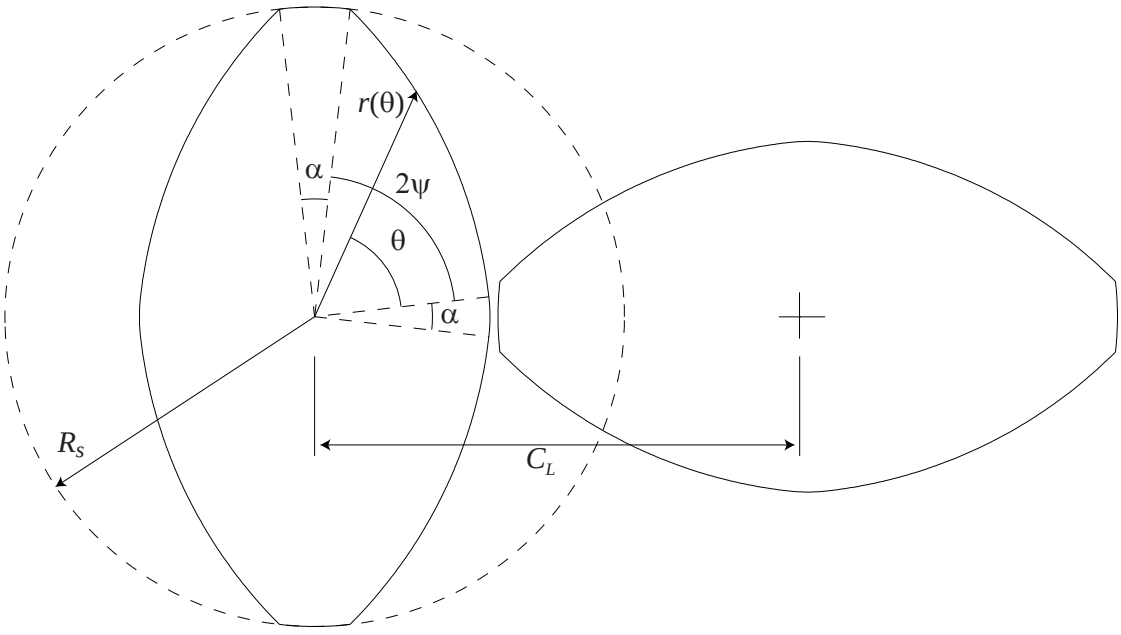

Figure 2.7: Parameters of the self-wiping screw.

and the cross-sectional area of the screw is given by:

$$A_{SX} = n_t \left(\psi_S C_L^2 - C_L R_s \sin\psi_S\right) + \frac{1}{2} n_t \alpha \left[R_s^2 + (C_L - R_s)^2\right] \tag{2.27}$$

The volume of a length L of the screw is therefore

$$V_S = A_{SX} L \tag{2.28}$$

The surface area of a length L of self-wiping screw is given by

$$\begin{aligned} A_S &= n_t L \Bigg[\alpha R_s + \alpha(C_L - R_s) \\ &\quad + 2 \int_0^{2\psi_S} r(\theta) \sqrt{1 + \frac{R_s^2 \sin^2\theta}{\sin^2\phi(r)\left(C_L^2 - R_s^2 \sin^2\theta\right)}} \mathrm{d}\theta \Bigg] \end{aligned} \tag{2.29}$$

where $r(\theta)$ is given by Equation 2.26 and $\phi(r)$ is the local helix angle given by

$$\phi(r) = \tan^{-1}\left(\frac{L_p}{2\pi r}\right) \tag{2.30}$$

The integral term in Equation 2.29 can be evaluated numerically to determine the surface area of the screw.

Self-wiping screw pairs have a phase difference ϕ_s given by

$$\phi_s = \pi - \frac{\pi}{n_t} \tag{2.31}$$

Consequently, a pair of self-wiping screws having two tips will have a phase difference of 90°, which is apparent in Figure 2.7.

2.2.4 Kneading Discs

Kneading discs are used in pairs and employ the same self-wiping geometry in their cross-section as self-wiping screws. The difference for kneading discs is that they have no pitch, and are usually arranged in blocks with successive elements slightly rotated with respect to their neighbours. A block of kneading discs is consequently defined by the parameters:

R_s : The disc radius.

C_L : The distance between the screw axes.

n_t : The number of tips.

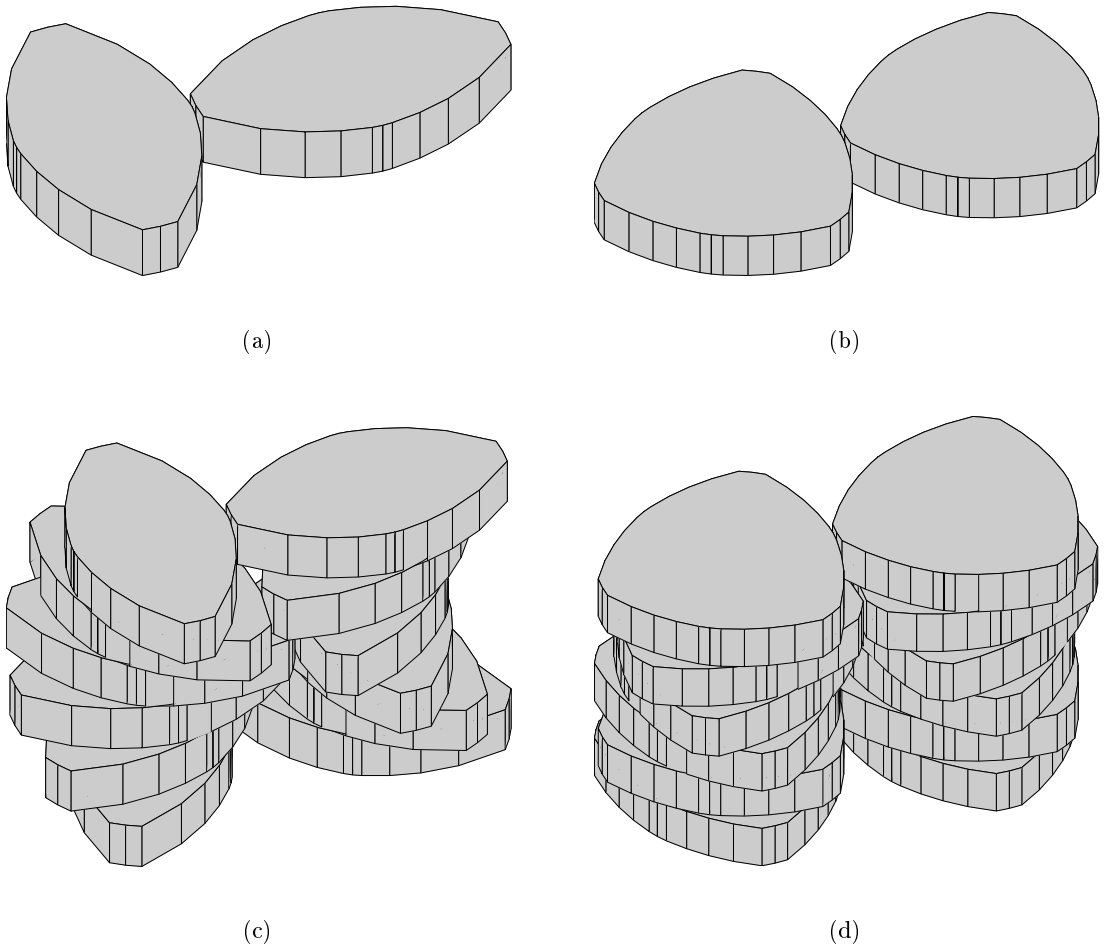

Figure 2.8: (a,b) Single pairs of 2 and 3 lobed kneading discs; and (c,d) blocks of kneading discs arranged in -30° increments.

L_d : The thickness of the disc.

λ_s : The staggering angle between successive discs.

Examples of two and three lobed kneading discs are illustrated in Figure 2.8.

The equations for shape and volume are the same as those given for self-wiping screws in Section 2.2.3. Because the elements have no pitch however, the expression for the surface area of a kneading disc as given by Booy (1978) is:

$$A_S = n_t L_d C_L \left(\alpha + 2\psi_S\right) \tag{2.32}$$

where α and ψ_S are defined in Equations 2.24 and 2.25 respectively.

Kneading discs are used for mixing and shearing the process material. The transport behaviour of kneading discs depends on the relative orientation of successive discs. The discs can be arranged to produce either a neutral, forward or reverse conveying action.

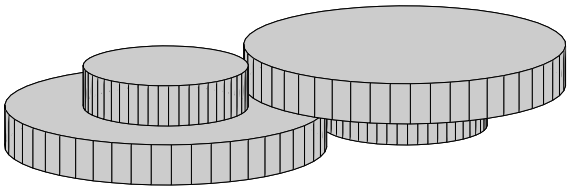

Figure 2.9: A pair of orifice discs.

2.2.5 Orifice Discs

A pair of orifice discs can be used to create a flow constriction at the point where they are placed on the screw shaft. A pair of orifice discs as they would be oriented on a screw shaft are shown in Figure 2.9. Both discs are identical in shape. Orifice disc elements are defined geometrically by three parameters:

R_s : The tip radius of the orifice disc.

R_r : The root radius of the orifice disc.

L_d : The total length of the orifice disc element.

The volume of an orifice disc element is given by

$$V_S = \frac{\pi L_d}{2}\left(R_s^2 + R_r^2\right) \tag{2.33}$$

and the surface area by

$$A_S = \pi L_d\left(R_s + R_r\right) + \pi\left(R_s^2 - R_r^2\right) \tag{2.34}$$

which does not include the top and bottom faces.

In this geometrical definition of orifice discs, no clearance has been allowed for between the overlapping flanks of the discs. In practical designs, a small gap is included.

Flow past a pair of orifice discs can only be through the annular region between the discs and the barrel. When included on a screw shaft, material accumulates in front of the orifice discs until a high enough pressure is generated to force the material through the annular slit. Orifice discs can be used in this way to create regions of high shear and viscous heat dissipation.

2.2.6 Reverse Screw Elements

Reverse screw elements, sometimes called left-handed screws, are threaded oppositely to the forward conveying screws so that they naturally convey material in the opposite direction. Their geometry is therefore a mirror image of the forward conveying version of the screw. The geometrical expressions in Section 2.2.2 and 2.2.3 therefore apply.

Reverse screws are used to create regions of high fill, high pressure and high shear in the extruder. They naturally convey material back towards the feed end of the extruder, so the preceding screw elements must generate high opposing pressures to pump material through them towards the die.

2.2.7 The Die

Process material which reaches the end of the screw shaft enters the die cavity reservoir, where it resides briefly until it is forced out of the extruder. The cavity and die are usually customised to meet individual process requirements, and may be very complex in shape. In this thesis only a simple die geometry is considered. The die is modelled as a reservoir with a circular aperture through which the process material leaves the extruder. The die is normally made of metal which contributes a significant thermal mass to the process. The important parameters concerning the die block are therefore

V_d : The volume of the die cavity.

R_d : The radius of the circular die aperture.

L_d : The length of the die.

V_m : The volume of metal comprising the die block.

2.3 Channel Geometry and Leakage Gaps in Co-rotating Screws

In a simplified analysis of fluid transport in co-rotating screws (i.e. one which does not entail a full 3D solution of the flow equations), it is practical to cut the flow channel into simpler sub-regions and consider the flows between them. This type of analysis requires an understanding of the shape of the flow channels and leakage gaps which connect the different regions of the flow volume.

Figure 2.10 shows a trapezoidal flight twin-screw pair which has been cut at the mid-point between the two screw axes. The screw and its mate both rotate in an anti-clockwise direction when viewed from above. The black arrows indicate the five types of flow route the process material can take between different parts of the flow volume. These five types of flow are identified as follows:

Q_c : The **channel flow** in the C-shaped channels away from the intermeshing region.

Q_t : The **tetrahedron gap flow** between the channels of adjacent screws.

Q_s : The **side gap flow** between the flanks of adjacent screw flights.

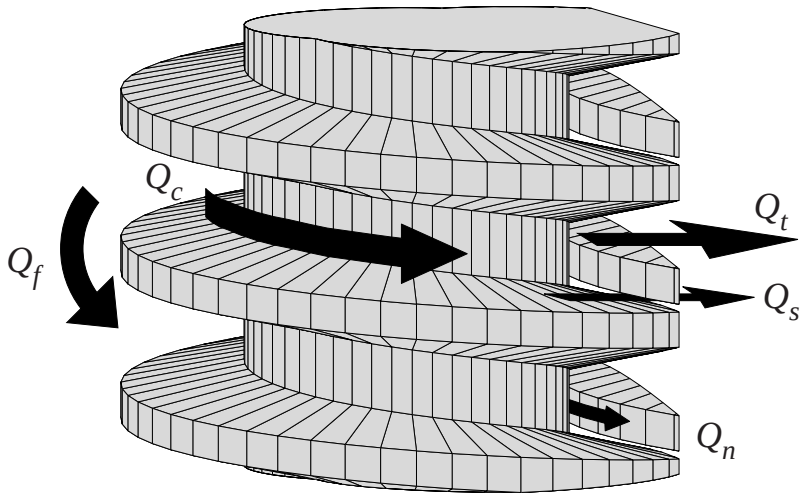

Figure 2.10: Flow in intermeshing screw pairs.

Q_n : The **calender gap flow** through the nip region between the tip of one screw and the root of the adjacent screw.

Q_f : The **flight gap flow** through the annular region between the flight tip and the barrel wall.

The terminology adopted here is identical to that used by Janssen (1978) for describing leakage gaps in counter-rotating equipment. Note, however, that the leakage gap geometries in the present co-rotating geometry are completely different to those reported in this reference.

The geometry of the channel flow and leakage gap cross-sections will be investigated in the following sections. Both trapezoidal flight and self-wiping screw geometries are considered.

2.3.1 The Screw Channel

Axial Cross-Section

Cross-sections through the screw axis of a trapezoidal flight and a double-tipped self-wiping screw are shown in Figures 2.11(a) and (b) respectively. The flow channel has width $G_c(r)$ at a radial distance r from the screw axis. For trapezoidal flight screws the function $G_c(r)$ can be written almost directly from the screw definition of Equation 2.6. It is given by

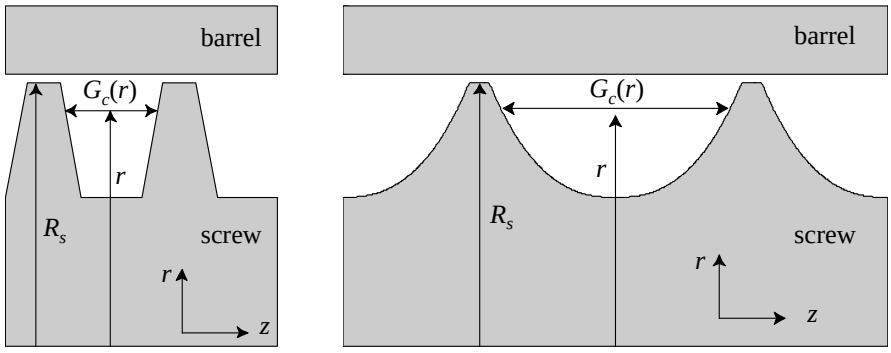

(a) (b)

Figure 2.11: Cross-sections of (a) trapezoidal flight and (b) self-wiping screw types showing channel shape.

$$G_c(r) = w_c + \frac{r - R_r}{R_s - R_r}(L_p - w_c - t_f) \qquad \text{for } R_r \leq r \leq R_s \tag{2.35}$$

For self-wiping screws the channel width is made up of a contribution from the screw root plus contributions from the flanks. The screw root with angle α given by Equation 2.25 makes a contribution of

$$G_c^{\text{root}}(r) = \frac{L_p \alpha}{2\pi} \tag{2.36}$$

The contribution from the flank $G_c^{\text{flank}}(r)$ is derived from Equation 2.26 by substituting for θ using Equation 2.7 and rearranging:

$$G_c^{\text{flank}}(r) = \frac{L_p}{2\pi} \cos^{-1}\left(\frac{C_L^2 - R_s^2 - r^2}{2R_s r}\right) \tag{2.37}$$

The total channel width of a self-wiping screw is therefore given by

$$\begin{aligned} G_c(r) &= w_r + 2w_f(r) \\ &= \frac{L_p \alpha}{2\pi} + \frac{L_p}{\pi} \cos^{-1}\left(\frac{C_L^2 - R_s^2 - r^2}{2R_s r}\right) \quad \text{for } (C_L - R_s) \leq r \leq R_s \end{aligned} \tag{2.38}$$

Transverse Cross-Section

Calculation of the flow in the screw channel using a helical coordinate system requires a description of the screw's transverse cross-section where the span between adjacent flanks is

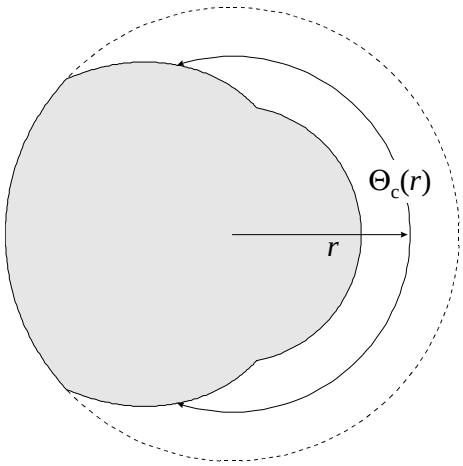

Figure 2.12: Angular span of the trapezoidal flight screw channel cross-section.

expressed as an angle. Figure 2.12 shows the transverse cross-section through a trapezoidal flight screw. The angular distance between flanks $\Theta_c(r)$ is given by

$$\Theta_c(r) = \frac{2\pi w_c}{L_p} + \frac{2\pi(r - R_r)(L_p - w_c - t_f)}{L_p(R_s - R_r)} \quad \text{for } R_r \leq r \leq R_s \tag{2.39}$$

A similar expression can be written for the angular span of a self-wiping screw channel:

$$\Theta_c(r) = \alpha + 2\cos^{-1}\left(\frac{C_L^2 - R_s^2 - r^2}{2rR_s}\right); \qquad \text{for } (C_L - R_s) \leq r \leq R_s \tag{2.40}$$

where α is the tip angle defined according to Equation 2.25.

2.3.2 The Tetrahedron Gap

Flow between the channels of adjacent screws occurs via the tetrahedron gap, as illustrated in Figure 2.13. The shape of the tetrahedron gap is shown in Figures 2.14(a) and (b). The tetrahedron gap is taken to lie on a plane parallel to the two screw axes and equidistant from them both.

In analysing the geometry of the tetrahedron gap, reference is made to Figure 2.15(a) which shows a transverse axial view of an intermeshing screw pair. The section plane AA through the intermeshing region passes through PQR, and the x-coordinate points from P towards R. Figure 2.15(b) shows the section AA indicating the width of the tetrahedron gap, $G_t(x)$, as a function of x.

The cosine rule applied to triangle POQ yields expressions for r and θ as functions of x:

$$r(x) = \sqrt{x^2 + R_s^2 - 2xR_s \sin\psi_S} \tag{2.41}$$

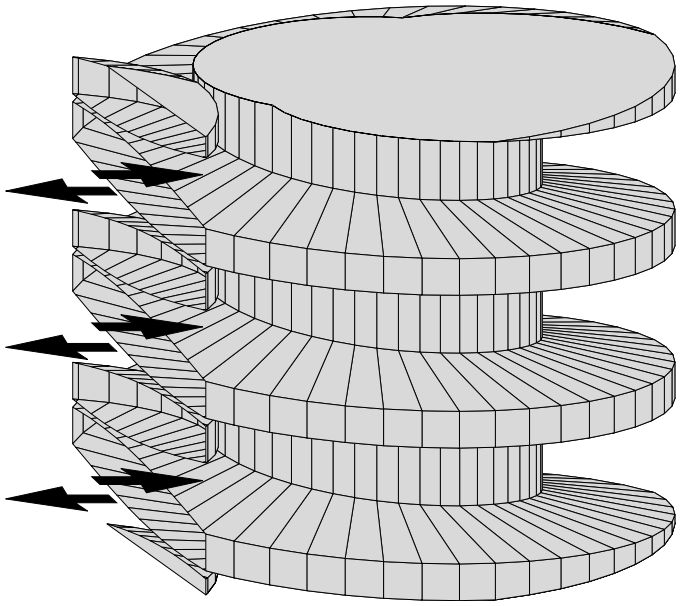

Figure 2.13: Section showing flow in the tetrahedron gap.

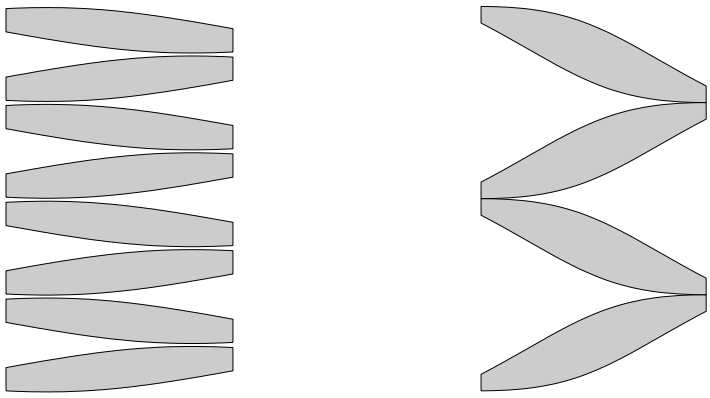

(a) (b)

Figure 2.14: Tetrahedron gaps for (a) trapezoidal flight; and (b) self-wiping screw pairs.

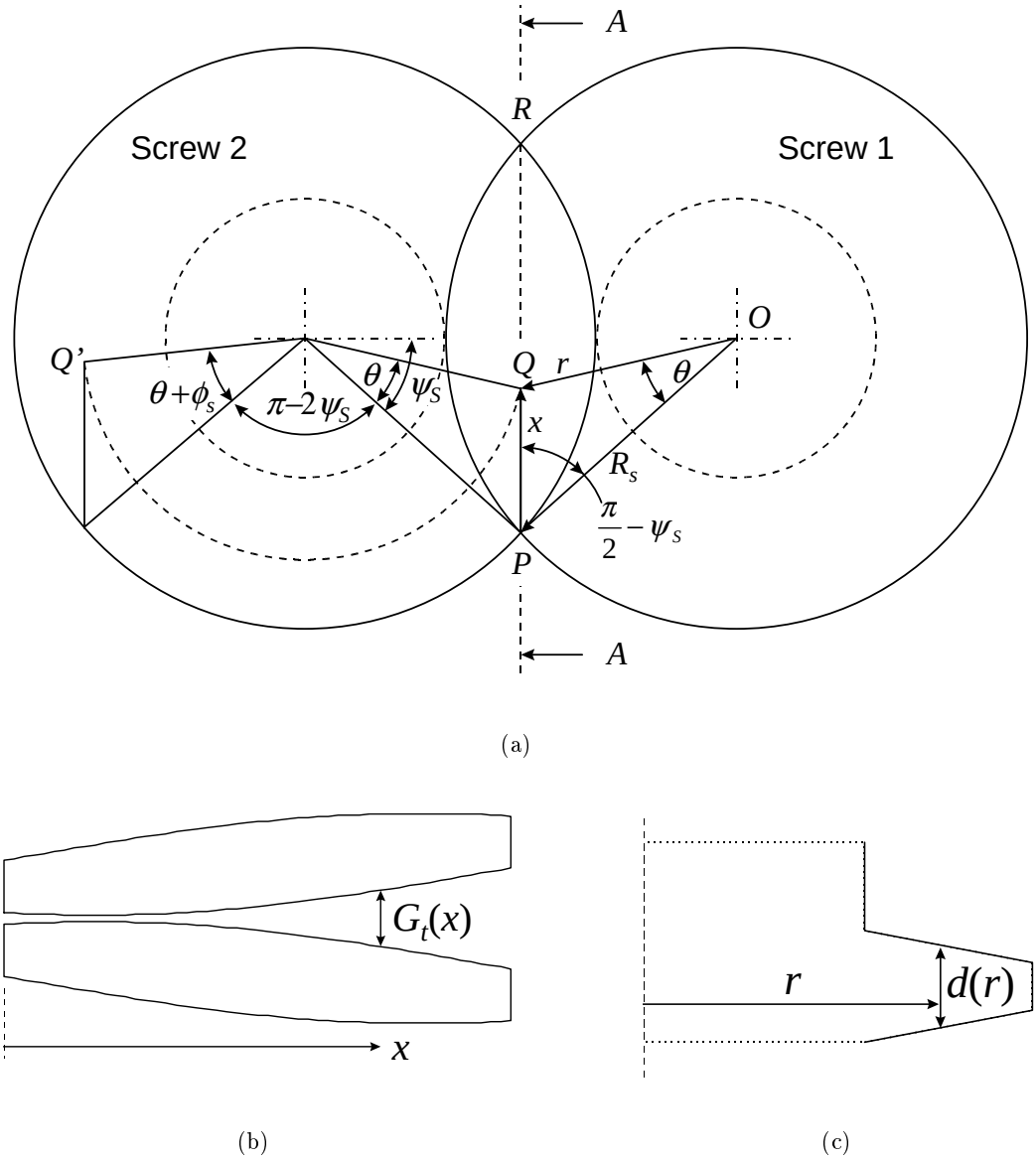

Figure 2.15: Deriving the shape of the tetrahedron gap.

$$\theta(x) = \cos^{-1}\left(\frac{r^2 + R_s^2 - x^2}{2rR_s}\right) \tag{2.42}$$

where

$$0 \leq x \leq \sqrt{4R_s^2 - C_L^2} \tag{2.43}$$

The distance $G_t(x)$ between screw flanks is determined by starting at the point Q on the underside of screw 1's flank, moving to the equivalent point Q' on screw 2, moving along screw 2 to the point directly below the starting point Q on screw 1, and then moving up through screw 2's flight to the top of its flank. By accounting for the vertical distances travelled along this path, $G_t(x)$ can be determined.

If the screws have a phase difference angle of ϕ_s, and the flight thickness at a radius r is given by the function $d(r)$, as shown in Figure 2.15(c), then $G_t(x)$ is given by

$$G_t(x) = \frac{\pi - 2\psi_S + 2\theta + \phi_s}{2\pi} L_p - d(r) - \left\lfloor \frac{\pi - 2\psi_S + 2\theta + \phi_s}{2\pi} n_t \right\rfloor \frac{L_p}{n_t} \tag{2.44}$$

where the delimiters $\lfloor \ldots \rfloor$ prescribe the integer part of, or *floor* of, the contained argument. The floor term is required to account for screws which have more than one tip, as the tetrahedron gap surface may lie between flank surfaces generated by different tips relative to each screw. Equation 2.44 is valid for any type of screw. For a single tipped trapezoidal flight screw, $\phi_s = 0$ and $d(r)$ is given by:

$$d(r) = \frac{(R_s - r)(L_p - w_c - t_f)}{R_s - R_r} + t_f \tag{2.45}$$

For a self-wiping screw, the phase difference ϕ_s is given by Equation 2.31 and $d(r)$ is given by:

$$d(r) = \frac{L_p}{n_t} - \frac{\alpha L_p}{2\pi} - \frac{L_p}{\pi} \cos^{-1}\left(\frac{C_L^2 - r^2 - R_s^2}{2rR_s}\right) \tag{2.46}$$

2.3.3 The Side Gap

The side gap allows material to pass between the flank of one screw and the tip of the other, as shown by Q_s in Figure 2.10. The side gap has an irregular shape as it is bound above and below by the helical surfaces of different screw flanks. Because the tip edge of the screw flight typically comes closest to the adjacent screw flank, the representative side gap geometry is chosen to lie along the tip edge so that it represents the maximum bottleneck to flow presented by the side gap.

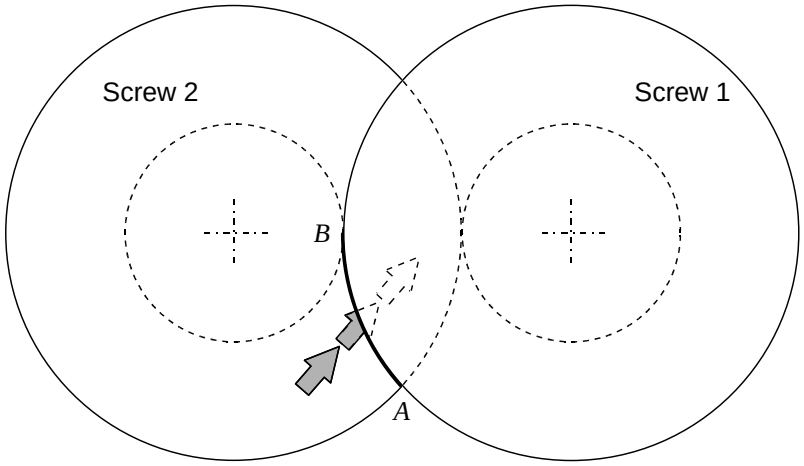

(a)

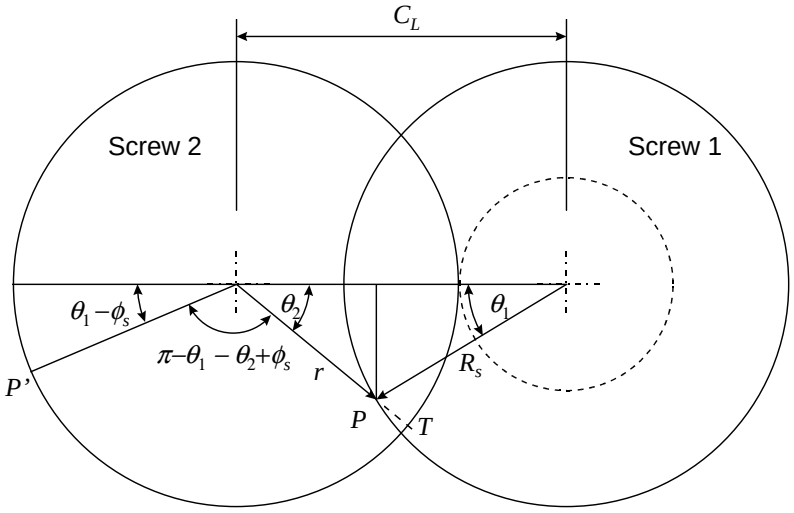

(b)

Figure 2.16: Deriving a representative shape for the side gap.

Figure 2.16(a) shows a plan view of two intermeshing screws. The flight of Screw 1 overlaps that of Screw 2 and the arrows indicate flow through the side gap. Consider points along the arc AB which lie on the flight tip edge of Screw 1, and their distance to the flank surface of Screw 2 *directly below* (i.e. along a path parallel to the screw axes). Figure 2.16(b) indicates such a point P which lies at distances R_s from Screw 1 and r from Screw 2. The position of P is defined by the coordinate θ_1.

The vertical distance $G_s(\theta_1)$ from P to the flank of Screw 2 is derived following a similar procedure to that used for the tetrahedron gap. A path can be taken from P on the tip of Screw 1 to the equivalent point P' on Screw 2 (taking into account the phase difference

between the screws); then moving along Screw 2 to point T at an angle θ_2 relative to Screw 2; moving up to the top of the tip; and then finally moving along the upper flank surface to a position directly below P at a distance r from the centre of Screw 2. By accounting for the vertical distances travelled along this path, $G_s(\theta_1)$ can be determined:

$$\begin{aligned} G_s(\theta_1) &= \frac{(\pi - \theta_1 - \theta_2 + \phi_s)\, L_p}{2\pi} - \frac{t_f}{2} - \frac{d(r)}{2} \\ &\quad - \left\lfloor \frac{(\pi - \theta_1 - \theta_2 + \phi_s)\, L_p}{2\pi} n_t \right\rfloor \left(\frac{L_p}{n_t} \right) \end{aligned} \tag{2.47}$$

where

$$r = \sqrt{(R_s \sin\theta_1)^2 + (C_L - R_s \cos\theta_1)^2} \tag{2.48}$$

$$\theta_2 = \tan^{-1}\left(\frac{R_s \sin\theta_1}{C_L - R_s \cos\theta_1} \right) \tag{2.49}$$

and $d(r)$ is given by Equation 2.45 for a trapezoidal flight screw and Equation 2.46 for a self-wiping screw. Note that Equation 2.47 is valid for all threaded screw types. The parameter θ_1 has the range:

$$0 \leq \theta_1 \leq \cos^{-1}\left(\frac{C_L}{2R_s} \right); \tag{2.50}$$

The floor term $\lfloor \ldots \rfloor$ in Equation 2.47 is required to account for screws which have more than one tip, as the required gap surface will lie between flank surfaces generated by different tips relative to each screw.

The θ_1 argument in Equation 2.47 can be converted to a length argument x representing the distance along the flight tip by making the substitution

$$x = \theta_1 R_s \tag{2.51}$$

Figures 2.17(a) and (b) show typical examples of $G_s(x)$ for trapezoidal flight and self-wiping screws respectively. Note that a perfectly self-wiping screw would have zero clearance between the screws and hence no side gap. The example shown in Figure 2.17(b) is for a self-wiping screw with a clearance $g_s = 0.5$ mm between the screw tip and root.

2.3.4 The Calender Gap

The calender gap is shown circled in Figure 2.18. It can be thought of as a narrow slit of width t_f and length $G_n = C_L - R_s - R_r$.

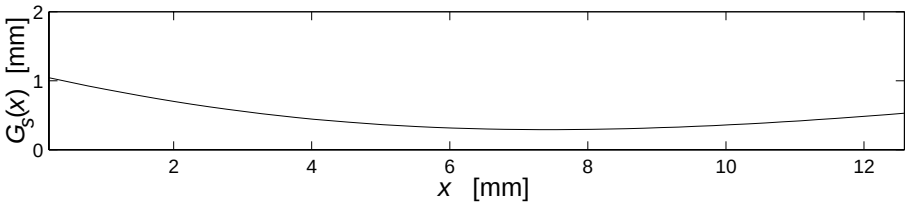

(a)

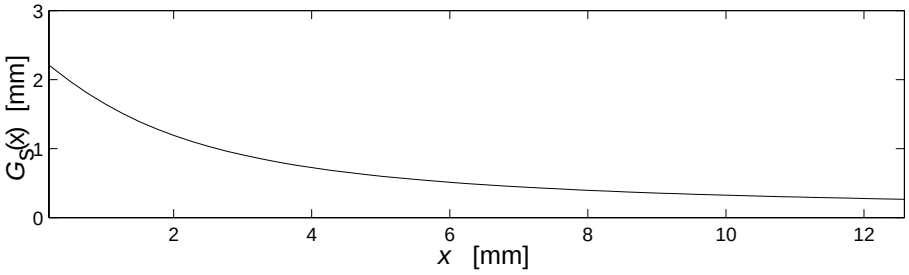

(b)

Figure 2.17: Examples of the width of the side gap for (a) a trapezoidal flight screw pair; and (b) a self-wiping screw pair with $g_s = 0.5$mm.

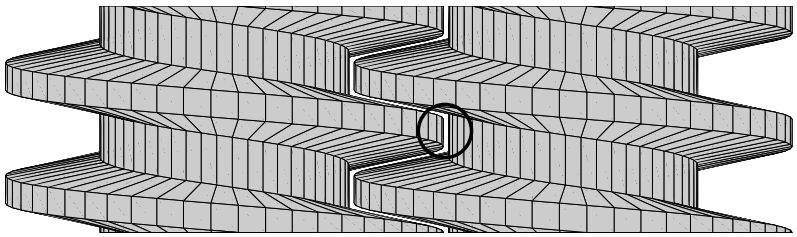

Figure 2.18: The calender gap.

2.3.5 The Flight Gap

The flight gap is the annular space between the screw tip and the barrel wall, as shown in Figure 2.19. The flight gap may be "unwrapped" and treated as a long slit of width $R_B - R_s$ and length L_y given by

$$L_y = \frac{\pi - \psi_B}{\pi}\sqrt{L_p^2 + (2\pi R_B)^2} \tag{2.52}$$

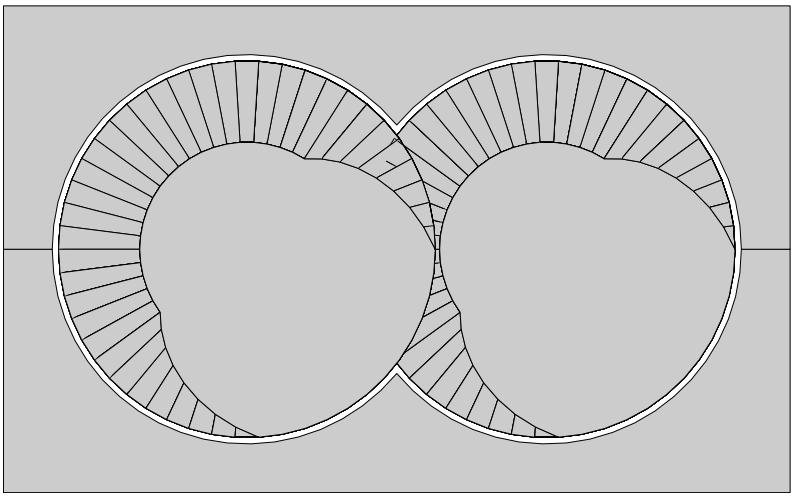

Figure 2.19: The flight gap is the clearance between the screw tips and the barrel wall.

2.4 Conclusions

In this chapter the geometry of co-rotating twin-screw extrusion equipment has been reviewed. The components considered are trapezoidal flight screws, self-wiping screws, kneading discs, orifice discs, reverse screw elements, the barrel and the die. The defining parameters and surface geometry of each component are discussed, and expressions for their surface area and volume are presented. The geometry of the screw channels and leakage gap cross-sections are also developed. The expressions presented here will be used in later chapters to develop models for fluid transport and heat transfer in co-rotating twin-screw extruders.

Chapter 3

Fluid Transport in Co-Rotating Twin-Screw Elements

Abstract: In this chapter a computationally cheap model for fully developed isothermal non-Newtonian fluid transport in co-rotating intermeshing screw pairs is presented. The free volume contained within each pitch length of the screws is divided into two types of volume element for analysis. These consist of C-shaped elements and intermeshing region elements. Six mechanisms for flow between model elements are identified: flow via the screw channel, tetrahedron gap, side gap, calender gap, flight gap, and pumping flow, which represents the positive displacement action of the screws. The forward and reverse flow rates for each type of flow are calculated using simplified flow models whereby the flow cross-section is divided into a one dimensional (1D) mesh for analysis. In this way the velocity fields are estimated iteratively with little computational effort while the results compare well with more accurate 2D approaches. The helical geometry of the C-shaped chambers is taken into consideration by employing a helical formulation of the flow equations. The overall transport behaviour of the screws is determined by writing the mass balances for each element and numerically integrating them to steady-state. By comparing the net throughput versus pressure gradient curves predicted for a sample trapezoidal flight screw pair, it is demonstrated that the simplified model achieves a comparable accuracy to a full 3D finite volume model of the screw pair. The 3D flow analysis is performed on a single pitch length of screws using periodic boundary conditions in a moving frame of reference which allows the exact boundary conditions to be specified. Expressions for the rate of viscous heat generation per unit flow volume as a result of the flows in the system are also presented.

3.1 Introduction

When modelling fluid transport in twin-screw extruders, the extent of detail required depends on the intended application of the model. Screw designers, who may be interested in the conveying efficiency or mixing properties of the screw, might require a full 3D solution of the flow fields around the screws. This can be a computationally demanding task, even on fast modern computers. Process engineers, on the other hand, are usually only interested in the properties of the product which comes out of the extruder.

In such cases where less extensive detail about the fluid transport behaviour is required, simplifications which reduce the computational requirements of the model may be possible. Faster solving models also find broader application in process control and optimisation investigations, which may in themselves be the motivation for developing simplified models.

It is vitally important to assess the accuracy of any simplified model before it can be applied with confidence. This assessment can be made by comparing model predictions with either experimental observations or with more accurate transport models. As the inaccessibility of the fluid inside an operating screw extruder makes good experimental data difficult to acquire, 3D finite element models provide the most appropriate benchmark for model accuracy.

The goal of the present chapter is to introduce a computationally inexpensive first principles model for fluid transport in co-rotating intermeshing screw pairs inside an extruder. Model accuracy is assessed by comparing its predictions with those made using a 3D finite volume model for conditions where the 3D model boundary conditions can be specified exactly.

This chapter begins with a review of the literature relating to the modelling of fluid transport in screw elements in co-rotating twin-screw extruders. Comment is made on the use of correct boundary conditions in the case of 3D finite volume models of screw pairs. This is followed by a brief discussion on the model structure capable of describing a co-rotating twin-screw pair, after which the presently used model structure and the division of the free volume of the screws into model elements is presented. The 1D approach for modelling flows between these volume elements is then derived, along with the boundary conditions used when it is applied to each type of flow channel. A 3D finite volume model for flow in intermeshing screw pairs is then presented. The results section presents a comparison of the flow rates calculated using the 1D and 3D models for a sample trapezoidal flight screw pair over a range of pressure gradients. The chapter closes with a review of the conclusions resulting from this work.

3.2 Review of Flow Modelling in Screw Elements

In this section the literature on modelling fluid transport in screw elements of co-rotating twin-screw extruders is reviewed. The studies are presented in roughly chronological order

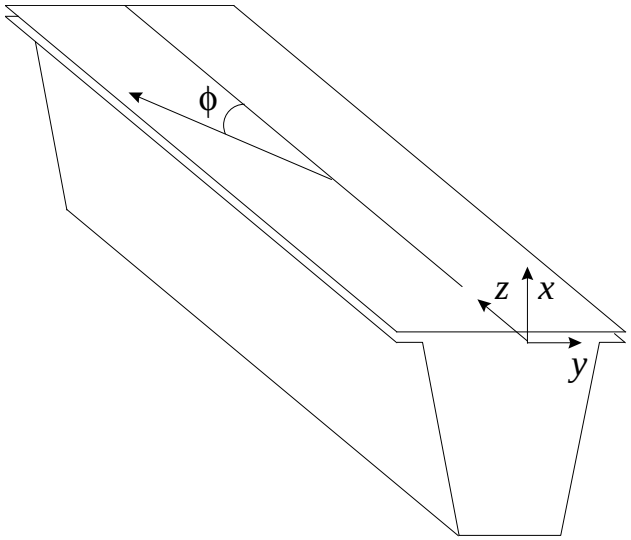

Figure 3.1: A common simplification of the helical screw geometry is to unwrap the channel, treating it as a straight trough with a moving wall.

of their publication and in increasing model complexity.

The first attempts to model screw extruders focused on the single-screw variety. These contributions are relevant to the development of twin-screw extruder models as the flow field in C-shaped regions of twin-screw pairs far away from the intermeshing region is well approximated by the flow field in the channel of a single-screw extruder.

A common approach for modelling flow in the C-shaped screw channel is to unwrap the channel from the screw as depicted in Figure 3.1. The barrel may then be viewed as a flat plate which moves with a velocity $\pi R_B N$ at an angle ϕ (the helix angle) relative to the unwound trough. Helicity and curvature effects are neglected by the unwrapping procedure, so this method is only valid for screw channels which are relatively shallow compared with the screw radius. Down-channel flow in this unwound geometry has an analytical solution for isothermal, Newtonian fluids when the channel cross-section is rectangular or semicircular (Rowell and Finlayson, 1922). Adaptions of this approach have been used to approximate down-channel flow in channels with different cross-sections by applying correcting shape-factors which depend on the depth-to-width ratio of the channel (Tadmor and Klein, 1970). Booy (1980), for instance, applied this technique to self-wiping screw channels; while Tayeb et al. (1988b) adapted the method to model flow in deep screw channels by using a cylindrical (r, θ, z) coordinate system which is tilted by the helix angle so that the angular θ-coordinate points in the down-channel direction at the point of analysis.

The advantage of unwrapping the screw channel or tilting the cylindrical coordinate axes as described above is that one of the coordinate vectors becomes aligned with the down-channel flow direction, reducing the fully developed flow problem in this direction

to 2D. However, this coordinate transform implicitly ignores the helical nature of the screw. To address this problem, Yu and Hu (1997) proposed a helical coordinate system whereby the velocity vector is decomposed into three orthogonal components pointing in the radial, cross-channel and down-channel directions. This helical coordinate system is particularly useful for analyzing fully developed down-channel flow in screws because the problem naturally reduces to 2D without altering the true geometry of the screw.

To accurately model down-channel flow in channel geometries of arbitrary shape, numerical schemes must be employed. To this end, Denson and Hwang (1980) numerically solved the momentum equation in the down-channel direction of an unwrapped self-wiping screw channel for an isothermal, Newtonian fluid. More accurate non-Newtonian approaches were employed by Wang and White (1989), who compared a modified flow analysis network (FAN) model (Tadmor et al., 1974) with a 3D finite element method. Down-channel flows predicted by the two models for unwrapped screw channels agreed within 10% and correlated well with the results of Denson and Hwang (1980) in the Newtonain fluid case.

One of the first attempts to model co-rotating intermeshing screw pairs was made by Booy (1980), who treated the flow region as a continuous channel wrapped around both screws. The twin-screw system is then represented by an equivalent single-screw geometry having an equivalent number of screw channels. This approach was originally proposed for self-wiping screw geometries where the flow across the intermeshing region is relatively uninterrupted. It is not, however, an appropriate simplification for trapezoidal flight screws, which are usually designed to intermesh tightly so to minimise flow across the intermeshing region and thereby maximise pressure development.

The major difficulty in modelling twin-screw extruders arises from the time dependent nature of the flow boundaries due to the screw rotation. This has resulted in many researchers applying various simplifications to the boundary conditions to formulate tractable models.

Tayeb et al. (1988b) and Vergnes et al. (1998) treated the intermeshing region as a local constriction in which only pressure flow is assumed. A more accurate treatment of the intermeshing region was given by Szydlowski and White (1987), who modelled the isothermal flow of Newtonian fluids in self-wiping screws using a 2D FAN approach. The intermeshing region was represented by a transverse offset between two aligned channels representing a pair of adjacent C-shaped chambers. This effectively introduced a flow constriction between the adjacent C-shaped chambers. The screws were assumed stationary with the barrel rotating around them, hence the relative motion of the screws was ignored. Chiruvella et al. (1996) considered flow in both the C-shaped channel and intermeshing regions for non-isothermal, non-Newtonian fluids using a 3D finite volume flow model. The translation and intermeshing regions were modelled separately and then coupled by matching the inlet and outlet conditions of each model in order to simulate the overall

transport in the screws. The geometry of the intermeshing region was simplified into a right-angled channel and the influence of the screw flights was ignored[1]. The relative motion of the screws was also ignored. Goffart et al. (1996) simulated isothermal Newtonian flow in the transport (i.e. C-shaped screw channels) and intermeshing regions of self-wiping screw pairs using a 3D finite element method. The correct 3D geometry of the flow region was used, but the relative motion of the screws was ignored.

No doubt due to the difficulty in representing the time dependent flow boundaries in co-rotating twin-screw extruders, there have been no references noted in the literature where the correct boundary conditions have been used in their modelling. The situation typically envisaged is one where the screws are kept stationary with the barrel wall sliding around the screws. The relative movement of the screws is ignored as a consequence. While such models can provide interesting insights into flow behaviour around such geometries, it must be recognized that the results produced do not correspond to real extruders.

3.2.1 Boundary Conditions in 3D Co-Rotating Twin-Screw Extrusion Simulations

Flow simulations of complete twin-screw extruders are complicated by the moving flow boundaries presented by the rotation of the screws, as there is no frame of reference in which the screw walls or housing do not move into the volume occupied by the model mesh. The numerical techniques for managing this situation involve either re-meshing the entire flow domain after every time step, or the use of mobile meshes and multiple frames of reference. Due to the enormous computational requirements of such approaches, and the fact that such algorithms are not included in many commercial flow simulation software packages, simplified boundary conditions are regularly used in twin-screw extrusion simulations.

However, there is a very useful situation which can be modelled exactly using a stationary mesh approach. This requires one to consider an infinitely long length of the screws so that the entry and exit effects can be ignored. The velocity and pressure fields can then be solved for in a frame of reference moving axially in the conveying direction of the screws at a speed of

$$v_z^{obs} = L_p N \tag{3.1}$$

where L_p is the screw pitch length and N is the rotational speed of the screws. To an observer in this frame of reference the screw and barrel surfaces move tangential to the flow volume at every point[2]. Consequently, the flow analysis can be performed using a stationary model mesh without simplifying the boundary conditions. The exact flow field is then obtained by adding v_z^{obs} to the computed velocity field in the axial direction.

[1] This is the so called parallel plate model where the screw channel is treated as a trough with a bottom and a top but no sides.

[2] This frame of reference is equivalent to an observer sitting on a nut while a screw is turned through it.

The limitation of this approach is that it requires periodic boundary conditions at each pitch length down the effectively infinitely long screws. As a result, this method cannot be used to model situations where the fluid's physical properties or the screw pitch changes down the length of the extruder. Consequently, non-isothermal systems, reacting mixtures and mixing effects cannot be modelled using this method. The benefit, however, is that the conveying properties of co-rotating screws under steady-state isothermal conditions can be calculated accurately using simple stationary mesh approaches.

While Cheng and Manas-Zloczower (1997) and Cheng and Manas-Zloczower (1998) used this moving coordinate system in their analysis of the dynamics of distributive mixing in intermeshing twin-screw conveying elements, they did not exploit the periodic boundary conditions at the entry and exit planes to their screw system. It is curious that there have been no reports in the literature of this approach being used specifically for modelling the fluid transport behaviour of screws.

This approach will be used later in this chapter to perform 3D simulations of fluid transport in co-rotating screw pairs to provide a benchmark for assessing the accuracy of a simplified modelling approach.

3.3 Model Development

3.3.1 Model Structure

The real fluid transport behaviour of twin-screw systems is complex, so some simplification is necessary in order to arrive at a model which solves reasonably rapidly. It is necessary then to reflect on what the fundamental process being performed by the screws is and to ensure that this functionality can be represented properly in the chosen model structure. It has been noted by Bounie (1988) that while model structure has a lesser effect on bulk transport properties, it has extremely important implications for mixing and residence time distribution predictions.

Figure 3.2 shows several possible mechanisms for material transport in a co-rotating twin-screw extruder. The first, shown in Figure 3.2(a), represents one extreme (though impossible) geometry where the screws intermesh perfectly inside a tightly fitting barrel so that the process material is trapped in the C-shaped chambers of the screws. In this situation the extruder acts as a positive displacement pump, conveying the material in each C-shaped chamber to the die cavity where it accumulates until pressure forces it out of the die. This situation is depicted by the analogy of a series of unconnected vessels on a conveyor belt which deposit their contents into a storage vessel, from which material can exit by hydrostatic pressure when sufficiently full.

The second case, shown in Figure 3.2(b), represents an extruder in which the screws do not intermesh at all, so there can be no positive displacement behaviour. The uninterrupted channel of each screw can be represented by a series of stationary reservoirs

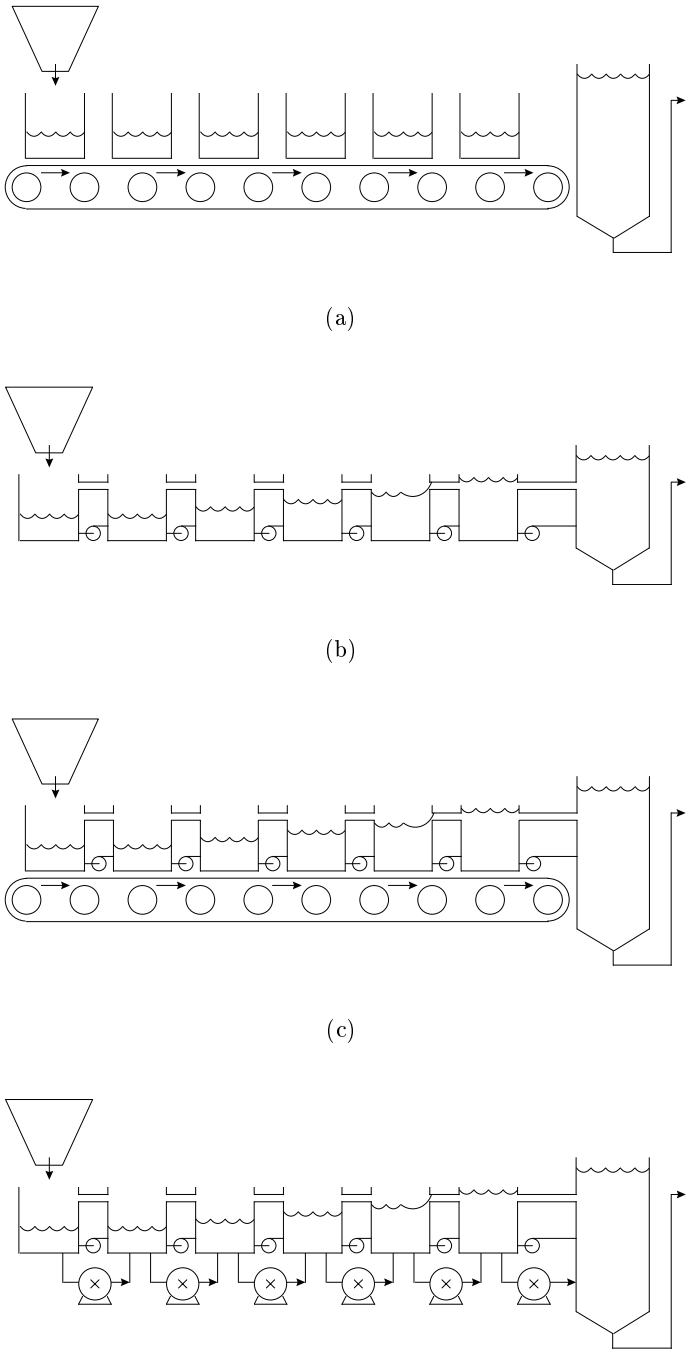

(a)

(b)

(c)

(d)

Figure 3.2: Several ways of modelling the twin-screw extrusion process; (a) pure conveying like a positive displacement pump; (b) pure drag and pressure flow as a series of linked CSTRs with flows both forwards and backwards; (c) the most realistic model structure incorporating both these elements, but requires moving model elements which are difficult to implement; (d) a compromise incorporating a CSTR network with positive displacement pumps (crossed centres) to emulate conveying behaviour.

with material being exchanged between each in series due to pressure and drag flows. This model structure is represented by a series of stationary continuous stirred tank reactors (CSTRs) connected by pumps in the forward direction and overflow pipes in the reverse direction.

The behaviour of a real co-rotating intermeshing extruder lies between these two previous cases. From a process viewpoint, there is a certain capacity for positive displacement behaviour and also for mixing between the imperfectly sealed screw channels due to pressure and drag flow. This situation is depicted in Figure 3.2(c) by a series of CSTRs on a conveyor belt connected by overflow pipes. Inconveniently, this type of model structure is difficult to implement in practice because it requires moving model elements. That is, elements would be required to gradually appear at the feed end of the extruder and gradually disappear as they deposit their contents into the die reservoir. The computational overhead required to implement a model having this structure is a major deterrent to its use as a fast solving simplified model.

The modelling in this chapter therefore employs a model structure having stationary elements. The structure is essentially a series of CSTRs as shown in Figure 3.2(d). In addition to pressure and drag flows between the elements, there is a pure positive displacement flow component represented by an additional pumping flow (depicted by crossed pump elements in Figure 3.2(d)) between the elements in the conveying direction of the screws equivalent to the ideal conveying rate.

3.3.2 Division of the Flow Volume into Model Elements

A twin-screw extruder can be modelled to high accuracy by dividing the flow volume into many (N) small elements and solving for the flows between them. This is the standard approach of finite volume analysis. The disadvantage of this approach is that the computational complexity of the model is approximately $O(N^3)$, as the solution process involves inverting an $N \times N$ matrix (Press et al., 1992)[3]. One can, however, reduce the computational load by strategically dividing the free volume of the extruder into fewer volume elements between which the flow rates can be readily determined. The volume division is completely arbitrary, therefore some heuristic judgement can be applied to ensure that the flows between the resulting elements can be computed easily and that the resulting network of elements captures the essential behaviour of the extruder.

Six mechanisms for flow inside co-rotating intermeshing screw pairs are identified:

Q_c: down-channel flow in the screw channel.

Q_t: flow through the tetrahedron gap between adjacent screw channels.

[3]Note that iterative solution techniques can alternatively be employed, and one can also take advantage of band-diagonal matrix structures to reduce the computational complexity.

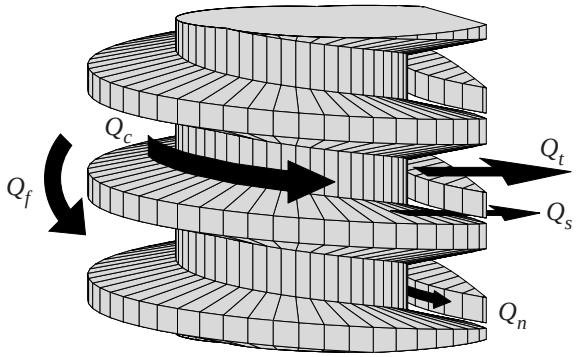

Figure 3.3: Flow through the five identified bottlenecks in intermeshing screw pairs.

Q_s: flow through the side gap between the tip edge of one screw flight and the flank of another.

Q_n: flow through the calender gap between the tip of one screw and the root of the other.

Q_f: flow across the screw flights in the annular region between the flight tip and the barrel wall.

Q_p: flow from the positive displacement action of the screw.

These flows, excluding Q_p, are depicted in Figure 3.3. Although this flow discrimination is entirely arbitrary, with this particular approach all of the bottlenecks and flow avenues around the screws are represented.

By partitioning the flow volume along these flow avenues, the screw volume can be divided into modelling elements. Figure 3.4 demonstrates one such approach for dividing the free volume contained within one pitch length of a single tipped trapezoidal flight screw pair. In this case the screw channel and the tetrahedron gap are partitioned along planes parallel to the screw axis passing through the screw centre and the barrel nip, as shown in Figure 3.5. The resulting six elements comprise two identical C-shaped elements and four identical (by symmetry arguments) intermeshing elements.

For screws with n_t tips, a similar division process produces $6n_t$ volume elements per pitch-length of the screws.

Note that if less than six volume elements were used to represent the present flow volume then some of the flows Q_c, Q_t, Q_s, Q_n or Q_f would occur internally within one of the elements and its influence would not be captured by the model. It might also be noted that although some of these flows may seem insignificant for the geometry shown, they may in fact be quite large in alternative geometries, or when the screws have been worn by

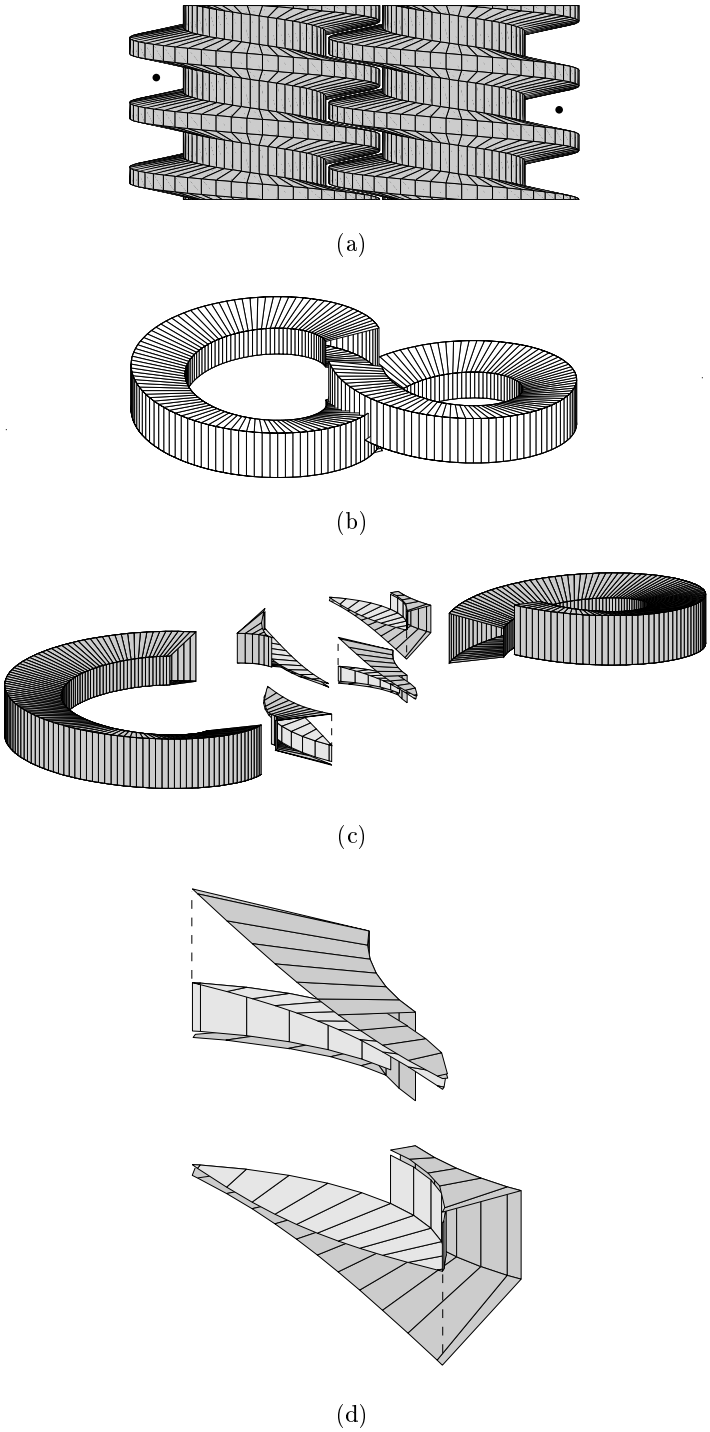

(a)

(b)

(c)

(d)

Figure 3.4: Segmentation of screw pair volume into model elements; (a) a trapeziodal flight screw pair with dots indicating one pitch length of flow volume; (b) the flow volume removed from the screw; (c) exploded view of the flow volume divided into six modelling elements; (d) close-up view of the intermeshing element from two perspectives.

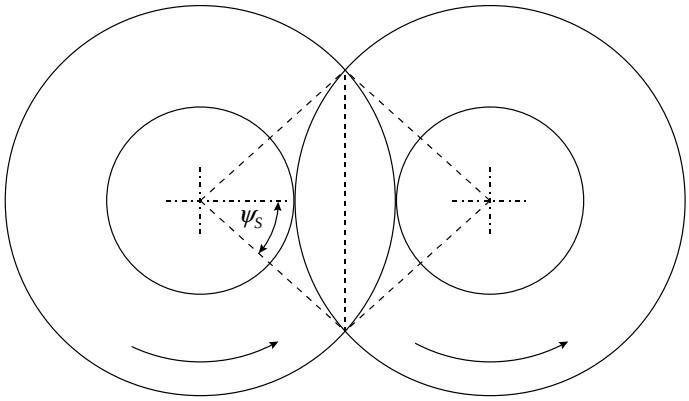

Figure 3.5: Plan view of screws showing divisions between the model sections as dashed lines.

extensive use. For this reason it is recommended that a minimum of $6n_t$ elements be used to represent the volume of one pitch length of an intermeshing screw pair. The division process just described will be used in all the screw analysis performed in this thesis.

Model Element Volumes

The volume of the identified C-shaped and intermeshing region elements follows from the analysis for barrel and screw volumes presented in Chapter 2. The volume of a single C-shaped chamber is given by:

$$V_C = \frac{L_p}{n_t}\frac{(\pi - \psi_S)}{\pi}\left[\pi R_s^2 - A_{SX}\right] \tag{3.2}$$

and the volume of a single intermeshing element is given by

$$V_I = \frac{L_p}{4n_t}\left[R_s C_L \sin\psi_S - \frac{2A_{SX}\psi_S}{\pi}\right] \tag{3.3}$$

where A_{SX} is the cross-sectional area of the screw given by Equation 2.12 for trapezoidal flight screws or Equation 2.27 for self-wiping screws. Note that the annular volume between the screw flight tip and barrel wall is not included in these volumes.

3.3.3 Flow Network Structure

If the free volume in an arbitrary number of pitch lengths of intermeshing screws is divided into volume elements as described in the previous sections, then these elements and the flows which connect them form what could be viewed as a network of CSTRs. Figure 3.6(a) shows a schematic representation of one such network for a single tipped screw, where the elements inside the dashed rectangle represent one pitch length of the screws.

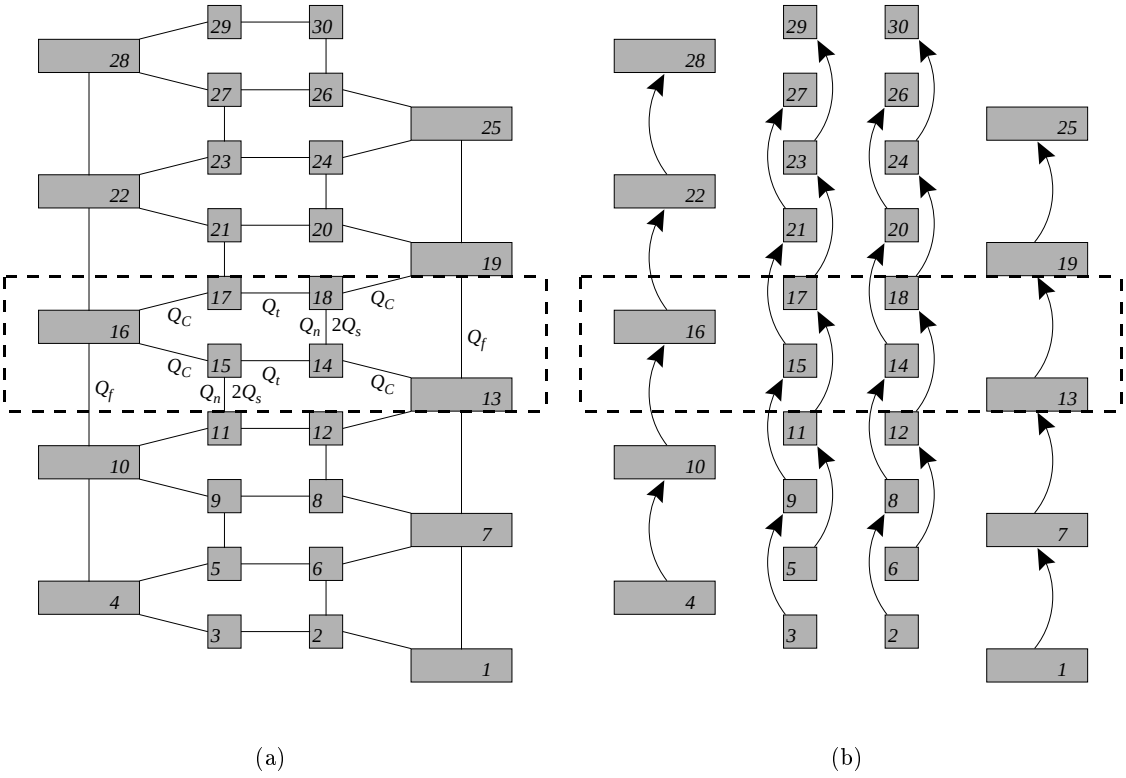

Figure 3.6: Flow network for a single-lobed screw pair; (a) leakage flows; (b) pumping flows. The elements inside the dashed rectangle represent one pitch length of the screws.

In this figure the long rectangles represent C-chamber elements and the squares represent intermeshing elements. In the interest of clarity, the positive displacement flows Q_p are shown separately in Figure 3.6(b). These pumping flows, which occur in addition to Q_c, Q_t, Q_s, Q_n and Q_f, are directed in the conveying direction of the screw only. Networks representing screws with two and three tips are shown in Figures 3.7 and 3.8, respectively.

Note that there are two side gaps connecting adjacent intermeshing regions – one above the intermeshing screw flight and one below it – resulting in a flow of $2Q_s$. This can be readily seen in Figure 3.9, which reveals that the two labeled intermeshing regions are connected by side gaps both above and below the intermeshing flight of the adjacent screw.

If the flow linkages between the elements in these flow networks are removed then one is left with a repeating pattern of six elements. If these elements are numbered sequentially as indicated in Figures 3.6, 3.7 and 3.8 then simple relationships can be written for the indices of connected elements in terms of the number of screw tips n_t. For example, C-shaped channel flow occurs between the C-shaped chamber of index k and intermeshing elements of index $k + i$ and $k - i$ where i is given by:

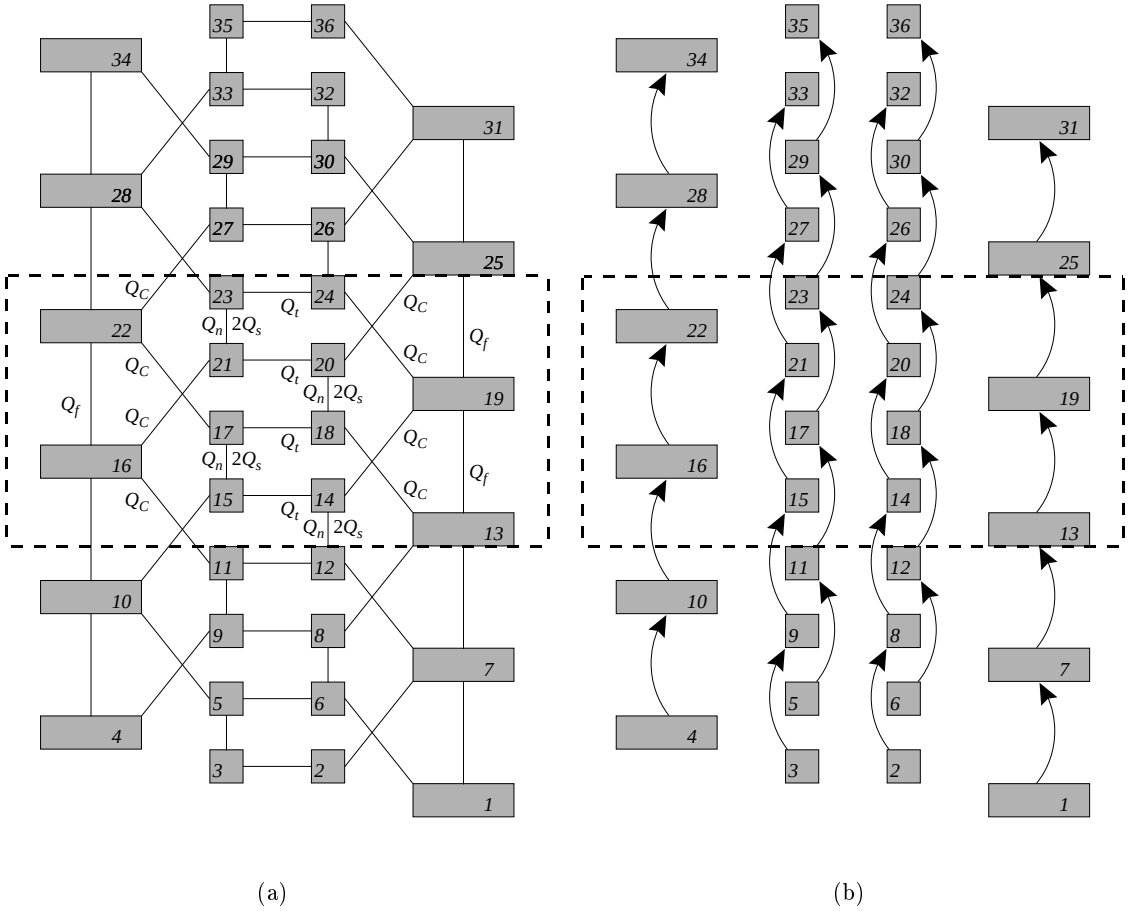

Figure 3.7: Flow network for a double-lobed screw pair; (a) leakage flows; (b) pumping flows. The elements inside the dashed rectangle represent one pitch length of the screws.

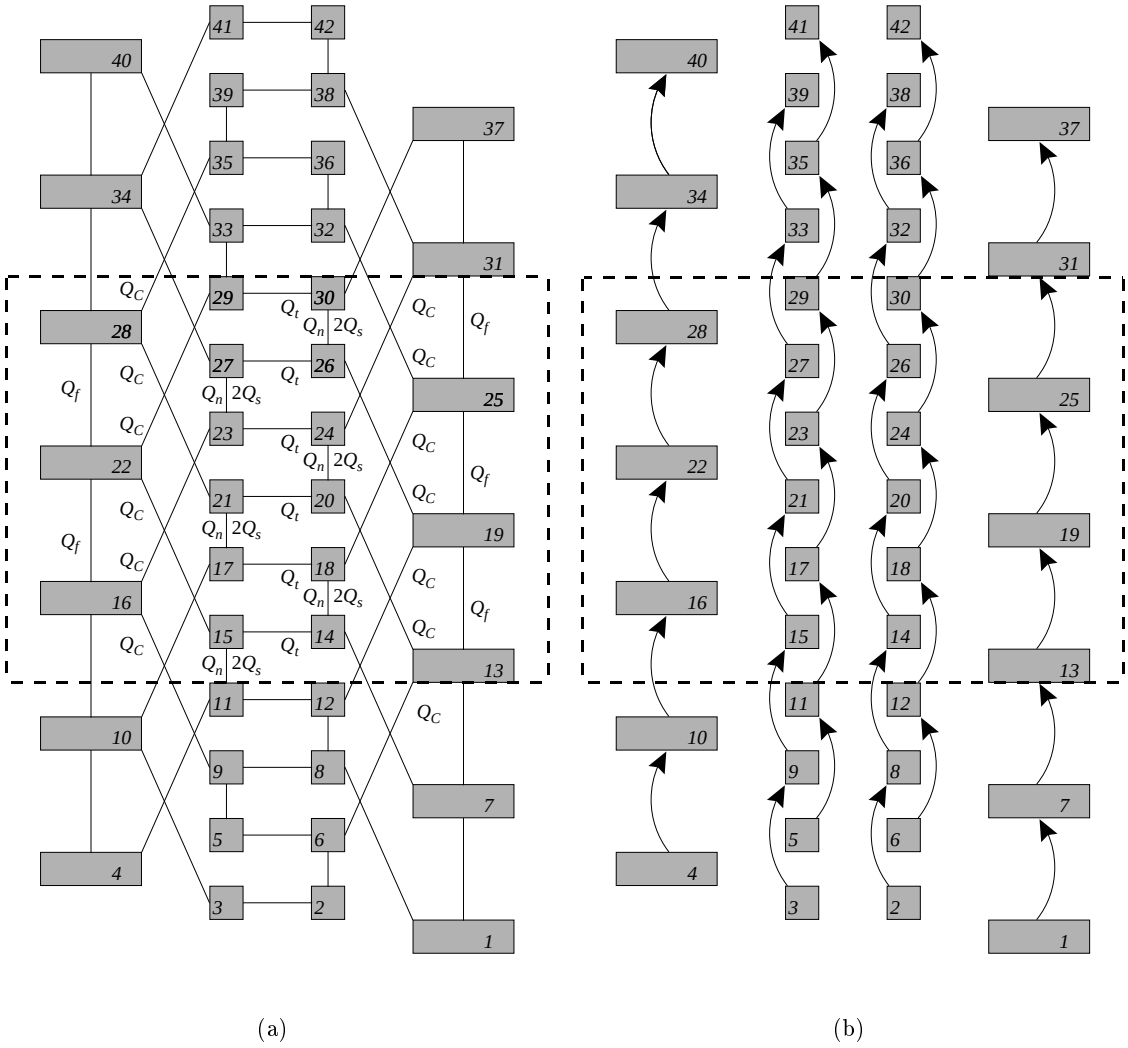

Figure 3.8: Flow network for a triple-lobed screw pair; (a) leakage flows; (b) pumping flows. The elements inside the dashed rectangle represent one pitch length of the screws.

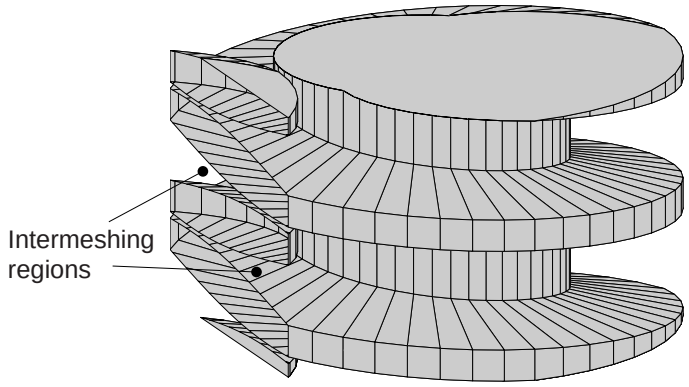

Figure 3.9: A slice through the intermeshing region clarifies that there are side gap flows both above and below the intermeshing flights.

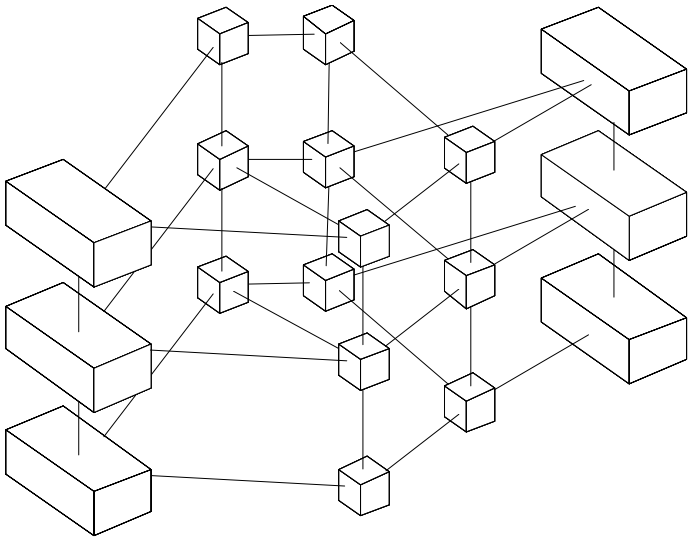

Figure 3.10: Three dimensional perspective view of a single-lobed screw flow network. Positions have been altered for clarity.

$$i = \begin{cases} 1 + 6(n_t - 1)/2 & \text{if } n_t \text{ is odd} \\ 5 + 6(n_t - 2)/2 & \text{if } n_t \text{ is even} \end{cases} \tag{3.4}$$

Similarly, the positive displacement flows Q_p take place between every element k and the corresponding element in the conveying direction of the screw which has index $k + 6$.

Each of the elements in the flow network has a position in space given by the volume's centre of mass along the screw channel's centre-line, so the flow network might also be viewed in a three dimensional diagram as shown in Figure 3.10. In this figure the element positions have been separated for visual clarity, so it is not a scale representation.

3.4 1D Flow Modelling

Having identified an appropriate flow network structure, it remains to determine the magnitude of Q_c, Q_t, Q_s, Q_n, Q_f and Q_p between the model elements under the prevailing conditions of pressure and screw speed. The problem of determining the down-channel flow rate in a conduit of arbitrary shape generally requires a 2D numerical finite element solution of the momentum equation over the conduit cross-section. Such 2D numerical approaches are moderately computationally demanding, requiring the solution of N linear simultaneous equations in the case of Newtonian fluids, where N is the number of 2D mesh elements. For non-Newtonian fluids the equations are nonlinear, necessitating a more computationally demanding iterative solution procedure.

Because the problem of determining the fully-developed flow rate in conduits of various shapes occurs repeatedly in the present screw transport model, a fast solving approach has

been developed where the computation complexity scales with $O(N)$ rather than $O(N^3)$ as for the full 2D case[4].

This approach begins by dividing the flow cross-section into slices along one dimension only. Within individual slices the non-Newtonian viscosity has a uniform average value based on the shear rate along the long axis of the slice only and a parabolic velocity profile ensues. Between adjacent slices, the cross-element shear rate is included in the rate of deformation tensor and the average velocity in each slice is determined numerically. This approach reduces the computational complexity to 1D while giving comparable accuracy to 2D non-Newtonian approaches. An Ostwald-de Waele, or power law, model (Bird et al., 1960) is used to describe the rheology of the process material.

3.4.1 Cartesian Model Formulation

In the present analysis, the channel cross-section is divided into a 1D mesh of rectangular elements inside which the physical properties are assumed to be constant, as indicated in Figure 3.11. The shape of the conduit is defined by $a(x)$ and $b(x)$, which specify the distance of the conduit's lower and upper boundaries from the x-axis. The velocity boundary conditions are specified in the variables $v_a(x)$, $v_b(x)$, v_0 and v_N, as indicated in Figure 3.11. Note that only down-channel flows are considered; circulating flows are ignored in this analysis. In this case, the momentum equation in rectangular coordinates can be written as:

$$0 = \frac{\partial p}{\partial z} - \frac{\partial}{\partial x}\left(\mu \frac{\partial v_z}{\partial x}\right) - \frac{\partial}{\partial y}\left(\mu \frac{\partial v_z}{\partial y}\right) \tag{3.5}$$

The viscosity in each element will be assumed constant, with its value calculated from the local average shear rate and material properties according to the material's rheological model. This will result in a simple Newtonian (parabolic) velocity profile in the y-direction. In the x-direction, for a non-Newtonian fluid, the average velocity in each element will form a non-Newtonian velocity profile. It will be shown in the course of this Chapter that this approach produces results of comparable accuracy to a full 2D solution in the channel. The advantage gained (at the expense of some loss in accuracy) is that iteration is only effectively required in the x direction, reducing the computational requirements to that of a 1D flow problem. This typically reduces the calculation time by several orders of magnitude.

Using this approach it is straightforward to use any rheological model for the extrudate's material properties. In this work the power law rheology model is used throughout, i.e.

[4] Although matrix inversion is an $O(N^3)$ process, the sparsity and band-diagonal nature of the matrix to be inverted in 2D flow problems often permits more efficient matrix inversion methods.

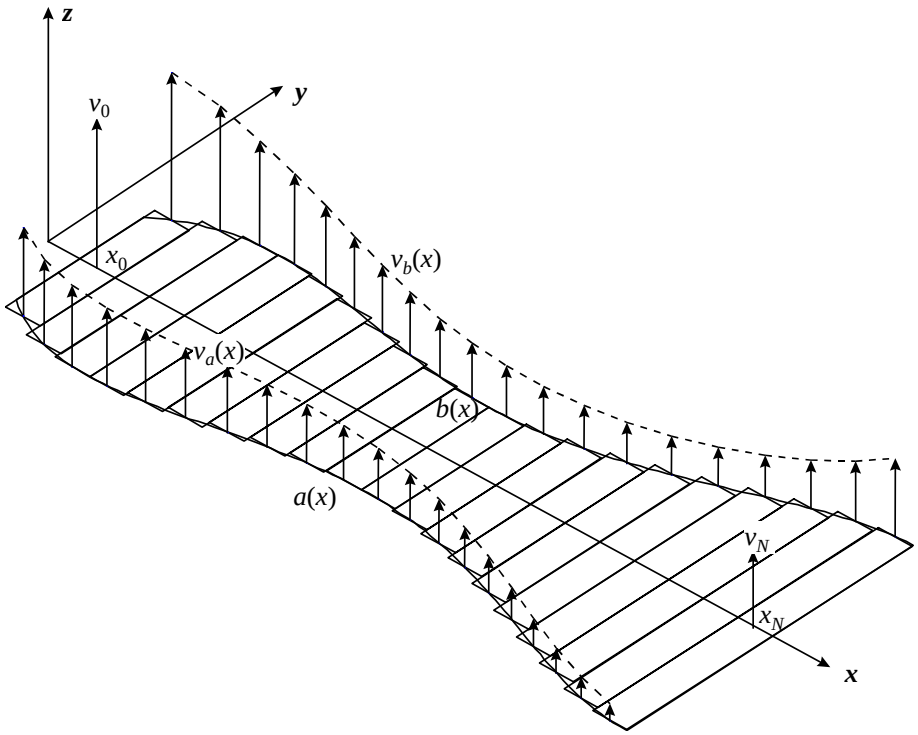

Figure 3.11: Derivation of flow through a general 2D conduit.

$$\mu = K \left[\left(\frac{\partial v_z}{\partial y} \right)^2 + \left(\frac{\partial v_z}{\partial x} \right)^2 \right]^{\frac{n-1}{2}} \tag{3.6}$$

where the consistency, K, and the pseudoplastic index, n, are the parameters of the power law rheology model. Studies by Dolan et al. (1989), Harper et al. (1971), Cervone and Harper (1978) and Vergnes and Villemaire (1987) suggest that a power-law relationship is suitable for describing the rheological behaviour of cereal doughs. Further details on dough rheology models will be presented in Section 6.5.3.

The assumption of constant viscosity in each model element allows the viscosity to be taken outside the y-derivative of the momentum equation. Equation 3.5 then becomes

$$\frac{\partial^2 v_z}{\partial y^2} = \frac{1}{\mu} \left[\frac{\partial p}{\partial z} - \frac{\partial}{\partial x} \left(\mu \frac{\partial v_z}{\partial x} \right) \right] \tag{3.7}$$

If the term in the square brackets in Equation 3.7 is represented by T then integrating Equation 3.7 twice with respect to y gives

$$v_z = \frac{T}{\mu} \frac{y^2}{2} + C_1 y + C_2 \tag{3.8}$$

The integration constants C_1 and C_2 are determined by the no-slip on the screw flights and barrel wall boundary conditions, i.e.

$$y = a(x),\ v_z = v_a(x); \quad y = b(x),\ v_z = v_b(x); \quad x = x_0,\ v_z = v_0; \quad x = x_N,\ v_z = v_N \tag{3.9}$$

The general expression for velocity in a given element is then

$$v_z = \frac{T}{\mu}\left(\frac{(a-y)(b-y)}{2}\right) + y\left(\frac{v_b - v_a}{b-a}\right) + \frac{bv_a - av_b}{b-a} \tag{3.10}$$

The problem remains that T is a function of the velocity v_z gradient in the x-direction, which will vary along the interface between each element. Here, the velocity gradient in the x-direction will be estimated based on the average velocity in each element. The average velocity in an element is given by

$$\overline{v_z} = \frac{\int_a^b v_z \, \mathrm{d}y}{\int_a^b \mathrm{d}y} = \frac{T}{\mu}\left(-\frac{(a-b)^2}{12}\right) + \frac{v_a + v_b}{2} \tag{3.11}$$

Substituting the full expression for T and expressing Equation 3.11 as a difference equation, where X represents the index of the element in the mesh, results in

$$\begin{aligned} \overline{v_z}(X) \;=\; & \frac{1}{\mu(X)}\left[\frac{\partial p}{\partial z} - \frac{1}{\Delta x}\left(\mu(X+1)\frac{\overline{v_z}(X+1) - \overline{v_z}(X)}{\Delta x}\right.\right. \\ & \left.\left. - \mu(X)\frac{\overline{v_z}(X) - \overline{v_z}(X-1)}{\Delta x}\right)\right]\left(-\frac{(a(X) - b(X))^2}{12}\right) \\ & + \frac{v_a(X) + v_b(X)}{2} \end{aligned} \tag{3.12}$$

Equation 3.12 can be written in the form

$$A\,\overline{v_z}(X-1) + B\,\overline{v_z}(X) + C\,\overline{v_z}(X+1) = D \tag{3.13}$$

Writing such equations for all elements X in the mesh provides a set of equations of a tridiagonal form which can be solved efficiently by standard methods (Press et al., 1992). The solution procedure then proceeds as follows:

1. Start with an initial estimate for the viscosity in each model element.
2. Solve Equation 3.13 for the average velocity in each element.
3. Update the viscosity estimates.

4. Repeat until converged.

When estimating the viscosity in each element, the square of the velocity gradient in the y-direction may be approximated by taking the average value over the element, i.e.

$$\overline{\left(\frac{\partial v_z}{\partial y}\right)^2} = \frac{\displaystyle\int_a^b \left(\frac{\partial v_z}{\partial y}\right)^2 \mathrm{d}y}{\displaystyle\int_a^b \mathrm{d}y} = \frac{(a-b)^4\left(\frac{T}{\mu}\right)^2 + 12(v_a - v_b)}{12(a-b)^2} \tag{3.14}$$

where T and μ can be estimated using the values from the previous iteration. The viscosity in element X is then estimated by

$$\mu(X) = K\left[\overline{\left(\frac{\partial v_z}{\partial y}\right)^2} + \left(\frac{\overline{v_z}(X+1) - \overline{v_z}(X)}{\Delta x}\right)^2\right]^{\frac{n-1}{2}} \tag{3.15}$$

Convergence is recognized when the maximum relative change in all the $\overline{v_z}$ between iterations is less than a specified tolerance (10^{-5} here). Convergence is normally obtained in less than 10 iterations.

It should be mentioned that the 1D mesh approach is most accurate when it is applied to symmetrical conduits so that the mesh extends along the axis of symmetry of the conduit, as is done in all cases where it is applied here. This way the shear rate approximation between adjacent elements is likely to be more accurate, as the centres of adjacent elements are aligned in the direction in which the velocity gradient is required.

Determining Forward and Reverse Flow Rates

Pressure and drag flows acting in opposing directions may produce a velocity profile between two elements similar to that shown in Figure 3.12. To correctly model the mixing between two such elements, the forward and reverse components of the flow must be determined separately. This is done by integrating the positive and negative regions of the velocity field separately over the channel cross-section. The positive and negative flow regions are separated by the zeros of the velocity field, which in the present case can be found by solving the quadratic $v_z(y) = 0$ in Equation 3.10. If the roots are labelled y_1 and y_2 in ascending order then the forward Q^+ and reverse Q^- flows are given by

$$Q^+(X) = \max\left(0, \int_a^{y_1} v_z(y)\Delta x\,\mathrm{d}y\right) + \max\left(0, \int_{y_1}^{y_2} v_z(y)\Delta x\,\mathrm{d}y\right) + \max\left(0, \int_{y_2}^{b} v_z(y)\Delta x\,\mathrm{d}y\right) \tag{3.16}$$

$$Q^-(X) = \min\left(0, \int_a^{y_1} v_z(y)\Delta x\,\mathrm{d}y\right) + \min\left(0, \int_{y_1}^{y_2} v_z(y)\Delta x\,\mathrm{d}y\right) + \min\left(0, \int_{y_2}^{b} v_z(y)\Delta x\,\mathrm{d}y\right) \tag{3.17}$$

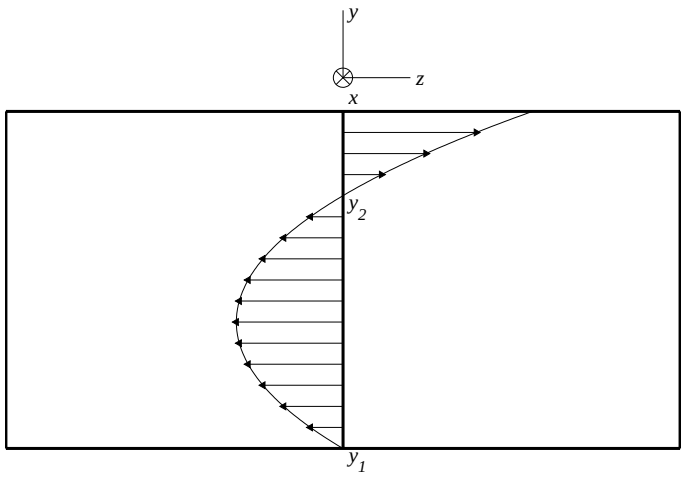

Figure 3.12: Velocity field resulting from pressure and drag flows acting in opposite directions.

Note that if y_1 and y_2 happen to lie outside the range $[a, b]$ they must be thresholded to lie within this range. If y_1 and y_2 are imaginary then the three integrals in Equations 3.16 and 3.17 are replaced by single integrals over the range $[a, b]$. The total forward and reverse flow rates in the conduit are found by summing the results for all X. The explicit integration results are straightforward and will not be included here.

Rate of Viscous Heat Generation

The rate of conversion of mechanical to heat energy per unit volume due to viscous heat dissipation in the channel, $\hat{\dot{U}}$, is given by the negative scalar product of the stress tensor and the velocity gradient, i.e. $(-\boldsymbol{\tau} : \nabla \mathbf{v})$ (Bird et al., 1960). For a power law fluid this term simplifies to $K\dot{\gamma}^{n+1}$, where $\dot{\gamma}$ is the shear rate. In the present case a weighted average value over the conduit cross-section is estimated according to

$$\hat{\dot{U}} = \overline{(-\boldsymbol{\tau} : \nabla \mathbf{v})} = \frac{\sum_X K \left[\overline{\left(\frac{\partial v_z}{\partial y} \right)^2} + \left(\frac{\overline{v_z}(X+1) - \overline{v_z}(X)}{\Delta x} \right)^2 \right]^{\frac{n+1}{2}} (b(X) - a(X))}{\sum_X (b(X) - a(X))} \tag{3.18}$$

The units of $\hat{\dot{U}}$ are $\mathrm{J\,s^{-1}\,m^{-3}}$.

3.4.2 Helical Model Formulation

Fully developed flow calculations naturally reduce to 2D when one of the coordinate vectors is aligned with the down-channel flow direction. For this reason, a common approach to calculating flow profiles in helical screw channels involves unwrapping the channel from

the screw and performing the analysis in Cartesian coordinates. The problem with this approach is that it becomes less accurate when the screw channels are deep relative to the screw pitch length. A more accurate approach is to use a helical coordinate system which naturally describes the helical geometry of the screw channel. The advantage of using helical coordinates for modelling flow in screw channels is that the model is valid for all screw geometries and requires no additional computational overhead compared with an equivalent model in rectangular coordinates. This section will outline the formulation of the flow model for C-shaped channels in helical coordinates.

Helical Coordinate System of Yu and Hu (1997)

Yu and Hu (1997) developed the flow equations in a helical coordinate frame based on the transformation

$$x = r\cos(\varphi(l)+\theta); \quad y = r\sin(\varphi(l)+\theta); \quad z = l\,. \tag{3.19}$$

where

$$\varphi(l) = \frac{2\pi}{L}l \quad \text{and} \quad \varphi' = \frac{\mathrm{d}\varphi}{\mathrm{d}l} = \frac{2\pi}{L}.$$

The natural basis of this helical coordinate system can be written as

$$\begin{bmatrix} \vec{e}_r \\ \vec{e}_\theta \\ \vec{e}_l \end{bmatrix} = \begin{bmatrix} \cos(\varphi(l)+\theta) & \sin(\varphi(l)+\theta) & 0 \\ -r\sin(\varphi(l)+\theta) & r\cos(\varphi(l)+\theta) & 0 \\ -r\varphi'\sin(\varphi(l)+\theta) & r\varphi'\cos(\varphi(l)+\theta) & 1 \end{bmatrix} \begin{bmatrix} \vec{i} \\ \vec{j} \\ \vec{k} \end{bmatrix} \tag{3.20}$$

The unit vectors $\vec{e}_r$, $\vec{e}_\theta$ and $\vec{e}_l$ of the natural basis are not orthogonal, as $\vec{e}_l \cdot \vec{e}_\theta \neq 0$. This non-orthogonality is apparent in Figure 3.13(a). Yu and Hu (1997) derived the momentum and continuity equations for compressible non-Newtonian flow in this coordinate system using an orthogonal decomposition of the velocity vector into its radial (r), cross-channel (w) and down-channel (l) directions, where the unit vectors of this orthogonal basis are related to the rectangular coordinates by

$$\begin{bmatrix} \vec{e}_r \\ \vec{e}_w \\ \vec{e}_l \end{bmatrix} = \begin{bmatrix} \cos(\varphi(l)+\theta) & \sin(\varphi(l)+\theta) & 0 \\ -\sin(\varphi(l)+\theta)/X & \cos(\varphi(l)+\theta)/X & -r\varphi'/X \\ -r\varphi'\sin(\varphi(l)+\theta)/X & r\varphi'\cos(\varphi(l)+\theta)/X & 1/X \end{bmatrix} \begin{bmatrix} \vec{i} \\ \vec{j} \\ \vec{k} \end{bmatrix} \tag{3.21}$$

with $X = \sqrt{1+(r\varphi')^2}$.

When using the helical flow equations of Yu and Hu (1997) one should be careful not to confuse the two coordinate bases in use. To be specific, the calculation is performed

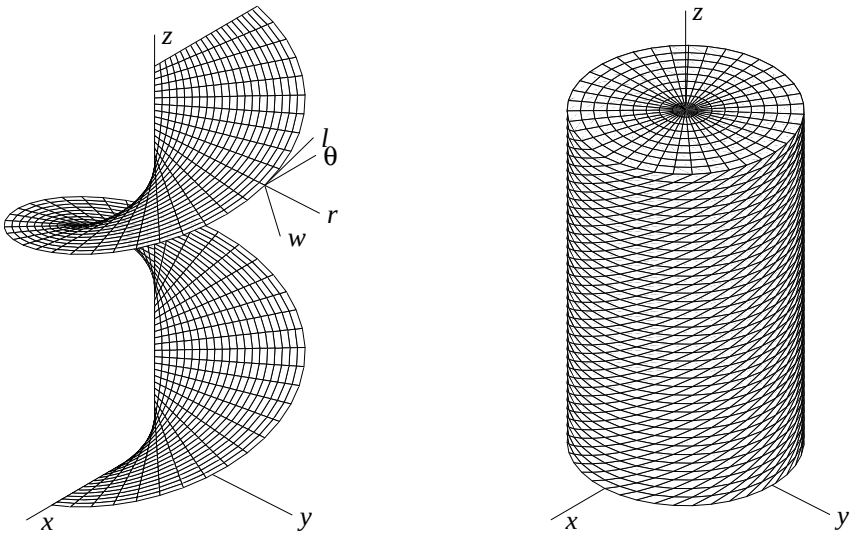

(a) (b)

Figure 3.13: The helical coordinate system used in this study; (a) helicoid surface and relationships between the basis vectors; (b) the non-orthogonal grid in which the calculations take place.

in a non-orthogonal mesh in (r, θ, l) coordinate space, such as the one depicted in Figure 3.13(b). The velocity quantities calculated, however, correspond to the components in the r, w and l-directions.

3.4.3 Flow in the Helical Screw Channel

The present analysis considers fully developed flow in the down-channel direction of a helical screw channel. Cross-channel flows are ignored. In this case the momentum equation of Yu and Hu (1997) in the l-direction reduces to

$$0 = -\frac{1}{X}\frac{\partial p}{\partial l} - \frac{X}{r}\frac{\partial \tau_{lw}}{\partial \theta} - \frac{\partial \tau_{lr}}{\partial r} - \left(\frac{1}{r} + \frac{r\varphi'^2}{X^2}\right)\tau_{lr} \tag{3.22}$$

where

$$\tau_{lw} = -\mu\frac{X}{r}\frac{\partial \tau_{lw}}{\partial \theta} \tag{3.23}$$

$$\tau_{lr} = -\mu\left(\frac{\partial v_l}{\partial r} - \frac{r\varphi'^2}{X^2}v_l\right) \tag{3.24}$$

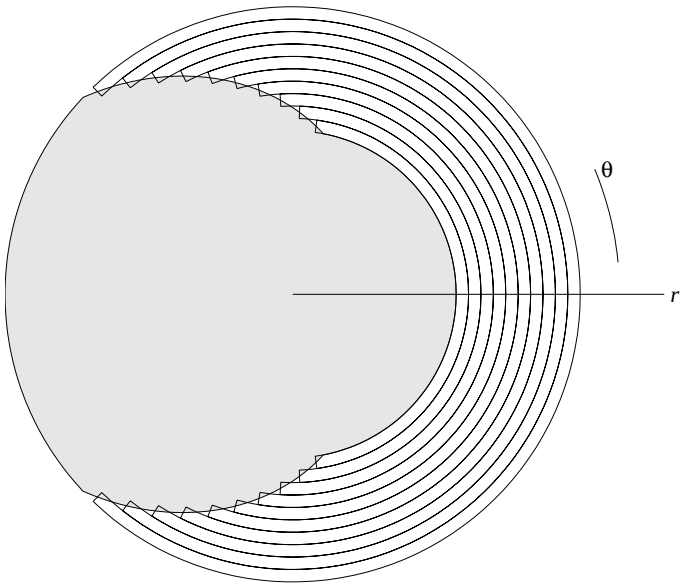

Figure 3.14: The helical screw channel is divided into a 1D mesh in the r-θ plane.

and the power law viscosity is given by

$$\mu = K\left[\left(\frac{X}{r}\frac{\partial v_l}{\partial \theta}\right)^2 + \left(\frac{\partial v_l}{\partial r} - \frac{r\varphi'^2}{X^2}v_l\right)^2\right]^{\frac{n-1}{2}} \tag{3.25}$$

Substituting Equations 3.23 and 3.24 into Equation 3.22 gives

$$\begin{aligned} 0 \;=\; & \frac{1}{X}\frac{\partial p}{\partial l} - \frac{\partial}{\partial \theta}\left(\mu\frac{X^2}{r^2}\frac{\partial v_l}{\partial \theta}\right) - \frac{\partial}{\partial r}\left(\mu\left(\frac{\partial v_l}{\partial r} - \frac{r\varphi'^2}{X^2}v_l\right)\right) \\ & - \left(\frac{1}{r} + \frac{r\varphi'^2}{X^2}\right)\mu\left(\frac{\partial v_l}{\partial r} - \frac{r\varphi'^2}{X^2}v_l\right) \end{aligned} \tag{3.26}$$

If the screw channel is divided into a 1D mesh of elements in the r-direction, as illustrated in Figure 3.14, and the viscosity inside each element is assumed constant, then Equation 3.26 can be rearranged to give

$$\begin{aligned} \frac{\partial^2 v_l}{\partial \theta^2} \;=\; & \frac{1}{\mu}\frac{r^2}{X^2}\left[\frac{1}{X}\frac{\partial p}{\partial l} - \frac{\partial}{\partial r}\left(\mu\left(\frac{\partial v_l}{\partial r} - \frac{r\varphi'^2}{X^2}v_l\right)\right)\right. \\ & \left. - \left(\frac{1}{r} + \frac{r\varphi'^2}{X^2}\right)\mu\left(\frac{\partial v_l}{\partial r} - \frac{r\varphi'^2}{X^2}v_l\right)\right] \end{aligned} \tag{3.27}$$

This equation is of the same form as Equation 3.7 and thus can be integrated and solved in an almost identical manner as described for Cartesian coordinates. The algebra is slightly more involved and in the interests of brevity the remainder of the derivation is omitted.

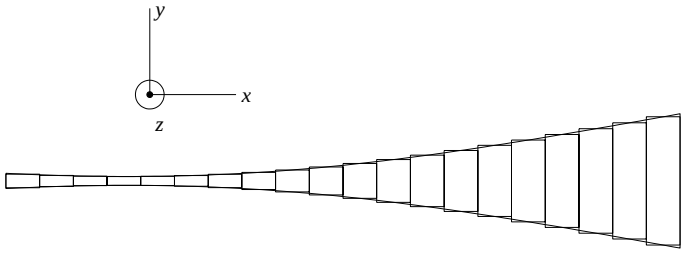

Figure 3.15: The tetrahedron gap divided into a 1D mesh.

The boundary conditions for the C-shaped channel follow on from the assumption of no slip at the screws and barrel wall, i.e.

$$\theta = \pm\frac{\Theta_c(r)}{2},\ v_l = -2\pi r N\cos\phi(r); \quad \theta\text{-direction}$$
$$r = R_r,\ v_l = -2\pi R_r N\cos\phi(R_r); \quad r = R_B,\ v_l = 0; \quad r\text{-direction}$$

where $\Theta_c(r)$ is the channel angular width given by Equation 2.39, N is the screw rotation speed, R_r is the radius of the screw root, R_B is the radius of the screw barrel, and the cosine of the helix angle is given by $\cos\phi(r) = r\varphi'/X(r)$.

3.4.4 Flow in the Tetrahedron Gap

The tetrahedron gap is an imaginary partition separating the two screw halves. Its bounding surfaces lie on the helical flanks of adjacent screws, so it is not exactly correct to model the tetrahedron gap as a conduit with a constant down-channel cross-section. However, in the interests of producing a practical model without going to a computationally demanding 3D solution of the flow equations, this simplification will be applied.

In the present approach the tetrahedron gap is divided into a 1D mesh of elements as shown in Figure 3.15 and the simplified flow model outlined in Section 3.4.1 is applied in a rectangular coordinate frame. The boundary conditions in this case with no slip at the walls are:

$$y = \pm\frac{G_t(x)}{2},\ v_z(x) = 2\pi r N\sin(\psi_S - \theta(x)) \quad y\text{-direction}$$
$$x = 0,\ v_z = 0; \quad x = \sqrt{4R_s^2 - C_L^2},\ v_z = 0; \quad x\text{-direction}$$

where $G_t(x)$ and ψ_S and θ are defined as in Section 2.3.2.

The specific rate of heat generation per unit volume due to viscous dissipation in the tetrahedron gap can be calculated using Equation 3.18.

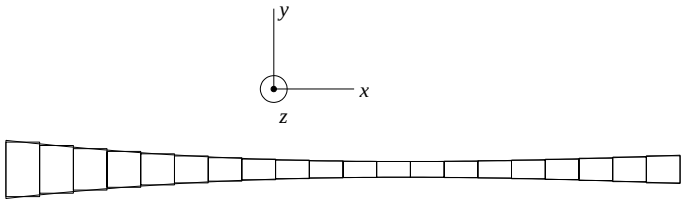

Figure 3.16: The side gap divided into a 1D mesh.

3.4.5 Flow in the Side Gap

Once again a trade-off between model accuracy and tractability must be applied, as the side gap has an irregular geometry in which the flow can only be precisely modelled in 3D. The same approach as used for the tetrahedron gap is applied: the (approximate) side gap cross-section is divided into a 1D mesh as shown in Figure 3.16, and the simplified flow model of Section 3.4.1 is used. The boundary conditions in this case with no slip at the walls are

$$y = \frac{-G_s(x)}{2},\ v_z(x) = -2\pi r(\theta_1)N\sin(\theta_1+\theta_2); \quad y = \frac{g(x)}{2},\ v_z = 0; \quad y\text{-direction}$$
$$x = 0,\ v_z = -2\pi(C_L - R_s)N; \quad x = \psi_S R_s,\ v_z = 0; \quad x\text{-direction}$$

where $G_s(x)$, ψ_S, $\theta_1(x)$ and $\theta_2(x)$ are defined as in Section 2.3.3.

The specific rate of heat generation per unit volume due to viscous dissipation in the side gap can be calculated using Equation 3.18.

3.4.6 Flow in the Calender Gap

The flow through the calender gap is considered at the narrowest point where the gap can be approximated as a long narrow slit of width t_f and height $C_L - R_s - R_r$, as shown in Figure 3.17. The momentum equation in this case reduces to

$$0 = \frac{\partial p}{\partial z} - \frac{\partial}{\partial x}\left(\mu\frac{\partial v_z}{\partial x}\right) \tag{3.28}$$

If an average viscosity in the calender gap is assumed, based on the average shear rate in the gap and the fluid's rheological model, then Equation 3.28 can be rearranged to give:

$$\frac{\partial^2 v_z}{\partial x^2} = \frac{1}{\mu}\frac{\partial p}{\partial z} \tag{3.29}$$

When a power-law viscosity model is used it reduces in the present case to

$$\mu = K\left|\frac{\partial v_z}{\partial x}\right|^{n-1} \tag{3.30}$$

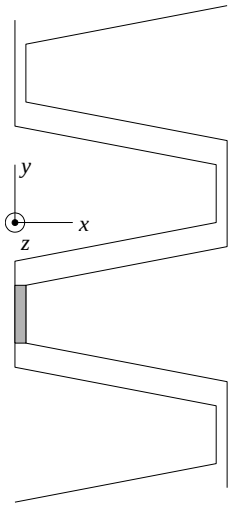

Figure 3.17: The calender gap (shaded) and coordinate system for flow calculation.

Integrating the now linear partial differential Equation 3.29 twice with respect to x and applying the boundary conditions (no slip at the walls), i.e.

$$x = 0,\ v_z = -2\pi R_r N; \quad x = C_L - R_s - R_r,\ v_z = +2\pi R_s N \tag{3.31}$$

leads to

$$v_z(x) = \frac{1}{\mu}\frac{\partial p}{\partial z}\left[\frac{x^2}{2} - \frac{x(C_L - R_s - R_r)}{2}\right] + \frac{x\,2\pi N(R_s + R_r)}{C_L - R_s - R_r} - 2\pi R_r N \tag{3.32}$$

The net forward and reverse flow rates in the calender gap can be determined without iteration by integrating the positive and negative regions of the velocity field separately. Following a similar procedure to that used in the case of general flow in a conduit, the forward and reverse flows are given by

$$\begin{aligned} Q^+(X) = \max\left(0, \int_0^{x_1} v_z(x) t_f \,\mathrm{d}x\right) &+ \max\left(0, \int_{x_1}^{x_2} v_z(x) t_f \,\mathrm{d}x\right) \\ &+ \max\left(0, \int_{x_2}^{C_L - R_s - R_r} v_z(x) t_f \,\mathrm{d}x\right) \end{aligned} \tag{3.33}$$

$$\begin{aligned} Q^-(X) = \min\left(0, \int_0^{x_1} v_z(x) t_f \,\mathrm{d}x\right) &+ \min\left(0, \int_{x_1}^{x_2} v_z(x) t_f \,\mathrm{d}x\right) \\ &+ \min\left(0, \int_{x_2}^{C_L - R_s - R_r} v_z(x) t_f \,\mathrm{d}x\right) \end{aligned} \tag{3.34}$$

where x_1 and x_2 are the roots of the quadratic equation $v_z(x) = 0$ in increasing order and t_f is the screw tip width. Once again, if x_1 and x_2 happen to lie outside the range

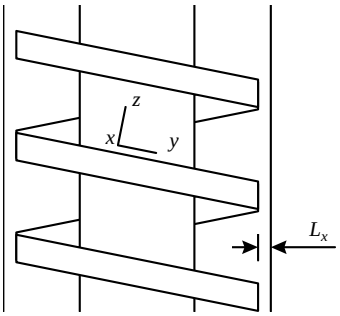

Figure 3.18: The orientation of the coordinate system used for calculating flow in the flight gap.

$[0, C_L - R_s - R_r]$ they must be thresholded to lie within the range. If x_1 and x_2 are imaginary then the three integrals in each of Equations 3.33 and 3.34 are replaced by single integrals over the range $[0, C_L - R_s - R_r]$.

The specific rate of heat generation per unit volume due to viscous dissipation in the calender gap is calculated using Equation 3.18, which simplifies to

$$\hat{\dot{U}}_n = K \left| \frac{\partial v_z}{\partial x} \right|^{n+1} \tag{3.35}$$

3.4.7 Flow in the Flight Gap

The annular geometry of the flight gap along the helical screw tip can be unwrapped and treated as a long narrow slit having length L_y given by

$$L_y = \frac{\pi - \psi_B}{\pi} \sqrt{L_p^2 + (2\pi R_B)^2} \tag{3.36}$$

and width L_x of

$$L_x = R_B - R_s \tag{3.37}$$

A frame of reference attached to the barrel is considered, oriented as shown in Figure 3.18. Flow through the flight gap is a combination of drag flow from the screw flights in the conveying direction of the screws, and pressure flow due to the pressure gradient across the flight. The flow in the flight gap is then described by the momentum equation

$$0 = \frac{\partial p}{\partial z} - \frac{\partial}{\partial x} \left(\mu \frac{\partial v_z}{\partial x} \right) \tag{3.38}$$

There is significant drag flow in the y-direction due to the rotation of the screw, so the power law viscosity is expressed as

$$\mu = K\left[\left(\frac{\partial v_y}{\partial x}\right)^2 + \left(\frac{\partial v_z}{\partial x}\right)^2\right]^{\frac{n-1}{2}} \tag{3.39}$$

The dependence of μ on the $\partial v_y/\partial x$ gradient makes the momentum equation, Equation 3.38, nonlinear requiring an iterative solution procedure. In the present formulation μ will represent the average non-Newtonian viscosity in the channel. Being constant between iterations, it can therefore be taken outside the x-derivative in Equation 3.38, which can then be rearranged to give

$$\frac{\partial^2 v_z}{\partial x} = \frac{1}{\mu}\frac{\partial p}{\partial z} \tag{3.40}$$

Integrating twice with respect to x gives

$$v_z(x) = \frac{1}{\mu}\frac{\partial p}{\partial z}\frac{x^2}{2} + C_1 x + C_2 \tag{3.41}$$

C_1 and C_2 can be determined from the boundary conditions (no slip at the screw or barrel surfaces), i.e.

$$\begin{aligned} x = 0, v_z = 2\pi R_s N \sin\phi(R_s); \quad x = R_B - R_s, v_z = 0; \\ x = 0, v_y = 2\pi R_s N \cos\phi(R_s); \quad x = R_B - R_s, v_y = 0; \end{aligned}$$

where the sine of the helix angle at a radial distance R_s is given by $\sin\phi(R_s) = L_p/\sqrt{L_p^2 + (2\pi R_s)^2}$. The velocity profile then becomes

$$v_z(x) = \frac{1}{\mu}\frac{\partial p}{\partial z}\left(\frac{x^2}{2} - \frac{R_B - R_s}{2}x\right) + \frac{2\pi R_s N \sin\phi(R_s)}{R_B - R_s}x - 2\pi R_s N \sin\phi(R_s) \tag{3.42}$$

When estimating the viscosity μ between iterations, the velocity gradient in the x-direction can be approximated by taking the average value according to

$$\begin{aligned} \overline{\left(\frac{\partial v_z}{\partial x}\right)^2} &= \frac{\int_0^{R_B - R_s}\left(\frac{\partial v_z}{\partial x}\right)^2 \mathrm{d}x}{\int_0^{R_B - R_s}\mathrm{d}x} \\ &= \left(\frac{\partial p}{\partial z}\frac{(R_B - R_s)}{12\mu}\right)^2 + \left(\frac{2\pi R_s N \sin\phi(R_s)}{R_B - R_s}\right)^2 \end{aligned} \tag{3.43}$$

where μ is the value from the previous iteration. The updated viscosity value is then given by

$$\mu = K\left[\overline{\left(\frac{\partial v_z}{\partial x}\right)^2} + \left(\frac{2\pi R_s N \cos\phi(R_s)}{R_B - R_s}\right)^2\right]^{\frac{n-1}{2}} \tag{3.44}$$

After μ converges, the net forward and reverse flow rates through the flight gap can be determined by integrating the positive and negative regions of the velocity field separately. Following a similar procedure to that used in the case of general down-channel flow in a conduit, the net flow rate may be written

$$\begin{aligned} Q^+(X) = \max\left(0, \int_0^{x_1} v_z(x) L_y \,\mathrm{d}x\right) &+ \max\left(0, \int_{x_1}^{x_2} v_z(x) L_y \,\mathrm{d}x\right) \\ &+ \max\left(0, \int_{x_2}^{R_B - R_s} v_z(x) L_y \,\mathrm{d}x\right) \end{aligned} \tag{3.45}$$

$$\begin{aligned} Q^-(X) = \min\left(0, \int_0^{x_1} v_z(x) L_y \,\mathrm{d}x\right) &+ \min\left(0, \int_{x_1}^{x_2} v_z(x) L_y \,\mathrm{d}x\right) \\ &+ \min\left(0, \int_{x_2}^{R_B - R_s} v_z(x) L_y \,\mathrm{d}x\right) \end{aligned} \tag{3.46}$$

where x_1 and x_2 are the roots of the quadratic equation $v_z(x) = 0$ in increasing magnitude. The positive and negative flow rates are therefore determined by adding the positive and negative integrals separately. Once again, if x_1 and x_2 happen to lie outside the range $[0, R_B - R_s]$ they must be thresholded to lie within the range. If x_1 and x_2 are imaginary then the three integrals in Equations 3.45 and 3.46 are replaced by single integrals over the range $[0, R_B - R_s]$.

The rate of heat generation per unit volume due to viscous dissipation in the flight gap is given by

$$\hat{\dot{U}}_f = K\left[\overline{\left(\frac{\partial v_z}{\partial x}\right)^2} + \left(\frac{2\pi R_s N \cos\phi(R_s)}{R_B - R_s}\right)^2\right]^{\frac{n+1}{2}} \tag{3.47}$$

3.4.8 Pumping Flow

The pumping flow is the ideal conveying rate of the screw element, given by

$$Q_p = VNn_t \tag{3.48}$$

where V is the volume of the element from which the flow originates.

Pumping flow is treated as a pure displacement process so there is no viscous heat dissipation resulting from it.

3.5 Solving the Flow Network

Having determined the flow rates Q_c, Q_t, Q_s, Q_n, Q_f and Q_p between the model elements, the dynamic response of each element in the flow network is determined by writing a mass balance over each element in the system, i.e.

$$\frac{\mathrm{d}(f_k V_k)}{\mathrm{d}t} = \sum_i Q_{i\to k} f_i - \sum_j Q_{k\to j} f_k \tag{3.49}$$

where V_k is the volume of element k and f_k is its fill fraction. The i refer to the indices of all the elements from which a flow originates and enters element k, and the j refer to the indices of all the elements which receive flow from element k. To facilitate the calculation, the fluid is assumed to be slightly compressible in which case the change in density of the fluid is related to the change in pressure by the bulk modulus of elasticity, E_v, according to

$$\int E_v \frac{\mathrm{d}\rho}{\rho} = \int \mathrm{d}p \tag{3.50}$$

If the fill fraction f is allowed to take on values slightly greater than one then integration of Equation 3.50 gives the relation

$$p_k = \begin{cases} E_v \ln(f_k) & \text{if } f_k > 1 \\ 0 & \text{if } f_k \leq 1 \end{cases} \tag{3.51}$$

Using the E_v for water of 2.15×10^9 N/m^2, a fill fraction of 1.01 corresponds to an element pressure of 2.13×10^7 Pa, which is unlikely to be reached in the normal safe operation of a screw extruder.

The details of solving the resulting system of ordinary differential equations will be discussed more fully in Chapter 6.

3.6 Three Dimensional Solution of the Flow Equations in Co-rotating Intermeshing Screw Pairs

In the absence of any simplifying approximations, the flow behavior in intermeshing screw pairs can be calculated using a computationally intensive finite volume approach. The three dimensional pressure and velocity fields in a pair of co-rotating intermeshing screws are calculated by numerically solving the continuity and momentum equations for steady-state isothermal creeping flow of an incompressible power-law fluid. An alternating direction implicit solution method is used. The equations to be solved are:

$$\nabla \cdot \mathbf{v} = 0 \tag{3.52}$$

$$-\nabla \cdot \boldsymbol{\tau} = \nabla p \tag{3.53}$$

where $\boldsymbol{\tau}$ is the stress tensor. For a non-Newtonian incompressible fluid the momentum Equation 3.53 in rectangular coordinates becomes:

$$\begin{aligned} 0 &= -\frac{\partial p}{\partial x} + \frac{\partial}{\partial x}\left(\mu \frac{\partial v_x}{\partial x}\right) + \frac{\partial}{\partial y}\left(\mu \frac{\partial v_x}{\partial y}\right) + \frac{\partial}{\partial z}\left(\mu \frac{\partial v_x}{\partial z}\right) \\ &\quad + \frac{\partial \mu}{\partial x}\frac{\partial v_x}{\partial x} + \frac{\partial \mu}{\partial y}\frac{\partial v_y}{\partial x} + \frac{\partial \mu}{\partial z}\frac{\partial v_z}{\partial x} \end{aligned} \tag{3.54}$$

$$\begin{aligned} 0 &= -\frac{\partial p}{\partial y} + \frac{\partial}{\partial x}\left(\mu \frac{\partial v_y}{\partial x}\right) + \frac{\partial}{\partial y}\left(\mu \frac{\partial v_y}{\partial y}\right) + \frac{\partial}{\partial z}\left(\mu \frac{\partial v_y}{\partial z}\right) \\ &\quad + \frac{\partial \mu}{\partial x}\frac{\partial v_x}{\partial y} + \frac{\partial \mu}{\partial y}\frac{\partial v_y}{\partial y} + \frac{\partial \mu}{\partial z}\frac{\partial v_z}{\partial y} \end{aligned} \tag{3.55}$$

$$\begin{aligned} 0 &= -\frac{\partial p}{\partial z} + \frac{\partial}{\partial x}\left(\mu \frac{\partial v_z}{\partial x}\right) + \frac{\partial}{\partial y}\left(\mu \frac{\partial v_z}{\partial y}\right) + \frac{\partial}{\partial z}\left(\mu \frac{\partial v_z}{\partial z}\right) \\ &\quad + \frac{\partial \mu}{\partial x}\frac{\partial v_x}{\partial z} + \frac{\partial \mu}{\partial y}\frac{\partial v_y}{\partial z} + \frac{\partial \mu}{\partial z}\frac{\partial v_z}{\partial z} \end{aligned} \tag{3.56}$$

For a power-law fluid the viscosity model is given by (Bird et al., 1960),

$$\mu = K \left| \sqrt{\frac{1}{2}(\Delta : \Delta)} \right|^{n-1} \tag{3.57}$$

where Δ is the symmetrical rate of deformation tensor with Cartesian components

$$\Delta_{ij} = \frac{\partial v_i}{\partial x_j} + \frac{\partial v_j}{\partial x_i} \tag{3.58}$$

and its second invariant $\frac{1}{2}(\Delta : \Delta)$ is given by

$$\begin{aligned} \frac{1}{2}(\Delta : \Delta) &= 2\left[\left(\frac{\partial v_x}{\partial x}\right)^2 + \left(\frac{\partial v_y}{\partial y}\right)^2 + \left(\frac{\partial v_z}{\partial z}\right)^2\right] \\ &\quad + \left[\frac{\partial v_y}{\partial x} + \frac{\partial v_x}{\partial y}\right]^2 + \left[\frac{\partial v_z}{\partial y} + \frac{\partial v_y}{\partial z}\right]^2 + \left[\frac{\partial v_x}{\partial z} + \frac{\partial v_z}{\partial x}\right]^2 \end{aligned} \tag{3.59}$$

Equations 3.54, 3.55 and 3.56 are coupled non-linear partial differential equations which cannot be solved directly. A fixed grid finite volume method was used to solve for the pressure and velocity fields. The free volume of one pitch length of the screw pair was divided into a 3D mesh of rectangular cells as shown in Figure 3.19. In each cell the pressure is defined at the centre of the cell and the velocities at the positive-most corner, as indicated in Figure 3.20. The viscosity is assumed constant in the cell. Conservation of mass over the cell with mesh indices (X, Y, Z) requires that

$$Q_x^{(X,Y,Z)} + Q_y^{(X,Y,Z)} + Q_z^{(X,Y,Z)} - Q_x^{(X-1,Y,Z)} - Q_y^{(X,Y-1,Z)} - Q_z^{(X,Y,Z-1)} = 0 \tag{3.60}$$

The flow $Q_x^{(X,Y,Z)}$ leaving the element (X, Y, Z) in the positive x-direction can be considered to be made up of pressure driven flow in the centre of the cell with superposed shear flow from the moving boundaries, as illustrated in Figure 3.21. Rearranging Equation 3.54 provides the governing equation for flow in the x-direction:

$$\begin{aligned} \frac{\partial^2 v_x}{\partial y^2} + \frac{\partial^2 v_x}{\partial z^2} &= \frac{1}{\mu}\left[\frac{\partial p}{\partial x} - \mu\frac{\partial^2 v_x}{\partial x^2} - \frac{\partial \mu}{\partial x}\frac{\partial v_x}{\partial x} - \frac{\partial \mu}{\partial y}\frac{\partial v_x}{\partial y} - \frac{\partial \mu}{\partial z}\frac{\partial v_x}{\partial z}\right. \\ &\quad \left. - \frac{\partial \mu}{\partial x}\frac{\partial v_x}{\partial x} - \frac{\partial \mu}{\partial y}\frac{\partial v_y}{\partial x} - \frac{\partial \mu}{\partial z}\frac{\partial v_z}{\partial x}\right] \\ &= \frac{1}{\mu}\left(\frac{\partial p}{\partial x} - C_x\right) \end{aligned} \tag{3.61}$$

The terms grouped under C_x on the right-hand side of Equation 3.61 can be approximated using the velocity fields from the previous iteration, so that it becomes a linear non-homogeneous partial differential equation. Equation 3.61 can be solved using separation of variables[5] for the velocity distribution v_x over the cell face. Integrating the velocity field over the cell face gives the total flow rate through the face, which can be expressed as the sum of a pressure induced flow rate and a drag induced flow rate, i.e.

$$Q_x = Q_x^{pressure} + Q_x^{drag} \tag{3.62}$$

The pressure induced flow rate is given by:

$$Q_x^{pressure} = -F_p(\Delta y, \Delta z)\frac{1}{\mu}\left(\frac{\partial p}{\partial x} - C_x\right) \tag{3.63}$$

where

$$F_p(a, b) = \frac{ab^3}{12}\left[1 - \frac{192b}{\pi^5 a}\sum_{k=1,3,5,\ldots}^{\infty}\frac{1}{k^5}\tanh\left(\frac{k\pi a}{2b}\right)\right] \tag{3.64}$$

[5]See Tadmor and Klein (1970), pp 194-199, for an outline of the solution method.

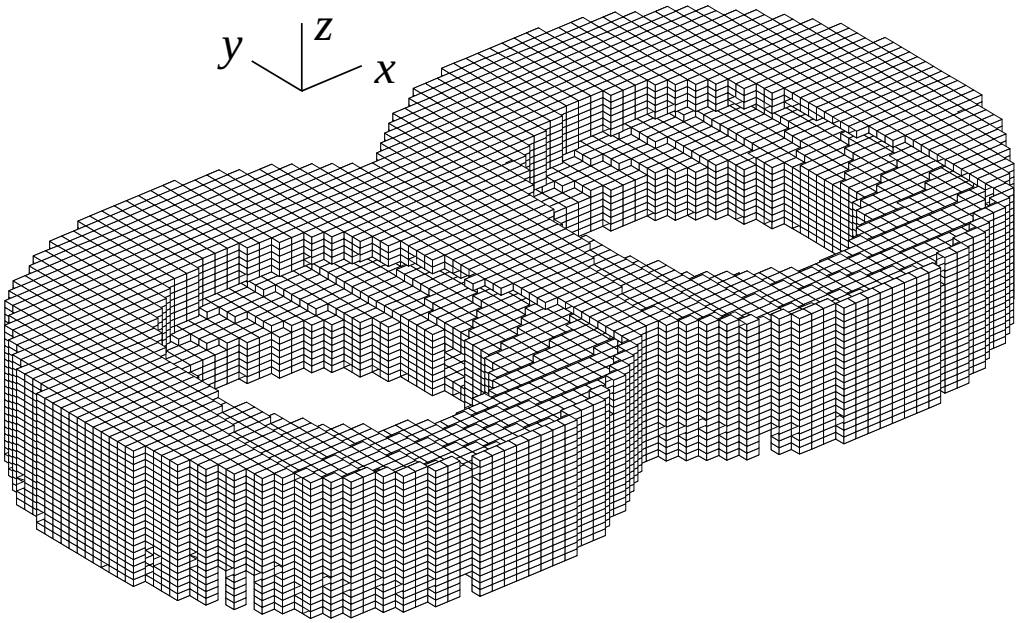

(a)

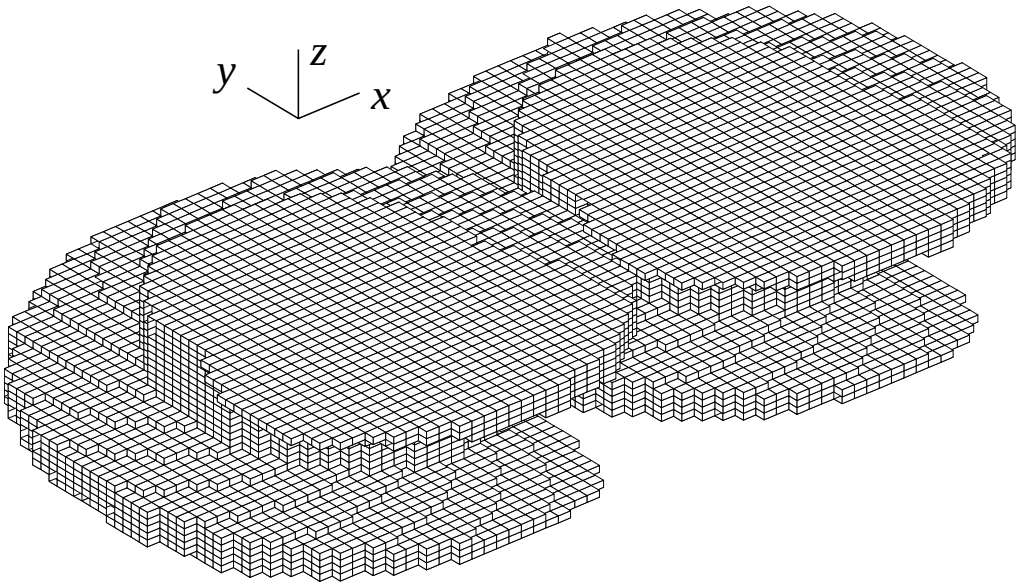

(b)

Figure 3.19: (a) The flow volume of the screws divided into a mesh of rectangular elements; (b) Geometry of the screw surface as represented by the 3D mesh.

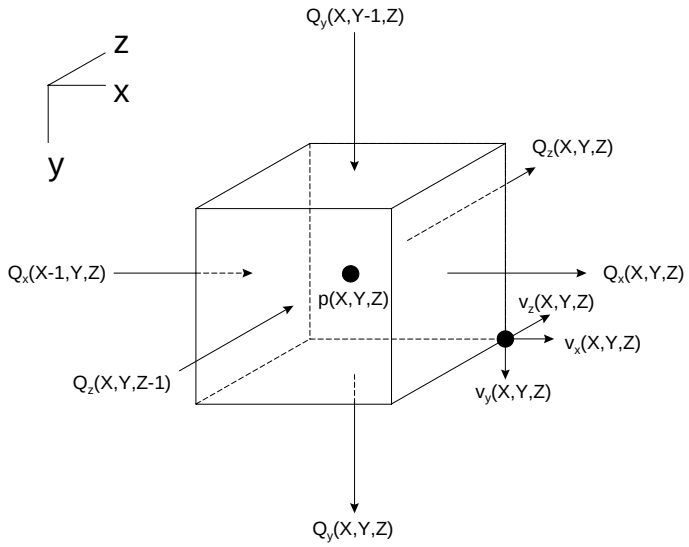

Figure 3.20: A single cell in the 3D mesh. Pressure is defined at the cell centre and velocities at the positive-most corner.

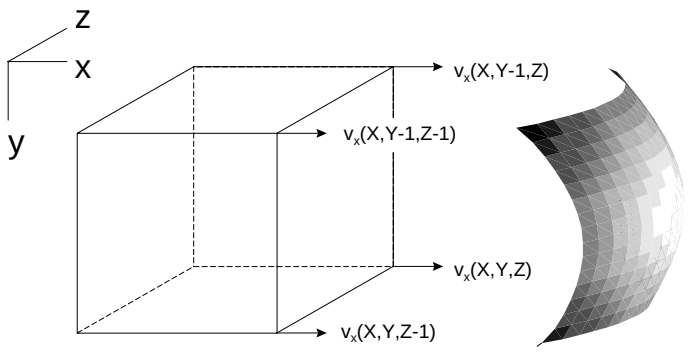

Figure 3.21: Schematic velocity profile of flow leaving cell (X, Y, Z) in the x-direction. Flow consists of superposed pressure flow and drag flow components.

Note that $F_p(a,b) = F_p(b,a)$, as might be expected given that the pressure induced flow rate in a channel is independent of the channel orientation.

The drag induced flow rate has a similar form to Equation 3.63 but contains considerably more terms. Its value is also dependent on the velocity boundary conditions chosen around the edge of the cell face. In the present case, only the velocities at the four corners of the cell face are known, so some form of interpolation is required to fully specify the boundary conditions. With this in mind, and given that the grid spacings are expected to be small and the velocity fields smooth, the drag flow component may be approximated well by:

$$Q_x^{drag} = \overline{v_x}\Delta y \Delta z \tag{3.65}$$

where the average velocity $\overline{v_x}$ through the face in the x-direction is given by the average of the four corner velocities, i.e.

$$\overline{v_x}^{(X,Y,Z)} = \frac{v_x^{(X,Y,Z)} + v_x^{(X,Y,Z-1)} + v_x^{(X,Y-1,Z)} + v_x^{(X,Y-1,Z-1)}}{4} \tag{3.66}$$

Similar expressions may be derived for $Q_y^{(X,Y,Z)}$ and $Q_z^{(X,Y,Z)}$, the flows leaving the element (X,Y,Z) in the y and z-directions respectively. Substituting these expressions into the mass balance Equation 3.60 for element (X,Y,Z) and discretising gives:

$$\begin{aligned}
0 \;=\; & \frac{F_p(\Delta y,\Delta z)}{\overline{\mu}^{(X,Y,Z)}}\frac{p^{(X+1,Y,Z)} - p^{(X,Y,Z)}}{\Delta x} + \frac{F_p(\Delta x,\Delta z)}{\overline{\mu}^{(X,Y,Z)}}\frac{p^{(X,Y+1,Z)} - p^{(X,Y,Z)}}{\Delta y} \\
& + \frac{F_p(\Delta y,\Delta x)}{\overline{\mu}^{(X,Y,Z)}}\frac{p^{(X,Y,Z+1)} - p^{(X,Y,Z)}}{\Delta z} - \frac{F_p(\Delta y,\Delta z)}{\overline{\mu}^{(X-1,Y,Z)}}\frac{p^{(X,Y,Z)} - p^{(X-1,Y,Z)}}{\Delta x} \\
& - \frac{F_p(\Delta x,\Delta z)}{\overline{\mu}^{(X,Y-1,Z)}}\frac{p^{(X,Y,Z)} - p^{(Z,Y-1,Z)}}{\Delta y} - \frac{F_p(\Delta y,\Delta x)}{\overline{\mu}^{(X,Y,Z-1)}}\frac{p^{(X,Y,Z)} - p^{(X,Y,Z-1)}}{\Delta z} \\
& - \frac{F_p(\Delta y,\Delta z)}{\overline{\mu}^{(X,Y,Z)}}C_x^{(X,Y,Z)} - \overline{v_x}^{(X,Y,Z)}\Delta y\Delta z - \frac{F_p(\Delta x,\Delta z)}{\overline{\mu}^{(X,Y,Z)}}C_y^{(X,Y,Z)} - \overline{v_y}^{(X,Y,Z)}\Delta x\Delta z \\
& - \frac{F_p(\Delta y,\Delta x)}{\overline{\mu}^{(X,Y,Z)}}C_z^{(X,Y,Z)} - \overline{v_z}^{(X,Y,Z)}\Delta x\Delta y + \frac{F_p(\Delta y,\Delta z)}{\overline{\mu}^{(X-1,Y,Z)}}C_x^{(X-1,Y,Z)} + \overline{v_x}^{(X-1,Y,Z)}\Delta y\Delta z \\
& + \frac{F_p(\Delta x,\Delta z)}{\overline{\mu}^{(X,Y-1,Z)}}C_y^{(X,Y-1,Z)} + \overline{v_y}^{(X,Y-1,Z)}\Delta x\Delta z + \frac{F_p(\Delta y,\Delta x)}{\overline{\mu}^{(X,Y,Z-1)}}C_z^{(X,Y,Z-1)} + \overline{v_z}^{(X,Y,Z-1)}\Delta x\Delta y
\end{aligned} \tag{3.67}$$

This equation can be written in the form

$$A\,p^{(X-1,Y,Z)} + B\,p^{(X,Y,Z)} + C\,p^{(X+1,Y,Z)} = D \tag{3.68}$$

by taking terms in p which do not appear in the left-hand side of Equation 3.68 over to the right-hand side. Terms on the right-hand side which are a function of the pressure or

velocity field can be estimated using the pressure and velocity field estimates from the previous iteration. Similar equations are obtained for all the other cells in the mesh along the row of constant Y and Z, giving a set of equations of a tridiagonal form which can be solved efficiently by standard methods (Press et al., 1992).

The partial derivatives within the C_x, C_y and C_z terms are estimated by differencing using the velocity and pressure fields from the previous iteration. The values are required at the centre of the cell face through which the flow is being evaluated. In the case of pressure and viscosity, these properties are defined at the centre of each cell, so their spatial derivatives can be calculated by direct differencing between adjacent cells, e.g.

$$\left.\frac{\partial p}{\partial x}\right|^{(X,Y,Z)} = \frac{p^{(X+1,Y,Z)} - p^{(X,Y,Z)}}{\Delta x} \tag{3.69}$$

On the other hand, velocities are defined at the cell corners, so the spatial velocity derivatives at the cell face centre must be evaluated by averaging the derivatives at the four corners of the cell face through which the flow is being evaluated, e.g.

$$\begin{aligned}\left.\frac{\partial v_x}{\partial x}\right|^{(X,Y,Z)} = \frac{1}{4}\Bigg[&\frac{v_x^{(X+1,Y,Z)} - v_x^{(X,Y,Z)}}{\Delta x} + \frac{v_x^{(X+1,Y-1,Z-1)} - v_x^{(X,Y-1,Z-1)}}{\Delta x} \\ &+ \frac{v_x^{(X+1,Y,Z-1)} - v_x^{(X,Y,Z-1)}}{\Delta x} + \frac{v_x^{(X+1,Y-1,Z)} - v_x^{(X,Y-1,Z)}}{\Delta x}\Bigg]\end{aligned} \tag{3.70}$$

The second derivative of velocity is also evaluated at the centre of each cell face, e.g.

$$\begin{aligned}\left.\frac{\partial^2 v_x}{\partial x^2}\right|^{(X,Y,Z)} = \frac{1}{4}\Bigg[&\frac{v_x^{(X+1,Y,Z)} - 2\,v_x^{(X,Y,Z)} + v_x^{(X-1,Y,Z)}}{\Delta x^2} \\ &+ \frac{v_x^{(X+1,Y-1,Z-1)} - 2\,v_x^{(X,Y-1,Z-1)} + v_x^{(X-1,Y-1,Z-1)}}{\Delta x^2} \\ &+ \frac{v_x^{(X+1,Y,Z-1)} - 2\,v_x^{(X,Y,Z-1)} + v_x^{(X-1,Y,Z-1)}}{\Delta x^2} \\ &+ \frac{v_x^{(X+1,Y-1,Z)} - 2\,v_x^{(X,Y-1,Z)} + v_x^{(X-1,Y-1,Z)}}{\Delta x^2}\Bigg]\end{aligned} \tag{3.71}$$

The term $\overline{\mu}$ appearing in Equation 3.67 represents the value of the viscosity at the centre of the face through which the flow is being calculated. This value is determined by averaging the viscosity between adjacent cells, i.e.

$$\overline{\mu}^{(X,Y,Z)} = \frac{\mu^{(X+1,Y,Z)} + \mu^{(X,Y,Z)}}{2} \tag{3.72}$$

It is important that the correct differencing scheme be used to ensure model convergence and stability.

Velocity Field Calculation

To calculate the velocities in the x-direction, Equation 3.54 is rearranged to give

$$\begin{aligned}\frac{\partial^2 v_x}{\partial x^2}+\frac{\partial^2 v_x}{\partial y^2}+\frac{\partial^2 v_x}{\partial z^2} &= \frac{1}{\mu}\left[\frac{\partial p}{\partial x}-\frac{\partial \mu}{\partial x}\frac{\partial v_x}{\partial x}-\frac{\partial \mu}{\partial y}\frac{\partial v_x}{\partial y}-\frac{\partial \mu}{\partial z}\frac{\partial v_x}{\partial z}\right.\\ &\quad \left.-\frac{\partial \mu}{\partial x}\frac{\partial v_x}{\partial x}-\frac{\partial \mu}{\partial y}\frac{\partial v_y}{\partial x}-\frac{\partial \mu}{\partial z}\frac{\partial v_z}{\partial x}\right]\\ &= \frac{1}{\mu}\left(\frac{\partial p}{\partial x}-C_x\right) \end{aligned} \tag{3.73}$$

Equation 3.73 can be written in finite difference form, i.e.

$$\begin{aligned}&\left[\frac{v_x^{(X+1,Y,Z)}-2\,v_x^{(X,Y,Z)}+v_x^{(X-1,Y,Z)}}{\Delta x^2}\right]+\left[\frac{v_x^{(X,Y+1,Z)}-2\,v_x^{(X,Y,Z)}-v_x^{(X,Y-1,Z)}}{\Delta y^2}\right]\\ &+\left[\frac{v_x^{(X,Y,Z+1)}-2\,v_x^{(X,Y,Z)}-v_x^{(X,Y,Z-1)}}{\Delta z^2}\right]\\ &= \frac{1}{\hat{\mu}}\left[\frac{\partial p}{\partial x}-\frac{\partial \mu}{\partial x}\frac{\partial v_x}{\partial x}-\frac{\partial \mu}{\partial y}\frac{\partial v_x}{\partial y}-\frac{\partial \mu}{\partial z}\frac{\partial v_x}{\partial z}-\frac{\partial \mu}{\partial x}\frac{\partial v_x}{\partial x}-\frac{\partial \mu}{\partial y}\frac{\partial v_y}{\partial x}-\frac{\partial \mu}{\partial z}\frac{\partial v_z}{\partial x}\right] \end{aligned} \tag{3.74}$$

which can be written as:

$$A\,v_x^{(X-1,Y,Z)}+B\,v_x^{(X,Y,Z)}+C\,v_x^{(X+1,Y,Z)}=D \tag{3.75}$$

Writing similar equations for every cell along rows of constant Y and Z yields a set of linear equations amenable to solution by tridiagonal matrix inversion, giving the updated v_x field. Similar approaches based on Equations 3.55 and 3.56 can be used to update the v_y and v_z velocity fields, respectively.

It should be noted that the partial derivative terms on the right-hand side of Equation 3.74 are evaluated at the corner of the cell where the velocity is being updated, using the pressure and velocity fields from the previous iteration. The spatial velocity derivative is therefore given by direct differencing between adjacent corners, e.g.

$$\left.\frac{\partial v_x}{\partial x}\right|^{(X,Y,Z)}=\frac{v_x^{(X+1,Y,Z)}-v_x^{(X,Y,Z)}}{\Delta x} \tag{3.76}$$

Spatial pressure and viscosity derivatives also need to be evaluated at the relevant cell corner. Remembering that the velocities in each cell are defined at the positive corner while the pressure and viscosity are defined at the cell centre, the spatial pressure derivative (and similarly for viscosity) is determined by averaging over the four adjacent cells, e.g.

$$\begin{aligned}\left.\frac{\partial p}{\partial x}\right|^{(X,Y,Z)} &= \frac{1}{4}\left[\frac{p^{(X+1,Y,Z)}-p^{(X,Y,Z)}}{\Delta x}+\frac{p^{(X+1,Y+1,Z+1)}-p^{(X,Y+1,Z+1)}}{\Delta x}\right.\\ &\quad \left.+\frac{p^{(X+1,Y,Z+1)}-p^{(X,Y,Z+1)}}{\Delta x}+\frac{p^{(X+1,Y+1,Z)}-p^{(X,Y+1,Z)}}{\Delta x}\right] \end{aligned} \tag{3.77}$$

The value of the viscosity term $\hat{\mu}$ at the corner of cell (X, Y, Z) is determined by averaging over the 8 cells which meet at that corner, i.e.

$$\begin{aligned}\hat{\mu}^{(X,Y,Z)} &= \frac{1}{8}\left[\mu^{(X+1,Y,Z)} + \mu^{(X,Y,Z)} + \mu^{(X+1,Y+1,Z+1)} + \mu^{(X,Y+1,Z+1)}\right. \\ &\quad \left. +\mu^{(X+1,Y,Z+1)} + \mu^{(X,Y,Z+1)} + \mu^{(X+1,Y+1,Z)} + \mu^{(X,Y+1,Z)}\right] \end{aligned} \tag{3.78}$$

3.6.1 Boundary Conditions

In order to devise a physical situation where the screw and barrel surfaces move tangentially to the fluid at all places, a frame of reference is used which moves axially in the positive (conveying) z-direction of the screws at a speed of

$$v_z^{obs} = L_p N \tag{3.79}$$

where L_p is the screw pitch length and N is the rotational speed of the screws. Consequently, the screw and barrel surfaces appear to have a velocity component of $-v_z^{obs}$ in the z-direction. Adding the rotational component of the screws' velocity, the velocity boundary conditions for any point on the screws' surface can be summarized as:

$$v_x = 2\pi r N \cos\theta, \quad v_y = 2\pi r N \sin\theta \quad \text{and} \quad v_z = -L_p N \tag{3.80}$$

where r is the distance of the point from the screw's axis and θ is its angular position. The barrel of course does not rotate, so its velocity boundary conditions are

$$v_x = 0, \quad v_y = 0 \quad \text{and} \quad v_z = -L_p N. \tag{3.81}$$

To convert results back to a stationary frame of reference v_z^{obs} must be added to the v_z velocity components.

If N_Z is the number of model elements in the z-direction equivalent to one pitch length of the screws, then periodic symmetry in the z-direction requires that the velocity in elements N_Z apart be equal, i.e.

$$v^{(X,Y,1)} = v^{(X,Y,N_Z+1)} \quad \forall \text{ integer } X, Y \tag{3.82}$$

The periodic pressure condition in the z-direction requires that the difference between pressures in elements N_Z apart matches the imposed axial pressure gradient, i.e.

$$p^{(X,Y,N_Z+1)} = p^{(X,Y,1)} + \frac{\partial p}{\partial z} L_p \quad \forall \text{ integer } X, Y \tag{3.83}$$

The pressures calculated therefore are all relative and not absolute values. No slip at the screw and barrel surfaces is assumed.

3.6.2 Solution Procedure

Initial pressures and velocities are set to zero. New pressure field estimates p^* are calculated by solving Equation 3.68 over every row in the mesh. New velocity field estimates v_x^*, v_y^* and v_z^* are similarly determined by solving Equation 3.75 (and its equivalents for v_y and v_z) over every row in the mesh. Unstable solution convergence can arise if the pressure and velocity fields are updated directly to p^*, v_x^*, v_y^* and v_z^*; especially when there are relatively large initial velocity gradients at the boundaries. To overcome this problem, updated values are chosen according to:

$$p^{new} = (1 - w_u)p^{current} + w_u p^* \tag{3.84}$$

$$v_x^{new} = (1 - w_u)v_x^{current} + w_u v_x^* \tag{3.85}$$

$$v_y^{new} = (1 - w_u)v_y^{current} + w_u v_y^* \tag{3.86}$$

$$v_z^{new} = (1 - w_u)v_z^{current} + w_u v_z^* \tag{3.87}$$

where the superscript 'current' refers to the current iteration value and 'new' refers to the next iteration value. The under-relaxation factor w_u is set to a value between 0 and 1.

Equations 3.68 and 3.75 are written for calculating along rows in the x-direction. Once an iteration has been performed across the rows in the x-direction, the next iteration is performed across rows in the y-direction, and the following iteration is done in the z-direction. Cycling in this way is not actually necessary to reach a valid solution, however, solution convergence is achieved more quickly by doing so as the effects of the boundary conditions may propagate more rapidly through the mesh. A value of $w_u = 0.2$ was found to give stable convergence for a $70 \times 50 \times 20$ ($x \times y \times z$) mesh.

3.7 Results

The numerical 1D mesh approach for calculating flows between the screw elements is a principal feature of the present extruder model and therefore requires validation. The accuracy of the 1D approach was assessed by comparing its predicted flow rates for pressure-driven non-Newtonian fluid flow in a circular tube with the exact analytical solution, given by

$$Q = -\frac{\pi R^{\frac{1}{n}+3}}{\frac{1}{n}+3}\left(\frac{1}{2K}\frac{\partial P}{\partial z}\right)^{\frac{1}{n}} \tag{3.88}$$

Figure 3.22(a) shows the manner in which a circular cross-section is divided into a 1D mesh according to the prescribed method. For the purpose of the exercise, a power law fluid described by $\mu = 5000\dot{\gamma}^n$ was used in the calculations. Figure 3.22(b) shows a comparison between the axial flow rates calculated using both the 1D mesh approximation (dashed line) and the exact analytical solution (solid line) for a range of pressures and pseudoplastic

indices. It can be seen in Figure 3.22(b) that the flow rates predicted by the 1D mesh approach compare reasonably well with the exact theoretical values. It is interesting that for this geometry the flow rate is over-estimated when $n = 1$ (Newtonian fluid) and under estimated when $n = 0.2$, with a very close agreement when $n \approx 0.4$. It may have been expected that in the Newtonian case the agreement would be perfect, seeing that the 1D mesh approach uses the approximate assumption of the fluid being locally Newtonian. However, the error arises due to the shear stress in the x-direction being calculated using the average fluid velocity in the element, as per Equation 3.12.

The validity of the proposed screw flow model, whereby the screw pair is divided into a network of connected volume elements, was assessed by comparing its predicted net flow rates over a range of pressure gradients with those predicted using a full 3D finite volume approach. A single pitch length of a trapezoidal flight screw was divided into 6 volume elements linked cyclically so that flows extending beyond the network were linked back into the corresponding element of the network, taking into account the externally applied pressure gradient. This situation is shown schematically in Figure 3.23. In this figure, the flows that extend beyond the network and cycle back into it are shown as dotted lines. Each linkage indicates flow in both directions, except for the pumping flows, which are only in one direction and are terminated in the figure with an arrowhead. If the material flows in this closed network are allowed to equilibrate, then the resulting flows (specifically, the ones that are dotted which represent flow beyond the network) can be summed to determine the steady-state net flow rate through the screws. In practice, this equilibrium is calculated by writing a dynamic mass balance over the elements in the network and integrating the resulting equations until steady-state is reached. A full description of this method is presented in Chapter 6 so it will not be discussed further here.

The 3D model calculations were made using a rectangular mesh consisting of $70 \times 50 \times 20$ ($x \times y \times z$) elements to represent one pitch length of the intermeshing screw pair. It was found that this resolution was sufficient to maintain adequate clearances between all screw surfaces while converging in around 4 hours on a 600 MHz Pentium 3 PC. Doubling the number of mesh elements in each dimension to produce a $140 \times 100 \times 40$ grid had no significant effect on the calculated flow rate values, so the coarser mesh was deemed to be fine enough to achieve acceptable accuracy.

Figure 3.24 shows the net flow rate versus pressure gradient for a power-law fluid ($K = 5000$ Pa·s^n, $n = 0.5$) inside a trapezoidal flight screw pair having geometrical parameters as listed in Column 1 of Table 3.1. The flow rates are determined using the 3D finite volume method and the 1D method using both helical and Cartesian coordinate systems for calculating the flow rate in the C-shaped screw channels. Negative flow rates indicate a net flow in the direction opposite to the conveying direction of the screws, as might be observed in reverse screw elements. It can be seen that the agreement between the 1D and 3D models is exceptionally good considering the numerical simplicity of the

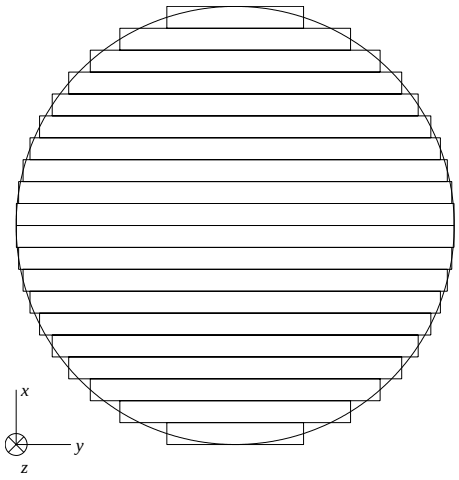

(a)

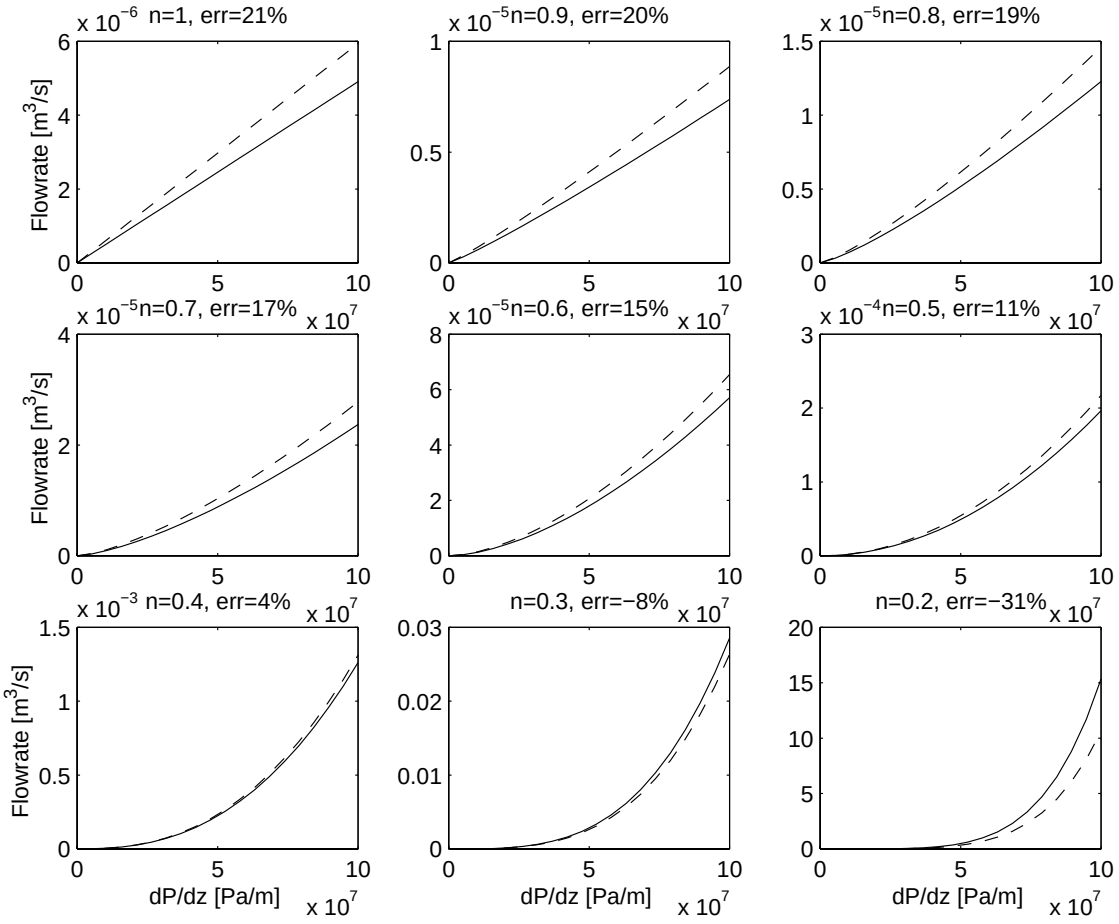

(b)

Figure 3.22: (a) Division of a circular tube into a 1D mesh. (b) Comparison between 1D mesh model and theory for power-law fluid flow in a circular tube, diameter 10 mm, power-law consistency $K = 5000$ Pa s^n.

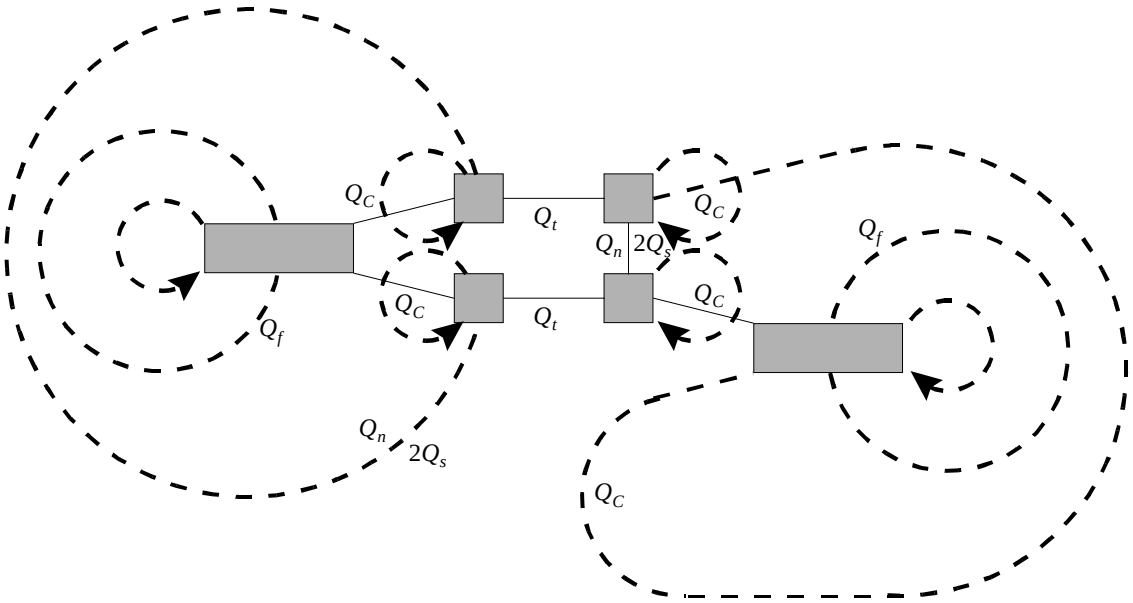

Figure 3.23: Flow network for a single tipped screw operating under periodic boundary conditions.

Table 3.1: Screw parameters and barrel radius used in the simulations. Dimensions are in millimetres.

Parameter	Screw 1	Screw 2
L_p	10.00	40.00
R_s	19.35	19.35
R_r	11.00	11.00
t_f	2.40	2.40
w_c	4.40	4.40
R_B	20.00	20.00

1D model. A single flow rate calculation using the 1D model requires around one second of CPU time on a 600MHz Pentium 3 desktop PC, while the 3D model requires several hours. As with the underlying 1D flow model it is based on, the discrepancy between the 1D and 3D models generally increases with increasing pressure gradient.

The difference between the helical and Cartesian 1D models appears to be only slight, which might be expected for screws where the helicity is not that great (i.e. when the screw pitch is small compared with the radial dimension).

Figure 3.25 shows the flow rate versus pressure gradient relationship for a screw geometry identical to that in the previous case, but having a longer pitch length, as indicated in Column 2 of Table 3.1. It can be seen that the 1D helical model is in close agreement with the more accurate 3D model, but that there is a more noticeable discrepancy between the

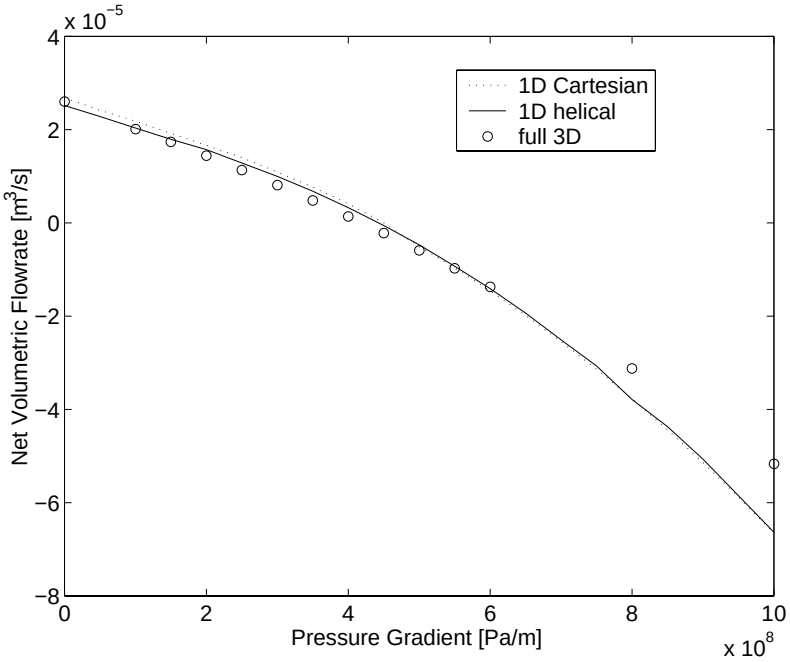

Figure 3.24: Comparison between 1D and 3D model predictions of net flow rate versus pressure gradient in a 10mm pitch trapezoidal flight screw pair.

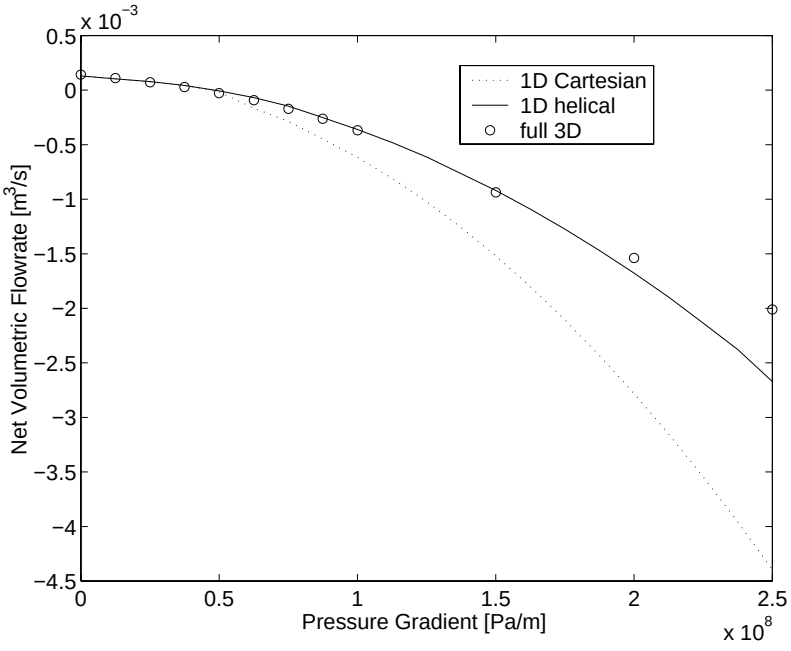

Figure 3.25: Comparison between 1D and 3D model predictions of net flow rate versus pressure gradient in a 40mm pitch trapezoidal flight screw pair.

predictions of the 1D helical and Cartesian formulations of the C-shaped channel flows. This result confirms that the helical flow model is accurate over a wider range of screw geometries than its Cartesian counterpart.

3.8 Conclusions

A computationally cheap method for modelling the flow behaviour in intermeshing screw pairs has been presented. The basis of this method is the division of the flow volume into sub-elements by partitioning along the natural bottlenecks to flow in the screws. The flows between the elements of the resulting flow network are calculated efficiently by dividing each gap's cross-section into a 1D mesh to compute the velocity profile. This 1D mesh approach is shown to give accurate results in the case of non-Newtonian creeping flow in a circular tube. When the flow network is run cyclically to steady-state the resulting predictions for the net forward flow rates in the screw pair were found to compare well with predictions made using a 3D finite volume model for a range of externally applied pressure gradients. Whereas the 3D model can take several hours to converge, flow rates in screw pairs can be calculated in around one second using the flow network approach.

In Chapter 6 it is shown how the flow network model can be combined with similar models for other types of screw elements to simulate the dynamic operation of an entire extruder.

Chapter 4

Fluid Transport in Kneading Disc Elements

Abstract: In this section different methods for modelling non-Newtonian flow in the kneading disc section of a twin-screw extruder are compared. The goal is to establish a computationally inexpensive method for predicting the forward and reverse flow components between kneading discs at various stagger angles. To simplify the analysis, the influence of the intermeshing region is neglected, reducing the problem to that of single-screw kneading disc flow. Three models of increasing complexity are implemented for comparison, these being a one-dimensional (1D) peripheral flow model, a 2D simplified flow analysis network (FAN) model, and a 3D finite volume model. Comparison of the models is made by simulating open discharge flow for a two-lobed disc geometry at a variety of stagger angles. Compared with the 2D FAN and 3D models, the 1D model was found to be quite inaccurate. The 2D FAN model proved accurate to within 20% of the 3D model at stagger angles less than 50°. Greater errors occur at stagger angles above 50°, primarily due to a counter-intuitive reversing of the flow direction predicted by the 3D model as stagger angles approach 90°. It was found that the FAN flow grid could be reduced to a single layer of 18 cells without significantly compromising accuracy, resulting in a model which solves in a fraction of a second on a 600 MHz Pentium 3 PC and captures the essential behaviour of kneading disc flow.

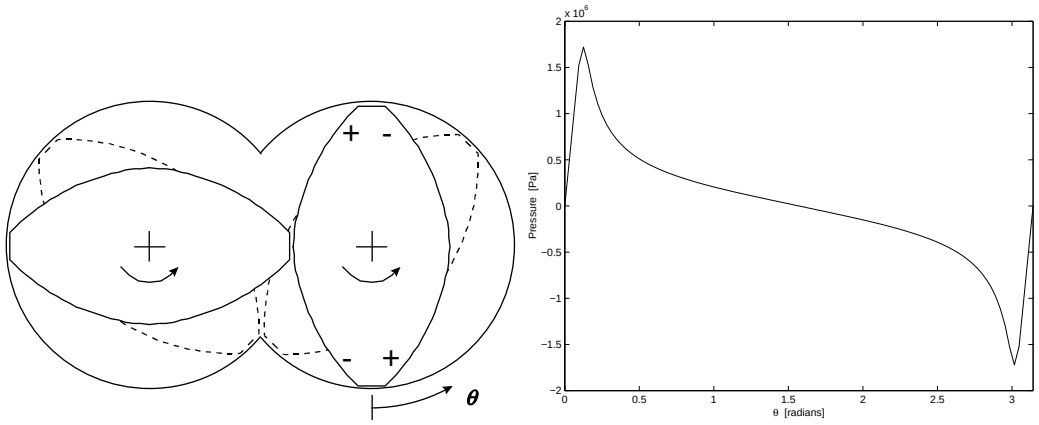

(a) (b)

Figure 4.1: (a) The geometry of the channel around a pair of two-lobed kneading discs; (b) the typical pressure profile in the region far from the intermeshing zone as a function of θ.

4.1 Introduction

The mechanism of flow through a block of kneading discs is different to that in conventional screw elements. Kneading disc elements have no pitch, so on their own they induce no net axial displacement of process fluid. The rotation of a kneading disc instead creates a pressure field in the flow channel with a high pressure region near the leading edge and a low pressure region near the trailing edge of the disc, as indicated with the '+' and '−' signs in Figure 4.1(a). A typical circumferential pressure profile around a two-lobed kneading disc away from the intermeshing region is illustrated in Figure 4.1(b). By staggering sequential discs so that the high pressure region of one disc lies next to a lower pressure region in an adjacent disc, axial flow is effected. While staggered discs may produce a net flow in one direction, the overlapping of the pressure profiles typically produces some degree of flow in the other direction as well. This results in mixing between adjacent discs which facilitates homogenisation of the process material.

Flow modelling in kneading disc elements of twin-screw extruders is complicated by the time dependent flow domain geometry due to the rotation of the screws. It can be seen in Figure 4.1(a) that at different stages of rotation, the position of the paddles relative to the barrel and each other changes. This temporal aspect of the geometry cannot be eliminated with a frame of reference transformation, which is possible in some circumstances for threaded intermeshing screws, as described in Section 3.2.1. Exact 3D simulations would require computationally intensive flow domain re-meshing at every time step, which has not been attempted in the literature to date. Simplifications are necessary to produce engineering estimates in an acceptable time frame.

The first analysis of kneading disc flow was performed by Werner and Eise (1979) who proposed a one-dimensional model for flow and mixing in blocks of twin-screw kneading discs. The model was used to predict residence time distributions. A two-dimensional model based on the flow analysis network (FAN) method of Tadmor et al. (1974) was employed by Szydlowski et al. (1987) to model the flow of Newtonian fluids in kneading discs away from the intermeshing region. Szydlowski and White (1988a) extended this model to include flow in the intermeshing region. Non-Newtonian effects were included by Szydlowski and White (1988b). Warren (1993) modelled the two-dimensional non-Newtonian fluid flow around a single kneading disc when studying nitrocellulose propellant extrusion. In recent years as computing power has become cheaper, detailed three-dimensional flow analyses using commercial computational fluid dynamics software packages are becoming more common in the literature. Yang and Manas-Zloczower (1992) modelled the isothermal 3D flow of a non-Newtonian fluid in the kneading disc section of a twin-screw co-rotating extruder by using a sequence of geometries representing a complete screw rotation. Van der Wal et al. (1996) used a simplified 3D geometry in order to study the effects of the flow field on various extruder parameters such as viscosity and throughput.

The objective of the present study is to establish a model for fluid transport in kneading discs that is appropriate for inclusion in an overall extrusion process model. The requirements of the model are that it be computationally inexpensive, non-Newtonian, and capable of predicting forward and reverse flow components between adjacent discs with acceptable accuracy. In order to assess which modelling approach offers the best accuracy for its computational effort, it is necessary to compare candidate models with an accurate 3D flow model or reliable experimental data. Such a study has not been reported in the literature, so it is the principal topic of inquiry in this chapter. The suitability of two models in particular is investigated, these being the 1D peripheral flow model of Werner and Eise (1979) and the 2D FAN model of Szydlowski and White (1988b). The accuracy of each model is assessed by comparing its open discharge flow rate predictions with those obtained using a 3D finite volume model. It is assumed that the predictions of the 3D model would be the most representative of the actual kneading disc extrusion process.

4.2 Modelling

In flow situations where the viscous forces $\mu\nabla^2\mathbf{v}$ dominate the inertial forces $\nabla\cdot\rho\mathbf{vv}$, the inertial term in the steady-state momentum equation can be neglected. This results in the Stokes, or creeping flow, equations. An indicator of the ratio of inertial forces to viscous forces is given by

$$\frac{\nabla\cdot\rho\mathbf{vv}}{\mu\nabla^2\mathbf{v}}\approx\frac{\rho UL}{\mu}=\mathrm{Re} \tag{4.1}$$

where L and U represent the characteristic length dimension and velocity respectively, ρ is the fluid density, μ is the fluid viscosity, and Re is the Reynolds number. Happel and Brenner (1965) noted that the creeping motion approximation is valid provided that the characteristic Reynolds number is small, i.e. $\rho UL/\mu \ll 1$. In the case of polymer and low moisture dough extrusion, rough estimates of $\rho = 1000\ \mathrm{kg\,m^{-3}}$, $U = 0.5\ \mathrm{m\,s^{-1}}$, $L = 0.02\ \mathrm{m}$ and $\mu = 1000\ \mathrm{Pa\,s}$ give a characteristic Reynolds number estimate of $\mathrm{Re} = 0.01$. Consequently, the present analysis is based on the equations of creeping motion.

An important simplification in the forthcoming analysis is that the intermeshing region is neglected. Consequently, the situation considered is that of a sequence of kneading discs, which have a consistent successive stagger angle, rotating inside a single cylindrical barrel. This simplification is used often in simplified kneading discs flow analysis (e.g. Werner and Eise, 1979; Szydlowski and White, 1988b; Vergnes et al., 1998). The advantage of this simplification is that the flow domain has a constant shape which is periodically symmetric in the axial direction, which significantly simplifies the geometry and boundary conditions. It is assumed in this analysis that the kneading discs remain stationary while the barrel rotates around them at the same angular speed as (but in the opposite direction to) the rotation of the screw shaft. It should be noted that this assumption is acceptable only when the Coriolis force is negligible in the system being modelled. It has been shown by Rauwendaal et al. (1998) that the stationary screw and moving barrel assumption results in negligible error when applied to single-screw extrusion of viscous fluids, so it would appear reasonable to employ this assumption here.

4.2.1 One-Dimensional Kneading Disc Model

The simplest kneading disc transport model is based on the one-dimensional approach originally proposed by Werner and Eise (1979). This model has been used by Vergnes et al. (1998) in their steady-state extruder process model, and the model description presented here is derived from this source. In their analysis, only the flow in the peripheral θ-direction is considered, as depicted in Figure 4.2. Because of the symmetry of kneading disc geometry, only the flow in a single chamber need be analysed. For a given angle θ, the velocity component v_θ in the θ-direction is assumed to be a function of r only. The momentum equation for an isothermal Newtonian fluid in this case reduces to:

$$\frac{1}{\mu}\frac{\mathrm{d}p}{\mathrm{d}\theta} = r\frac{\mathrm{d}}{\mathrm{d}r}\left(\frac{1}{r}\frac{\mathrm{d}}{\mathrm{d}r}\left(rv_\theta\right)\right) \tag{4.2}$$

By twice integrating Equation 4.2 with respect to r and using the boundary conditions of no slip on the disc or barrel walls, the relationship between the pressure gradient and corresponding flow rate in the θ-direction is obtained:

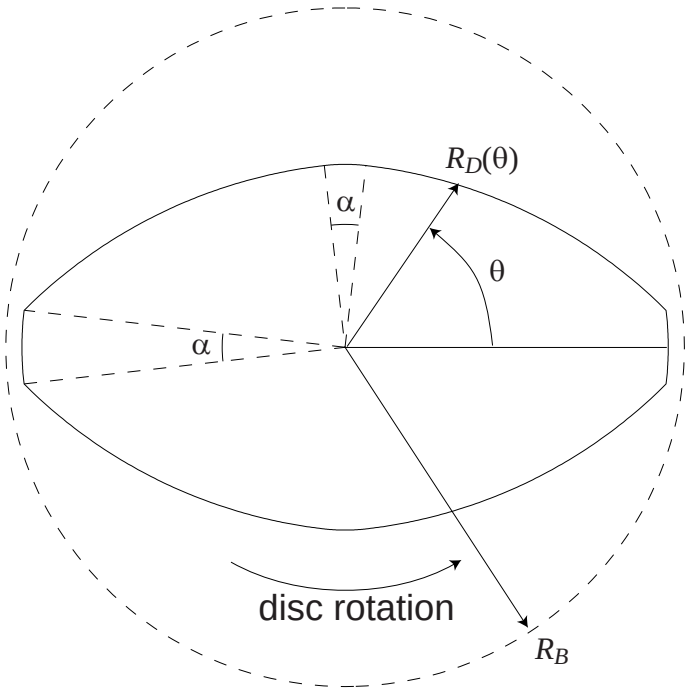

Figure 4.2: Geometry of the kneading disc used in the 1D flow analysis.

$$\frac{\mathrm{d}p}{\mathrm{d}\theta} = \frac{\pi N R_B^2 \left(1 - \frac{R_D(\theta)^2}{R_B^2 - R_D(\theta)^2} \ln\left(\left(\frac{R_B}{R_D(\theta)}\right)^2\right)\right) - \frac{Q_\theta}{L_d}}{\frac{1}{8\mu}\left(R_B^2 - R_D(\theta)^2\right)\left(1 - \left(\frac{2R_B R_D(\theta)}{R_B^2 - R_D(\theta)^2} \ln\left(\frac{R_B}{R_D(\theta)}\right)\right)^2\right)} \tag{4.3}$$

where L_d is the thickness of the kneading disc in the axial direction, R_B is the barrel radius and $R_D(\theta)$ is the disc radius given by Equation 2.26 with the tip angle α given by Equation 2.25. The peripheral pressure profile can be determined by numerically integrating Equation 4.3 between 0 and $2\pi/n_t$, where n_t is the number of disc lobes. Symmetry requires that $p(\theta)$ and $p(\theta+2\pi/n_t)$ be identical. This additional boundary condition allows the peripheral flow rate Q_θ to be determined. This is done by guessing an initial value for Q_θ, determining the estimated pressure change over an interval of $2\pi/n_t$ using Equation 4.3, and then adjusting the value of Q_θ accordingly using the secant method (Press et al., 1992). At every iteration the average shear rate in the channel is calculated according to:

$$\bar{\dot{\gamma}} = \frac{\int_0^{2\pi/n_t} \int_{R_D(\theta)}^{R_B} r\left(\frac{\mathrm{d}v_\theta}{\mathrm{d}r} - \frac{v_\theta}{r}\right) \mathrm{d}r\,\mathrm{d}\theta}{\int_0^{2\pi/n_t} \int_{R_D(\theta)}^{R_B} r\,\mathrm{d}r\mathrm{d}\theta} \tag{4.4}$$

Having determined the peripheral pressure profile, the axial flow can be determined by staggering the pressure profiles by the desired stagger angle λ_s and summing the in-

cremental flows in the axial direction. The total net flow in the axial direction is given by

$$\begin{aligned} Q_z &= \int_0^{2\pi/n_t} \int_{R_D(\theta)}^{R_B} v_z r \, \mathrm{d}r \, \mathrm{d}\theta \\ &= \int_0^{2\pi/n_t} \int_{R_D(\theta)}^{R_B} \frac{1}{4\mu} \frac{\mathrm{d}p}{\mathrm{d}z} \left[r^2 - \frac{R_B^2 \ln\left(\frac{r}{R_D(\theta)}\right) R_D(\theta)^2 \ln\left(\frac{r}{R_B}\right)}{\ln\left(\frac{r}{R_B}\right)} \right] r \, \mathrm{d}r \, \mathrm{d}\theta \\ &= \int_0^{2\pi/n_t} -\frac{1}{16\mu} \frac{p(\theta - \lambda_s) - p(\theta)}{L_d} \\ &\quad \times \left[R_B^4 - R_D(\theta)^4 - \frac{\left(R_B^2 - R_D(\theta)^2\right)^2}{\ln\left(\frac{R_B}{R_D(\theta)}\right)} \right] \mathrm{d}\theta \end{aligned} \tag{4.5}$$

This equation may be integrated numerically. Note that in the chosen coordinate system θ is positive in the direction of screw rotation and z is positive in the direction from the feed port towards the die. Forward and backward flow components can be determined similarly by integrating the positive and negative parts of the integrand separately.

4.2.2 Two-Dimensional Flow Analysis Network Model

The flow analysis network (FAN) method has found wide application in polymer flow analysis since its introduction by Tadmor et al. (1974). The FAN method was originally derived to analyse two-dimensional flow in narrow gaps of varying thickness. It has since been applied to modelling flow in extruder dies (Gutfinger et al., 1975), screws (Szydlowski and White, 1987; Wang and White, 1989), kneading discs (Szydlowski and White, 1988b) and mixing elements (Wang and Tsay, 1996).

When the FAN method is applied to extruder screw elements, the common approach is to unwrap the flow channel from the screw axis and lay it flat, as depicted in Figure 4.3(a). Curvature effects are neglected as a consequence of the unwrapping process. In the new cartesian coordinate system, x points along the screw axis in the direction of the die, y points in the circumferential direction, and z points perpendicularly to the barrel surface. The x-y flow region is divided into a two-dimensional grid, shown in Figure 4.3(b), with each grid element having an associated channel depth $H(x, y)$. The barrel wall moves across the upper surface of the grid at $z = 0$ in the positive y direction with a velocity U_y of

$$U_y = 2\pi R_B N \tag{4.6}$$

A plan view of an extended grid which includes adjacent flow channels might look like that shown in Figure 4.4(a). However, because of the repeating geometry, it is only necessary to consider the single channel region contained within the bold outline.

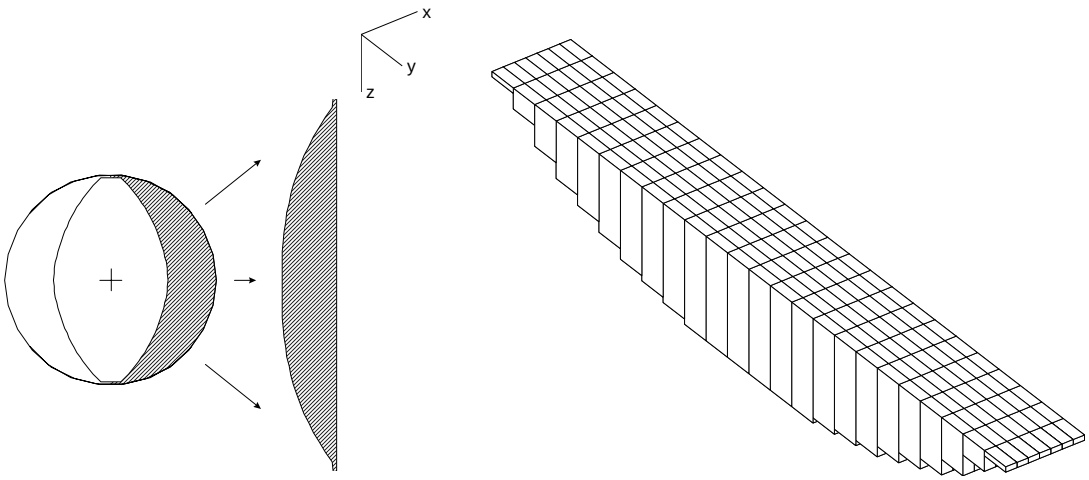

(a) (b)

Figure 4.3: (a) The kneading disc flow channel is unwrapped from the screw. (b) The flow region is divided into a 2D grid for analysis using the FAN method.

The FAN approach begins by writing a steady-state mass balance over each element in the grid. For the element at (x, y), illustrated in Figure 4.4(b), the mass balance at steady-state can be written:

$$q_x(x - \Delta x, y) + q_y(x, y - \Delta y) - q_x(x, y) - q_y(x, y) = 0 \tag{4.7}$$

A simplified form of the momentum equation is used to solve for the flows q_x and q_y. Provided that the variation in gap thickness H is sufficiently small, hydrodynamic lubrication theory (Tadmor and Klein, 1970) applies, and the momentum equation reduces to

$$0 = -\frac{\partial p}{\partial x} + \frac{\partial}{\partial z}\left(\mu \frac{\partial v_x}{\partial z}\right) \tag{4.8}$$

$$0 = -\frac{\partial p}{\partial y} + \frac{\partial}{\partial z}\left(\mu \frac{\partial v_y}{\partial z}\right) \tag{4.9}$$

For a power-law fluid, the viscosity term can be written in the present case as

$$\mu = K\left[\left(\frac{\partial v_x}{\partial z}\right)^2 + \left(\frac{\partial v_y}{\partial z}\right)^2\right]^{\frac{n-1}{2}} \tag{4.10}$$

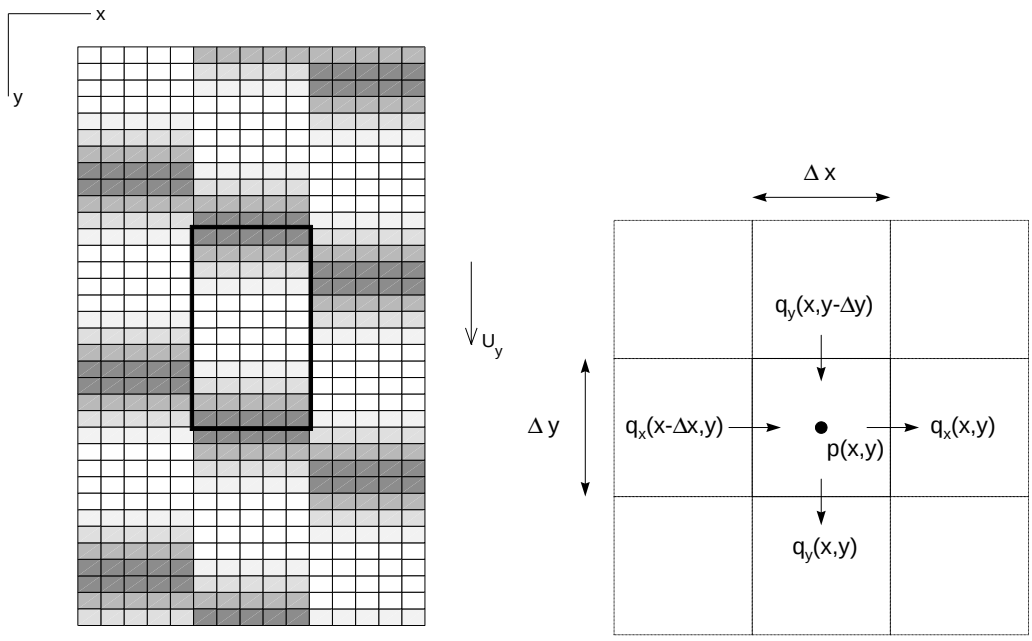

(a) (b)

Figure 4.4: (a) The repeating geometry of an unwrapped kneading disc screw block, the bold outlined region representing a single flow channel. (b) Geometry of a single element used in the FAN analysis with pressures evaluated at the cell centre and flow rates evaluated at cell boundaries.

where the rheological parameters K and n are called the consistency and pseudoplastic index, respectively. The shearing associated with the circumferential rotation of the screws is expected to be much greater than that associated with pressure flow along the screw axis, i.e.

$$\frac{\partial v_y}{\partial z} \gg \frac{\partial v_x}{\partial z} \tag{4.11}$$

Neglecting the smaller of the two velocity gradient terms in Equation 4.10 leads to

$$\mu = K \left(\frac{\partial v_y}{\partial z} \right)^{n-1} \tag{4.12}$$

The velocity gradient term in Equation 4.12 may be approximated as

$$\mu = K \left(\frac{U_y}{H} \right)^{n-1} \tag{4.13}$$

Substituting this simplified expression for μ into Equations 4.8 and 4.9 leads to

$$0 = -\frac{\partial p}{\partial x} + \mu \frac{\partial^2 v_x}{\partial z^2} \tag{4.14}$$

$$0 = -\frac{\partial p}{\partial y} + \mu \frac{\partial^2 v_y}{\partial z^2} \tag{4.15}$$

Solving Equations 4.14 and 4.15 for the velocity fields with the assumption of no slip at the walls allows the flows in the x and y-directions to be determined:

$$q_x = -\frac{H^3 \Delta y}{12K\left(U_y/H\right)^{n-1}} \frac{\partial p}{\partial x} \tag{4.16}$$

$$q_y = \frac{U_y H \Delta x}{2} - \frac{H^3 \Delta x}{12K\left(U_y/H\right)^{n-1}} \frac{\partial p}{\partial y} \tag{4.17}$$

Substituting these expressions into the conservation of mass Equation 4.7 and discretising results in:

$$\begin{aligned} &S_x(X,Y)\frac{p^{(X+1,Y)} - p^{(X,Y)}}{\Delta x} + S_y(X,Y)\frac{p^{(X,Y+1)} - p^{(X,Y)}}{\Delta y} \\ &- S_x(X-1,Y)\frac{p^{(X,Y)} - p^{(X-1,Y)}}{\Delta x} - S_y(X,Y-1)\frac{p^{(X,Y)} - p^{(X,Y-1)}}{\Delta y} \\ &= \frac{\Delta x U_y \overline{H_y}(X,Y)}{2} - \frac{\Delta x U_y \overline{H_y}(X,Y-1)}{2} \end{aligned} \tag{4.18}$$

where X and Y are grid element indices. The superscripts $^{(X,Y)}$ indicate the value of a field variable at position (X,Y) in the grid, while the normal script (X,Y) indicates a functional dependence of a variable on the indices. The $S_x(X,Y)$ and $S_y(X,Y)$ terms are functions given by

$$S_x(X,Y) = \frac{\overline{H_x}(X,Y)^3 \Delta y}{12K\left(U_y/\overline{H_x}(X,Y)\right)^{n-1}} \tag{4.19}$$

$$S_y(X,Y) = \frac{\overline{H_y}(X,Y)^3 \Delta x}{12K\left(U_y/\overline{H_y}(X,Y)\right)^{n-1}} \tag{4.20}$$

and the average heights $\overline{H_x}(X,Y)$ and $\overline{H_y}(X,Y)$ in the x and y-directions respectively are functions given by

$$\overline{H_x}(X,Y) = \frac{H^{(X+1,Y)} + H^{(X,Y)}}{2} \tag{4.21}$$

$$\overline{H_y}(X,Y) = \frac{H^{(X,Y+1)} + H^{(X,Y)}}{2} \tag{4.22}$$

Periodic Boundary Conditions

A knowledge of the boundary conditions is required in order to write the mass balance in cells which lie at the border of the grid. Referring to Figure 4.4, due to circular symmetry in the y-direction, the pressure and velocities at the top of the grid must be the same as those adjacent to the bottom elements. Also, because the pattern of discs repeats itself down the length of the extruder in the x-direction, the conditions to the right of the right-most grid elements must be the same as those in the left-most column shifted up or down by the number of cells equivalent to the stagger angle plus any externally applied pressure change across the paddle element.

Solution Procedure

Writing the mass balance over each cell in the grid provides a system of linear algebraic equations which can be written in the following matrix form

$$\mathbf{AP} = \mathbf{B} \tag{4.23}$$

where $\mathbf{P}$ is a vector containing all the pressures in the flow grid. Matrix $\mathbf{A}$ was found to be typically ill-conditioned, so its inverse was computed using the Moore-Penrose pseudoinverse method (Albert, 1972). Solving Equation 4.23 yields the pressure distribution in the grid. Once the pressure in each cell has been found, the local flow rates can be determined from Equations 4.16 and 4.17 according to

$$q_x^{(X,Y)} = S_x(X,Y)\frac{p^{(X+1,Y)} - p^{(X,Y)}}{\Delta x} \tag{4.24}$$

$$q_y^{(X,Y)} = S_y(X,Y)\frac{p^{(X,Y+1)} - p^{(X,Y)}}{\Delta y} \tag{4.25}$$

The net flow rate Q_x between successive discs in the down-channel x-direction is calculated by adding all the q_x flows along a strip of grid elements in the y-direction, i.e.

$$Q_x = \sum_Y q_x^{(X,Y)} \quad \text{for any } X. \tag{4.26}$$

To model the mixing between successive kneading discs correctly, the forward Q_x^+ and reverse Q_x^- flow components between successive kneading discs need to be calculated. This is done by adding the positive and negative q_x flows along a strip in the y-direction separately, i.e.

$$Q_x^+ = \sum_Y \max\left(0, q_x^{(X,Y)}\right) \quad \text{for any } X. \tag{4.27}$$

$$Q_x^- = \sum_Y \min\left(0, q_x^{(X,Y)}\right) \quad \text{for any } X. \tag{4.28}$$

Rate of Viscous Heat Dissipation

The shearing of the fluid results in viscous heat dissipation. In element (X, Y), the specific rate of viscous heat dissipation is given by (Bird et al., 1960)

$$\hat{\dot{U}}(X,Y) = -\boldsymbol{\tau} : \nabla \mathbf{v} = K \left(\frac{U_y}{H^{(X,Y)}} \right)^{n+1} \tag{4.29}$$

The average value of the specific rate of viscous heat dissipation, $\overline{\hat{\dot{U}}}$, is found by taking a volume-weighted average over all elements in the grid. As the height $H^{(X,Y)}$ only varies in the y-direction, the averaging need only be performed in this direction along a single slice, i.e.

$$\overline{\hat{\dot{U}}} = \frac{\sum_Y \hat{\dot{U}}(X,Y)\, H^{(X,Y)}}{\sum_Y H^{(X,Y)}} \quad \text{for any } X. \tag{4.30}$$

Implementation Remarks

The FAN implementation described here follows the simplified method outlined in Szydlowski and White (1988b). The major difference to their implementation is that advantage is made of the periodic geometry of the single-screw kneading disc sequence. Because of the periodic symmetry, only the flow in a single channel needs to be computed. This appears to have been overlooked by Szydlowski and White, who used extended grids incorporating several neighbouring discs. More rigorous implementations of the FAN method are available (e.g. Wang and White, 1989) which do not neglect the shear in the x-direction, as done here. Such implementations result in a non-linear set of equations for the pressure distribution which must be solved iteratively. In the present search for a computationally inexpensive model, the speed advantage offered by the present simplified FAN implementation offsets the expected loss in model accuracy.

4.2.3 Three-Dimensional Solution of the Flow Equations

The three-dimensional pressure and velocity fields around a block of staggered kneading discs were determined by numerically solving the continuity and momentum equations for steady-state isothermal creeping flow of an incompressible power-law fluid. The equations to be solved are:

$$\nabla \cdot \mathbf{v} = 0 \tag{4.31}$$

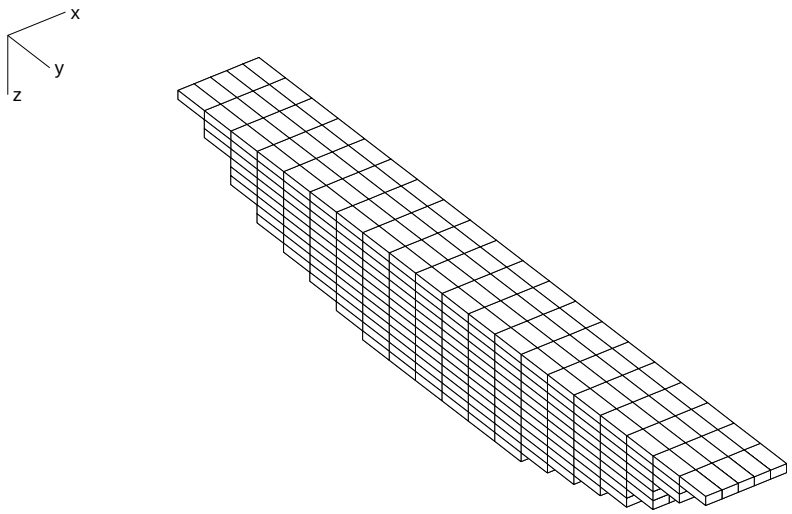

Figure 4.5: Geometry of the kneading disc flow channel mesh used in the 3D flow simulations.

$$-\nabla \cdot \boldsymbol{\tau} = \nabla p \tag{4.32}$$

where $\boldsymbol{\tau}$ is the stress tensor. The technique used for solving these equations in this thesis has already been discussed in Section 3.6. For the present application, the kneading disc channel was unwrapped from the screw as in the FAN model, shown in Figure 4.3(a). The channel was then divided into a 3D mesh of rectangular cells as represented in Figure 4.5.

Boundary conditions

In a frame of reference attached to the kneading disc, the barrel wall is seen to be moving at a velocity of $2\pi R_B N$ in the positive y-direction. No slip at the disc and barrel surfaces is assumed. Circular symmetry requires that the pressure and velocities in the y-direction be periodic with period $2\pi/n_t$. In the x-direction the pattern of discs repeats cyclically down the length of the extruder, hence the conditions down-stream of the x-most-positive grid elements must be the same as those in the first x layer shifted in the y-direction by the number of cells equivalent to the stagger angle.

Solution procedure

Initial pressures and velocities are set to zero, and the solution procedure described in Section 3.6.2 was applied. Due to the moving barrel wall in the present geometry, under-relaxation factors, w_u, of 0.3 were used when iterating in the x and y-directions and 0.03 when iterating in the z-direction. These values were found to give stable convergence.

4.3 The Kneading Disc Flow Network

The 1D, 2D and 3D models described so far in this chapter can be used to calculate the flow rate entering and leaving a single chamber of a kneading disc. Material passing through the kneading disc section of an extruder would pass through several such chambers on its journey, so a tidy way of modelling this bulk flow mechanism needs to be devised.

In Section 3.3.3 the notion of a flow network representing the volume of the flow domain of a screw and the flow rates occurring between different parts of it was introduced. A similar, and very simple, representation can be introduced for a sequence of kneading discs, as shown in Figure 4.6. As can be seen, a sequence of kneading discs is represented as a linear network of identical elements. The volume of each flow network element is equal to the flow volume surrounding a pair of kneading discs. Calculating the flows occurring between each flow network element requires further analysis, as the flow rates derived in Equations 4.27 and 4.28 apply only to a single kneading disc chamber, shown as the shaded region in Figure 4.7(a). To calculate the total axial flow Q_m produced by the kneading discs, the axial flow contribution from the entire flow domain, shown shaded in Figure 4.7(b), needs to be determined. This is done by a simple consideration of the ratio of flow areas. If A_{SX} is the cross-sectional area of a single kneading disc, A_c is the cross-sectional area of a single chamber, and A_{BX} is the entire figure-eight cross-sectional area of the barrel bores, then the ratio F_r of the entire flow area's cross-section to that of the single chamber is

$$F_r = \frac{A_{BX} - 2A_{SX}}{A_c} \tag{4.33}$$

These quantities can be calculated easily from the screw geometry as described in Chapter 2. The forward and reverse components of the total flow can now be written as

$$Q_m^+ = F_r Q_x^+ \tag{4.34}$$

$$Q_m^- = F_r Q_x^- \tag{4.35}$$

For the two-lobed disc pairs shown in figures throughout this chapter, F_r has a value of 3.47.

4.4 Results

The 1D, 2D and 3D models described in the previous sections were implemented in C computer code. Each model was used to calculate the net forward and reverse axial throughputs in a series of kneading discs at a variety of stagger angles. Consistent geometrical and fluid

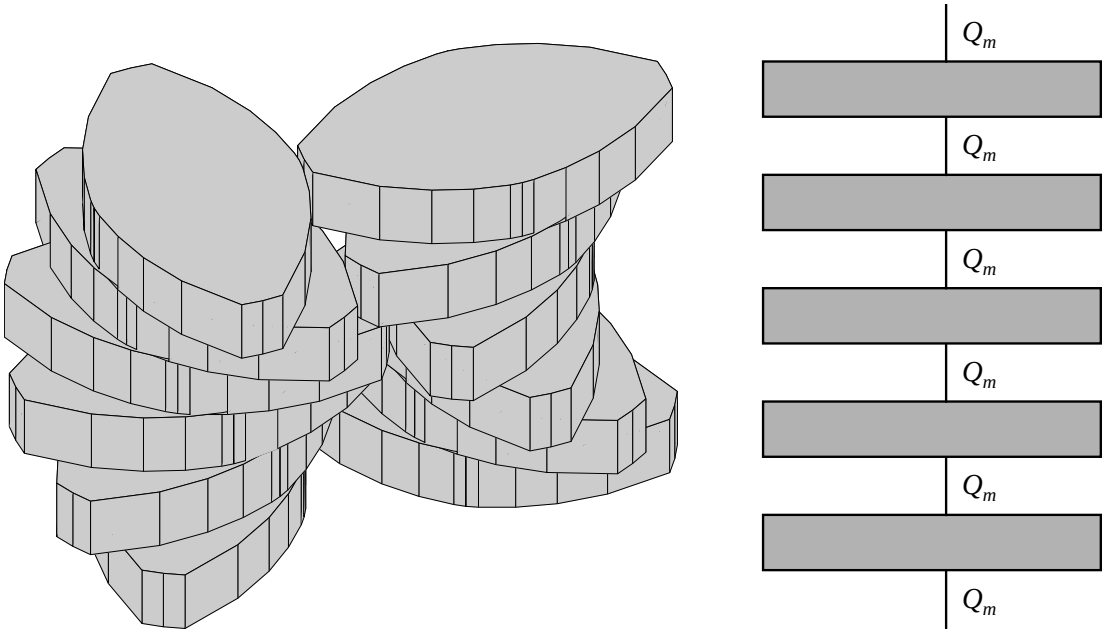

(a) (b)

Figure 4.6: (a) A sequence of six kneading discs; and (b) its representation as a flow network. Flows can occur in both directions between successive elements.

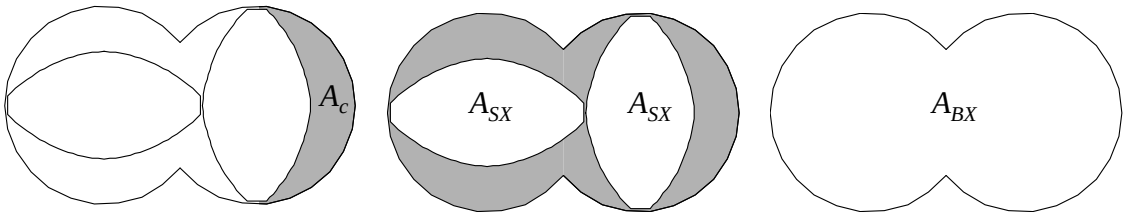

(a) (b) (c)

Figure 4.7: Nomenclature of the cross-sectional areas.

Table 4.1: Parameter values used in the kneading disc simulations.

Parameter	Value	Parameter	Value
L_d	7.00×10^{-3} m	R_B	20.00×10^{-3} m
R_s	19.35×10^{-3} m	C_L	30.80×10^{-3} m
R_r	11.00×10^{-3} m	K	5000 Pa s^n
n_t	2	n	0.5
		N	5 s^{-1}

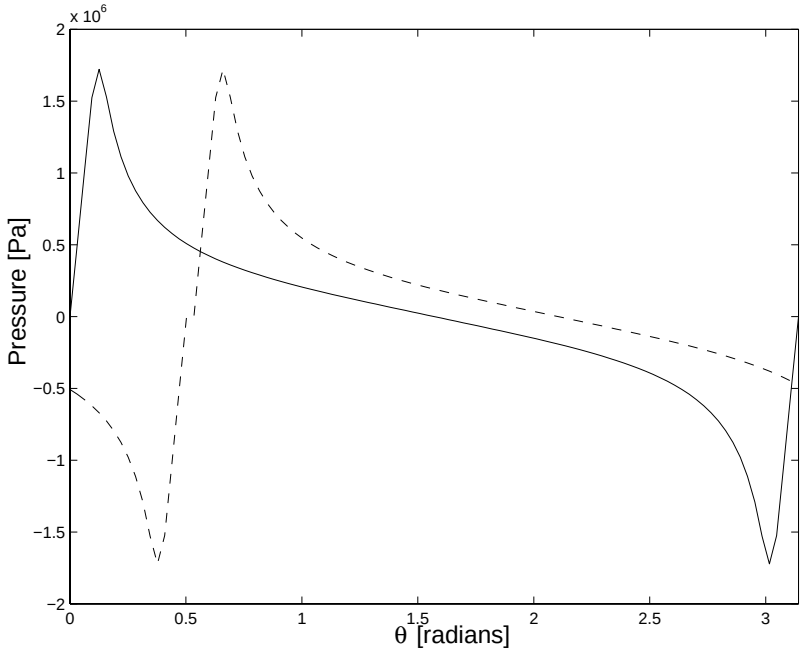

Figure 4.8: Pressure profiles generated by the 1D model.

properties were used in each simulation, with the parameters listed in Table 4.1. All simulations were performed assuming that the flow channels were fully filled and that the outlet was open discharge (i.e. there was no externally applied pressure gradient).

Typical results generated by each of the models are reviewed first. Figure 4.8 shows the peripheral pressure field (i.e. in the direction of rotation) around the kneading disc calculated using the 1D model. The pressure field is symmetrical and has its greatest value just in front of the leading edge of the kneading disc. The dashed line shows the pressure field staggered by 30° to give some indication of the axial pressure gradient at different locations around the disc.

Figure 4.9 shows the flow fields generated by the FAN model at forward stagger angles of 0°, 30°, 60° and 90° using a 7×24 ($x \times y$) grid. The velocity flow field at a stagger angle of 0° indicates flow in the direction of the moving barrel wall (down the page) above the kneading disc tips. However, in the middle of the channel the flow is in the negative

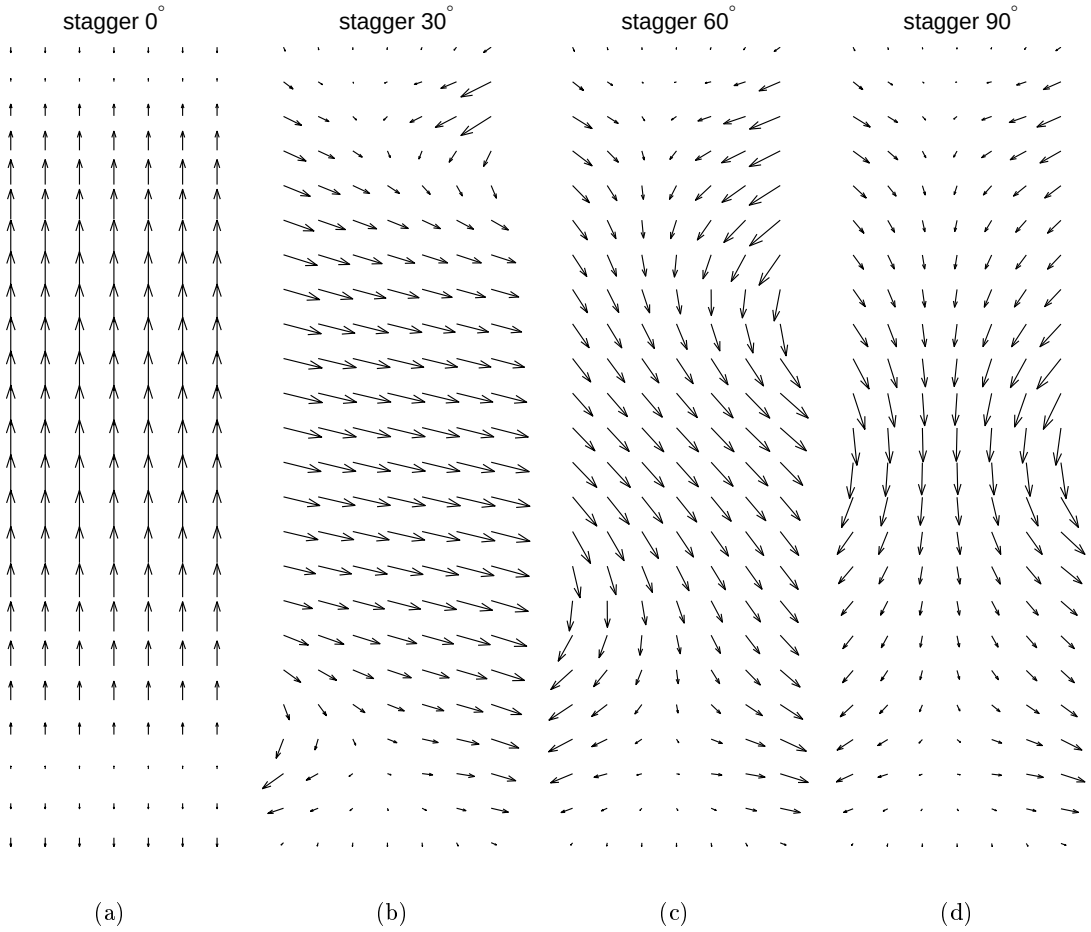

Figure 4.9: Flow velocity fields relative to the kneading disc generated by the FAN model at various stagger angles. The x-axis points to the right of the page and the y-axis points down the page. The barrel wall moves in the positive y-direction in all cases.

direction, which is clearly incorrect. It needs to be reiterated that the approximations of the FAN method are valid only when the variation in channel depth is sufficiently small. The geometry used in this example is borderline, with the ratio between the shallowest and deepest sections of the channel being 1:22. The error at 0°stagger-angle is not large, but is exaggerated by the scaling of the arrows in the vector plot. Importantly, zero net flow in the x-direction is still correctly predicted. Fortunately, such low stagger angles are not commonly used in practice. In cases with higher stagger angles, the positive flow component due to the staggering dominates any minor negative flows in the mid-channel region. Figures 4.9(b)-(d) show that at higher stagger angles the forward and reverse flow components in the axial x-direction become more noticeable until at 90° there is no net axial flow, but significant circulating flows between adjacent discs.

In the full 3D flow simulations a $7 \times 40 \times 40$ ($x \times y \times z$) element mesh was used. For

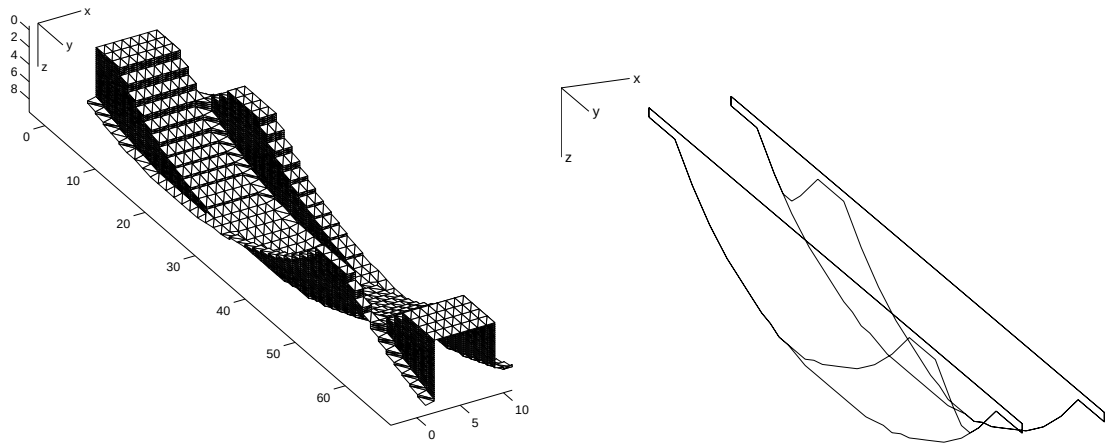

(a) (b)

Figure 4.10: (a) Flow channel geometry for kneading discs staggered at +45°. Dimensions are in mm. (b) Simplified representation of the flow channel.

a forward 45° staggered geometry, Figure 4.10(a) shows the disc surfaces forming the flow channel, including parts of the adjacent discs to illustrate the 45° staggering. For greater clarity when displaying results, Figure 4.10(b) shows a simpler representation used for overlaying flow curves.

Figure 4.11(a) shows velocity vectors relative to the kneading disc indicating the relative magnitude and direction of the flow at various positions in the channel. The fluid near the barrel surface moves almost directly in the y-direction, while fluid closer to the centre of the channel has a greater component in the x-direction. There is little flow in the z-direction in this case. The absence of flow in the z-direction indicates that the approximations of the FAN model should be quite accurate for this geometry.

Figure 4.11(b) shows streamlines entering the flow domain over the disc tip at the $y = 0$ side. Fluid in this case is swept along with the barrel wall and exits the channel at the opposite tip. Figure 4.11(c) shows that streamlines entering the flow domain from the up-stream $x = 0$ plane generally pass straight through the channel and exit at the $x = L_d$ plane, with a small component returning to the $x = 0$ plane between the disc tips near the extreme in the positive y-direction. Figure 4.11(d) shows that streamlines enter the flow domain from the downstream $x = L_d$ plane mostly via the gap between the disc tips near the $y = 0$ region, usually leaving again via the $x = L_d$ plane.

A comparison of the open discharge net flow rates predicted by the different models at various stagger angles is shown in Figure 4.12(a). Because angles have been defined positive in the direction of screw rotation, staggering adjacent kneading discs in negative angle increments in the positive screw axis direction results in forward axial conveying

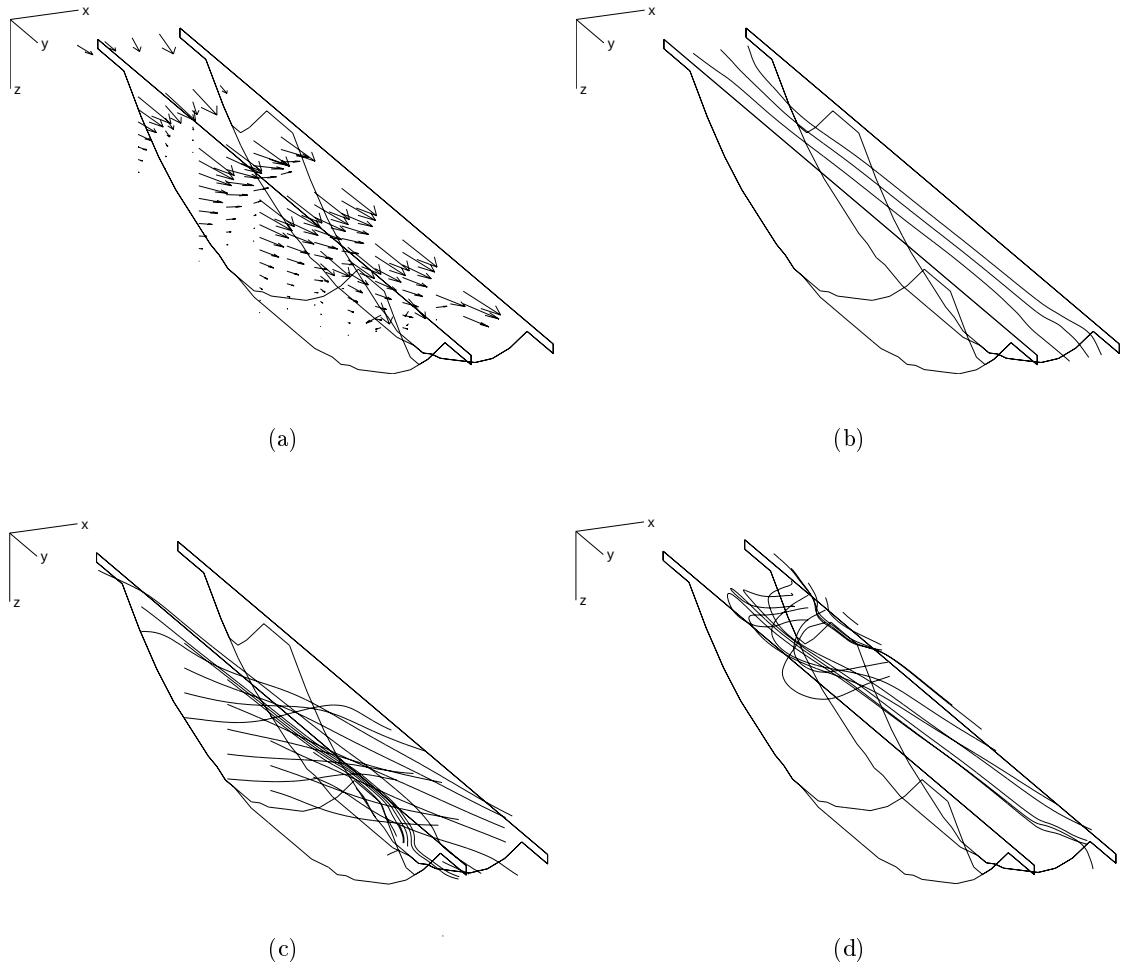

Figure 4.11: Flow in 45° forward staggered kneading discs. (a) velocity vectors relative to the kneading disc; (b) streamlines entering from the $y = 0$ side; (c) streamlines entering from the upstream $x = 0$ side; (d) streamlines entering from the downstream face.

action, while positive angles act to convey fluid in the reverse axial direction. The resulting flow curves are odd functions of stagger angle with a 180° period, which is reflected in the dual abscissa axis labelling. It can be seen in Figure 4.12(a) that the 1D model predicts net axial flow rates considerably larger than those predicted by the 3D model. The 2D FAN model, in contrast, agrees reasonably well with the 3D model.

When the net flow rates predicted by the 2D FAN and 3D models are displayed on a finer scale, as in Figure 4.12(b), an unexpected trend in the 3D model predictions can be seen. At forward and reverse stagger angles of between approximately 70° and 90° the net flow direction *reverses*. Additional simulations were carried out using a finer mesh and also reversing the relative disc rotation direction to establish that this was indeed the predicted behaviour and not an artifact of the model implementation. Similar behaviour was also observed in simulations with Newtonian fluids, so it cannot be attributed to non-

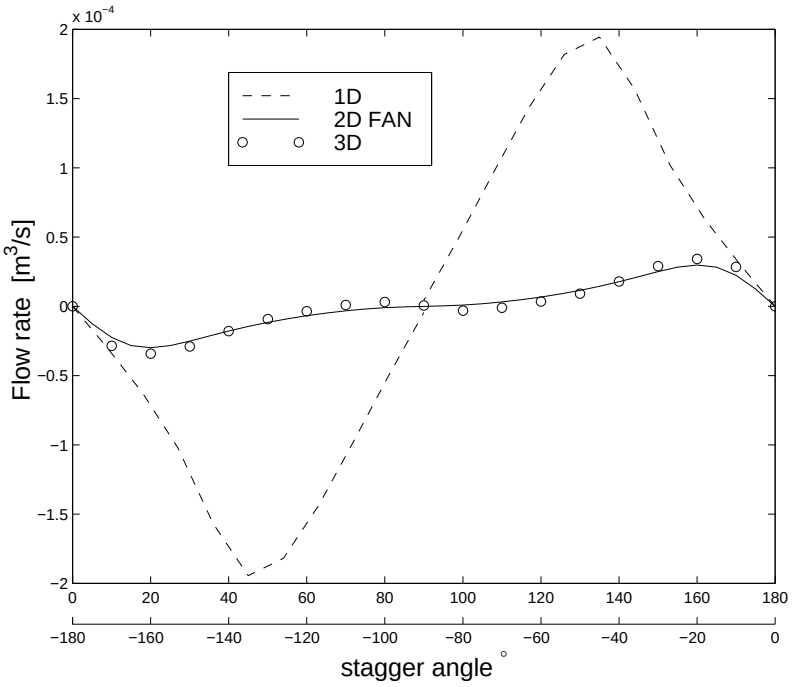

(a)

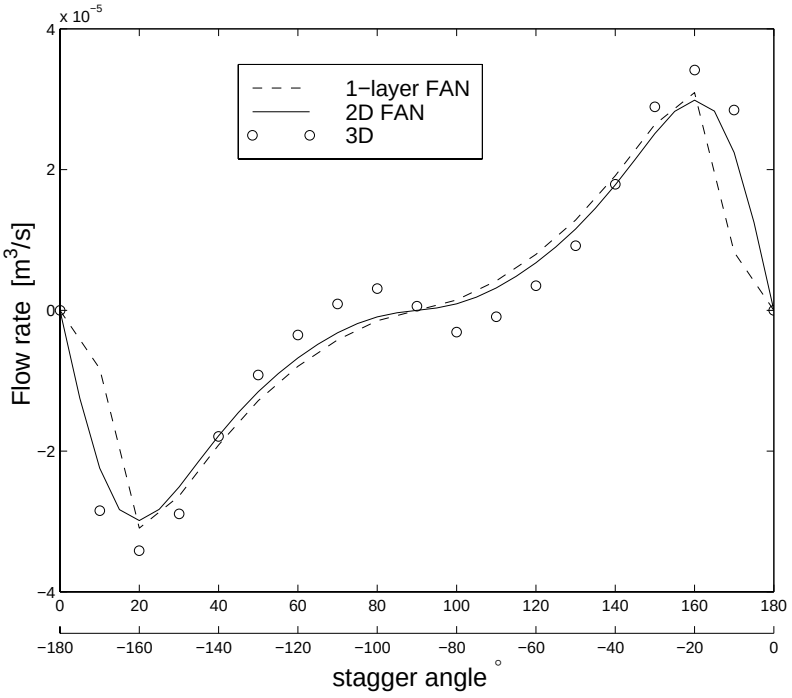

(b)

Figure 4.12: Comparison of flow rates predicted by the kneading disc models as a function of stagger angle. (a) 1D, 2D FAN and 3D model net flow rates; (b) single-layer FAN, 2D FAN and 3D net flow rates on a finer scale.

Newtonian flow behaviour. An explanation for this phenomenon will be presented in the next section.

It is apparent in Figure 4.12(b) that the 2D FAN model does not predict the reverse flow behaviour noted above (the single-layer FAN model curve shown in this plot will be discussed later in this section). There is consequently a poor correspondence between the 2D FAN and 3D models at stagger angles above 60°. At lower angles the agreement between the net flow predictions of the 2D FAN and 3D models is generally within 15%.

When modelling the entire extrusion process, it is important that the model used not only predicts the net flow rate through a screw component with accuracy, but also the forward and reverse flow components. Whereas the net flow rate is important for calculating the material distribution and pressures generated within the extruder, the forward and reverse flow components are important for predicting mixing and residence time distributions.

Comparing the forward and reverse components of the FAN and 3D models separately, it can be seen in Figure 4.13 that there is reasonably good agreement between the 2D FAN and 3D models at low stagger angles, with differences generally within 20% at stagger angles up to 50°. At larger angles the 2D FAN model can over-estimate forward and reverse flow components by more than 100%. This seems again related to the reverse flow behaviour predicted by the 3D model at higher stagger angles, which the FAN model does not predict.

In practice it was found that quite a small number of grid elements could be used in the FAN model without significantly sacrificing model accuracy. The only requirement on the number of grid elements is that the number of elements used in representing the circumferential (y-direction) dimension of the channel should allow the stagger angle to be represented by an integer number of grid elements, or close to. Figures 4.12(b) and (c) show the net, forward and reverse flow components predicted by the FAN model using a single-layer grid of 1×18 ($x \times y$) cells. The performance of the single-layer FAN model is nearly as good as the 7×36 ($x \times y$) cell FAN model, with significant deviations only seen at stagger angles less than 20°. As matrix inversion is an $O(N^3)$ process, reducing the number of cells used in the FAN model significantly reduces the calculation time. The single-layer FAN model runs in a fraction of a second on a 600 MHz Pentium 3 PC, making it very appealing for use in an overall extruder process model.

Finally it might be noted that the stagger angles used in practical two-lobed kneading disc applications are typically 30°, 45°, 60° or 90°. The FAN model compares reasonably well with the 3D model at these angles, as the reverse behaviour occurs only at small deviations from 90°.

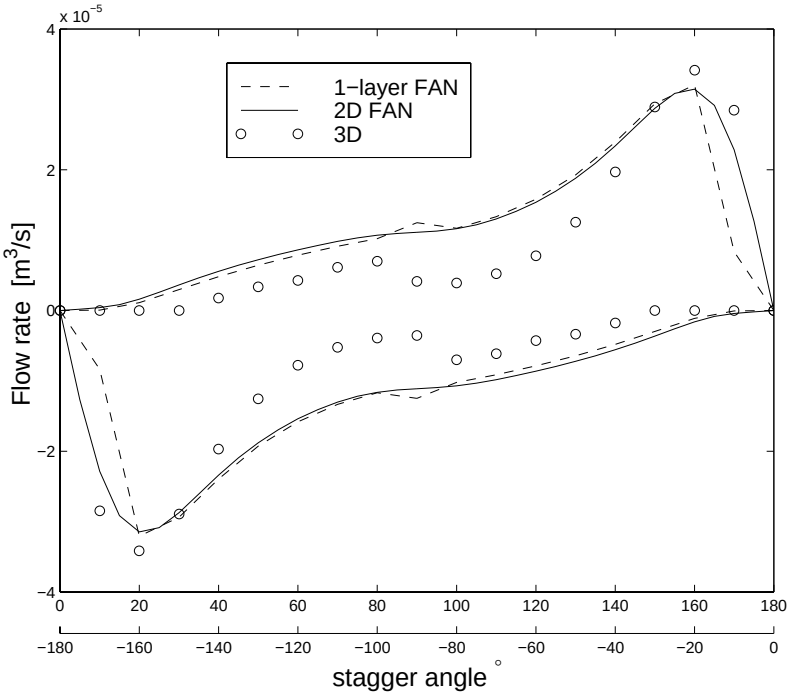

(a)

Figure 4.13: Forward and reverse flow components predicted by the single-layer FAN, 2D FAN and 3D models. The upper curve is the forward flow component and the corresponding lower curve is the reverse flow component.

4.4.1 Discussion on Flow Reversal at High Stagger Angles

Figure 4.14 shows the 3D flow simulation results for an 85° forward stagger arrangement which exhibits reversing flow behaviour. For this geometry, net flow might be expected to be in the $+x$-direction, whereas the 3D simulations predict a net flow in the $-x$-direction. Figure 4.14(b) shows velocity vectors relative to the disc illustrating the relative magnitude and direction of the flow at various positions in the channel. Figures 4.14(c) and (d) show streamlines entering the flow channel via the $x = 0$ and $x = L_d$ planes, respectively. These plots indicate that fluid entering the channel at the $x = 0$ plane tends to leave again via the $x = 0$ plane, while fluid entering at the $x = L_d$ plane mostly leaves via the $x = L_d$ plane, although there are a few streamlines that cross over and leave via the $x = 0$ plane. Figures 4.14(e) and (f) show two selected streamlines entering the $x = 0$ and $x = L_d$ planes at corresponding points on either side of the channel. These plots serve to illustrate the marked differences in flow at the $x = 0$ and $x = L_d$ faces despite the geometry being nearly 90° staggered, at which nearly symmetrical flow might be expected at the $x = 0$ and $x = L_d$ faces.

An explanation for this counter-intuitive reversing of the net flow direction becomes apparent when one considers the relative position of the disc flanks on either side of each channel. Figure 4.15(a) shows an unwrapped kneading disc geometry having a small forward staggering angle. The 'H' and 'L' indicate the high and low pressure regions, respectively, on each side of the disc tips, which are drawn in solid black. The arrow indicates the general flow direction through the disc block. Figure 4.15(b) shows a similar unwrapped disc geometry with a larger forward staggering angle approaching 90°. Based on the observed trends at low stagger angles, one might expect the net flow to be in the direction of the dashed arrow. However, looking to the left and right of the centre channel in Figure 4.15(b) it can be seen that the high pressure regions of the right-most channels are aligned with slightly lower pressure regions in the left-most channels, while the high pressure regions of the left-most channels are aligned with the disc tips of the right-most discs. As a result, the net flow direction is towards the left of the figure, as the equivalent flows towards the right are partially blocked by the presence of the disc tip, indicated with the crossed flow towards the top of the diagram.

Reversing flow behaviour is therefore attributed to disc flanks near the tips on either side of a flow channel partially blocking flow at appropriately high stagger angles. The disc tip angle is consequently expected to be a significant parameter in the reversing flow direction behaviour, as it is an indicator of the extent to which disc flanks can block flow in their adjacent channels. It is noted that reversing flow direction behaviour only occurs in the present simulations when the staggering angle deviated from 90° by angles approximately less than the tip angle, which is 13° for the present geometry, hence providing some support for the disc flank blocking argument.

It should be noted that the simulations performed here relate to *single* screw extruders

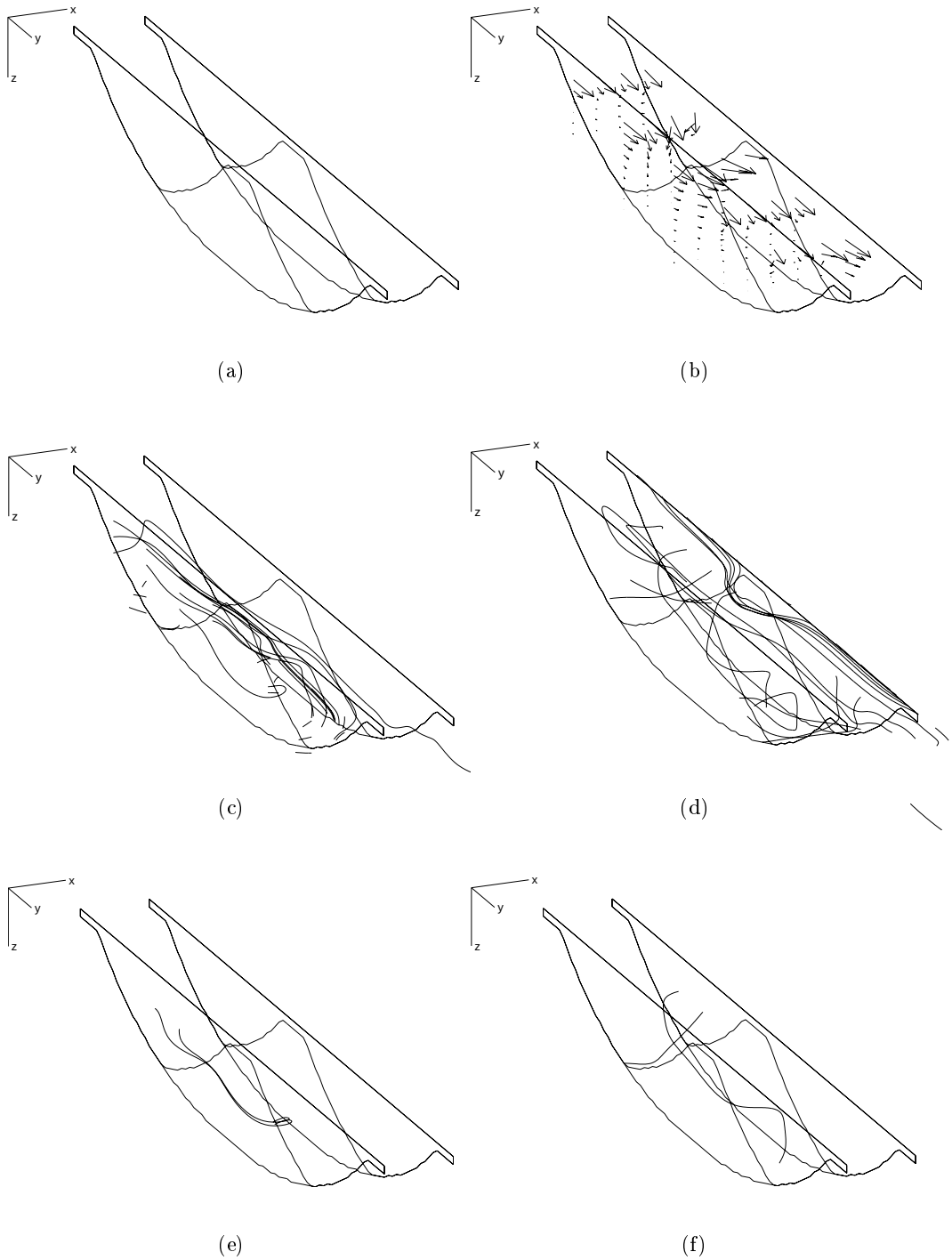

Figure 4.14: Flow in 85° forward staggered kneading discs. (a) Simplified representation of the flow channel; (b) velocity vectors relative to the kneading disc; (c) streamlines entering from the $x = 0$ plane; (d) streamlines entering from the $x = L_d$ plane; (e) selected streamlines entering from the $x = 0$ plane; (f) streamlines entering from the $x = L_d$ face at the corresponding positions to those in (e).

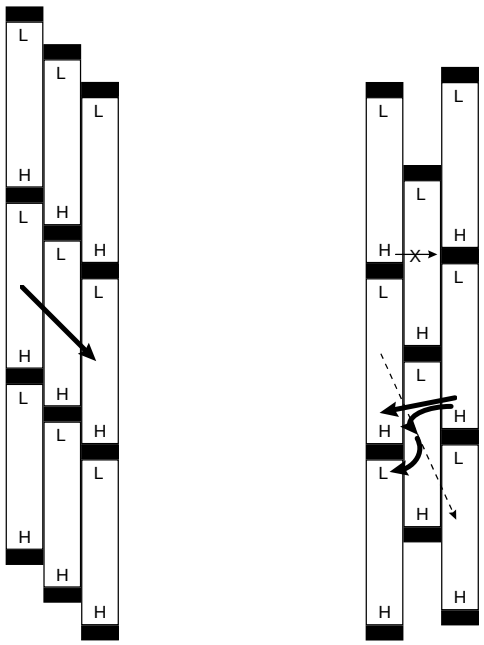

Figure 4.15: Mechanism of reversing flow in kneading discs, (a) forward staggering producing net flow in the forward direction; (b) forward staggering approaching 90° producing net flow in the reverse direction. The expected flow is shown as a dashed arrow whereas the flow is actually in the direction of the bold arrows.

only, and that experiments have not yet been performed to confirm the reversing flow direction prediction. Insufficient data are available to allow speculation as to whether the same reversing effect might be observed in *twin*-screw extruders at similarly high stagger angles.

4.5 Conclusions

In this chapter a case study was undertaken to identify which simplified kneading disc fluid transport model offers the best accuracy for its computational effort. The study was necessary because such an evaluation of simplified kneading disc flow models has not been reported in the literature. The models evaluated were a 1D peripheral flow model, a 2D FAN model, a single-lay FAN model, and the benchmark for accuracy was a full 3D finite volume model. The intermeshing region was neglected in all models, thereby simplifying the analysis to single-screw kneading disc flow. By comparing the predictions of the models at a range of stagger angles at open discharge for a two-lobed kneading disc, it was determined that the 1D model is highly inaccurate, with errors of up to 800%. The net flow rates predicted by the 2D FAN model are accurate to within around 15% of the 3D model at forward and reverse stagger angles up to 60°. Individual forward and reverse flow rate components are accurate to within 20% of the 3D model predictions at stagger angles up to 50°. Predictions using the FAN model outside these ranges are subject to larger errors due to the unexpected reversing of the net flow direction at stagger angles approaching 90°. It was found that the 2D FAN model still gives acceptable accuracy over the commonly used range of stagger angles when the calculation grid is reduced to a single layer of 18 elements in the dimension aligned with the direction of disc rotation. The execution of the single-layer FAN model requires only a fraction of a second of CPU time on a 600 MHz Pentium 3 PC.

Chapter 5

Modelling Fluid Transport in Orifice Discs and the Die

Abstract: In this chapter expressions for the flow rate and specific rate of viscous heat dissipation in orifice discs and circular dies are developed. The representation of each component as a flow network compatible with those described in previous chapters is also presented.

5.1 Introduction

Modelling fluid transport in orifice discs and circular dies is one of the easier tasks in extruder modelling. Orifice discs present a narrow annular gap for flow, as seen in Figure 5.1, so the flow can be modelled in a similar way to that used for the screw flight gap as discussed in Section 3.4.7. Flow though a circular die has a simple analytical solution for both Newtonian and power-law fluids.

The purpose of the present chapter is to outline the methods used here for modelling flow in orifice discs and circular dies. The models are intended for use in a dynamic model of the complete extrusion process. Consequently, a flow network structure representation of the orifice discs and die compatible with the flow networks described in the previous chapters for screws and kneading discs is presented. As the orifice disc flow model is implicitly validated in Chapter 3 and the flow in circular channels has a well known analytical solution, there are no simulation or experimental results presented in this chapter.

5.2 Fluid Transport in Orifice Discs

The annular gap presented by orifice disc pairs can be unwrapped and treated as a long narrow slit having length L_y given by

$$L_y = 2(\pi - \psi_B)(R_B + R_s) \tag{5.1}$$

and width L_x of

$$L_x = R_B - R_s \tag{5.2}$$

where R_B is the barrel bore radius, R_s is the orifice disc tip radius, and ψ_B is defined according to Equation 2.1. A frame of reference attached to the barrel is considered, oriented as shown in Figure 5.1(b). Flow through the flight gap in the z-direction is driven by pressure only. The rotation of the screw in the y-direction is responsible for considerable shear in the gap. The flow in the flight gap is then described by the momentum equation

$$0 = \frac{\partial p}{\partial z} - \frac{\partial}{\partial x}\left(\mu \frac{\partial v_z}{\partial x}\right) \tag{5.3}$$

and the power-law viscosity is expressed as

$$\mu = K\left[\left(\frac{\partial v_y}{\partial x}\right)^2 + \left(\frac{\partial v_z}{\partial x}\right)^2\right]^{\frac{n-1}{2}} \tag{5.4}$$

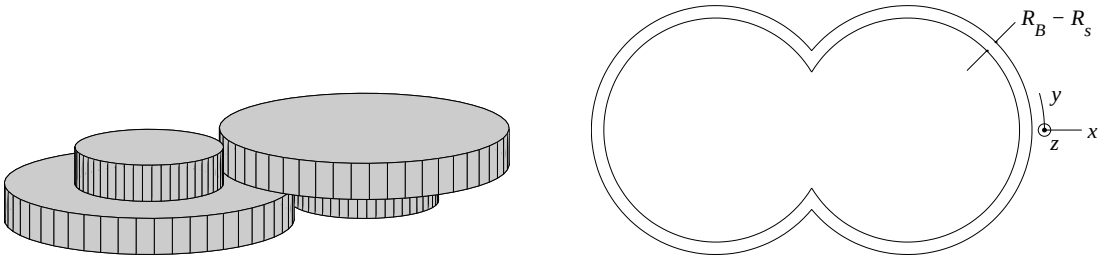

(a) (b)

Figure 5.1: (a) A pair of orifice discs; and (b) the geometry of the annular slit formed between the discs and the barrel wall.

There is assumed to be no slip at the screw or barrel surfaces, and the velocity boundary conditions are expressed as

$$x = 0, \quad v_z = 0; \quad x = R_B - R_s, \quad v_z = 0;$$
$$x = 0, \quad v_y = 2\pi R_s N; \quad x = R_B - R_s, \quad v_y = 0;$$

where N is the screw rotation rate. The analysis proceeds identically to that used for calculating flow through the screw flight gap in Section 3.4.7. An iterative solution procedure must be used. Using the current viscosity estimate μ, the velocity profile in the z-direction is given by

$$v_z(x) = \frac{1}{\mu}\frac{\partial p}{\partial z}\left(\frac{x^2}{2} - \frac{R_B - R_s}{2}x\right) \tag{5.5}$$

The updated viscosity μ^* between iterations is given by

$$\mu^* = K\left[\left(\frac{\partial p}{\partial z}\frac{R_B - R_s}{12\mu}\right)^2 + \left(\frac{2\pi R_s N}{R_B - R_s}\right)^2\right]^{\frac{n-1}{2}} \tag{5.6}$$

After μ converges, the net forward or reverse flow through the orifice disc constriction can be calculated. The direction of the flow depends on the direction of the pressure gradient, so the forward and reverse flow components, Q_o^+ and Q_o^- respectively, can be expressed generally as

$$Q_o^+ = \max\left(0, \int_0^{R_B - R_s} v_z(x) L_y \, \mathrm{d}x\right) \tag{5.7}$$

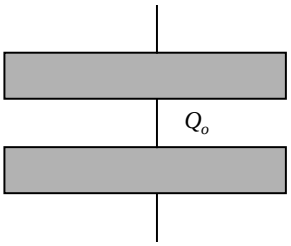

Figure 5.2: The orifice disc flow network representation.

$$Q_o^- = \min\left(0, \int_0^{R_B - R_s} v_z(x) L_y \, \mathrm{d}x\right) \tag{5.8}$$

The rate of heat generation per unit volume due to viscous dissipation in the orifice disc gap is given by

$$\hat{\dot{U}}_o = K\left[\left(\frac{\partial p}{\partial z}\frac{R_B - R_s}{12\mu}\right)^2 + \left(\frac{2\pi R_s N}{R_B - R_s}\right)^2\right]^{\frac{n+1}{2}} \tag{5.9}$$

5.2.1 The Orifice Disc Flow Network Representation

An orifice disc pair on a screw shaft may be represented as a flow network consisting of two identical elements representing the free volume on either side of the flow disc. They are connected by a single flow Q_o, which represents the flow through the orifice disc gap. An illustration of the simple orifice disc flow network is shown in Figure 5.2.

5.3 Fluid Transport in Circular Die Elements

The volumetric flow rate Q_d of a power-law fluid through a circular aperture has a well known analytical solution (see for example Bird et al., 1960) given by

$$Q_d = -\frac{\pi R_d^{\frac{1}{n}+3}}{\frac{1}{n}+3}\left(\frac{1}{2K}\frac{\Delta p}{L_d}\right)^{\frac{1}{n}} \tag{5.10}$$

where R_d is the die hole radius, Δp is the pressure gradient across the die, L_d is the length of the die aperture, and K and n are the consistency and pseudoplastic parameters of the power-law rheology model. The rate of viscous heat dissipation per unit volume due to the flow is given by

$$\hat{\dot{U}}_d = -\mathrm{sign}\left(\frac{\Delta p}{L_d}\right) 2K \left|\frac{1}{2K}\frac{\Delta p}{L_d}\right|^{\frac{1}{n}+1} \frac{R_d^{\frac{1}{n}+1}}{\frac{1}{n}+3} \tag{5.11}$$

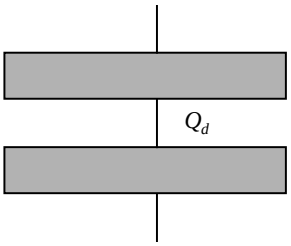

Figure 5.3: The die flow network representation.

5.3.1 The Die Flow Network Representation

The die flow network consists of two volume elements connected by the die flow Q_d, as shown in Figure 5.3. The volume of the first element is equal to that of the die cavity, V_d. The second volume element is a dummy element which resides outside the extruder at a distance L_d away from the first element. It is essentially an accounting measure so that each flow in the network can be expressed in terms of a flow type, an originating element index and a terminating element index. This allows the die flow network to be represented in a similar manner to the flow networks of the other screw types, and thereby simplifies the flow accounting procedure when performing process simulations.

5.4 Conclusions

In this chapter expressions for the flow rate and specific rate of viscous heat dissipation in orifice discs and circular dies has been presented. Each component can be represented by a simple flow network consisting of two separate volume elements and a single flow between them.

This thesis up until now has focussed on developing fluid transport models for the common screw components and die. Emphasis was placed on developing computationally inexpensive models that are reasonably accurate based on comparisons with full 3D flow simulations. There was also an emphasis on representing each screw component as a flow network that describes the component in terms of the major fluid reservoirs around it and the flows between them.

Now that these simple flow representations are available, the following chapter describes how an entire extrusion process can be simulated dynamically by simply linking the flow networks of the components which make up the screw shaft and accounting for the mass and energy flows occurring between them.

Chapter 6

Dynamic Simulation of the Co-rotating Twin-Screw Extrusion Process

Abstract: In this chapter a new technique for modelling the dynamic behaviour of co-rotating twin-screw extruders is presented. Given the geometry of the system, the operating conditions and a description of the process material rheology, the model predicts the dynamic profiles of the degree of fill of the screws, temperature, pressure, specific mechanical energy, residence time distribution, moisture content and concentrations of reacting species. For modelling purposes, the free volume of the extruder is divided into model elements along the natural flow bottlenecks and screw boundaries. The forward and reverse flow-rates between the model elements are determined using the flow models presented in Chapters 3, 4 and 5. By assuming a slight compressibility for the process material, the pressure in each element is directly related to the degree of over-fill via the fluid's bulk modulus of elasticity. This allows the dynamic mass balance over each element to be written in terms of the fill fraction only. Mass and energy balances over each model element provide a system of stiff ordinary differential equations which are integrated to determine the dynamic behaviour of the system. Results of a process startup simulation and an extrusion cooking dynamic response simulation are presented. Comparison of the model with dynamic temperature, pressure and residence time distribution data from an extrusion cooking process indicates a good predictive capability.

6.1 Introduction

The number of variables available for manipulation in an extrusion process is large. These not only include screw speed, feed rates and barrel temperature settings, but also the multitude of different screw configurations which are possible in modular extruders. In the absence of a process model, product development or process optimisation must be done through lengthy experimental investigations, where the various permutations of operating conditions and screw configurations are tried. This is expensive in terms of human resources, process down-time and raw material consumption, which can be hundreds of kilograms per hour for large extruders.

An accurate process model offers the potential to perform large portions of such investigations cheaply on a computer. Dynamic process models in particular also enable process control strategies to be simulated and residence time distributions to be estimated. Models also provide process insights which can be difficult to obtain experimentally, as the physical nature of the extrusion process complicates direct observation of its interior. Investigators such as Kim and White (2000) have gone to considerable trouble to incorporate glass windows into their extruder barrels to allow observation of material transport during operation.

Full 3D finite element simulations of complete twin-screw extruders have not been forthcoming in the literature, no doubt owing to the problems associated with representing the time dependent flow boundaries, mobile air-liquid phase boundaries, and the computing power required to handle the large number of elements necessary to represent the geometry accurately. Due to the complexity and magnitude of the complete problem, it is unlikely that full 3D simulations will be available in the near future. All modelling attempts to date rely on significant process simplifications to achieve practical solutions. Dynamic modelling in particular has received little attention and has so far only been modelled as a plug flow reactor (Kulshreshtha and Zaror, 1992), though residence time distribution experiments indicate that this is not an appropriate flow mechanism (Bounie, 1988).

In this chapter a new technique for modelling the dynamic behaviour of co-rotating twin-screw extruders is presented. The chapter begins with a process description and a review of the previous work done in this field, followed by a description of the model development and a discussion on its implementation. The utility of the model is demonstrated with a simulation of process start-up and the simulation of dynamic step changes in a cooking extrusion process. Model predictions are also compared with experimental temperature, pressure and residence time distribution data from a cooking extrusion process.

6.2 Process Description

Extrusion is a shaping operation in which a material is pressurised by some means to force it through a die. The material is generally a solid at ambient temperature, and extrusion

usually requires processing the material at a higher temperature, at which the material softens or melts to facilitate flow.

A typical screw extruder consists of a barrel inside which one or more helical screws rotate to propel the feed material towards a die opening at the discharge end of the extruder. Twin-screw extruders are typically operated under starved conditions, which is to say that the feed from the hopper is metered at a rate which is lower than the maximum throughput capacity[1]. The shaft may also comprise reverse threaded screws or non-threaded elements such as kneading discs and orifice discs which are effective at mixing, creating local flow constrictions, and imparting shear to the process material. Depending on the screw configuration therefore, different regions of the extruder may be either partially filled (sometimes called *conveying zones*) or fully filled (sometimes called *melt zones* when the contained material is in the molten state). The temperature of the process material changes due to friction, viscous shear and heat transfer between the material and the barrel wall, which often contains heat exchangers to control the wall temperature.

The high pressure generated by the forward conveying screw elements eventually forces the material to exit the extruder through the die.

6.3 Literature Review

Flow modelling in screw extruders dates back to Rowell and Finlayson (1922), and various models for fluid transport in fully filled screws (e.g. Denson and Hwang, 1980) and partially filled screws (e.g. Booy, 1980) ensued. Transport models for kneading disc sections were also developed (e.g. Werner and Eise, 1979). Twin-screw extruders during this time were modelled in a similar way to single-screw extruders by adding extra flow channels to account for the intermeshing region.

One of the first to consider the complete twin-screw extrusion process was Yacu (1985), who modelled the conveying sections and melt sections separately to calculate the steady-state axial temperature and pressure profiles. A temperature dependent power-law rheology model was used based on approximate average shear rates in the screw channel. The operating point of the extruder was calculated using an iterative procedure to estimate the length of the fully filled melt section. Whereas Yacu's approach used simplistic transport models, Meijer and Elemans (1988) improved matters slightly by modelling transport in their screws using the parallel plate model (Tadmor and Klein, 1970), whereby the screw channel is treated as a trough having a top and bottom (corresponding to the barrel and screw root) but no sides. Leakage flow phenomena were also taken into consideration.

Tayeb et al. (1988b) modelled the steady-state axial temperature and pressure profiles using a more accurate version of the parallel plate model incorporating shape correction

[1] As opposed to being force-fed and unregulated like some types of extruders.

factors to account for the influence of the screw flights. The intermeshing region was treated as a local constriction between the two screws in which only pressure flow was assumed. The melt zone was assumed to be isothermal, while a separate model for material transport and frictional heat generation in the partially filled conveying section was also introduced. Vergnes et al. (1998) extended this work to include kneading disc elements and a non-isothermal melt. Bawiskar and White (1997) present a similar style of model using the 2D flow analysis network treatment of Szydlowski and White (1987) to describe transport in the screws, and distinct considerations of the solids conveying and polymer melting processes.

There is little published work, however, on modelling the dynamic behaviour of twin-screw extruders. Levine et al. (1987) calculated the isothermal dynamic response of die pressure, moisture fraction and fill length resulting from variations in feed rate and composition. It appears that the calculation was based on a mass balance over the melt zone to compute its change in length with time, though the solution scheme is not discussed in detail. Kulshreshtha and Zaror (1992) modelled the transient axial profiles of temperature, pressure, moisture fraction, fill fraction and mechanical energy input. Only forward conveying screw elements were considered. Material transport in the screws was modelled as one-dimensional positive displacement plug-flow with leakage back-flow proportional to the pressure gradient. Their solution scheme used a steady-state version of the model (Kulshreshtha et al., 1991a) as a starting point. A mass balance over the melt zone provided an equation describing how the interface between the solids conveying zone and the melt zone moves with time. At each time step, the temperature and pressure profiles in the solids conveying and melt zones are recalculated, shifted, and re-meshed based on the new location of the interface (Kulshreshtha, 1991b).

A more recent exercise by Kim and White (2000) considered the isothermal start-up of a twin-screw extruder with a Newtonian liquid feed material by applying a mass balance over the system to give the length of the fully filled zone. Simple drag and pressure flow relationships were used in the screw elements, while the kneading disc elements were modelled as inefficient conveying screws by applying flow correction factors to screw transport models.

6.3.1 Literature Discussion

In view of the existing literature, the methodology for steady-state extrusion process modelling is reasonably well developed, although there is still room for improvement of the flow models. The solution scheme used in all published steady-state models requires a one-dimensional flow path through the extruder, which limits the ability to model complex mixing and bypassing behaviour.

Dynamic modelling has received little attention in the literature, and consequently there is no well established modelling methodology. The existing solution schemes are

complicated and computationally expensive, requiring the flow domain to be re-meshed at every time-step. These solution techniques limit the flow analysis to simplistic one-dimensional plug flow models, which are unable to incorporate back-mixing behaviour.

There appears to be a general requirement for a robust modelling approach which addresses the problem of moving flow boundaries and allows a more flexible and accurate description of the flows in the extruder. Providing a solution to this problem is the goal of the present chapter.

6.4 Model Development

In the following sections a model for calculating the dynamic behaviour of a co-rotating twin-screw extruder is presented. An outline of the modelling approach is given here and the details are provided in the following sections.

The modelling procedure begins by dividing the free volume of the screws into model elements along the natural flow bottlenecks and screw boundaries. Over each model element, dynamic mass and energy balances are written which describe how each of the variables of interest, such as fill fraction and temperature, vary with time. In order to write these balances, the current flow rates between all the model elements are required. The calculation of these flow rates, which was discussed in detail in the previous chapters, requires a knowledge of the material rheology, screw speed, and pressure in each element. The principal feature of the present process model is the way in which pressure is calculated. By assuming a slight compressibility for the process material, the pressure in each element is directly related to the degree of over-fill via the fluid's bulk modulus of elasticity. This allows the dynamic mass balance over each element to be written in terms of the fill fraction only. The resulting system of ordinary differential equations (ODEs) describing the temporal rate of change of each variable can then be integrated in a straightforward manner to determine the dynamic behaviour of the extruder. No iteration or re-meshing is required during the solution process, as the system moves towards steady-state from the initial conditions during the integration.

The material transport and mode of heat generation is strongly dependent on the properties of the material being extruded. Different treatments are required for liquids and solids. In the formulation that follows, the extrusion of a viscous fluid will be considered first. In Section 6.6 the required changes to the mass and energy balances in order to model the extrusion of solid feed materials are discussed.

6.4.1 The Process Flow Network

The modelling procedure begins by sectioning the free volume of the screws into model elements by dividing along the natural flow bottlenecks and screw boundaries. The division methods, which are specific for threaded screw elements, are described in Chapters 3, 4

and 5. The resulting model elements and the flows that connect them form what can be thought of as a process flow network. Figure 6.1 shows flow network diagrams for several common screw types, such as forward conveying screw elements, reverse screw elements, kneading discs, orifice discs and die elements. Note that each element in the flow network resides at a fixed position in three-dimensional space. By linking the flow networks of successive screw sections together, a complete extruder screw configuration can be built up. An example of a complete screw configuration is shown in Figure 6.2 along with its representation as a flow network in three dimensions.

In building a process flow network, care needs to be taken when joining unlike screw elements as their flow networks may not interface with each other directly. This happens, for instance, when a threaded screw element feeds into a kneading disc element, because some elements in the screw's flow network typically exchange material with network elements several indices away from their own, as indicated by Equation 3.4. In this case the flows which extend beyond the first non-screw element need to be reassigned to connect to the first adjacent non-screw element, as shown in Figure 6.3. Incongruities also arise when screw elements having different numbers of lobes meet. In these cases the indices of all the flow linkages are maintained, but the duplicated flows are eliminated, as shown in Figure 6.3.

Having established a complete process flow network representing the extruder, one can start to consider the movement of mass and energy between the network elements. This requires a knowledge of the physical properties and state variables in each element.

The Physical Properties and State Variables in Each Element

This model is based on the assumption that each element is well-mixed and of sufficiently small size that the physical properties within the element can be taken as constant. The physical properties of interest are the parameters of the power-law rheology model, K and n; the material density, ρ; the thermal conductivity of the material, λ; the heat capacity of the material, C_p; and the heat capacity of the metal screws, C_{p_m}.

The state variables in each element are also assumed to be constant within the element, and acting at the element's centre. The state variables of interest in each element are the fill fraction, f; pressure, p; temperature, T; and the specific mechanical energy, $\hat{W}$. Depending on the process being modelled, additional states of interest might include the moisture fraction, M, or the concentration of a chemical species, C.

To formulate a dynamic model, given the values of the state variables at any instant, one needs to derive equations describing how each state variable changes with time. This is done by writing the temporal mass and energy conservation equations over each element.

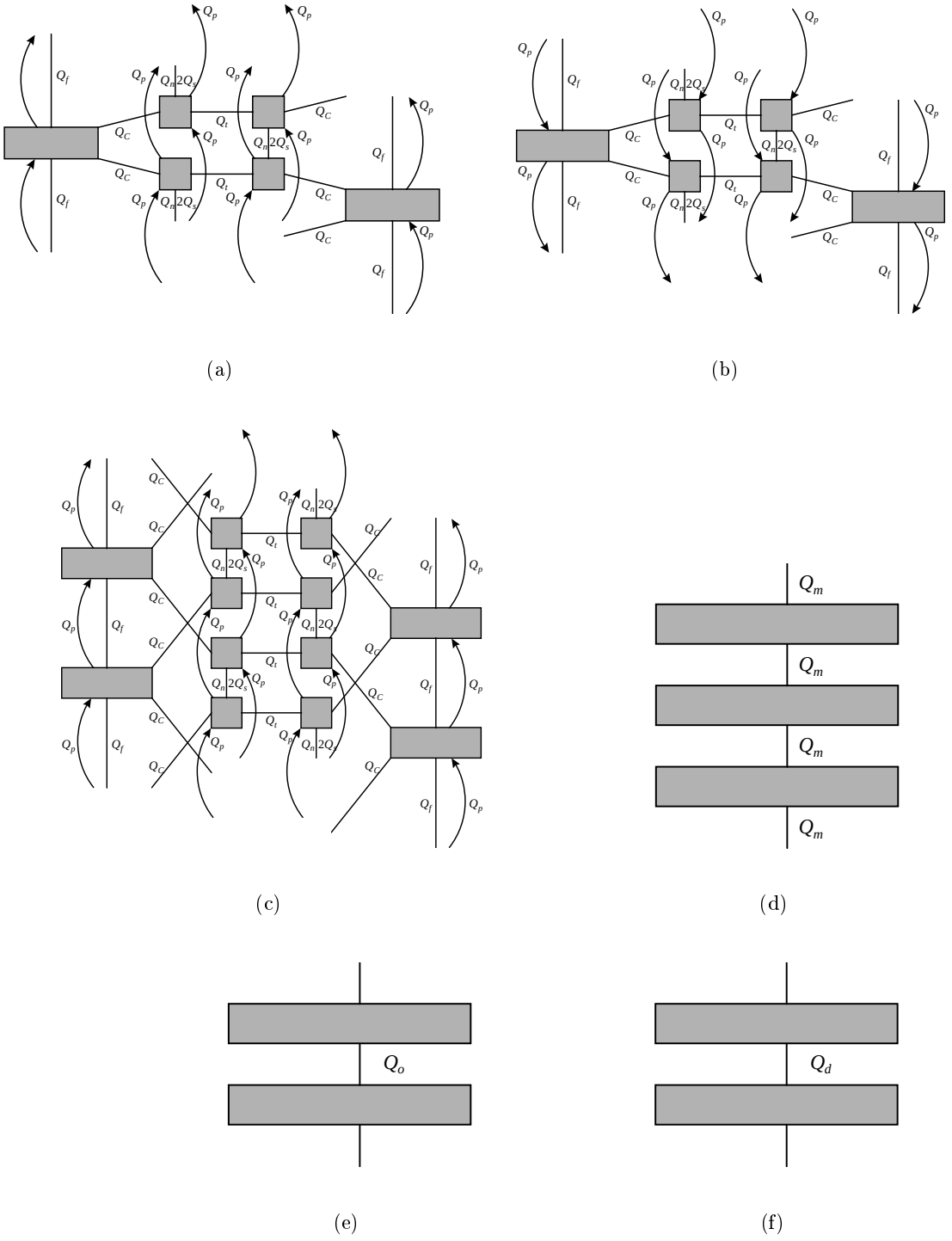

Figure 6.1: Flow networks for various screw types: (a) one pitch length of a single lobed forward conveying screw; (b) one pitch length of single lobed reverse conveying screw; (c) one pitch length of a double lobed forward conveying screw; (d) four kneading disc elements in series; (e) one orifice disc pair; (f) one die element. Refer to Chapters 3, 4 and 5 for definitions of the variables Q_c, Q_t, Q_s, Q_n, Q_f, Q_p, Q_m, Q_o and Q_d.

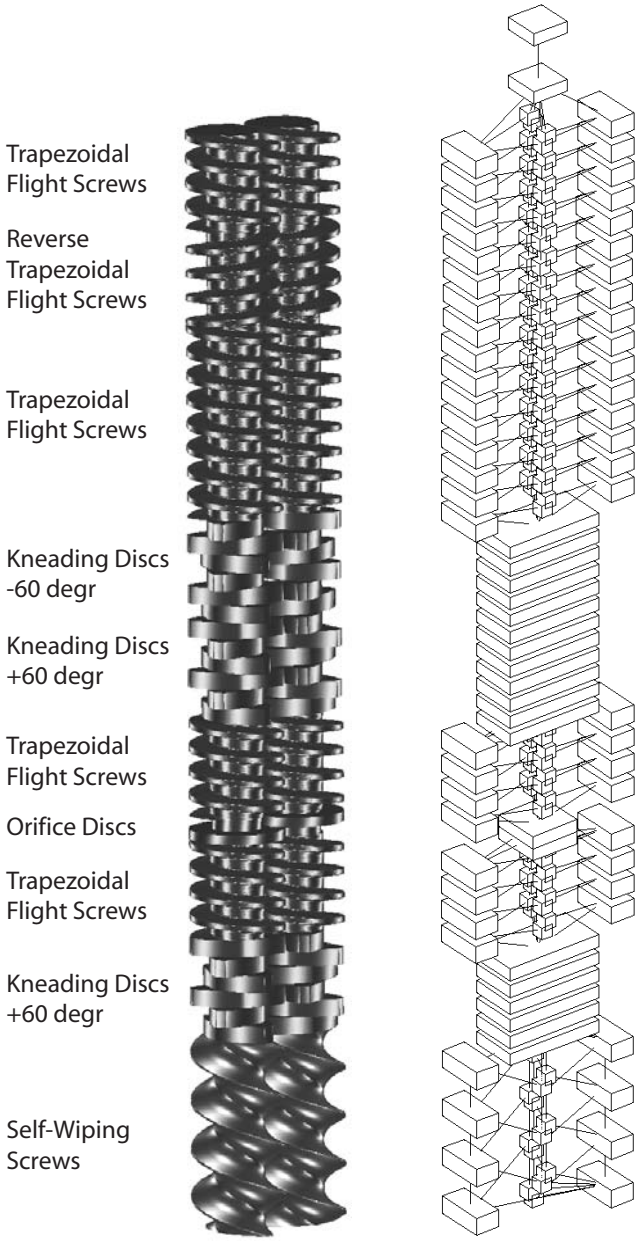

Figure 6.2: (a) A sample screw configuration (excluding the die element); and (b) its representation as a flow network. The screws rotate in the anti-clockwise direction when viewed from above, and the feed end is at the bottom of the diagram.

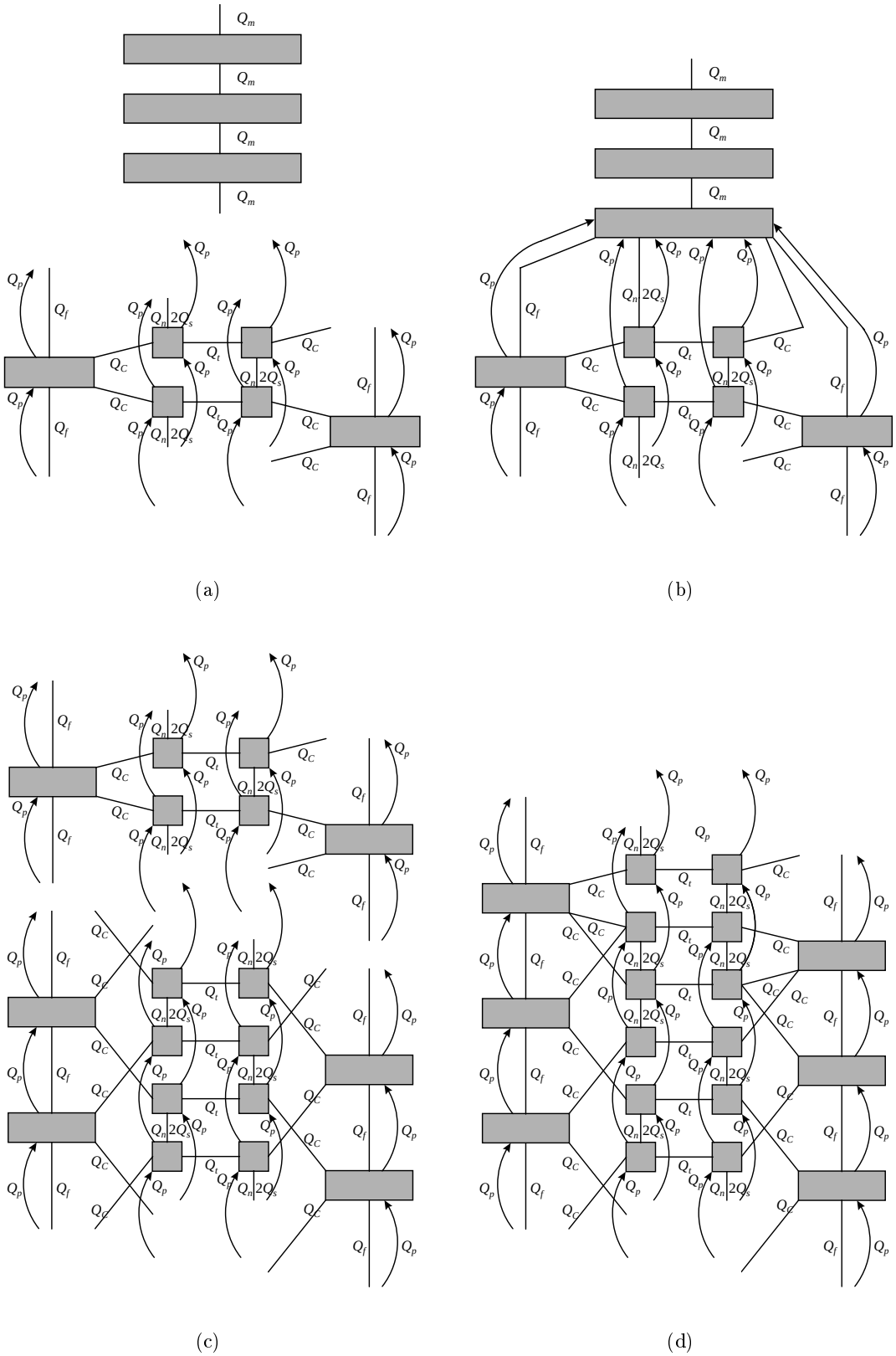

Figure 6.3: Unlike flow networks can be joined using simple rules; (a) and (b) show a single-lobed screw meeting a kneading disc section; (c) and (d) show a double-lobed screw meeting a single-lobed screw.

6.4.2 Pressure in each Element

In the present model the pressure in each element is calculated directly from the fill fraction in the element. This is accomplished by assuming that the process material is slightly compressible, in which case the change in density of the fluid is related to the change in pressure by the bulk modulus of elasticity, E_v, according to

$$\int E_v \frac{\mathrm{d}\rho}{\rho} = \int \mathrm{d}p \tag{6.1}$$

The fill fraction normally would lie in the range $[0, 1]$. However, if the fill fraction f is allowed to take on values slightly greater than one then integration of Equation 6.1 gives the relation

$$p = \begin{cases} E_v \ln(f) & \text{if } f > 1 \\ 0 & \text{if } f \leq 1 \end{cases} \tag{6.2}$$

Using the E_v for water of 2.15×10^9 N/m^2, a fill fraction of 1.01 corresponds to an element pressure of 2.13×10^7 Pa, which is unlikely to be reached in the normal safe operation of a screw extruder.

Note that this method, while having a physical basis, is purely a numerical technique. Any suitably large value of E_v may be used as long as the typical pressures achieved in the process do not result in fill fractions significantly greater than 1. However, the value used cannot be so large that the degree of over-fill over the operating pressure range is in the order of the floating-point precision of the computer used for the calculation, as this will lead to round-off errors. In practice, increasing or decreasing the value of E_v by several orders of magnitude from that of water did not produce any noticeable change in the modelling results.

6.4.3 The Mass Balance

In order to perform a mass balance over an element in the flow network, the rates of flow entering and exiting the element are required. The element may be partially or fully-filled, as measured by its fill fraction f. The transport analyses presented in Chapters 3, 4 and 5 described how to calculate the flows between elements when they are fully-filled with a viscous fluid. When the elements are only partially-filled, it will be assumed that the flow is directly proportional to the fill fraction. If this is not exactly the case, then it is certainly not an unreasonable first approximation for the following reasons: Firstly, most of the work done on the material in an extruder occurs in the fully-filled regions. Regardless of the transport model used in partially-filled elements, the length of the extruder's fully-filled region will not be affected *at all*. The fill fraction in the remainder of the extruder may vary, but seeing that these partially-filled regions typically have very low fill fractions and

predominantly serve the function of materials conveying, they have only a minor influence on the outcome of the process. Secondly, to model the mechanics of material transport in the partially-filled zone of an extruder is a complex task which does not generalise well. Such models would need to be different for a dry powder, a sticky powder, a viscous liquid and a runny liquid, as they would distribute differently in the screw cavity. Therefore a simple proportional relationship will be used here in order to proceed with the modelling of more dominant processes. The mass balance over an element k in the flow network can then be written as

$$\frac{\mathrm{d}(f_k V_k)}{\mathrm{d}t} = \sum_i Q_{i\to k} f_i - \sum_j Q_{k\to j} f_k \tag{6.3}$$

where V_k is the volume of element k and f_k is its fill fraction. The index i refers to the indices of all the elements from which a flow originates and enters element k, and the index j refers to the indices of all the elements which receive flow from element k. The volume V_k is, of course, constant with time, so the derivative of the fill fraction can be written explicitly as

$$\frac{\mathrm{d}f_k}{\mathrm{d}t} = \frac{1}{V_k}\left(\sum_i Q_{i\to k} f_i - \sum_j Q_{k\to j} f_k\right) \tag{6.4}$$

6.4.4 The Energy Balance

A simple back-of-the-envelope calculation reveals that the heat capacity of the metal comprising the screw shaft is typically around three times that of the material which may fill the void spaces around it. In order to ensure that the temperature change dynamics are realistic, one needs a strategy for dealing with the thermal mass of the screw shaft.

One possible approach is to have a separate model for heat transfer in the screw shaft running in parallel with the flow network model which simulates the heat conduction in the screw and the transfer of heat between it and the material in the flow network. A simpler approach, which will be used here, is to assume that the heat exchange between the process material and the screw is rapid. In this case the thermal mass of the material in each flow network element can be combined with the thermal mass of the screw in its vicinity. The energy balance over an element k in the flow network can then be written

$$\begin{aligned}\frac{\mathrm{d}}{\mathrm{d}t}\left(f_k V_k \rho C_p T_k + V_{m_k}\rho_{m_k} C_{p_m} T_k\right) &= \sum_i Q_{i\to k} f_i \rho C_p T_i - \sum_j Q_{k\to j} f_k \rho C_p T_k \\ &\quad + f_k \hat{\dot{U}}_k V_k + h_k A_k (T_{B_k} - T_k)\end{aligned} \tag{6.5}$$

where T_k is the temperature of element k; ρ and C_p are the density and specific heat capacity respectively of the process material; ρ_{m_k} and C_{p_m} are the density and specific heat

capacity of the metal comprising the screw; V_{m_k} is the volume of screw metal associated with element k of the flow network; $\dot{\hat{U}}_k$ is the specific rate of conversion of mechanical energy into heat energy; h_k is the heat transfer coefficient between the process material and the barrel; A_k is the area of barrel surface in contact with flow network element k; and T_{B_k} is the temperature of the barrel surface in contact with flow network element k. As before, the i refers to the indices of all the elements from which a flow originates and enters element k, and the j refers to the indices of all the elements which receive flow from element k. In Equation 6.5 the rate of convective heat transfer between the fluid and the barrel is independent of the fill fraction, as it is assumed that the bulk of the material in the screws resides close to the barrel surface as it is pushed along by the screw flights. If it is felt that this is not appropriate for the material being modelled, then a "fill proportional" convective heat transfer term such as $f_k h_k A_k (T_{B_k} - T_k)$ could be used.

Algebraic manipulation of Equation 6.5 provides an expression for the derivative of temperature in terms of calculable quantities, i.e.

$$\begin{aligned}\frac{\mathrm{d}T_k}{\mathrm{d}t} &= \frac{1}{f_k V_k \rho C_p + V_{m_k} \rho_{m_k} C_{p_m}} \left(\sum_i Q_{i\to k} f_i \rho C_p T_i - \sum_j Q_{k\to j} f_k \rho C_p T_k \right. \\ &\quad \left. + f_k \dot{\hat{U}}_k V_k + h_k A_k (T_{B_k} - T_k) - T_k V_k \rho C_p \frac{\mathrm{d}f_k}{\mathrm{d}t} \right) \end{aligned} \tag{6.6}$$

For non-threaded screw components, V_{m_k} is simply the volume of the screws associated with element k, calculated from the screw's geometrical parameters as described in previous chapters. For C-shaped and intermeshing elements of threaded screw components, the V_{m_k} are given by

$$V_{m_k}^{\text{C-chamber}} = \frac{A_{SX} L_p (\pi - \psi_S)}{\pi n_t} \tag{6.7}$$

$$V_{m_k}^{\text{intermeshing}} = \frac{A_{SX} L_p \psi_S}{\pi n_t} \tag{6.8}$$

where A_{SX} is defined according to Equation 2.12 or 2.27 in Chapter 2.

The specific rate of viscous heat generation term $\dot{\hat{U}}$ requires some further discussion. In the non-threaded shaft components, such as kneading discs, there is only a single $\dot{\hat{U}}$ associated with the flow volume. For the screw intermeshing elements, however, there is a value of $\dot{\hat{U}}$ associated with each of the tetrahedron gap, side gap, calender gap and screw channel flow avenue. In such cases where there are multiple $\dot{\hat{U}}$ adjoining the flow volume, a flow area weighted average $\overline{\dot{\hat{U}}}$ is used, i.e.

$$\overline{\dot{\hat{U}}} = \frac{\sum_i A_{c_i} \dot{\hat{U}}_i}{\sum_i A_{c_i}} \tag{6.9}$$

where the i refers to the flow conduits which adjoin the volume element, $\hat{\dot{U}}_i$ is the specific viscous heat dissipation in the conduit, and A_{c_i} is the cross-sectional area of conduit i.

Convective Heat Transfer Coefficients Between the Barrel and Process Fluid

Numerical analysis of the convective heat transfer between the process fluid and barrel wall in screw extruders requires calculation of the temperature field. Due to the enormous computational requirements of the complete problem, simplified models must be used to estimate the convective heat transfer coefficients.

Jepson (1953) calculated heat transfer coefficients by considering the transient heat conduction between the barrel and melt during the time interval between successive sweeps of the screw flight. Domschke and Justus (1993) used a more involved numerical analysis which considered the transient temperature field between the passing of the flight and screw channel, including the viscous heat dissipation in the flight clearance. More recently, White et al. (2001) used an analysis similar to that for the Graetz-Nusselt problem for temperature profiles in laminar flow pipes.

Due to its simplicity and sound basis, the model of Jepson (1953) is used in the present work. Figure 6.4 shows a schematic representation of the temperature field in the extruder between flight passes. Because of the short time interval between flight passes, the problem can be considered that of heat conduction in a semi-infinite medium. In this situation the one-dimensional heat conduction governing equation

$$\frac{\partial T}{\partial t} = \frac{\lambda}{\rho C_p}\frac{\partial^2 T}{\partial x^2} \tag{6.10}$$

has the solution

$$\frac{T(x,t) - T_w}{T_m - T_w} = \operatorname{erf}\left(\frac{x}{2}\sqrt{\frac{\rho C_p}{\lambda t}}\right) \tag{6.11}$$

where T_w is the wall surface temperature and T_m is the initial temperature of the melt. If A_w is the area of wall in contact with the melt, then the average rate of heat transfer $\dot{q}$ to the material during the time interval t is found by integrating the heat transferred to the semi-infinite medium after time t and dividing by the time, i.e.

$$\dot{q} = \frac{1}{t}\int_0^\infty \rho C_p (T(x,t) - T_m) A_w \,\mathrm{d}x \tag{6.12}$$

Performing the integration gives the result

$$\dot{q} = h_t A_w (T_w - T_m) \tag{6.13}$$

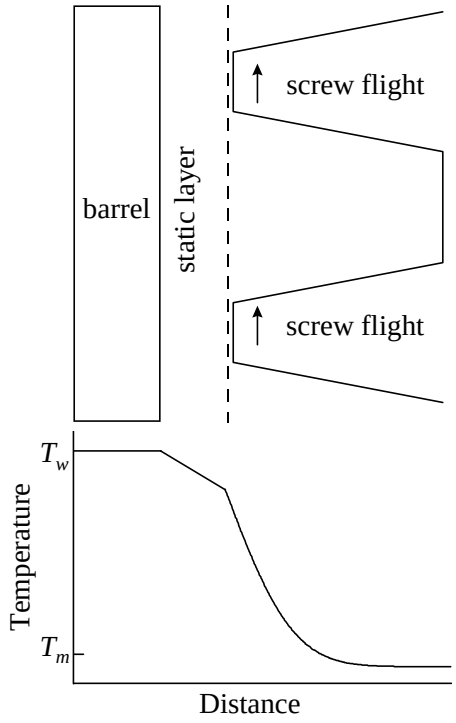

Figure 6.4: Temperature field in the cross-section of an extruder between flight passes.

where the effective heat transfer coefficient h_t is given by

$$h_t = \frac{2}{\sqrt{\pi}}\sqrt{\frac{\rho C_p \lambda}{t}} \tag{6.14}$$

The analysis so far has not taken into account the thermal resistance presented by the layer of melt in the (static) clearance gap between the screw flight and the barrel, which has thickness L_m. Adding the contribution of this static layer gives the overall heat transfer coefficient h as

$$\frac{1}{h} = \frac{1}{h_t} + \frac{1}{\lambda / L_m} \tag{6.15}$$

The clearance gap L_m for a screw is the difference between the barrel radius and the screw radius, $R_B - R_s$. The time interval t over which the heat transfer is calculated is given by the revolution period divided by the number of screw flights, $1/Nn_t$. It is thus clear from Equations 6.14 and 6.15 that the heat transfer coefficient can be increased by increasing the screw speed, by using screws with a larger number of tips, or by decreasing the clearance gap.

6.4.5 Specific Mechanical Energy

The specific mechanical energy $\hat{W}$ ($\mathrm{J\,m^{-3}}$) measures the cumulative mechanical energy expended on the process material due to viscous dissipation. The mechanical energy balance equation can be written as

$$\frac{\mathrm{d}(f_k V_k \hat{W}_k)}{\mathrm{d}t} = \sum_i Q_{i\to k} f_i \hat{W}_i - \sum_j Q_{k\to j} f_k \hat{W}_k + \hat{\dot{U}}_k V_k f_k \tag{6.16}$$

Equation 6.16 can be rearranged to give the time derivative of specific mechanical energy explicitly as

$$\frac{\mathrm{d}\hat{W}_k}{\mathrm{d}t} = \frac{1}{f_k V_k}\left(\sum_i Q_{i\to k} f_i \hat{W}_i - \sum_j Q_{k\to j} f_k \hat{W}_k\right) + \hat{\dot{U}}_k - \frac{\hat{W}_k}{f_k}\frac{\mathrm{d}f_k}{\mathrm{d}t} \tag{6.17}$$

6.4.6 Moisture Fraction

The moisture balance over element k can be written

$$\frac{\mathrm{d}(f_k V_k M_k)}{\mathrm{d}t} = \sum_i Q_{i\to k} f_i M_i - \sum_j Q_{k\to j} f_k M_k \tag{6.18}$$

where M_k is the moisture fraction by weight in element k which can take values between zero and one. Rearranging Equation 6.18 provides an explicit expression for the time derivative of the moisture fraction:

$$\frac{\mathrm{d}M_k}{\mathrm{d}t} = \frac{1}{f_k V_k}\left(\sum_i Q_{i\to k} f_i M_i - \sum_j Q_{k\to j} f_k M_k\right) - \frac{M_k}{f_k}\frac{\mathrm{d}f_k}{\mathrm{d}t} \tag{6.19}$$

6.4.7 Component Concentration

The dynamic mass balance on an inert chemical species in element k of the extruder is identical in form to Equation 6.19 for moisture transport. The rate change in concentration C_k in element k is thus written as

$$\frac{\mathrm{d}C_k}{\mathrm{d}t} = \frac{1}{f_k V_k}\left(\sum_i Q_{i\to k} f_i C_i - \sum_j Q_{k\to j} f_k C_k\right) - \frac{C_k}{f_k}\frac{\mathrm{d}f_k}{\mathrm{d}t} \tag{6.20}$$

Equation 6.20 could be used to model an inert tracer pulse added to the feed of the extruder to determine the residence time distribution of the process, which will be discussed later in this chapter.

6.5 Modelling Extrusion Cooking of Starches

Several investigations in this thesis relate to an extrusion cooking process where the material being extruded is a low moisture corn flour. The following subsections describe techniques for extending the basic extrusion model to include two product quality attributes of interest in such a process: the degree of gelatinisation and the product bulk density. The models and parameters are obtained directly from the literature, and no attempt has been made here to verify them experimentally. The intention is to simulate the general behaviour of these product quality attributes with models that respond in a realistic way, rather than aim for absolute model accuracy. The rheology of low moisture starch mixtures under extrusion conditions is also discussed.

6.5.1 Starch Gelatinisation

Starch is a partially crystalline mixture of glucose polymer chains occurring naturally in plants. When starch granules are heated in the presence of a solvent such as water, the crystalline structure irreversibly melts and the individual polymer chains become mobilised (Camire et al., 1990). Starch gelatinisation is thought to influence product consistency and flavour. Starch molecules are also subject to fragmentation (Davidson et al., 1984), a transformation which is also thought to be correlated with product quality, though it will not be discussed further here.

It has been observed that the rate of starch reactions during extrusion cooking is usually very fast compared with conventional thermal cooking (Wang et al., 1992). The high shear forces present during extrusion appear to have the effect of physically tearing apart the starch granules, and allow faster transfer of water into the interior of the starch granules (Gomez and Aguilera, 1984).

Few reports exist on the kinetics of starch conversion in extruders. Several experiments have been performed (Bhattacharya and Hanna 1987; Burros et al. 1987; Wang et al. 1989) to determine the gelatinisation rate constant parameters and reaction order under extrusion conditions. Such experiments provide pseudo-kinetic models of the gelatinisation process, generally having non-integer reaction orders. However, the effects of shear which make extrusion such a unique process were not modelled specifically. Wang et al. (1992) and Cai and Diosady (1993) have both attempted to incorporate shear effects into their kinetic models. Given that the model of Cai and Diosady has been validated over a wider range of operating conditions, it will be the model of choice for incorporation into the present extrusion process model.

In a shearless environment the rate constant for starch gelatinisation is assumed to conform to the Arrhenius equation

$$k_g = k_0 \exp\left(-\frac{E}{\mathbf{R}T_K}\right) \tag{6.21}$$

where k_g is the rate constant, k_0 is the pre-exponential factor, $\mathbf{R}$ is the ideal gas constant, T_K is the temperature in Kelvin, and E is the activation energy. Since starch gelatinisation is due to the rupture of hydrogen bonds (Birch and Priestley, 1973), Cai and Diosady suggested that the theories for the effect of shear stress on bond rupture could be adapted to describe the effect of shear stress on starch gelatinisation. When the bonds are mechanically strained, E in Equation 6.21 is replaced by the expression for the strength of the elastically deformed bond. The rate constant equation was thus rewritten by Cai and Diosady as

$$k_g = k_0 \exp\left(-\frac{E_0 - \vartheta\tau}{\mathbf{R}T_K}\right) \tag{6.22}$$

where E_0 is the new activation energy, τ is the shear stress and ϑ is the so called 'activation volume'. Reaction orders of around 1 were reported, whereas other experimentalists (Bhattacharya and Hanna 1987; Burros et al. 1987; Wang et al. 1989) reported zero order kinetics. Using Equation 6.22 the mass balance on gelatinised starch over a model element k of the extruder can be written as

$$\frac{\mathrm{d}(f_k V_k g_k)}{\mathrm{d}t} = \sum_i Q_{i\to k} f_i g_i - \sum_j Q_{k\to j} f_k g_k + k_g(1 - g_k) f_k V_k \tag{6.23}$$

where g_k is the gelatinisation fraction in element k and k_g is the gelatinisation rate constant described by Equation 6.22. The magnitude of the shear stress in Equation 6.22 is described by the power-law relationship

$$\tau = K\dot{\gamma}^n \tag{6.24}$$

where $\dot{\gamma}$ is the shear rate and K and n are the power-law parameters. Rearrangement of Equation 6.23 allows the time derivative of the gelatinisation fraction in element k to be written explicitly as

$$\frac{\mathrm{d}g_k}{\mathrm{d}t} = \frac{1}{f_k V_k}\left(\sum_i Q_{i\to k} f_i g_i - \sum_j Q_{k\to j} f_k g_k\right) + k_g(1 - g_k) - \frac{g_k}{f_k}\frac{\mathrm{d}f_k}{\mathrm{d}t} \tag{6.25}$$

Cai and Diosady (1993) reported parameter values of $k_0 = 5716.3$ s^{-1} and $E_0 = 45636.9$ J/kg-mol, which were also used in this work. The activation volume ϑ used in this work was estimated from Cai and Diosady's data to be 2.25×10^{-4} m^3/kg-mol.

6.5.2 Bubble Growth and Product Bulk Density

When process material exits an extruder, entrained volatile substances can flash causing tiny bubbles to grow, resulting in a cellular foam structure. The resulting product bulk

density is clearly an important indicator of product quality which needs to be controlled because it quantifies the difference between a hard pelletised product and a puffed foam. The final product bulk density depends on the size of the bubbles which grow and the number of nucleation sites per unit volume.

Fan et al. (1994) modelled the dynamics of single bubble growth and shrinkage in superheated moist extrudates by considering momentum conservation, continuity of mass and balancing forces acting on the bubble wall, and the energy balances relating to water vaporisation and convective cooling. The final bubble size is a function of the properties of the material exiting the extruder, namely the moisture content, die temperature and rheology; which is itself a function of the temperature and moisture content[2]. Having determined the final bubble size, Fan et al. calculated an approximate product bulk density by applying an estimate for the number of bubble nucleation sites available per unit weight. A full description of their model development is quite lengthy so it will not be reproduced here. Suffice it to say, the model of Fan et al. was incorporated into the present extruder model without significant modification.

For the purpose of expediting the estimation of the product bulk density in the present extruder model, it is noted that the final bubble size for a given feed material is a function of the die temperature and moisture content only. Using the bubble growth model of Fan et al., a look-up table can be generated for the final bubble radius, indexed by both die temperature and moisture content. Figure 6.5 shows the data of one such table generated for corn starch using the rheological model of Vergnes and Villemaire (1987), which will be discussed in the following section. Using this look-up table, given the extruder product outlet temperature and moisture content, the corresponding final bubble radius r_b can be found, allowing the product bulk density ρ_B to be calculated rapidly according to

$$\rho_B = \frac{1}{\frac{1}{\rho} + N_s \frac{4}{3}\pi r_b^3} \tag{6.26}$$

where N_s is the number of nucleation sites per unit mass and ρ is the density of corn starch. As suggested by Fan et al., for rough estimation purposes only, a value of $N_s = 2 \times 10^6$ kg^{-1} was used, while the density of corn starch was taken to be $\rho = 1400$ $\mathrm{kg/m}^3$.

Presumably bubbles are also subject to coalescence while the number of nucleation sites may vary significantly with processing conditions, so the presently described model is not expected to provide more than a basic insight into the influence of operating variables on the bulk density. It is interesting to note from Figure 6.5 that the maximum bubble radius (and therefore minimum product bulk density) occurs at a moisture fraction of around 0.17 w/w, and increases with increasing temperature. In Chapters 7 and 8 the product bubble size distribution will be measured directly and modelled in greater detail.

[2]Thermo-mechanical degradation is not taken into account in the present implementation of the bubble growth rheology model.

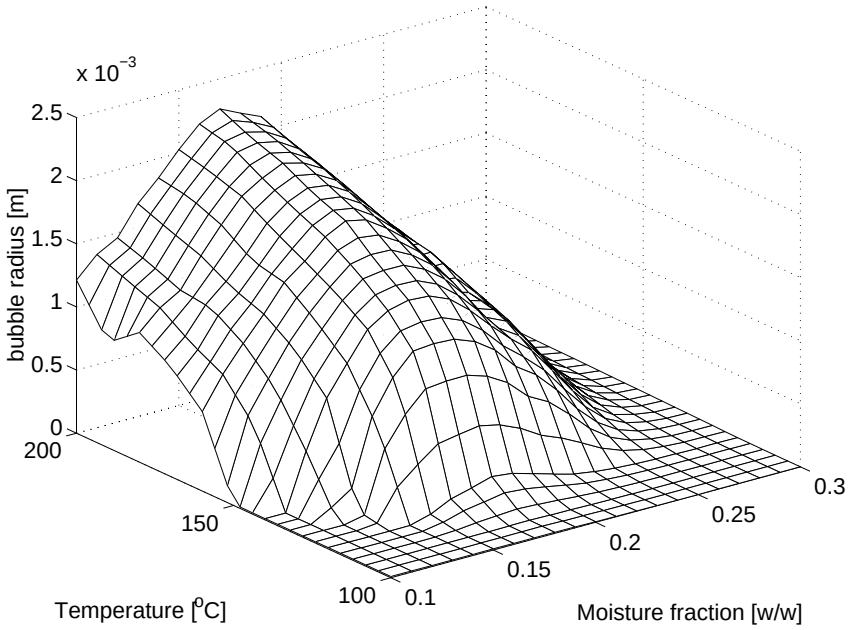

Figure 6.5: Product bubble radius as a function of moisture content and temperature.

6.5.3 Dough Rheology

The extruder model, and indeed the physical process itself, is highly sensitive to changes in material rheology, so a good mathematical description of the rheological behaviour is necessary to accurately simulate the process.

Unfortunately, from a modelling point of view, the rheological characteristics of low moisture starch mixtures are influenced by many different variables. In addition to being sensitive to natural variations in protein and oil contents, the rheology of a given flour is typically a function of temperature, moisture content and thermo-mechanical history (Dolan et al., 1989).

There have been relatively few studies on the rheological behaviour of biological materials under extrusion conditions. This is due to the difficulty in replicating inside a rheometer the low moisture, high temperature and high shear conditions typically found inside a cooking extruder. Several researchers have performed rheological investigations by attaching a customised capillary rheometer die to their extruders, allowing the product viscosity to be measured (e.g. Harper et al., 1971; Cervone and Harper, 1978). Of particular note is the work of Vergnes and Villemaire (1987), who constructed a pre-shearing rheometer so that the thermal and mechanical treatment of the dough could be controlled prior to viscosity measurement in a capillary rheometer. A power-law viscosity model was used, i.e.

$$\mu = K\dot{\gamma}^{n-1} \tag{6.27}$$

Table 6.1: Parameters in molten corn starch rheology model of Vergnes and Villemaire (1987).

Parameter	Value	Parameter	Value	Parameter	Value
K_0	428 000 Pa×s	α_m	10.6	κ_1	-6.74×10^{-2}
$E/\mathbf{R}$	4 250 K	α_w	8.8×10^{-10}	κ_2	1.88×10^{-3}
T_{K_0}	353 K	α_1	6.59×10^{-4}	κ_3	1.01
M_0	0.10 w/w	α_2	1.12×10^{-1}	κ_4	3.28×10^{-3}
$\hat{W}_0$	10^7 J/m^3	α_3	7.28×10^{-3}	κ_5	2.23×10^{-13}

where μ is the viscosity, $\dot{\gamma}$ is the shear rate, and the power-law parameters K and n have the form

$$K = K_0 \exp\left[\frac{E}{\mathbf{R}}\left(\frac{1}{T_K} - \frac{1}{T_{K_0}}\right) - \alpha_m\left(M - M_0\right) - \alpha_w\left(\hat{W} - \hat{W}_0\right)\right] \tag{6.28}$$

$$n = \alpha_1 T_C + \alpha_2 M + \alpha_3 T_C M \tag{6.29}$$

where T_K is the temperature in Kelvin, T_C is the temperature in Celsius, M_0 is the reference moisture fraction, $\hat{W}_0$ is the reference specific mechanical energy, and the α_i are model parameters. The parameters reported by Vergnes and Villemaire are listed in Table 6.1.

The independent variables covered the ranges 110 – 170°C for temperature, around 10 – 1000 s^{-1} for shear rate, 26 – 49% dry basis moisture fraction and 0.55 – 8.25×10^{-8} J/m^3 for specific mechanical energy. These values span much of the conditions normally found within a cooking extruder, hence the model was felt to be appropriate for performing extrusion simulations.

It was found, however, that application of this model resulted in some unexpected rheological behaviour. In particular, under certain conditions, when simulating non-Newtonian flow through a circular tube, the flow rate *decreased* as the moisture content was increased. This effectively meant that adding water to the dough made it more viscous, which is not only contrary to common experience, but also to the observations of the researchers who developed the model. This behaviour was not reflected in the raw data published in Vergnes and Villemaire (1987), so it was attributed to Equation 6.29 having an inappropriate functional form for describing the functional dependence of the pseudoplastic index n.

Using the original data published by Vergnes and Villemaire (1987) a new regression model for n was designed using a symbolic regression algorithm known as *genetic programming* (GP). The GP algorithm (Koza, 1992; Kinnear, 1994) uses concepts borrowed from Darwinian evolutionary theory to evolve mathematical structures which describe relationships between input and output data sets. The original temperature, moisture content and

specific mechanical energy data, along with the corresponding measured values for n, were presented to a GP algorithm and the following relationship was evolved:

$$n = \kappa_1 + \kappa_2 T_C + \kappa_3 M^2 + \kappa_4 T_C M + \kappa_5 T_C \hat{W}; \tag{6.30}$$

The κ_i parameters are listed in the third column of Table 6.1. It was found that the correlation coefficient between the original data for n and the values predicted by Equation 6.30 was 0.998, and that the behaviour of the rheology model in regard to non-Newtonian tube flow trends using Equation 6.30 for n became consistent with the trends observed by the experimenters in the original paper.

6.6 Solids Conveying

It will be noted that the experimental component of this thesis was performed on an extrusion cooking process where the water and flour feed mixture was assumed to rapidly form a viscous dough. This is not an unreasonable assumption given that Kulshreshtha et al. (1991a) and Barrès et al. (1991) observed significant temperature rises in the conveying zones of their extrusion cooking processes. This observation is more consistent with viscous flow and viscous heat dissipation than solid particle conveying and frictional heat generation. Consequently, for the purposes of this thesis, there is no reason as yet to incorporate solids conveying behaviour into the extrusion process model. However, seeing that solids conveying is relevant to many types of extrusion processes, the following discussion on modelling solids conveying is included for completeness only. No comment can be made as to whether it produces reasonable simulation results or agrees well with experimental observations.

In many extrusion processing applications, such as plastics extrusion, the feed material enters the extruder as a solid powder or as pellets. While the material remains below its melting temperature, it is transported as a solid according to the laws of particle mechanics. The temperature change in the solids conveying region is due to heat exchange with the screw and barrel wall, and frictional heat generation.

Potente et al. (1996) reported that the nature of the feed material has a strong influence over the conveying mechanism, as does the feed rate. Polymer pellets at low feed rates, for instance, tend to fall to the bottom of one screw and are conveyed at the maximum conveying velocity $L_p N$ in the axial direction. A sticky substance, however, may adhere to the screws and barrel and experience more drag effects.

In regard to modelling the solids conveying process during extrusion, Yacu (1985) assumed conveying occurred at the maximum (ideal) rate and that the temperature rise was due only to heat transfer with the barrel. Tayeb et al. (1988b) included a frictional heat generation term in their model for hydrated maize starch conveying, but the same group (Barrès et al., 1991) later removed it. Their experiments did show, however, that

significant temperature rises take place in the solids conveying region[3] for their hydrated maize material. Bawiskar and White (1997), in the context of polymer pellet extrusion, only consider temperature rises in the solids conveying regions where the barrel is fully filled and pressurisation has occurred. Their heat balance equation then considers heat conduction at the barrel and friction between the barrel wall and the solids.

It has to be concluded that the mechanism of solids conveying is strongly dependent on the properties of the feed material. Solids conveying models therefore need to be tailored to the process at hand.

To adapt the present model to describe solids conveying in the screws, it will be assumed that positive displacement, Q_p, is the predominant mechanism, while some part of the drag components of Q_c, Q_t, Q_s, Q_n and Q_f may contribute, depending on the nature of the feed material. The general mass balance therefore may be written as

$$\frac{\mathrm{d}(f_k V_k)}{\mathrm{d}t} = \sum_i m_i Q^d_{i\to k} f_i - \sum_j m_j Q^d_{k\to j} f_k \tag{6.31}$$

where the m_i and m_j are fraction multipliers applied to each flow type indicating its contribution to drag transport for the particular feed solid. While the temperature is below the melting point of the solid, it will be assumed that no pressure flow can contribute to any of the flow rates in Equation 6.31, hence the superscript d is used to indicate that only the drag component of the flow applies.

When solid feed is conveyed towards a screw component which produces a flow constriction, such as an orifice disc, reverse screw section or die, the solid material compacts and the temperature rises rapidly due to friction and irreversible deformation until the solid melts. The rate of work done on the solid per unit volume $\hat{\dot{F}}$ is the scalar product of the stress tensor and the velocity gradient, which are determined in terms of the coefficient of friction F_s, the compaction pressure p_c, and the shear rate $\dot{\gamma} = \sqrt{(\Delta : \Delta)/2}$, giving the expression (Tayeb et al., 1988b)

$$\hat{\dot{F}} = \frac{\int_V F_s\, p_c\, \dot{\gamma}\, \mathrm{d}V}{\int_V \mathrm{d}V} \tag{6.32}$$

The coefficients of friction between the solid and screw surface, solid and barrel surface, and the solid with itself all need to be determined experimentally for the solid in question. The energy balance in the solids conveying zone may then be written as

$$\begin{aligned}\frac{\mathrm{d}}{\mathrm{d}t}\left(f_k V_k \rho C_p T_k + V_{m_k} \rho_{m_k} C_{p_m} T_k\right) &= \sum_i m_i Q^d_{i\to k} f_i \rho C_p T_i - \sum_j m_j Q^d_{k\to j} f_k \rho C_p T_k \\ &\quad + \hat{\dot{F}}_k V_k \,\mathrm{sign}(p_{c_k}) + f_k h^*_k A_k (T_{B_k} - T_k)\end{aligned} \tag{6.33}$$

[3]Though the possibility of heat conduction along the screw shaft was not raised.

where the sign(p_{c_k}) term has a value of 1 only when the chamber is fully-filled and thus pressurised, and h_k^* is the heat transfer coefficient between the solid and the barrel.

6.7 Solution Scheme

The equations for $\frac{\mathrm{d}f}{\mathrm{d}t}$, $\frac{\mathrm{d}T}{\mathrm{d}t}$, $\frac{\mathrm{d}\hat{W}}{\mathrm{d}t}$, $\frac{\mathrm{d}M}{\mathrm{d}t}$ and $\frac{\mathrm{d}C}{\mathrm{d}t}$ in each element constitute a system of ODEs which can be numerically integrated from an initial set of starting conditions to give the dynamic behaviour of the extruder. The steps in the solution procedure are as follows:

1. Define the geometrical parameters of the screws used in the simulation.
2. Define the screw configuration.
3. Define the barrel geometry, including the location of any controlled barrel temperature zones.
4. Define the parameters of the rheological model.
5. Define values for all physical properties (such as λ, C_p and ρ).
6. Construct the flow network. Calculate the position in 3D space of every element in the flow network.
7. Construct a flow-list, which is a data structure containing an entry for each flow link in the flow network, listing the indices of the two elements in the network between which the flow occurs, the type of flow, and a pointer to the geometrical parameters of the screw type in which the flow occurs.
8. Calculate the volumes of all the elements in the flow network, as well as the volume of the screw metal associated with each element in the flow network.
9. Define the initial values of the state variables f, T, $\hat{W}$, M and C in every element of the flow network.
10. Define the operating conditions of the extruder: the feed rate, feed temperature, feed moisture fraction, feed concentration, screw speed and the barrel temperature profile.
11. Calculate the values of the state derivatives $\frac{\mathrm{d}f}{\mathrm{d}t}$, $\frac{\mathrm{d}T}{\mathrm{d}t}$, $\frac{\mathrm{d}\hat{W}}{\mathrm{d}t}$, $\frac{\mathrm{d}M}{\mathrm{d}t}$ and $\frac{\mathrm{d}C}{\mathrm{d}t}$ in each element based on the current f, T, $\hat{W}$, M, C and operating conditions. This is facilitated in practice by cycling through the flow list (created in step 7) and calculating the contribution of each flow to the derivative terms.
12. Step Δt into the future and calculate the states f, T, $\hat{W}$, M and C in each element at the new time.

13. Repeat from step 10 until the maximum simulation time is reached.

Steps 11–13 are performed using a stiff ordinary differential equation (ODE) solver.

6.7.1 Stiffness of Model ODEs

The ODEs describing the state variables in the extruder model possess a property called stiffness. This property arises when the modelled phenomena possesses characteristic time scales that vary by several orders of magnitude. In the present case, the ODEs used to model the extruder are stiff because the pressure (via the fill fraction state variable) adjusts to changing conditions much faster than other quantities (such as temperature).

The computational cost of numerically integrating stiff ODEs is enormous when using non-stiff algorithms such as Runge-Kutta methods or predictor-corrector methods such as Adams-Bashforth (Press et al., 1992). To maintain stability, the non-stiff ODE solver must use a step-size which is small enough to track the part of the solution corresponding to the shortest time scale, even when this component has decayed to some quasi-steady value. Stiff ODE solvers adjust their step-size based on considerations of accuracy rather than stability. The computational expense of using a stiff ODE solver is much greater per time-step than using a non-stiff algorithm, but the advantage is that much larger step-sizes can be used when accuracy considerations permit, so the overall computational cost is much less when applied to stiff problems.

In the present extruder model solution scheme, the ODEs describing the extruder state variables are numerically integrated using the MATLAB (Mathworks, 1998) `ode15s` software routine, which is a variable order multi-step ordinary differential equation solver based on the Klopfenstein-Shampine numerical differentiation formulas (Shampine and Reichelt, 1997). Typical computer run times are given in the following sections.

6.8 Results

6.8.1 Startup Simulation

Initially, the model was used to simulate the start-up of a hypothetical twin-screw extruder which is initally empty and at room temperature. The screw configuration used in the simulation is shown in Figure 6.2(a) and its representation as a flow network in three dimensions is shown in Figure 6.2(b). Note that the screw configuration has been contrived to include all of the screw types discussed in this thesis. Table 6.2 lists the geometry and screw configuration details of the extruder used in this simulation. A short-hand is used to describe the screw types and configuration: TFS signifies a trapezoidal flight screw; TFSR signifies a reverse-threaded trapezoidal flight screw; SWS signifies a self-wiping screw; KD signifies a kneading disc; and OD signifies an orifice disc. The lengths of each screw section are indicated by the number of barrel diameters, such as "$2 \times D$", while the kneading discs

Table 6.2: Geometric and physical data parameters used in the startup simulation.

Barrel Data		*Screw Data*				*Shaft Configuration*	
C_L	30.8×10^{-3}m	Name	TFS1	Name	TFSR1	(Feed)	
R_B	20.0×10^{-3}m	Type	TFS	Type	TFS	$2 \times D$	SWS2
d_1	0.8600 m	L_p	10.0×10^{-3}m	L_p	10.0×10^{-3}m	$6 \times +60°$	KD1
d_2	0.7540 m	n_t	1	n_t	1	$1 \times D$	TFS1
d_3	0.6540 m	R_s	19.35×10^{-3}m	R_s	19.35×10^{-3}m	1	OD1
d_4	0.5620 m	R_r	11.0×10^{-3}m	R_r	11.0×10^{-3}m	$1 \times D$	TFS1
d_5	0.4520 m	t_f	2.40×10^{-3}m	t_f	2.40×10^{-3}m	$6 \times +60°$	KD1
d_6	0.3390 m	w_c	4.40×10^{-3}m	w_c	4.40×10^{-3}m	$6 \times -60°$	KD1
d_7	0.2410 m	direction	+1	direction	-1	$2 \times D$	TFS1
d_8	0.1560 m	Name	SWS2	Name	KD2	$1 \times D$	TFSR1
d_9	0.0510 m	Type	SWS	Type	KD	$1 \times D$	TFS1
		L_p	40.0×10^{-3}m	L_d	7.0×10^{-3}m	1	DIE1
Physical Data		n_t	2	n_t	2	(Die)	
E_v	2.15×10^{9}Pa	R_s	19.35×10^{-3}m	R_s	19.35×10^{-3}m		
ρ	1400 kg m^{-3}	R_r	11.0×10^{-3}m	R_r	11.0×10^{-3}m		
C_p	3616 J kg^{-1} K^{-1}	direction	+1	Name	DIE1		
λ	0.25 W m^{-1} K^{-1}	Name	OD1	Type	DIE		
ρ_m	7900 kg m^{-3}	Type	OD	L_d	28.0×10^{-3}m		
C_{p_m}	447.2 J kg^{-1} K^{-1}	L_d	10.0×10^{-3}m	R_d	1.5×10^{-3}m		
λ_m	16.3 W m^{-1} K^{-1}	R_s	18.0×10^{-3}m	V_d	8.5×10^{-6}m^3		
		R_r	10.0×10^{-3}m	V_m	9.51×10^{-4}m^3		

configurations are described by the number of discs and the stagger angle used, such as "$6 \times +60°$".

A power-law rheology model, as in Equation 6.27, was used with the parameters $K = 5000\text{Pa s}^n$ and $n = 0.5$. No temperature dependence was included in the rheology model in order to exemplify the fluid transport and viscous heat dissipation effects separately. To illuminate the rate of viscous heat dissipation occurring in each element, the barrel was modelled as though it were constructed from an insulating material so that there is no heat transferred between the barrel and the fluid. Temperature rises in the fluid are consequently due to mixing and viscous heat dissipation effects only.

Figure 6.6(a) shows the development of the fill fraction profile during the first 80 seconds of start-up. It can be seen that the elements up-stream of the orifice discs, reverse paddles, reverse screws and die element become fully filled as the extruder approaches steady-state. The opposing kneading paddle and the opposing forward-reverse screw sections fill symmetrically from the middle outwards.

Figure 6.6(b) shows pressure development during the first 80 seconds of start-up, which is calculated directly from the fill fraction according to Equation 6.2. It can be seen that the pressure built-up in the kneading disc section is low compared to the screw elements up-stream of the orifice discs, and very low compared to the elements up-stream of the

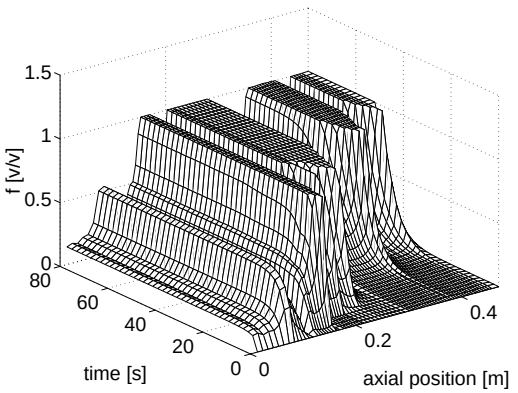

(a)

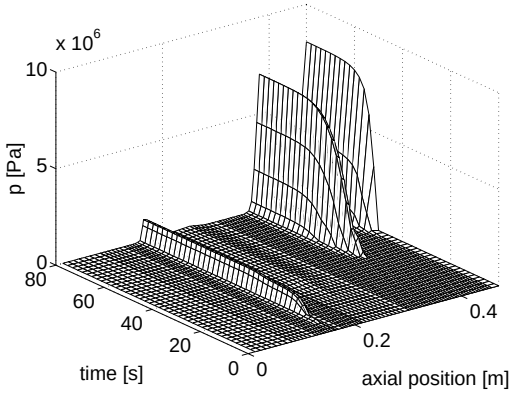

(b)

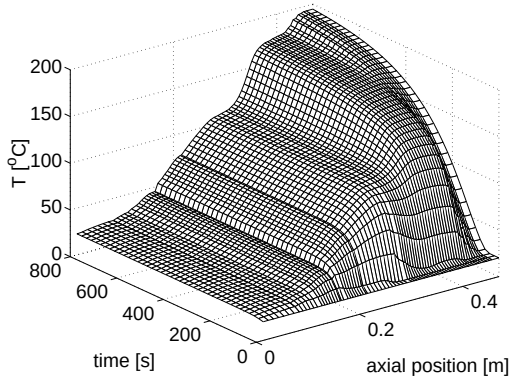

(c)

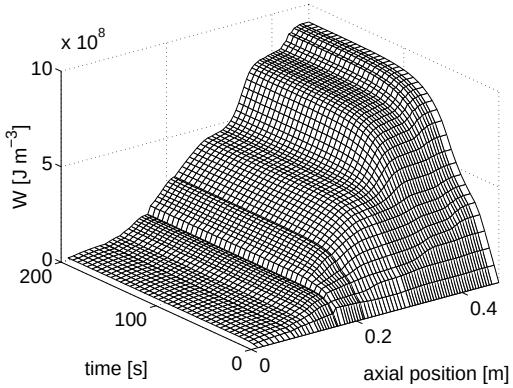

(d)

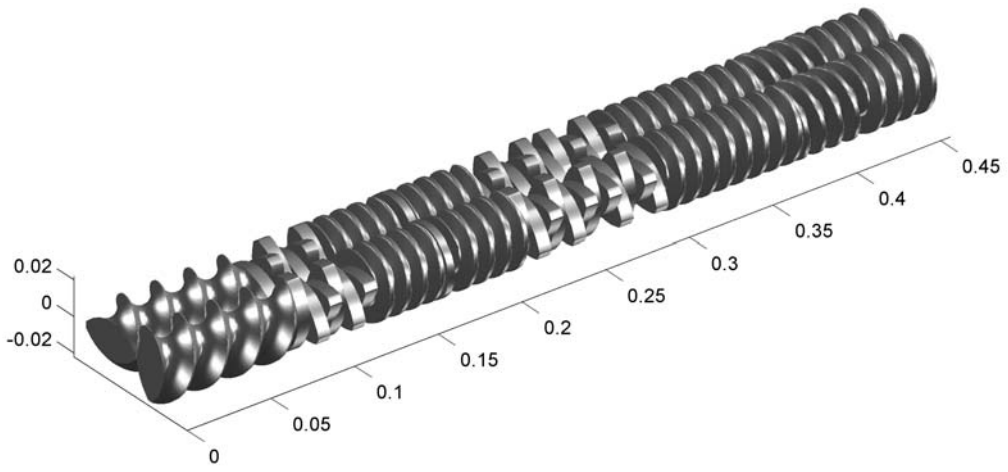

(e)

Figure 6.6: Startup simulation dynamic axial profile surfaces; (a) fill fraction; (b) pressure; (c) temperature; (d) specific mechanical energy; (e) the screw configuration used in the simulation, dimensions in metres. Note that the feed enters at axial position zero and that different time scales are used on each plot.

reverse screw and die elements.

Figure 6.6(c) shows the evolution of temperature over the first 800 seconds of start-up. It can be seen that temperature approaches steady-state slower than fill fraction or pressure does, partly due to the thermal mass of the screw elements. The temperature rises in the reverse kneading disc and reverse screw sections are particularly large. The viscous heat generating behaviour of these sections is also seen in the contributions they make to the specific mechanical energy profile shown in Figure 6.6(d). The steady-state axial profiles are shown in Figure 6.7.

It must be mentioned that the degree of fill was found to vary significantly among the model elements of each screw. Figure 6.8(a) shows a schematic axial cross-section through a screw pair and barrel indicating the direction of rotation of the screws. It is often noted in the literature (e.g. Potente et al., 1996) that the flow constriction created by the intermeshing region causes material to accumulate around the inlet side, leading to different material distributions around the screws, though this has never been quantified. The present model predicts this behaviour. Figure 6.8(b) shows the calculated steady-state fill fractions across the cross-section of the trapezoidal flight screw in the partially filled zone at the axial position marked with a vertical line in Figure 6.8(c). The degree of fill down the extruder therefore does not vary smoothly unless one considers successively the C-shaped elements, successive inlet intermeshing regions, or successive outlet intermeshing regions along the screws. The difference between these profiles is shown in Figure 6.8(c). To permit the viewing of coherent trends along the axial direction in the screw sections, the figures in this chapter always display the values of the state variables in the inlet intermeshing regions of the screws unless otherwise stated. It should be noted that the ability of the present model to simulate this uneven filling behaviour is a result of the flow network structure chosen for the screws, which includes specific model elements on either side of the intermeshing region in addition to the C-shaped elements. Previous models have employed simpler flow structures which are incapable of capturing this behaviour. The entire start-up simulation required around 20 minutes of CPU time on a 600MHz Pentium 3 personal computer.

6.8.2 Extrusion Cooking Dynamic Response Simulation

Next the dynamic behaviour of a low moisture corn flour extrusion process was simulated using the model described in this chapter. Step changes in screw speed, feed rate, moisture content and screw wear were simulated and the transient effect on die temperature, die pressure, product moisture content, product specific mechanical energy, product bulk density and product gelatinisation fraction were recorded. The simple "high shear" screw configuration shown in Figure 6.9 was used in this simulation. The geometrical parameters and screw configuration are listed in Table 6.3. The rheological model of Vergnes and Villemaire (1987), as described by Equations 6.28 and 6.30, was used to describe the low

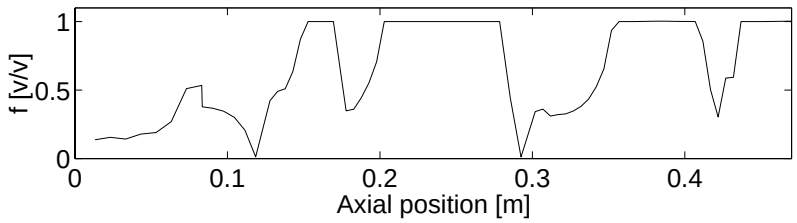

(a)

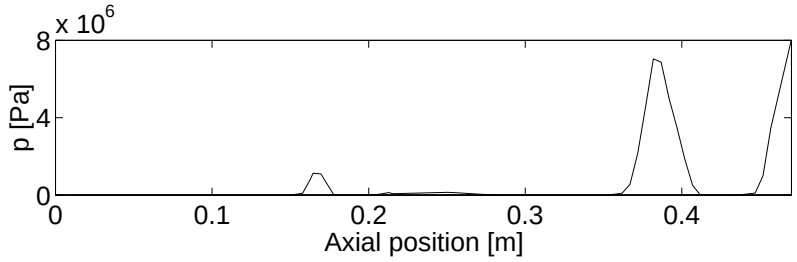

(b)

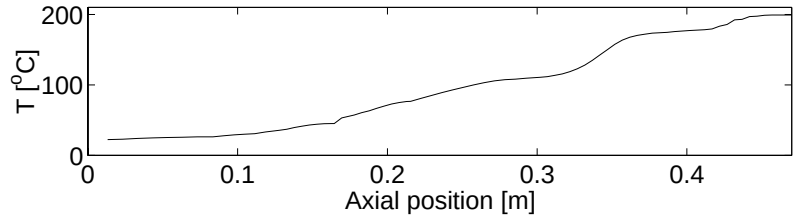

(c)

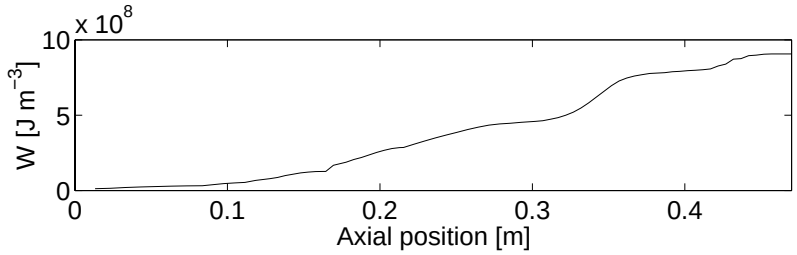

(d)

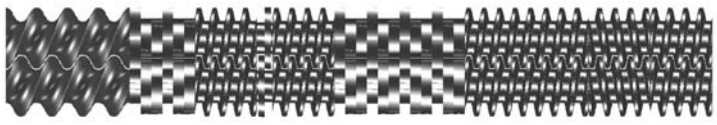

(e)

Figure 6.7: Steady-state axial profiles after startup showing (a) fill fraction; (b) pressure; (c) temperature; (d) specific mechanical energy; (e) the screw shaft used in the simulation.

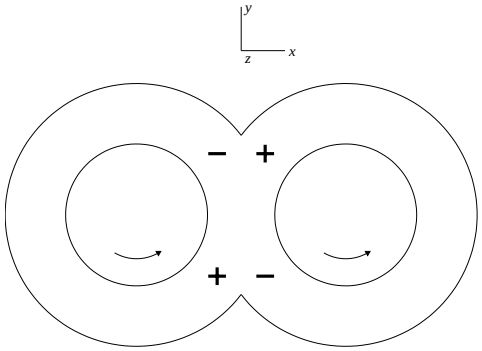

(a)

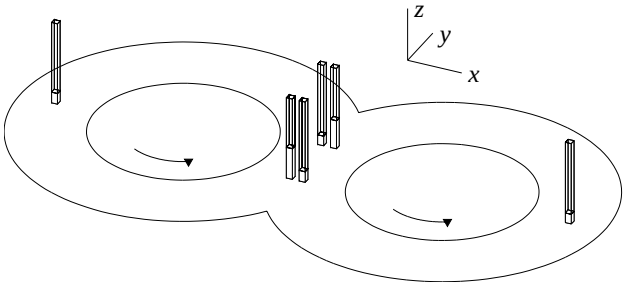

(b)

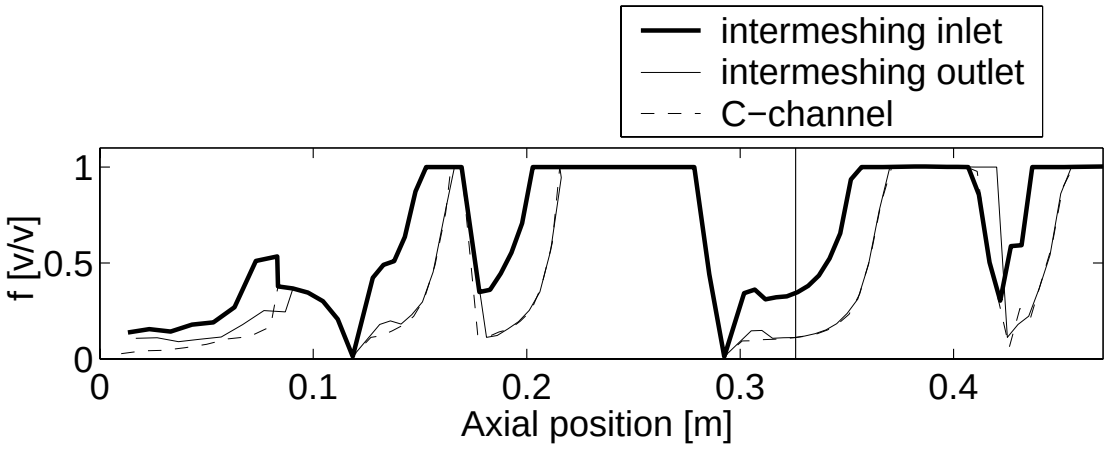

(c)

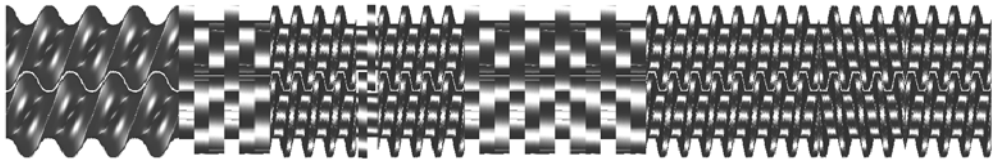

(d)

Figure 6.8: (a) Schematic cross-section through screw shafts and barrel indicating areas of high (+) and low (−) fill; (b) screw fills predicted by the model in the startup simulation, the wire-frame bars indicating the height corresponding to a completely filled model element; (c) steady-state profiles along the extruder through different screw regions; and (d) the screw shaft used in the simulation.

Table 6.3: Geometric and physical data parameters used in the extrusion cooking dynamic response simulations.

Barrel Data		*Screw Data*				*Shaft Configuration*	
C_L	30.8×10^{-3}m	Name	TFS1	Name	TFSR1	(Feed)	
R_B	20.0×10^{-3}m	Type	TFS	Type	TFS	$2 \times D$	SWS2
d_1	0.8600 m	L_p	10.0×10^{-3}m	L_p	10.0×10^{-3}m	$1 \times D$	TFS1
d_2	0.7540 m	n_t	1	n_t	1	$7 \times +60°$	KD1
d_3	0.6540 m	R_s	19.35×10^{-3}m	R_s	19.35×10^{-3}m	$7 \times -60°$	KD1
d_4	0.5620 m	R_r	11.0×10^{-3}m	R_r	11.0×10^{-3}m	1	OD1
d_5	0.4520 m	t_f	2.40×10^{-3}m	t_f	2.40×10^{-3}m	$1 \times D$	TFS1
d_6	0.3390 m	w_c	4.40×10^{-3}m	w_c	4.40×10^{-3}m	1	DIE1
d_7	0.2410 m	direction	+1	direction	-1	(Die)	
d_8	0.1560 m	Name	SWS2	Name	KD2		
d_9	0.0510 m	Type	SWS	Type	KD	*Barrel Temp.*	
		L_p	40.0×10^{-3}m	L_d	7.0×10^{-3}m	*Set-points*	
Physical Data		n_t	2	n_t	2	T_1	25°C
E_v	2.15×10^{9}Pa	R_s	19.35×10^{-3}m	R_s	19.35×10^{-3}m	T_2	25°C
ρ	1400 kg m^{-3}	R_r	11.0×10^{-3}m	R_r	11.0×10^{-3}m	T_3	25°C
C_p	3616 J kg^{-1} K^{-1}	direction	+1	Name	DIE1	T_4	40°C
λ	0.25 W m^{-1} K^{-1}	Name	OD1	Type	DIE	T_5	60°C
ρ_m	7900 kg m^{-3}	Type	OD	L_d	28.0×10^{-3}m	T_6	80°C
C_{p_m}	447.2 J kg^{-1} K^{-1}	L_d	10.0×10^{-3}m	R_d	1.5×10^{-3}m	T_7	100°C
λ_m	16.3 W m^{-1} K^{-1}	R_s	18.0×10^{-3}m	V_d	8.5×10^{-6}m^3	T_8	130°C
		R_r	10.0×10^{-3}m	V_m	9.51×10^{-4}m^3	T_9	150°C

moisture corn starch rheology. The rheology model parameters are listed in Table 6.1.

Figure 6.10 shows the dynamic response of the extruder to a step increase in screw speed. Note that a logarithmic time scale is used to magnify the initial transients. It can be seen that the die pressure eventually decreases to a steady-state value less than the initial value, though there is a large initial inverse response. The die temperature response displays a long settling time and the temperature increases as the screw speed increases. The specific mechanical energy also increases as the screw speed increases, exhibiting second-order type dynamics with overshoot. The product bulk density decreases gradually in line with the increasing die temperature. The product gelatinisation fraction increases with increasing screw speed, though it exhibits a measure of inverse response behaviour.

Figure 6.11 shows the dynamic response of the extruder to a step increase in feed rate. It can be seen that the die pressure increases, which is to be expected in order to achieve the higher throughput. The die temperature decreases slightly and displays a long settling time. The product specific mechanical energy decreases with some overshoot, while the product bulk density increases in line with the decreasing die temperature. The product gelatinisation fraction decreases in line with the decreasing temperature and specific mechanical energy input.

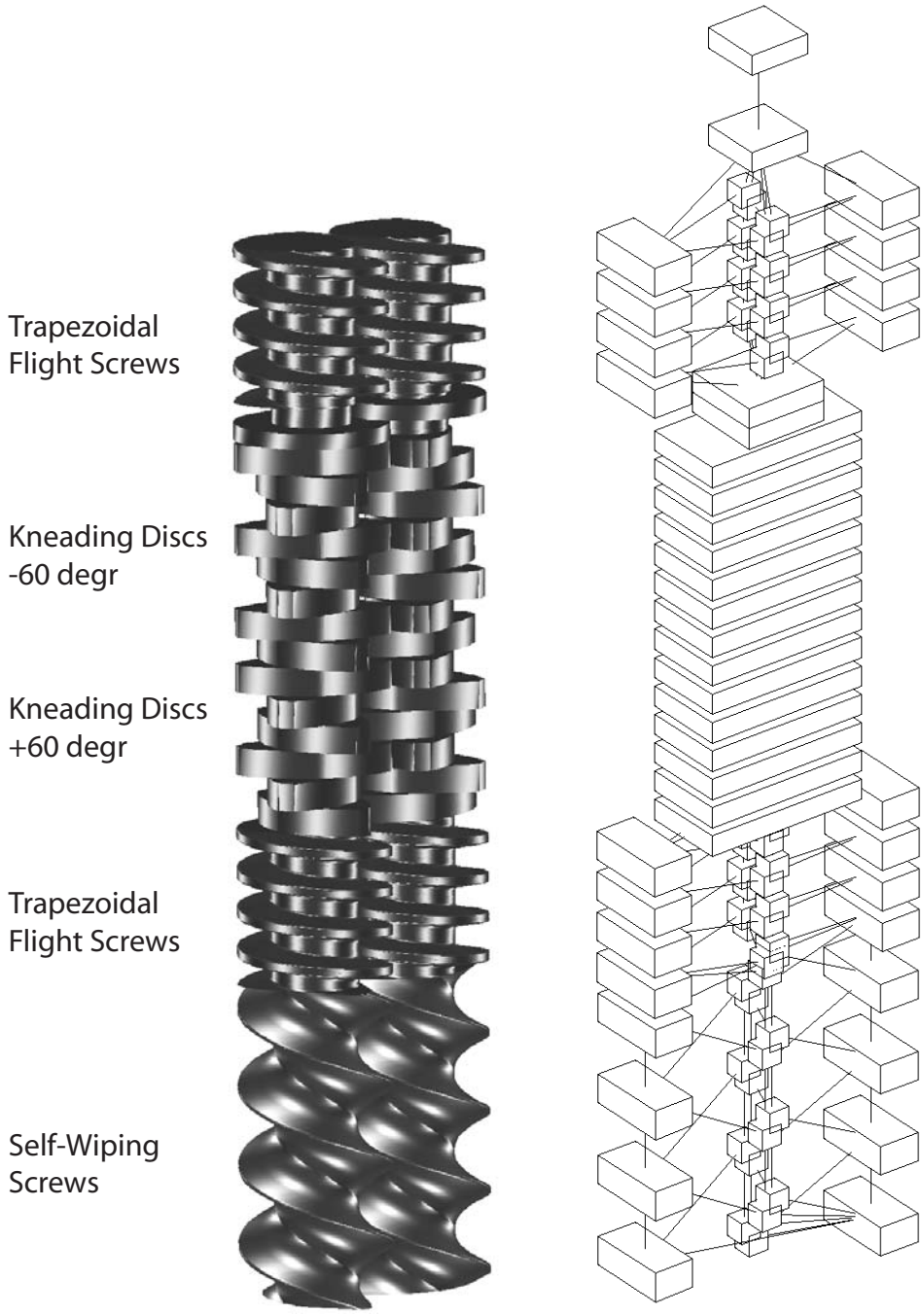

Figure 6.9: (a) The screw shaft configuration (excluding the die element) used in the cooking extruder dynamic response simulations; and (b) its representation as a flow network. The element locations are drawn to scale but volumes are not. The screws rotate in the anti-clockwise direction when viewed from above, and the feed end is at the bottom of the diagram.

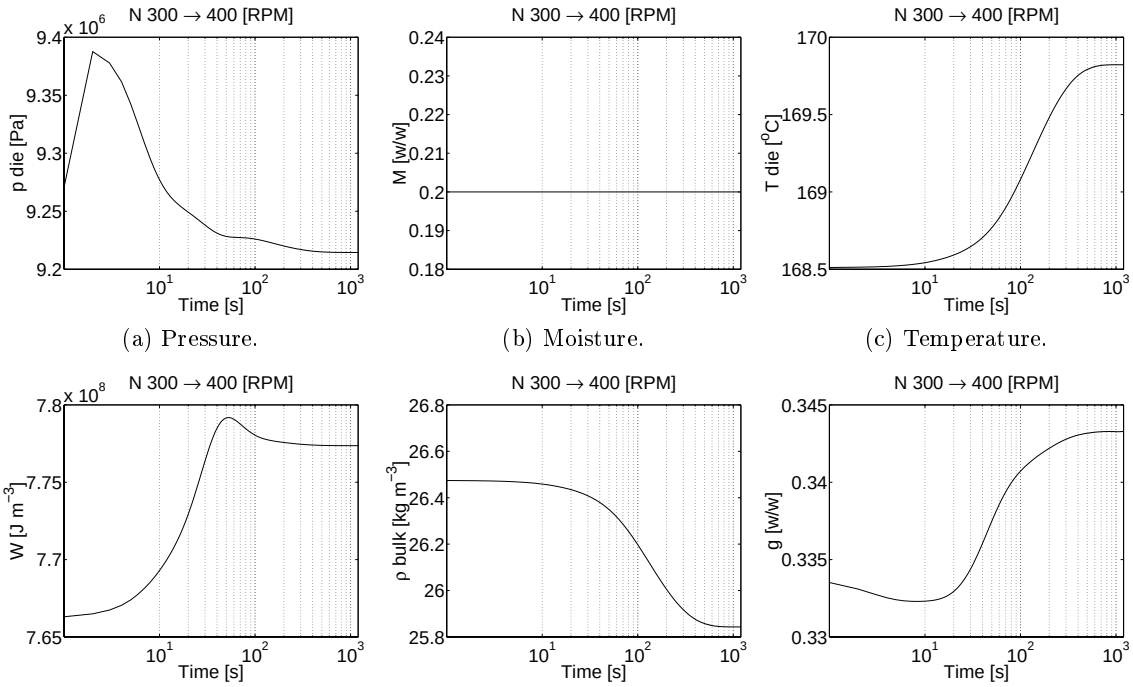

(a) Pressure. (b) Moisture. (c) Temperature.

(d) Specific mechanical energy. (e) Bulk density. (f) Gelatinisation.

Figure 6.10: Dynamic response at the die to a step change in screw speed.

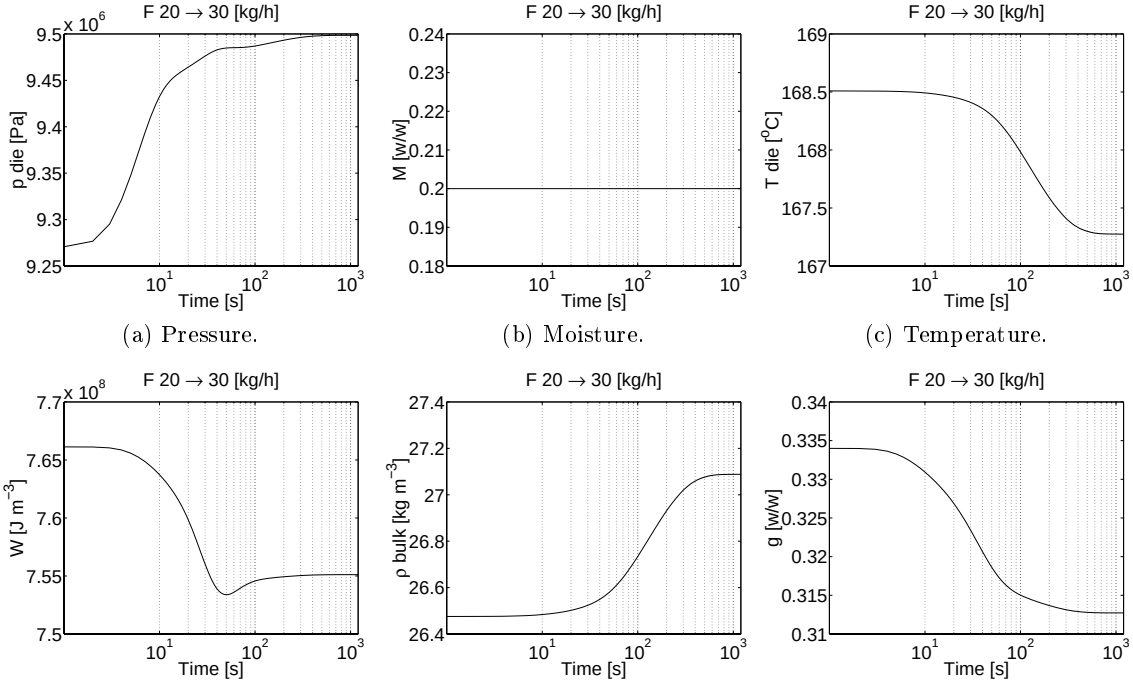

(a) Pressure. (b) Moisture. (c) Temperature.

(d) Specific mechanical energy. (e) Bulk density. (f) Gelatinisation.

Figure 6.11: Dynamic response at the die to a step change in feed rate.

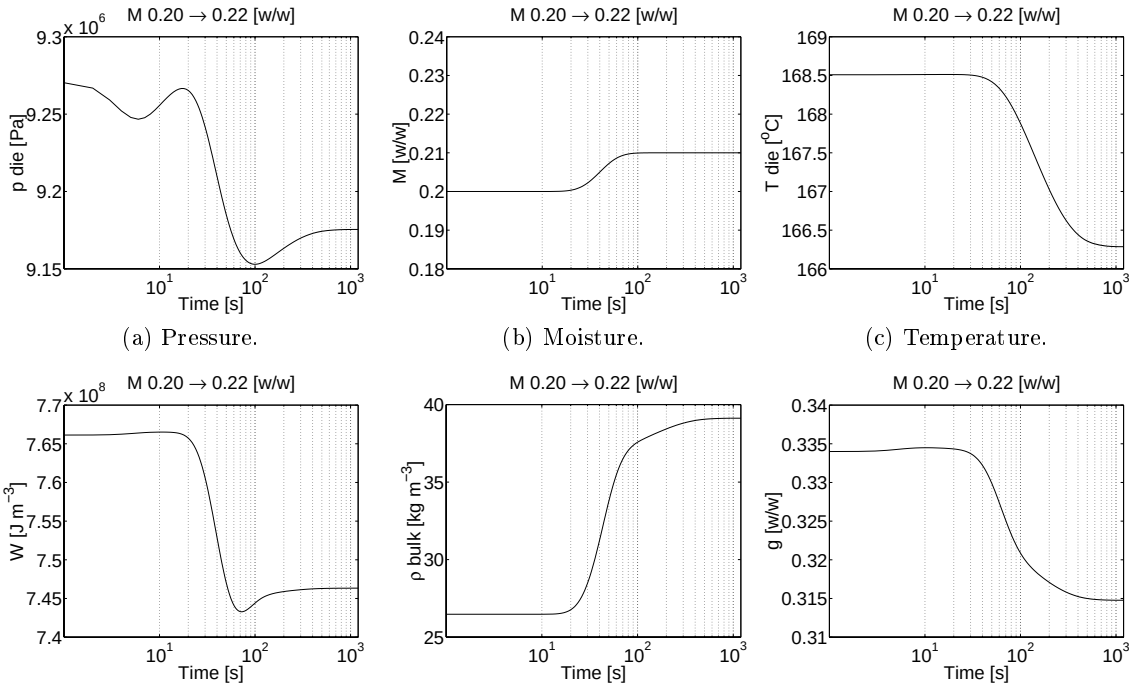

(a) Pressure. (b) Moisture. (c) Temperature.

(d) Specific mechanical energy. (e) Bulk density. (f) Gelatinisation.

Figure 6.12: Dynamic response at the die to a step change in moisture fraction.

Figure 6.12 shows the dynamic response of the extruder to a step increase in moisture fraction of the feed. The change in moisture fraction affects the process through its influence on the rheological behaviour of the feed material, though generally there is a large dead-time due to the hold-up of moisture in the extruder. The response in die pressure eventually decreases but displays an unusual ripple along the way. The die temperature decreases as does the product specific mechanical energy (with overshoot) most likely as a result of the reduced viscosity of the process material. The product bulk density increases as a result of the lower temperature and higher moisture content reducing the extent of product puffing. The moisture fraction itself at the die displays a smooth transition from the initial value to the final one.

Figure 6.13 shows the dynamic response of the extruder to a step decrease in screw tip radius. It is unlikely this would ever occur in reality unless the screw tip breaks for some reason. It is intended to demonstrate the ultimate (i.e. long term) effect of screw wear on the process. It may be seen, perhaps surprisingly, that after the initial spike, the final pressure is approximately unchanged from the starting value. The temperature and specific mechanical energy decrease slightly, while the bulk density and gelatinisation fraction increase slightly.

The process dead-time varies greatly among the various dynamic responses simulated, with values between zero and 20 seconds. There was no observable dead-time in pressure

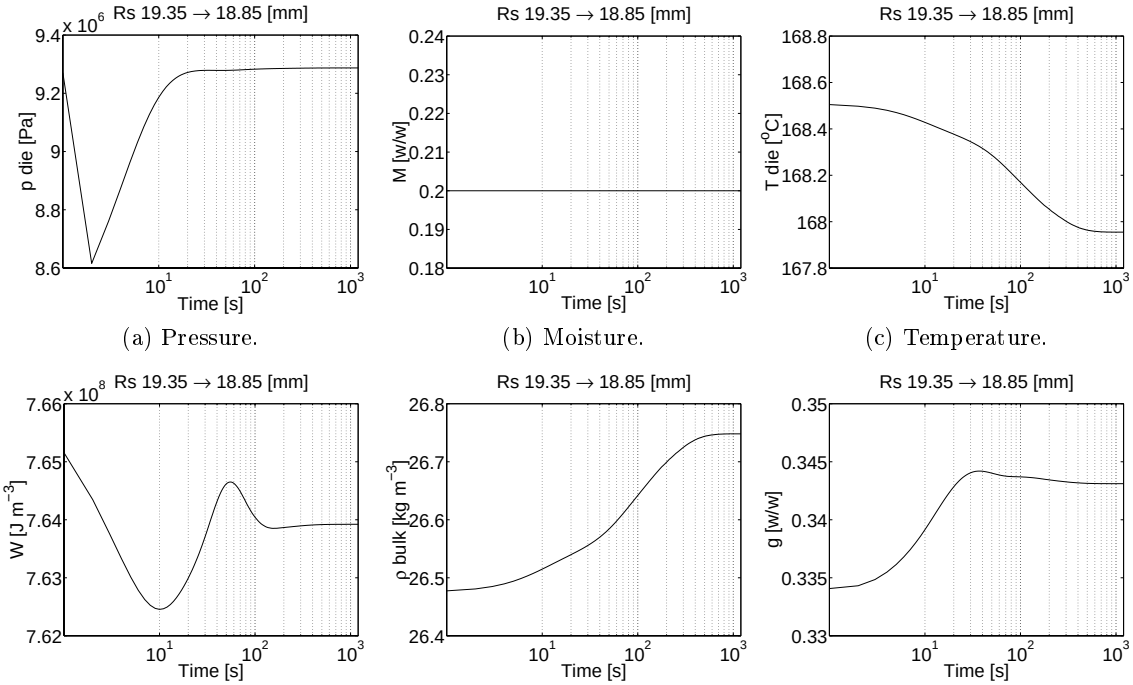

(a) Pressure. (b) Moisture. (c) Temperature.

(d) Specific mechanical energy. (e) Bulk density. (f) Gelatinisation.

Figure 6.13: Dynamic response at the die to a step change in screw radius.

responses to changes in screw speed. Most other responses involve the propagation of changes in the rate of viscous heat dissipation or the propagation of changes in the feed conditions, and the dead-time for such responses at the die is typically several seconds. Changes in moisture fraction can result in dead-times in the order of 15 seconds. The presence of process dead-time presents a controllability issue which will be discussed further in Chapter 10.

It may be concluded that the dynamics of the twin-screw extrusion cooking process can be approximated as first or second-order although in some cases inverse response behaviour is also observed. The high degree of interaction between input and output variables is mostly due to the rheology model, which is temperature, moisture and shear history dependent.

Each step change simulation required around 30 seconds of CPU time on a 600 MHz Pentium 3 PC, which is modest for the amount of detailed information obtained.

6.8.3 Model Comparison with Experimental Data

An APV-Baker MPF-40 cooking extruder (Figure 6.14) was operated with the screw configuration shown in Figure 6.15(a) using a low moisture corn flour feed. The representation of the extruder as a flow network is shown in Figure 6.15(b). The geometrical parameters of the screws, die and barrel are shown in Table 6.4. Transducers fitted to the extruder

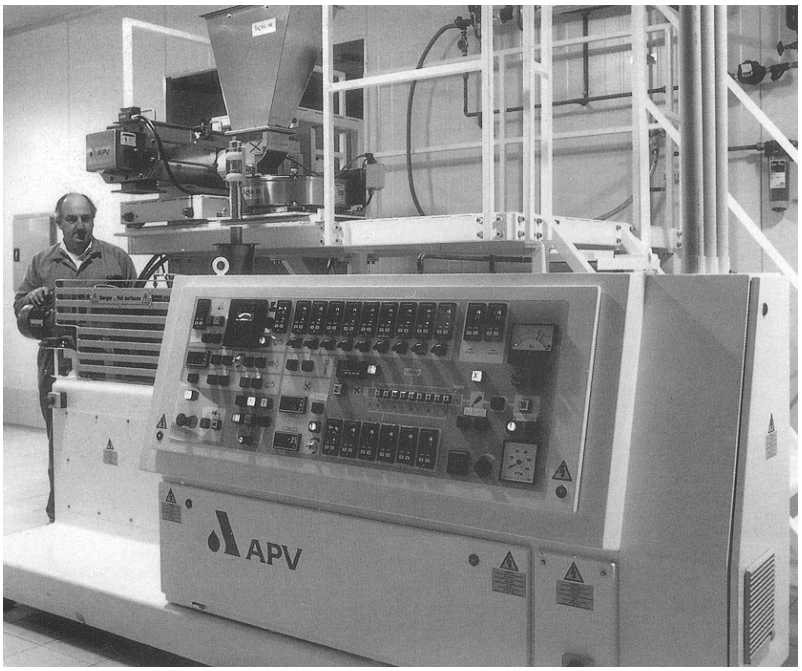

Figure 6.14: Photograph of the APV-Baker MPF-40 co-rotating twin-screw cooking extruder.

allowed the measurement of die temperature and die pressure. The sampling interval was 20 seconds. The power-law rheology parameters for the feed material were modelled as per Equations 6.28 and 6.30. The moisture fraction of the feed material was not varied throughout the experiments and was constant at 0.20 w/w.

Figures 6.16(a) and (b) show the experimental die temperature and die pressure measurements as dotted lines with the model predictions overlayed as a solid line. The feed rate and screw speed were varied as shown in Figures 6.16(c) and (d).

The model predicted die temperature in Figure 6.16(a) follows the trends of the experimental values quite well, although there is a consistent offset of around +5°C. Considering that the rheology model used in the simulations was obtained from the literature and not from any direct experiments, some error is to be expected. It was also noticed after the experiments were completed that the tip of the thermocouple was encrusted with a layer of cooked starch. This insulating crust, and stagnation resulting from the generally lower fluid velocities in the die volume, may both have contributed to the lower than measured die temperature values.

It can be seen that the time constant for the experimental die temperature response is slightly slower than for the model. This may be due to the heavy die plate (7.5 kg) that was used in the experiments being exposed to ambient air, resulting in significant heat loss and a temperature gradient in the die metal between the process fluid and the air exposed surfaces. Recalling that the thermal mass of the metal comprising the die is

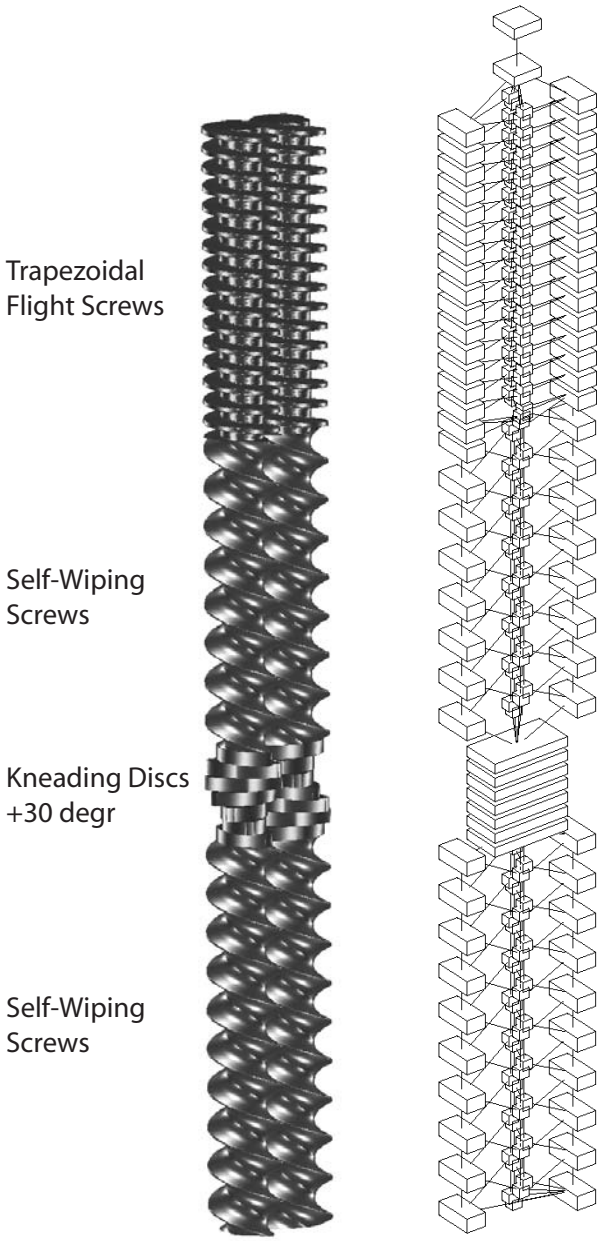

Figure 6.15: (a) The screw shaft configuration (excluding the die element) used in the experiments; and (b) its representation as a flow network. The element locations are drawn to scale but volumes are not. The screws rotate in the anti-clockwise direction when viewed from above, and the feed end is at the bottom of the diagram.

Table 6.4: Geometric and physical data parameters used in the experiments.

Barrel Data		*Screw Data*				*Shaft Configuration*	
C_L	30.8×10^{-3}m	Name	TFS1	Name	TFSR1	(Feed)	
R_B	20.0×10^{-3}m	Type	TFS	Type	TFS	$5 \times D$	SWS2
d_1	0.8600 m	L_p	10.0×10^{-3}m	L_p	10.0×10^{-3}m	$7 \times +30°$	KD1
d_2	0.7540 m	n_t	1	n_t	1	$4 \times D$	SWS2
d_3	0.6540 m	R_s	19.35×10^{-3}m	R_s	19.35×10^{-3}m	$4 \times D$	TFS1
d_4	0.5620 m	R_r	11.0×10^{-3}m	R_r	11.0×10^{-3}m	1	DIE1
d_5	0.4520 m	t_f	2.40×10^{-3}m	t_f	2.40×10^{-3}m	(Die)	
d_6	0.3390 m	w_c	4.40×10^{-3}m	w_c	4.40×10^{-3}m		
d_7	0.2410 m	direction	+1	direction	-1		
d_8	0.1560 m	Name	SWS2	Name	KD2	*Barrel Temp.*	
d_9	0.0510 m	Type	SWS	Type	KD	*Set-points*	
		L_p	40.0×10^{-3}m	L_d	7.0×10^{-3}m	T_1	25°C
Physical Data		n_t	2	n_t	2	T_2	25°C
E_v	2.15×10^9Pa	R_s	19.35×10^{-3}m	R_s	19.35×10^{-3}m	T_3	25°C
ρ	1400 kg m^{-3}	R_r	11.0×10^{-3}m	R_r	11.0×10^{-3}m	T_4	25°C
C_p	3616 J kg^{-1} K^{-1}	direction	+1	Name	DIE1	T_5	30°C
λ	0.25 W m^{-1} K^{-1}	Name	OD1	Type	DIE	T_6	60°C
ρ_m	7900 kg m^{-3}	Type	OD	L_d	28.0×10^{-3}m	T_7	90°C
C_{p_m}	447.2 J kg^{-1} K^{-1}	L_d	10.0×10^{-3}m	R_d	1.5×10^{-3}m	T_8	120°C
λ_m	16.3 W m^{-1} K^{-1}	R_s	18.0×10^{-3}m	V_d	8.5×10^{-6}m^3	T_9	150°C
		R_r	10.0×10^{-3}m	V_m	9.51×10^{-4}m^3		

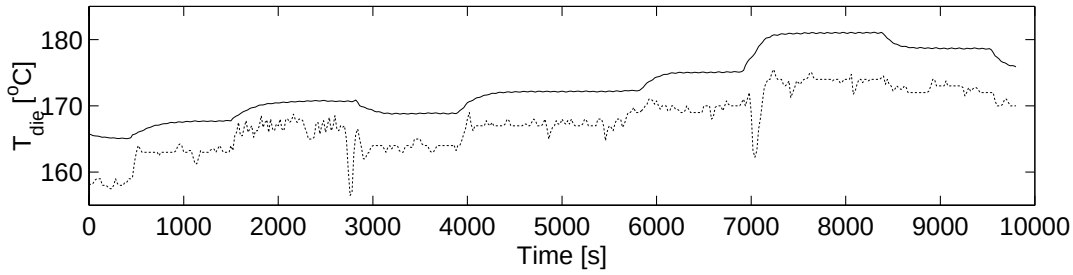

(a)

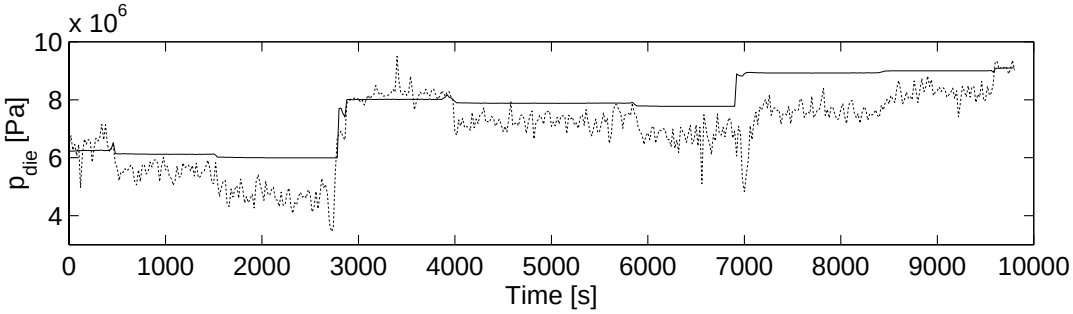

(b)

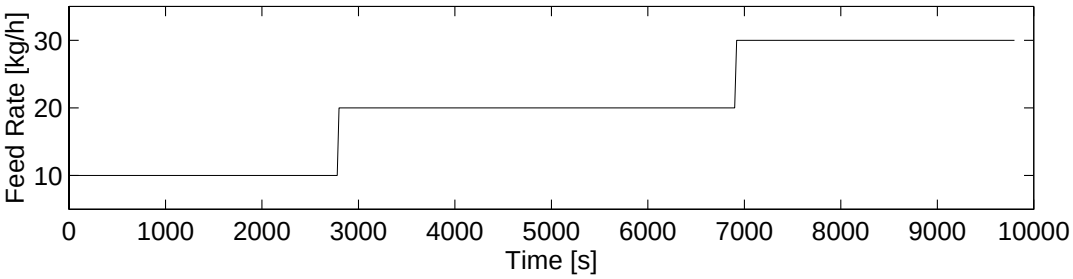

(c)

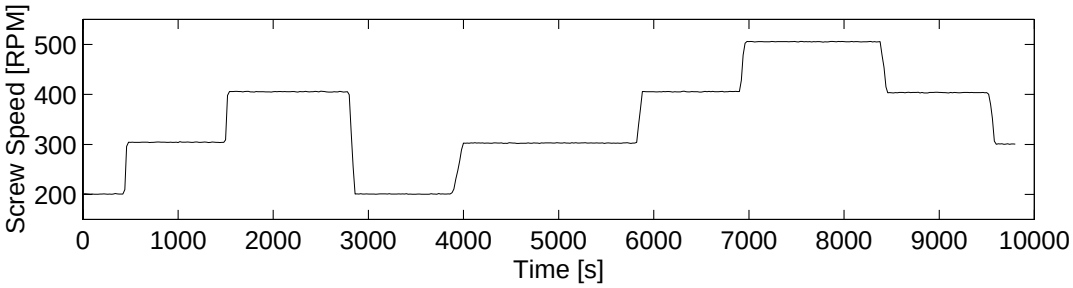

(d)

Figure 6.16: Model comparison with experimental set-point changes in feed rate and screw speed. Plots show the time varying (a) die temperature; (b) die pressure; (c) feed rate; and (d) screw speed. The experimental data, where applicable, is shown as a dotted line.

included in the die model element, a temperature gradient in the metal and heat loss to the surroundings would result in lower temperatures and a faster dynamic response.

The model predicted die pressure shown in Figure 6.16(b) is in reasonably good agreement with the experimental trends, though the experimental data indicates that changes in screw speed have a much greater influence on the die pressure than is predicted by the model. It can be seen that increasing the screw speed causes a noticeable reduction in experimentally measured pressure, while the model predicts only a small decrease. This may be a result of several factors that are not taken into account in the model. Firstly, there are almost certainly inaccuracies in the rheological model as mentioned previously. Secondly, there may be a transient shear memory effect in the long chain starch molecules that is not included in the rheology model. Thirdly, due to the screw tips being adjacent to the die reservoir, they may in reality impart shear to the material there and affect its viscosity. And lastly, the presently used model for flow in the die does not take into account the complete 3D die geometry, which may in fact have a significant influence on the extruder performance.

The time constant for the dynamic pressure response is predicted quite well by the model, though the sampling rate is too slow to capture the finer details of the pressure transients.

It might be reiterated that the model predictions shown here involved no data-fitting whatsoever. They are based purely on the geometry of the extruder and a published rheological model. Under these circumstances the prediction capability of the model is impressive.

6.8.4 Model Comparison with Experimental Residence Time Distribution Data

The residence time distribution (RTD) of an extruder gives an indication of the mixing and uniformity of treatment of the product (Jager et al., 1992), and thus has important implications for product quality and composition when the feed material undergoes any chemical reactions. The RTD in twin-screw extruders has been measured experimentally, e.g. De Ruyck (1997), and various models for estimating the RTD have been proposed, such as those of Bounie (1988) and Puaux et al. (2000). The most common modelling approach is to represent the extruder by a network of plug-flow reactors (PFRs) and continuously stirred tank reactors (CSTRs) and to simulate the change in concentration at the outlet as the result of a tracer pulse passing through the system. The flow structure is usually derived by heuristic judgement and trial-and-error, while the model parameters, such as back-flow and recycle rates, are determined using regression analysis to fit the model to experimental data.

The present dynamic model can be readily adapted to calculate the RTD by using Equation 6.20 to model the concentration of an inert chemical tracer in the feed. By simu-

lating a pulse change in concentration in the feed and monitoring the outlet concentration $C(t)$, the RTD $E(t)$ can be determined by normalising $C(t)$ by dividing by the total time integrated concentration, i.e.

$$E(t) = \frac{C(t)}{\int_0^\infty C(t)\,\mathrm{d}t} \tag{6.34}$$

Experiments were performed on the APV-Baker MPF-40 extruder using the screw configuration shown in Figure 6.15 with the geometrical parameters listed in Table 6.4. An 0.20 moisture corn flour was used as the feed material and its power-law rheology model parameters were modelled as per Equations 6.28 and 6.30. Feed rates of 10, 20 and 30 kg/s and screw speeds of 200, 300, 400 and 500 RPM were used. At the commencement of each experimental run, the extruder was allowed to reach steady-state operation, after which 10g of NaCl tracer was added to the feed. A product sample was collected every 5 s for 100 s. The samples were ground and dissolved in distilled water and the conductivity measured using a portable conductivity meter. By comparing the measured conductivity with a calibration curve, the concentration of NaCl in each sample could be estimated.

It can be seen in Figure 6.17 that increasing screw speed has the effect of reducing the dead-time of the process, but has little effect on the overall variance of the RTD. Increasing feed rate, however, has little effect on the dead-time of the process, but leads to a noticeably narrower RTD. The good agreement between the experimental and model predicted RTD curves and their trends is a strong indicator that the flow network model structure adequately describes the mixing behaviour of the real extrusion process. It also implies that the hold-up of material within the extruder must be reasonably well predicted by the model.

6.9 Conclusions

A dynamic model of the co-rotating twin-screw extrusion process has been presented. The extruder is represented by a stationary flow network structure, which is formed by dividing the free volume of the screws into discrete elements along the natural flow bottlenecks and screw boundaries. The ordinary differential equations describing the state variables in the extruder model have a neat and simple structure owing to the linking of pressure to the fill fraction via the bulk modulus of elasticity. The model can be easily extended to describe additional phenomena, such as reacting feed materials, by adding the ODEs which describe these phenomena in each element to the basic model ODEs. This was demonstrated with the modelling of the starch gelatinisation reaction in a cooking extruder. The three-dimensional structure of the flow network provides realistic information on the uneven filling of the screws around the intermeshing region, which has not been simulated previously.

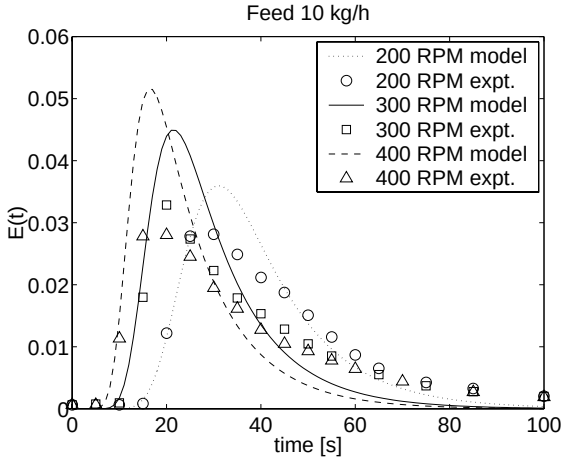

(a)

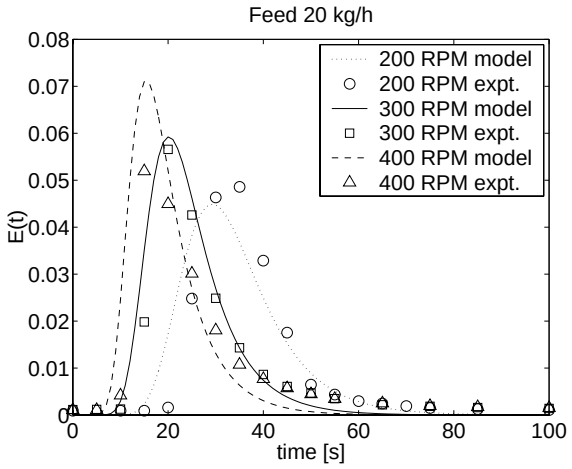

(b)

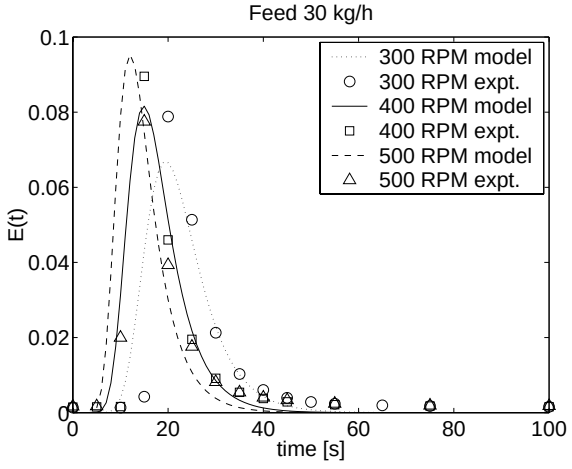

(c)

Figure 6.17: Comparison between model predicted and experimentally measured residence time distributions for feed rates of (a) 10 kg/h; (b) 20 kg/h; and (c) 30 kg/h.

The model can simulate situations which were not possible previously, such as a "cold" start-up. The model produces realistic predictions of die pressure and temperature that compare well with experimental data using only the extruder geometry and published rheological data. The close agreement with experimentally determined residence time distribution data suggests that the model structure provides an adequate description of the internal mixing behaviour and material hold-up in the extruder.

The fast calculation times (around 30 seconds for the set-point changes), the flexibility to incorporate reaction kinetics, and the implicit modelling of mixing all suggest that this model would be practical for use as a steady-state process simulation tool, in addition to its value as an indicator of dynamic behaviour.

6.10 Recommendations

There are a number of areas open for further work in dynamic extruder modelling. For example, a more thorough treatment of the flow in the die block is recommended, as the the present treatment may be too simplistic. Further experimental investigations might also be performed using a material with better known rheological properties, such as a viscous silicone oil. This would reduce rheological modelling errors thereby allowing a better evaluation of the process model. Full 3D dynamic simulation of the co-rotating twin-screw extrusion process has so far proved impractical using grid-based finite element methods because of the continual re-meshing necessitated by the mobile flow boundaries. An interesting topic for future investigation would be to model the 3D dynamic extrusion process using a Lagrangian fluid modelling technique such as *smoothed particle hydrodynamics* (SPH) (Monaghan, 1992). SPH simulates fluid motion without using a grid, which allows complex free surfaces and material interface behaviour to be modelled. The fluid is instead represented by a field of disordered particles which follow the fluid motion. The particles are treated as interpolation points at which the properties of the fluid are computed. This approach has not yet been applied to extrusion simulation, but the ease with which mobile flow boundaries and multi-phase flow behaviour can be coded makes it highly appealing for such applications.

Chapter 7

Measurement of Bubble Size Distributions in Puffed Extruded Food Products using Digital Image Analysis

Abstract: In this chapter an automatic technique for measuring the bubble size distribution in puffed extruded products from cross-sectional images is presented. A suitable edge discrimination routine together with an algorithm for detecting holes, which may have incomplete boundaries, are described. The actual bubble size distribution can be inferred from the distribution observed in the cross-sectional slices by a deconvolution procedure. The results from applying this method to several extruded products are presented, and it is shown that the bubble size distributions, weighted according to the void volume contained within each diameter range, are well described by a Gaussian distribution. It was also found that several thousand individual bubbles need to be measured in order to calculate the distribution with meaningful accuracy. It is anticipated that this technique may prove to be a useful tool in product quality assessment.

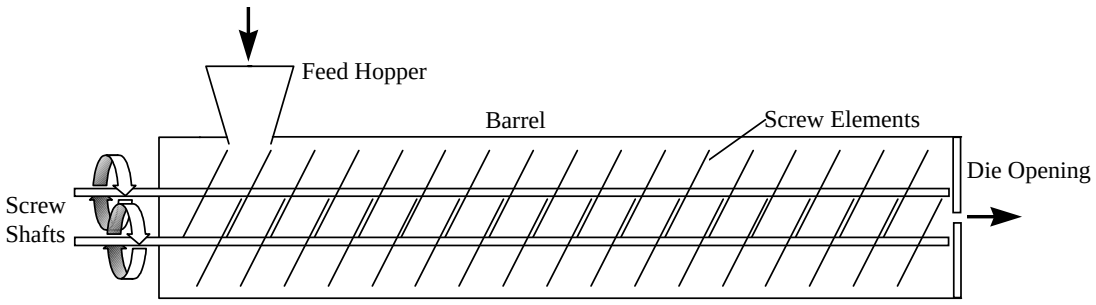

Figure 7.1: Schematic representation of a co-rotating twin-screw extruder.

7.1 Introduction

Cooking extruders are commonly used to produce puffed snack foods, crispbreads and breakfast cereals. A typical extruder consists of a barrel inside which one or two helical screws rotate to convey the feed material towards one end, as illustrated in Figure 7.1. At some point along the extruder, the channels between the screws become completely filled and the temperature and pressure increase considerably as a result of friction and material compression. This has the effect of cooking the material, which then leaves the extruder through a die, an opening several millimetres in diameter at the end of the extruder. If the temperature is high enough on leaving, the water present partially flashes causing bubbles of steam to form and the extrudate to puff. As the extrudate cools below its glass transition temperature it sets in the expanded state.

The formation of steam bubbles is influenced by the moisture content of the extrudate, the die exit temperature, the rheological properties of the extrudate, the surface tension and the number of sites available for nucleation. The steam bubbles can also coalesce before the product sets, resulting in larger bubbles. As a result of the various factors and mechanisms involved, the final product can display a range of different bubble sizes.

The aim of this chapter is to develop a reliable digital image analysis method for measuring the bubble size distribution in puffed extruded products. The chapter begins with a review of the literature relating to this problem, followed by a description of the experimental procedure and image acquisition techniques. The image processing algorithms that were found to be successful and the procedure for reconstructing the true distribution from the observed distribution are then discussed. The results from applying the analysis to three different extruded products are then presented, followed by conclusions and recommendations for future work in this field.

7.2 Literature Review

The problem of determining bubble (or particle) size distributions in a material is encountered often in the literature, as it is often this distribution which quantifies important product characteristics. The most direct approach for measuring the bubble size distribution involves analysing a slice through the material and measuring the observed bubble size distribution. As bubbles are equally likely to be cut at any position eccentric to their diameter, the observed bubble size distribution usually differs from the true bubble size distribution. A method for reconstructing the true distribution from the observed distribution was first described by Wicksell (1925), and various modifications to this procedure have been reviewed by Cruz-Orive (1983).

A practical application of this technique is reported by Campbell et al. (1991), who measured bubble size distributions in bread doughs by freezing dough samples and viewing thin slices with a microscope. The bubble diameters in the sample were measured manually, and the true bubble size distribution was reconstructed from the observed distribution using the technique described by Goldsmith (1967), which is an extension of the Wicksell technique applicable to slices having finite thickness. The manual measurement was no doubt a tedious task considering that the authors recommend several thousand bubbles per sample be measured to ensure accurate results.

Since the advent of cheap image acquisition hardware and image analysis software, digital image analysis has become a well established method for quantifying pore space from images of thin sections. It is difficult, however, to find precedents for all possible applications, as digital image analysis often consists of applying a sequence of established and customised techniques in an *ad hoc* fashion to suit the problem at hand (Haralick, 1983). One pertinent example is the work of Anselmetti et al. (1998), who used digital image analysis to measure pore sizes in carbonate minerals. The technique applied there involved impregnating samples with a blue dye and thresholding the resulting blue-filtered images to highlight the pores. The areas of the identified pores were then calculated using a pixel counting technique.

It may not be possible, however, to accurately measure individual pores sizes using simple pixel counting techniques when the pore boundaries are not well defined. This is often the case for puffed food extrudates, as the thin bubble walls are easily fractured when slicing the sample, resulting in small connections between adjacent bubbles that would result in their areas being combined, even though they are clearly separate structures. For this reason, new edge discrimination and bubble size measurement techniques needed to be designed for use in the present investigation.

Table 7.1: Extruder operating conditions and product expansion ratios.

Product Label	*Moisture Fraction* [w/w]	*Feed Rate* [kg/h]	*Screw speed* [RPM]	*Expansion Ratio*
A	18	15	300	3.1
B	18	20	300	3.8
C	18	25	200	5.2

7.3 Experimental Procedure

7.3.1 Sample Preparation

An APV-Baker MPF 40 twin-screw cooking extruder was used to extrude a mixture of corn flour and water at a number of different operating conditions as shown in Table 7.1. Three different products (labelled 'A', 'B' and 'C') with visibly different bubble sizes were selected for image analysis. The expansion ratio, defined as the ratio of the product diameter to the die diameter, was in each case measured off-line and averaged over a sample size of 20 product pellets.

The samples were allowed to cool to room temperature and then prepared for photographing by using a disc grinder to remove approximately half of each sample and expose a longitudinal cross-section. Sample images of each product are reproduced to the same scale in Figure 7.2.

7.3.2 Photographic Procedure

The extrudate samples were photographed against a black background using a Pentax MZ-50 camera with a 28-80mm macro zoom lens as shown in Figure 7.3. Three close-up lenses giving an additional magnification of +7 dioptres were fitted to the camera lens. The sample was viewed through a 12.5cm 5× magnifying lens mounted inside a 22 watt circular fluorescent light tube. Exposures were made using a camera shutter speed of 0.25s with an f22 aperture on 100 ASA colour film. A total of 72 samples of product A and 36 samples of both products B and C were prepared and photographed. Each sample was photographed beside a ruler with 1mm gradations so that the scaling of the photograph could be determined. A flat-bed scanner was used to digitise the developed photographs giving 8-bit colour images with a resolution of approximately 0.05mm per pixel.

The form of lighting used during the photography was found to be important as the objective was to highlight the edges of the cut bubbles to facilitate discrimination between the bubble cavities and their borders. Illumination using the circular fluorescent light tube proved to be more effective than back lighting, diffuse lighting, or point source lighting, as a low incidence angle of light could be achieved that favoured illumination of the sample edges, as shown in Figure 7.4.

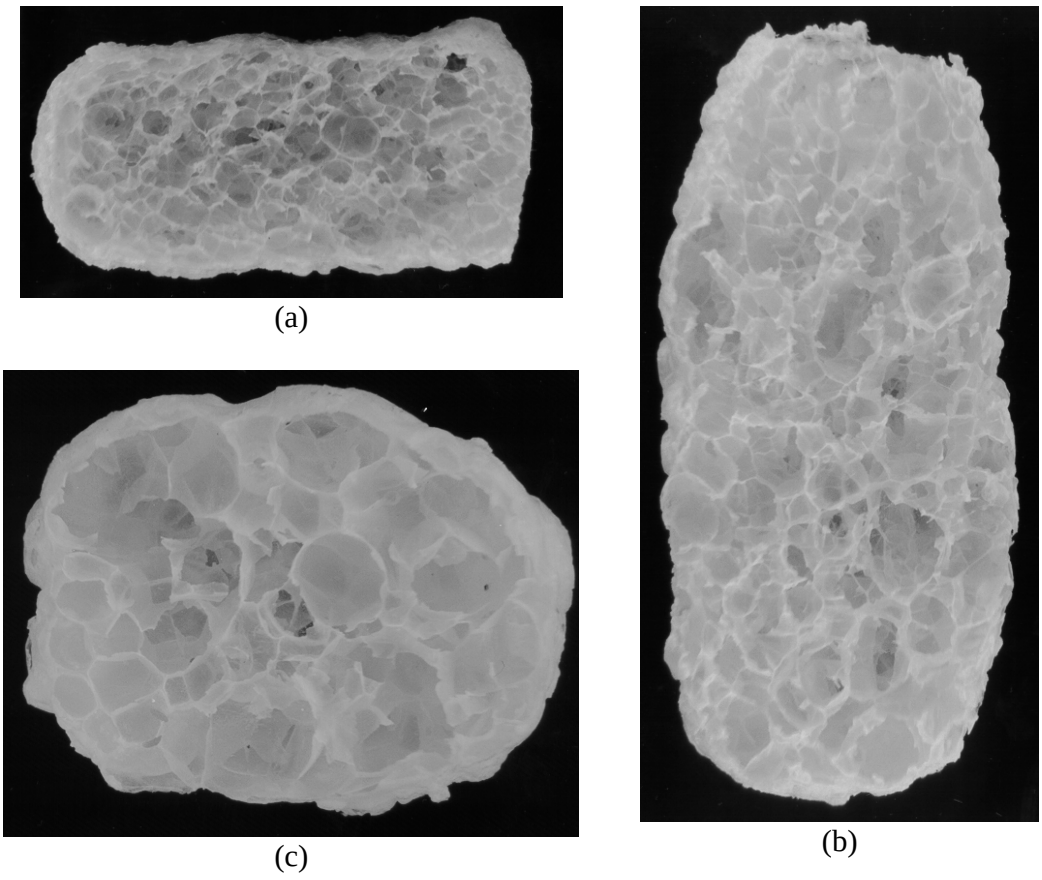

Figure 7.2: Sample cross-sectional images of the products analysed, reproduced at the same relative scale. (a) Product A; (b) product B; (c) product C.

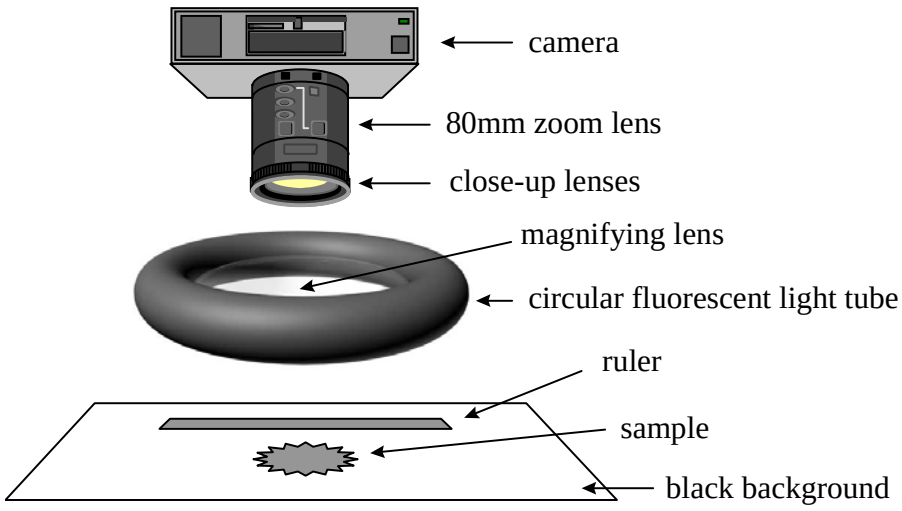

Figure 7.3: Photographic equipment.

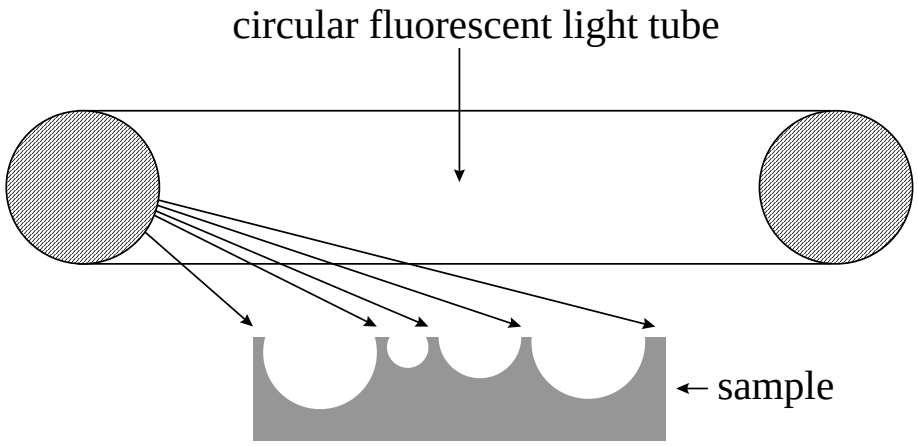

Figure 7.4: A circular fluorescent light tube gives improved edge illumination.

7.4 Image Analysis

In order to determine the true bubble size distribution of a sample, the bubble diameter distribution in cross-sectional images of the sample needs to be determined. This image processing task is achieved in two stages. The first step requires a binary image to be calculated which discriminates between the edges of the bubbles and the bubble cavities themselves. Once this edge map has been obtained, the areas of the image corresponding to the bubble cavities can be calculated using a separate algorithm. Each of these steps is described in the following two sections.

7.4.1 Edge Discrimination

A technique was required that could discriminate between points in an image belonging to the cut bubble edges and the cavities of the bubbles themselves. The technique employed needed to be very specific in its discrimination between edges and cavities, as the bottom walls of the cavities (that is, the uncut portions) were usually patterned with fine detail which could possibly be interpreted as an edge. Consequently, two or more smaller holes might be inferred instead of one large hole.

Image segmentation is a common image processing task and although many approaches are reported in the literature, there is no dominant methodology (Haralick, 1983). For the present purposes, satisfactory results were obtained using a modified thresholding approach.

Due to the lighting method used, it was observed that pixels on the bubble edges had a greater luminance than those in cavities. Points brighter than the average of their k-by-k pixel locality can be found by convolving the image with a k-by-k averaging filter and thresholding each pixel in the original image with the corresponding pixel in the averaged image, i.e.

$$M_k(x,y) = \begin{cases} 1 & \text{if } I(x,y) > I(x,y) * h_k \\ 0 & \text{otherwise} \end{cases} \tag{7.1}$$

where $I(x,y)$ is the original grayscale image, x and y are the coordinates of a pixel, $*$ is the two-dimensional convolution operator, and h_k is the k-by-k two-dimensional averaging filter (where k is an odd number) with coefficients

$$h_k = \frac{1}{k^2} \begin{bmatrix} 1 & \dots & 1 \\ \vdots & \ddots & \vdots \\ 1 & \dots & 1 \end{bmatrix} \tag{7.2}$$

The resulting binary image M_k (where 1 indicates an edge and 0 a bubble cavity) proved to be a poor edge map, as low values for k (in the range 3–21) tended to highlight fine details within a bubble cavity which should be omitted, while larger k values (in the range 21–99) omitted fine edge details. However, a very good edge map was obtained by summing the edge maps M_k over a range of odd-numbered k values and then thresholding the resulting image, i.e.

$$E(x,y) = \begin{cases} 1 & \text{if } \sum_{i=1}^{n} M_{2i+1}(x,y) > m \\ 0 & \text{otherwise} \end{cases} \tag{7.3}$$

Values for n and m of 60 and 50, respectively, were arrived at via numerical experimentation and were found to give excellent results.

Some speckling in the binary image E, however, was apparent and needed to be removed, as anomalous speckle pixels in a cavity region can interfere with the measurement of the cavity's area. Speckles were removed by applying two successive algorithms to the pixels in E. Speckles with a value of one in the binary image were removed by setting a pixel to zero when three or more of its four neighbouring pixels (those at $(x-1,y)$, $(x+1,y)$, $(x,y-1)$ and $(x,y+1)$) had a value of zero. Speckles with a value of zero were then removed by setting a pixel to one if five or more pixels (out of a possible total of eight) in its 3-by-3 neighbourhood had a value of one.

While this approach may seem somewhat *ad hoc*, it proved to be highly successful in distinguishing between bubble cavities and edges, whereas standard approaches failed. An example of the algorithm applied to a sample of product A is shown in Figure 7.5(b).

7.4.2 Cavity Detection

Once the binary image distinguishing bubble edges from cavities has been found, the area and average diameter of the observed cavities can be determined. All images produced by the edge discrimination routine, however, showed cavities connected by breaks in their

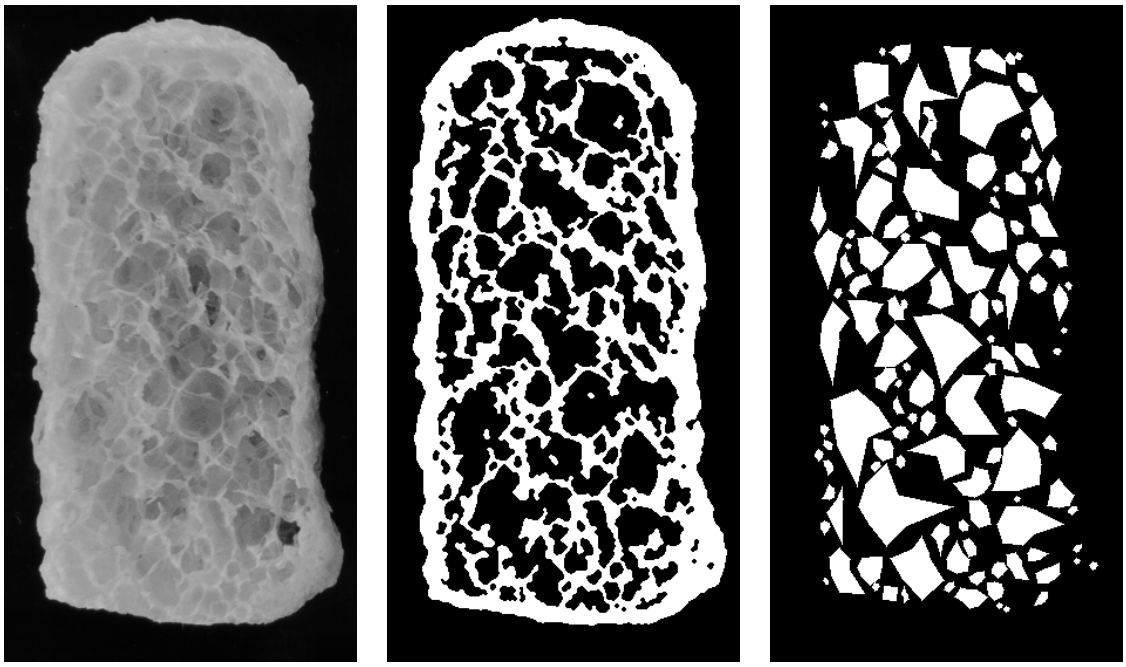

(a) (b) (c)

Figure 7.5: Image analysis applied to a sample image. (a) Original product A image; (b) edge map; (c) detected cavities.

boundaries to other cavities. This connectivity meant that the area of each cavity could not be found simply by counting all connected pixels in an edge-bounded region. An image processing technique known as *erosion and dilation* (Allen, 1999) can be used to separate connected features in some cases by eroding edge pixels until the features separate and then dilating them to reform the image. However, this can lead to loss of image information and is inappropriate when the connecting regions between features are relatively large, significantly non-spherical, or differ greatly in size. This technique was not effective when applied to the present images.

Rather, cavities were detected, and their areas measured, by an algorithm which works by growing polygons from the centre of every 5-by-5 pixel region in the image. If the starting point fell on a pixel classified as being part of a cavity, N_p rays with an angle $360/N_p$ between each adjacent pair, would be traced from the centre until they met with a pixel classed as a bubble edge. These N_p end-points form the vertices of an N_p-sided polygon which approximates the shape of the cavity. If all the points inside the polygon were not contained within any previously detected cavity, then this polygon was included in the set of detected cavities.

This basic algorithm was improved upon by avoiding polygons grown from pixels near the corners of unevenly shaped cavities, as this often gave a poor estimate of the cavity's shape and area. This modification involved growing each polygon from an initial starting point, calculating the point representing the polygon's geometric centre of mass, and then growing a new polygon from there. Iterating this procedure several times usually results in a final polygon that gives a significantly better estimate of a cavity's area. Figure 7.5(c) shows the result of applying this algorithm to the edge map shown in Figure 7.5(b). Figures 7.6(a)–(f) show a series of snapshots following the progress of the cavity detection algorithm when applied to a small region of a sample edge map.

Values of N_p (that is, the number of rays used) between 4 and 360 were tested. The best results were achieved using a value of around 8, as this reduced the likelihood of the polygon corners passing through small gaps in the detected edges and thus lying partially inside adjacent cavities.

The equivalent diameter of a bubble cavity was approximated by equating its area A_b to that of a circle of diameter d, hence:

$$d = \sqrt{\frac{4A_b}{\pi}} \tag{7.4}$$

For a 412-by-844 pixel image, the processing time for these algorithms implemented in C code and run on a Pentium II processor was 13 minutes for the edge discrimination routine and 7 minutes for the cavity detection routine.

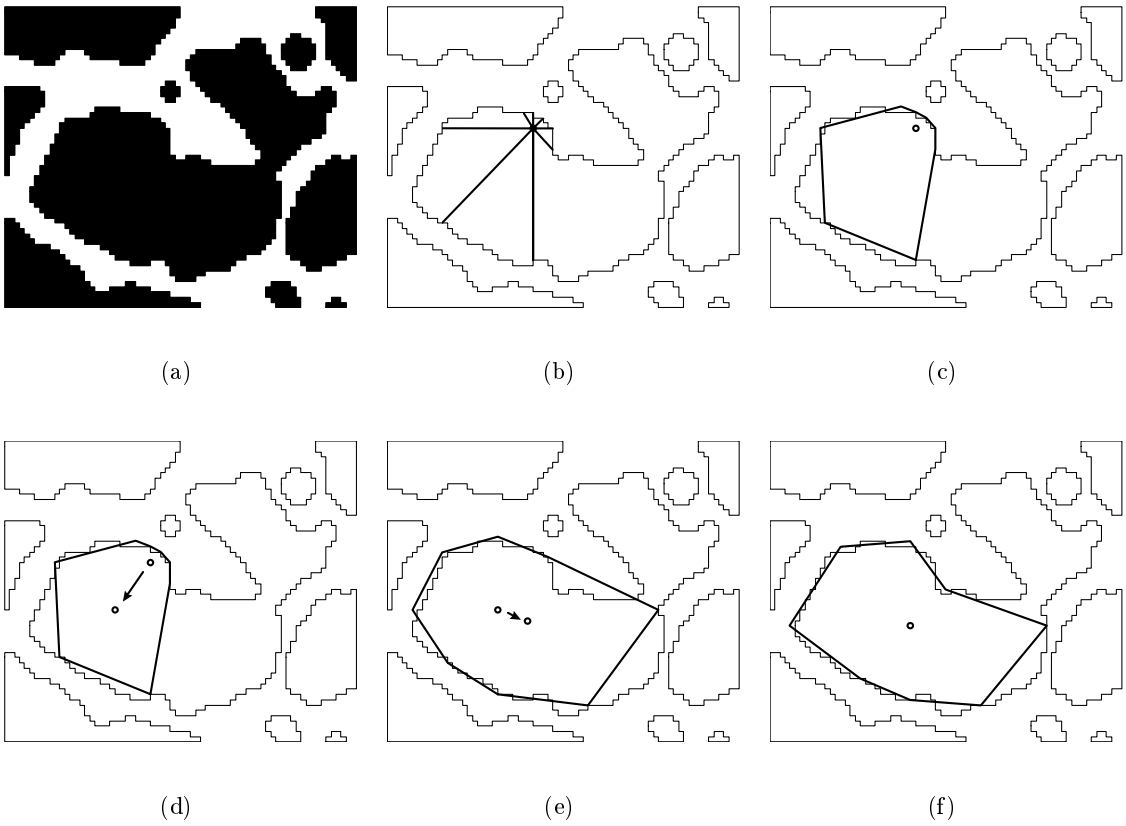

Figure 7.6: Demonstration of the cavity detection algorithm applied to a region of an edge map image. (a) Region of edge map with black indicating extrudate cavities. (b) Rays sent out in 8 directions from starting point to edges. (c) Polygon formed by joining end-points. (d) Polygon's geometric centre of mass is located. (e) A new polygon is grown from the previous polygon's centre of mass, and its centre of mass located. (f) Result after several repetitions.

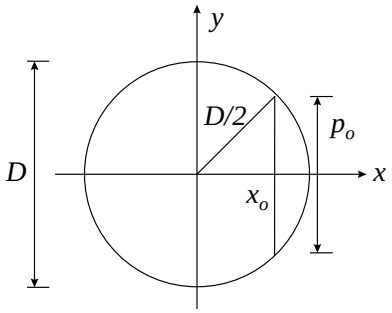

Figure 7.7: Apparent diameter of a sphere which has been cut off-centre.

7.5 Data Analysis

The distribution of bubble diameters observed in a product's cross-sectional image is different from the true bubble size distribution, as the cross-sectional slices will rarely pass through the exact centre of each bubble. Consequently, many bubbles will appear smaller than their actual size.

The problem of reconstructing the true distribution from that observed in a slice was first addressed by Wicksell (1925), who was interested in calculating the size distribution of corpuscles in organ tissue samples. Wicksell solved this problem for both continuous distributions and discrete histograms. The analysis presented here is an alternative derivation which is equivalent to the discrete case studied by Wicksell. Whereas he integrated over each observed frequency interval, a discrete summation form is retained here. This leads to a simpler derivation where there is no loss of accuracy when the observed histogram is also in discrete form, which is likely to be the case for experimentally observed distributions. It also permits irregular histogram intervals to be easily employed.

To understand the relationship between the observed and true distributions, it is instructive to consider the case of a product which has a uniform bubble diameter. Figure 7.7 shows a sphere of diameter D that has been cut at a point x_o so that the observed diameter is p_o. The relationship between p_o and x_o is given by:

$$p_o = \sqrt{D^2 - 4x_o^2} \quad \text{for } 0 < x_o < \frac{D}{2} \tag{7.5}$$

For a random cut through the sphere, the probability $H(p, D)$ that the observed diameter p_o is less than a given diameter p (corresponding to a cut at x_p) can be calculated as:

$$H(p, D) = \frac{x \text{ range which gives } p_o < p}{\text{total } x \text{ range}} = \frac{\frac{D}{2} - x_p}{\frac{D}{2}} = 1 - \sqrt{1 - \frac{p^2}{D^2}} \tag{7.6}$$

$H(p, D)$ is a cumulative distribution function. The probability density function $h(p, D)$ can be found by taking the derivative of $H(p, D)$ with respect to p, i.e.

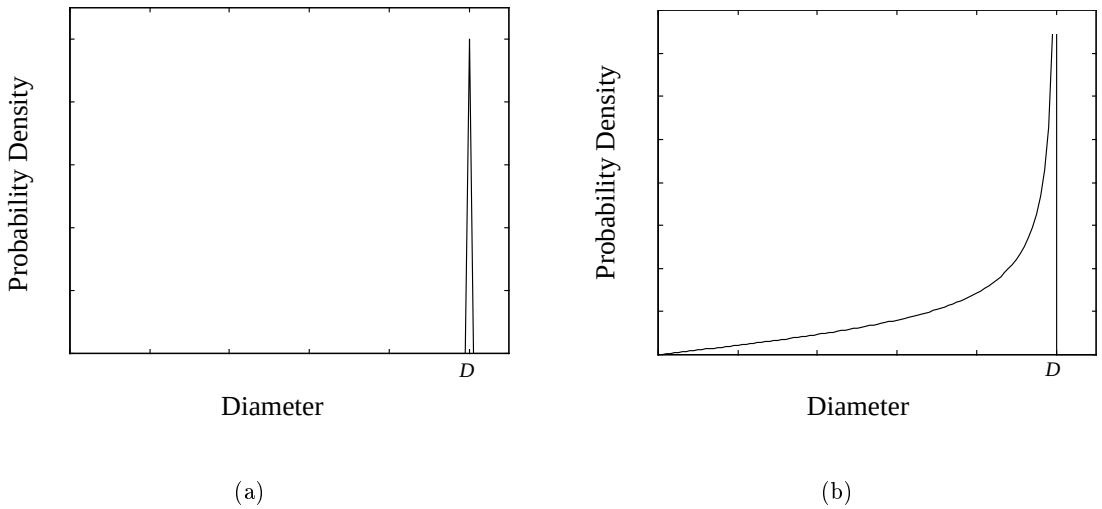

Figure 7.8: (a) Diameter distribution in a product with a uniform bubble diameter D. (b) Expected observed diameter distribution in a cross-sectional slice.

$$h(p, D) = \frac{\mathrm{d}}{\mathrm{d}p} H(p, D) = \frac{p}{\sqrt{D^2 - p^2}} \tag{7.7}$$

Thus, if a material has a uniform bubble diameter D, as depicted in Figure 7.8(a), then the diameter distribution observed in a cross-sectional slice through the material is given by $h(p, D)$, which is plotted in Figure 7.8(b). It should be noted that the total area under the curves in Figures 7.8(a) and (b) is unity, while the shape of the measured distribution is quite different from the true (mono-value) distribution.

Now consider the case where a material sample has a true bubble size probability density function $f(x)$, as shown in Figure 7.9.

To determine the expected distribution $g(s)$ of bubble diameters observed in cross-sectional images, the contribution of each part of the curve $f(x)$ to $g(s)$ needs to be considered. Here s refers to the diameter variable in the observed distribution. The fraction of bubbles in the shaded region between x and $x + \Delta x$ will make a contribution to $g(s)$ given by

$$g(s)\Big|_{x \to x + \Delta x} \approx f(x) \Delta x \, h(s, x) \tag{7.8}$$

Summing over all values of x and taking the limit as Δx tends to zero gives:

$$g(s) = \lim_{\Delta x \to 0} \sum_{x} f(x) \, \Delta x \, h(s, x) = \int_0^\infty f(x) \, h(s, x) \, \mathrm{d}x \tag{7.9}$$

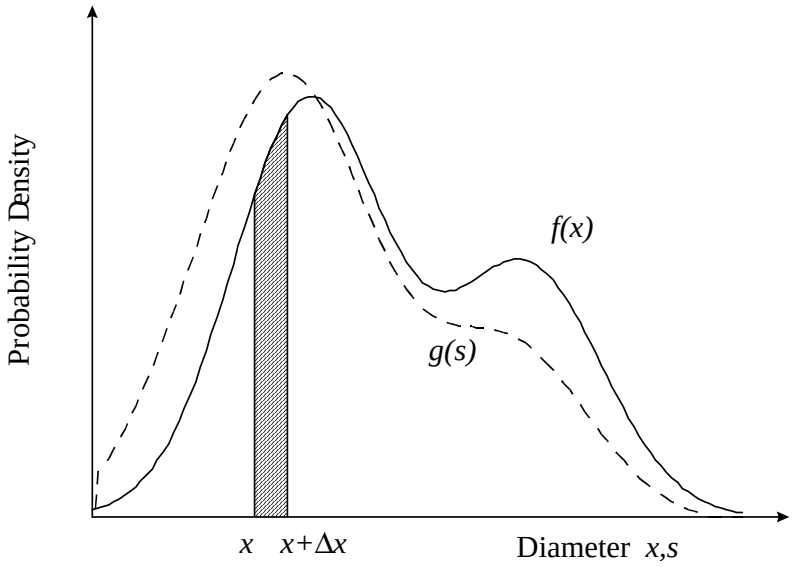

Figure 7.9: Bubble diameter distributions. $f(x)$ is the true bubble diameter distribution, while $g(x)$ is the distribution observed in cross-sectional images.

The curve $f(x)$ shown in Figure 7.9 was, for demonstration purposes, constructed by summing two normal distribution curves, while $g(s)$ was calculated using Equation 7.9. Note that the two curves are shaped differently and that their peaks are located at different diameter values.

The reverse procedure, that is, obtaining the true distribution $f(x)$ from the observed distribution $g(s)$, can be performed by considering the relationship between n discrete points on each curve, as shown in Equation 7.10 below where the s_i and x_i abscissa positions can be chosen arbitrarily. If all $g(s_i)$ values are known, then Equation 7.10 constitutes a set of n linear equations in n unknown values of $f(x_i)$.

$$\begin{aligned} g(s_1) &= h(s_1,x_1)f(x_1)\Delta x_1 + h(s_1,x_2)f(x_2)\Delta x_2 + \ldots + h(s_1,x_n)f(x_n)\Delta x_n \\ g(s_2) &= h(s_2,x_1)f(x_1)\Delta x_1 + h(s_2,x_2)f(x_2)\Delta x_2 + \ldots + h(s_2,x_n)f(x_n)\Delta x_n \\ &\vdots \\ g(s_n) &= h(s_n,x_1)f(x_1)\Delta x_1 + h(s_n,x_2)f(x_2)\Delta x_2 + \ldots + h(s_n,x_n)f(x_n)\Delta x_n \end{aligned} \tag{7.10}$$

The solution of this linear system is straightforward requiring a single matrix inversion. Note when $s > x$ that $h(s,x)$ is zero, so many of the coefficients in Equation 7.10 will be zero. In fact, when the s_i and the x_i take on the same values for each i, then solving Equation 7.10 involves the inversion of an upper triangular matrix, which can be solved efficiently by successive substitution.

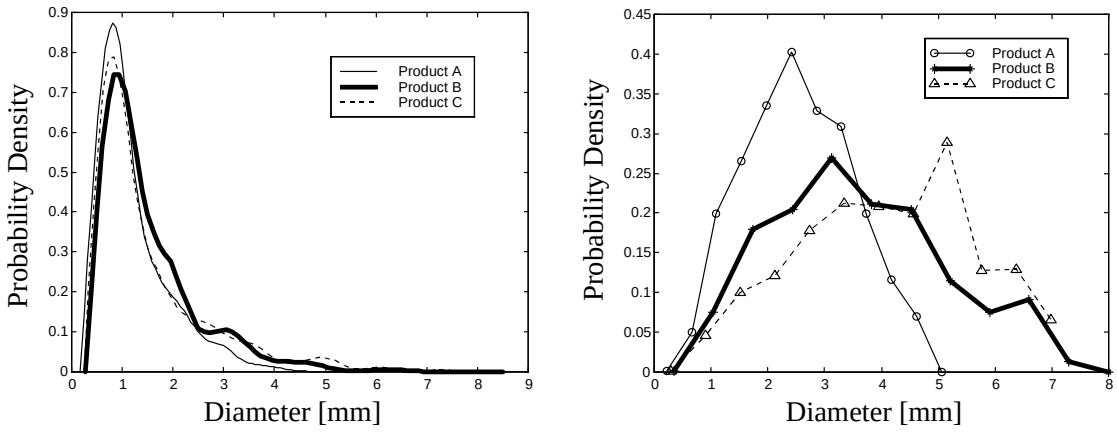

(a) (b)

Figure 7.10: Product bubble size distributions on a (a) diameter basis; and (b) volumetric basis.

7.6 Results

The cross-sectional images of products A, B and C were analysed using the techniques described previously so as to obtain estimates of their actual bubble diameter distributions. For each product the data from all available images were combined so that the number of cavities measured for product A, B and C were 9976, 7423 and 4405, respectively. The resulting probability density functions for each product are plotted in Figure 7.10(a).

It is difficult to see any significant difference between the three extruded products from these curves, as equal weighting is given to both small and large bubbles. A more informative way of viewing the data is to plot the bubble distributions according to the relative volume contained in each diameter sizing, i.e.

$$v(x) = f(x)x^3 \tag{7.11}$$

which is closer to what is perceived when the products are viewed, or eaten. Figure 7.10(b) shows a plot of $v(x)$ for each product, where, for example, it is easier to see that for product A bubbles of approximately 2.5mm diameter are most prevalent on a volumetric basis.

Normal, log-normal and Rosin-Rammler distribution curves were fitted to each of the calculated bubble diameter distributions on a volumetric basis, with the results shown in Figures 7.11(a)–(c). A normal (or Gaussian) distribution is described by the equation,

$$P(x) = \frac{1}{\sigma\sqrt{2\pi}} \exp\left(-\frac{(x-\bar{x})^2}{2\sigma^2}\right) \tag{7.12}$$

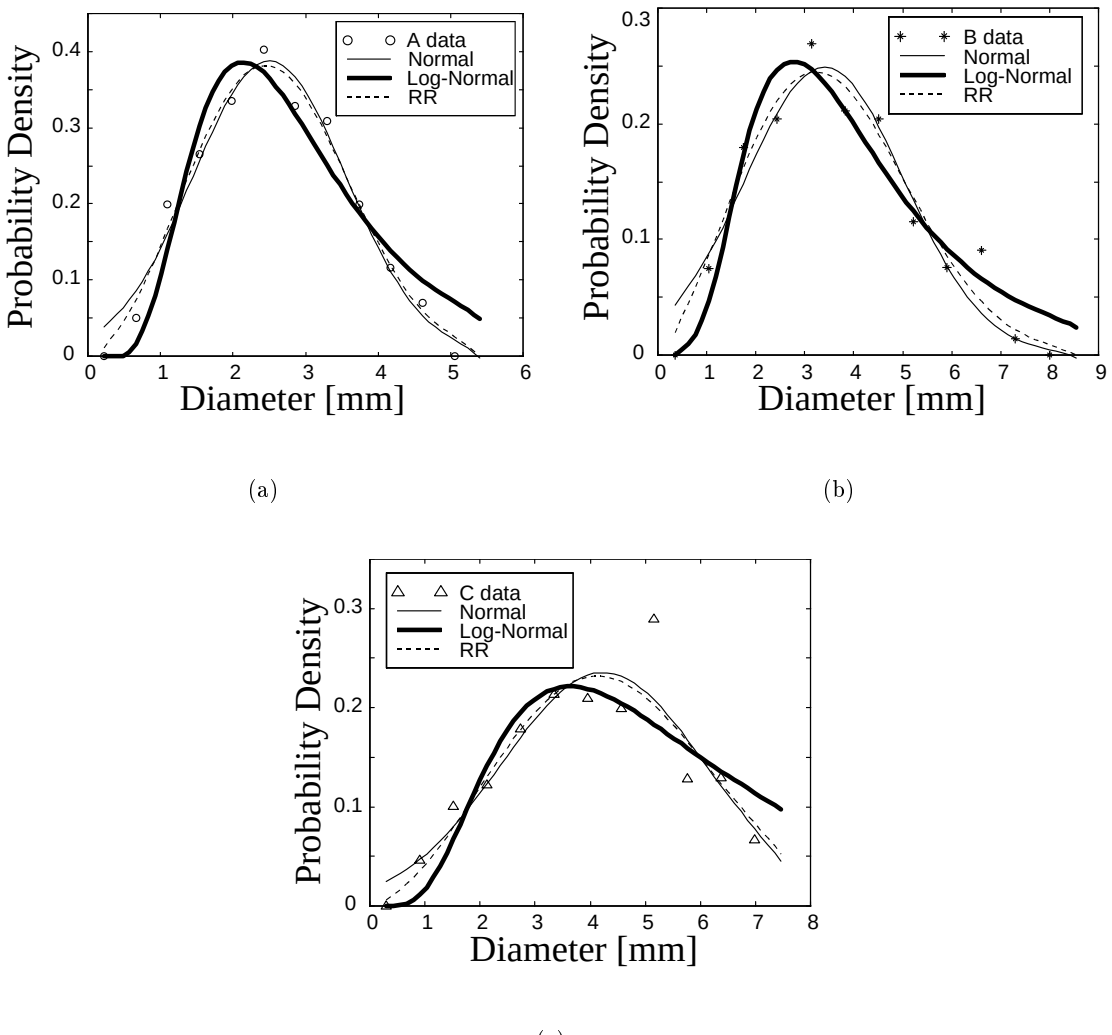

Figure 7.11: Normal, log-normal and Rosin-Rammler curves fitted to the measured bubble diameter distributions on a volumetric basis; (a) product A; (b) product B; and (c) product C.

Table 7.2: Summary of product bubble characteristics on a volumetric basis.

Product	*Mean Diameter* [mm]	*Standard Deviation* [mm]
A	2.50	1.06
B	3.40	1.63
C	4.24	1.85

where the parameters $\bar{x}$ and σ are the mean and standard deviation, respectively. A log-normal distribution is described by the same equation except that in this case $\ln(x)$ is normally distributed. The Rosin-Rammler distribution is commonly used to describe particle size distributions and is described by

$$P(x) = \alpha\beta x^{\beta-1} \exp\left(-\alpha x^{\beta}\right) \tag{7.13}$$

where the parameters α and β are greater than zero.

Normal and Rosin-Rammler distributions gave the best fits to the experimental data, with average correlation coefficients of 0.955 and 0.962, respectively, while a log-normal distribution gave an average correlation coefficient of 0.923. Table 7.2 lists the mean and standard deviation of the best-fit normal curve for each of the three products analysed.

A comparison of Tables 7.1 and 7.2 shows a strong correlation between expansion ratio and mean bubble diameter on a volumetric basis, as might be expected. It is somewhat surprising though that the bubble diameter distributions on a volumetric basis are fitted, in each case, so well by a normal distribution. A brief investigation into the mechanics of bubble nucleation and coalescence is presented in the following chapter in order to explain this result, so it will not be discussed further here.

The reliability of the present analysis technique was investigated by comparing the bubble diameter distributions obtained for product A using different sample sizes. The 72 product A images were divided successively into smaller groups containing 36, 24, 18, 12, 9, 8, 6, 4, 3, 2, and 1 images each, and the mean bubble diameter for each group was calculated. Assuming that the "correct" diameter is the value obtained by including all 72 images (that is, all 9976 cavities) in the analysis, the root-mean-square (RMS) error of the mean bubble diameters is calculated for each grouping. This RMS value is plotted against the number of points used in the analysis (that is, the number of cavities measured) in each grouping, and the result is shown in Figure 7.12.

Figure 7.12 indicates that in order to achieve even a modest accuracy of around 0.2mm in the estimated mean bubble diameter of this product on a volumetric basis, at least 2500 cavities should be included. As each image typically contains 70–100 cavities, this result implies that approximately 25 separate images (certainly more than a single image) need to be analysed to provide a meaningful estimate of the bubble diameter distribution.

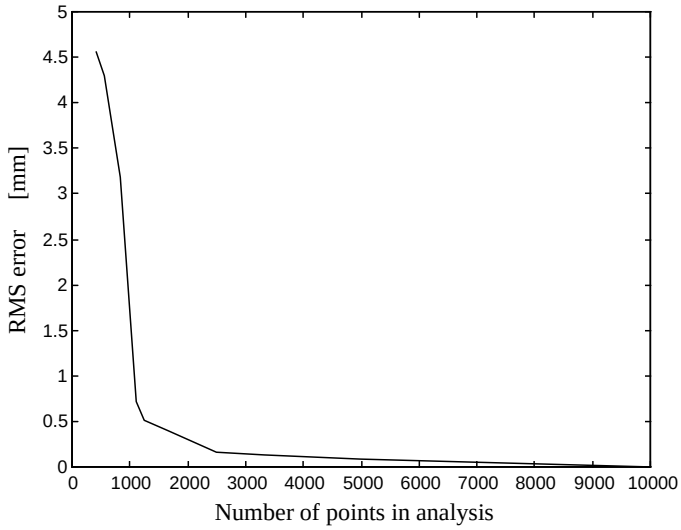

Figure 7.12: RMS error as a function of the number of cavities used in the analysis.

7.7 Conclusions

Using digital image analysis techniques it is possible to estimate the bubble size distribution in puffed extruded products. The photographic and lighting methods used when capturing the images are critical in achieving a reliable result, as are the edge discrimination and cavity detection algorithms used. Commercial image processing software proved inappropriate for this task. The algorithms described in this chapter were implemented in C code and required approximately 20 minutes of Pentium II CPU time for a typical 412-by-844 pixel image.

The true bubble size distribution can be calculated from the observed distribution by a simple deconvolution procedure, with the bubble diameter distribution on a volumetric basis being well approximated by a Gaussian distribution for each of the three extruded products considered. There was a strong correlation between the measured expansion ratio for the extruded pellets and the mean bubble diameter on a volumetric basis, as might be expected. At least 2500 cavities (approximately 25 separate product cross-sectional images) are required to produce a bubble size distribution whose mean is accurate (relative to a large sample estimation) to within 0.2mm.

Unlike the acoustic estimation technique that will be discussed in Chapter 9, the relatively slow and manual nature of this method indicates that it will not be of immediate use for on-line process control of puffing attributes. The value of this technique lies in its ability to supply process operators with an accurate quantification of a physical property that is known to have a significant bearing on product quality. This, for example, allows the bubble size distributions of various products to be compared with certainty, which may improve the understanding of exactly what is desirable in puffed products. It is also

likely to be of use in calibrating polymer foaming models to experimental data, as the large number of material dependent parameters in such models would be extremely difficult to estimate by any other means.

Chapter 8

Simulation of Bubble Nucleation, Growth and Coalescence During the Extrudate Puffing Process

Abstract: This chapter describes a simple methodology for simulating puffing in moist extruded doughs. The simulation program considers an initial volume of the extrudate to which simple models for bubble nucleation, growth and coalescence are applied at each time step. The size and position of each bubble in the system is then monitored over time. For a wide range of initial conditions the model predicts that total bubble volume is normally distributed over the diameter range, which agrees with the experimental measurements of bubble size distribution made in Chapter 7. The simulation results indicate that coalescence is an important factor in determining the the final bubble size distribution. It was also found that the mean bubble diameter on a volumetric basis is approximately the same as that of a single bubble grown in isolation under the prevailing conditions from the start of the simulation. This suggests that single bubble growth models might provide a reasonably accurate prediction of the mean bubble size.

8.1 Introduction

When doughs are extruded at sufficiently high temperatures the moisture present flashes causing bubbles of steam to form and grow. This puffing phenomenon imparts textural properties to the final product which can be highly desirable. There has been an emphasis in recent times on understanding such post-extrusion processes because of their important influence on product characteristics and quality.

Fan et al. (1994) proposed a model for bubble growth in extruded corn dough by considering momentum conservation, continuity of mass and balancing forces acting on a single bubble and the energy balances relating to water vaporisation and convective cooling. This model was able to describe the expansion and shrinkage that has been experimentally observed during the puffing of extruded products. Such products, however, do not display a uniform bubble size, so additional factors must also contribute to the final foam properties. For example, nucleation of new bubbles occurs during puffing, while neighbouring bubbles may coalesce to create larger bubbles. Bubble nucleation in polymer foaming processes has been studied previously, for example, by Lee and Flumerfelt (1996) and Joshi et al. (1998). Bubble formation and coalescence during foaming in polymers has also been observed experimentally by Yarin et al. (1999), however, there have been no investigations into the effect of coalescence on the resulting bubble size distribution in such foams. Although the formation and coalescence of foams in flotation columns has been studied widely (e.g. Pelton, 1996), the conditions in these typically aqueous flotation devices, where the bubbles are mobile, are quite different to the expanding but essentially fixed matrix of a foaming polymer.

The objective here is to simulate the combined effect of bubble nucleation, growth and coalescence in order to estimate bubble size distributions in puffed extruded doughs. Although each of these phenomena are highly complex in themselves, the purpose here is to garner a general understanding of the effects of various operating parameters on the resulting bubble size distribution, so simplified models for each of these processes will be employed. In particular, it was noted in Chapter 7 that in several different puffed corn starch products the total void volume was distributed approximately normally across the range of bubble diameters in the sample. It was hoped that the present analysis might provide some insight into this result.

8.2 Model Development

In order to simulate the nucleation, growth and coalescence of bubbles in a moist dough, a direct simulation approach is used. This involves considering an initial volume of dough which, over time, becomes populated with bubbles. The position and diameter of each bubble is monitored/recorded and the bubbles grow and coalesce as time progresses. New seed bubbles are also added at every time step to simulate nucleation.

This direct simulation approach is necessitated by the need to model bubble coalescence in a realistic manner, as the coalescence of two or more bubbles depends on their proximity, which is best handled using a direct spatial representation with random seeding. The consequence of choosing this modelling approach is that many thousands of bubbles need to be simulated in order to achieve a realistic spatial distribution and allow an accurate estimation of the bubble size distribution. Although detailed models are available for nucleation and bubble growth, the computational cost of modelling the heat, mass and momentum transfer effects in a detailed manner for every bubble in the system would be prohibitive. In addition, the large number of difficult to measure material specific parameters and the inherent difficulties in modelling nucleation phenomena accurately suggest that a simplified modelling approach would be justified initially to investigate basic trends.

8.2.1 Nucleation

Nucleation of new bubbles is perhaps the most important and complex phenomenon involved in determining the attributes of the final puffed product. Lee and Flumerfelt (1996) present a model for the steady-state homogeneous nucleation rate J_N in expanding viscoelastic media as

$$J_N = N_g \left(\frac{2\sigma}{\pi m_g E_c} \right)^{1/2} \exp\left(-\frac{W_c}{k_B T} \right) \tag{8.1}$$

where N_g is the dissolved gas concentration, σ is the surface tension, m_g is the mass of a gas molecule, E_c is a coefficient (of the order of one), W_c is the critical work of formation, k_B is the Boltzmann constant, and T is the absolute temperature. The dependence of nucleation rate on the dissolved gas concentration and melt temperature implies that the nucleation rate would decrease throughout the puffing process as the temperature and concentration of "dissolved steam" decrease. The present simple model does not treat dissolved gas concentration or temperature directly. Instead, a simple first-order approximation to Equation 8.1 depending only on total bubble volume was devised. If V_t represents the total volume that would be filled if all the moisture present in the control volume evaporated, then N_g as a function of V, the total volume of steam already evaporated, is given by

$$N_g = N_0 \left(\frac{V_t - V}{V_t} \right) \tag{8.2}$$

where N_0 is the initial moisture concentration. Vaporisation will only occur while the temperature remains above the atmospheric boiling point, while the temperature will decrease as latent heat of vaporisation is consumed by the forming vapour. Temperature thus, to a first approximation, will decrease linearly with vapour formation akin to

$$T = T_0 - k_v V \tag{8.3}$$

where T_0 is the initial temperature and k_v is a constant relating steam formation to temperature drop calculated via

$$k_v = \frac{\lambda_v}{V_s M_e C_p} \tag{8.4}$$

where λ_v is the latent heat of vaporisation of water, V_s is the specific volume of steam at temperature T_0, M_e is the mass of extrudate in the control volume and C_p is the heat capacity of the extrudate.

Substituting Equation 8.2 for concentration and Equation 8.3 for temperature into Equation 8.1 and grouping constants with unknown second-order terms under J_0 and k_t gives

$$J_N(V) = J_0 N_0 \left(\frac{V_t - V}{V_t}\right) \exp\left(-\frac{1}{k_t(T_0 - k_v V)}\right) \tag{8.5}$$

The values of parameters J_0 and k_t were set through trial and error at 5×10^{22} and 5×10^{-5}, respectively, which gave final bubble diameters and densities similar to those observed in puffed corn products. V_t was calculated using steam tables. During high temperature extrusion of doughs a large proportion of the steam from moisture flashing escapes to the atmosphere and therefore does not finally reside in the bubbles. Based on experimental measurements of moisture loss and expansion it was assumed that this loss figure was 90%.

8.2.2 Bubble Growth

The equation of motion for an expanding bubble is, according to Scriven (1959),

$$p_b - p_m = \rho\left(R\ddot{R} + \frac{3}{2}\dot{R}^2\right) + \frac{2\sigma}{R} + 4\mu\frac{\dot{R}}{R} \tag{8.6}$$

where p_b is the pressure inside the bubble, p_m is the pressure of the melt, ρ is the density of the melt, R is the bubble radius, σ is the surface tension of the melt fluid and μ is the melt viscosity. Here, in the interests of simplicity, rather than use Equation 8.6, it will be assumed that the rate of increase in bubble volume is proportional to the bubble surface area, which is equivalent to

$$\frac{\mathrm{d}R}{\mathrm{d}t} = K_B \tag{8.7}$$

where K_B is a constant. Noting that bubbles grow due to the diffusion of moisture to the bubble surface, to a first approximation the assumption that bubble growth is proportional to bubble surface area is not unreasonable.

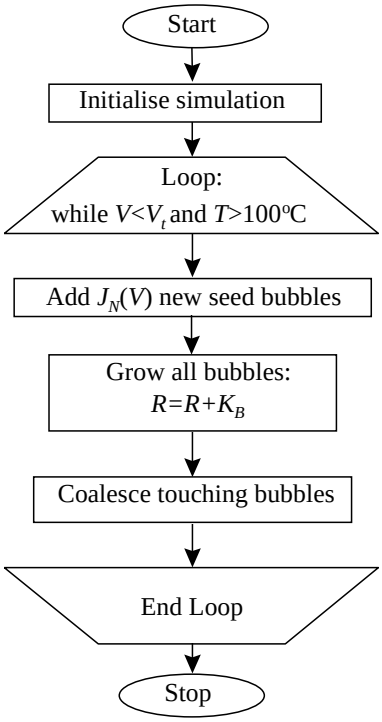

Figure 8.1: Simulation flow chart.

8.2.3 Coalescence

Two or more bubbles, treated as spheres, were coalesced within the simulation when it was calculated that their volumes "overlapped". In this case the touching bubbles are replaced by a single bubble of volume equal to the sum of the volumes of the original bubbles and positioned at the centre of mass of the original bubbles. Secondary influences such as surface tension and viscosity are ignored in this analysis.

8.2.4 Simulation Implementation

Figure 8.1 shows a flow chart describing the steps in the simulation procedure. The starting volume was taken as 1cm^3 and the initial diameter of nucleated bubbles was set at 10^{-6}cm. A K_B value of 0.001cm per time-step was used, meaning that at every time interval the diameter of all bubbles was increased by 0.001cm. Also at every time interval $J_N(V)$ new bubbles were distributed randomly throughout the control volume. As the bubbles grow, the increase in volume of the extrudate results in the bubble centres moving away from each other, which is taken into account in the program. The total volume of the simulated dough mass changes according to the bubble growth, and the temperature decreases due to the loss of latent heat of vaporisation. The simulation stops when all the moisture has evaporated or the estimated temperature falls below 100°C where puffing can no longer occur.

8.3 Simulation Results

To convert the raw bubble diameter distribution $f(x)$, where x is diameter, into the volume weighted diameter distribution $v(x)$ the following relationship is employed:

$$v(x) = f(x)\, x^3 \tag{8.8}$$

Figure 8.2 shows the three resulting void volume distributions calculated when the initial temperature in the simulation is set to 150, 160, and 170°C. According to these results, a higher temperature leads to an increased nucleation rate but the overall bubble sizes are reduced. Figure 8.3 shows the resulting void volume distributions calculated when the initial moisture fraction is set at 0.15, 0.20 and 0.25 w/w. This result suggests that the higher nucleation rate occurring at higher moisture contents results in a lower mean bubble size.

In can be observed in Figures 8.2 and 8.3 that the volume distributions produced in the simulations are fitted well by normal curves. A chi-square test for goodness of fit indicated that all of the distributions were normal at the 95% confidence level. While many approximations were made in developing the present simulation model, it is interesting to note that a normal volume distribution results from a wide range of operating conditions. These results agree qualitatively with the experimentaly measured bubble size distributions from Chapter 7, which were measured using image analysis techniques. In that study, the results of which are reproduced in Figure 8.4, normal distributions were measured in each case.

The importance of coalescence to the final volumetric diameter distribution is illustrated in Figure 8.5. It can be seen that if coalescence did not occur then the distribution would be markedly one-sided. Also shown in this figure is a dashed line indicating the diameter a single bubble would reach if grown from the onset of puffing in isolation. Bubbles larger than this can only occur as a result of coalescence. It can be seen that this point lies approximately at the mean of the distribution. This result suggests that an estimate of the bubble size distribution's mean might be calculated using an accurate single bubble growth model, such as that of Fan et al. (1994). This is certainly a speculative hypothesis and further investigations would be necessary to confirm its validity.

Finally, a brief comment on the assumption of Equation 8.7 is in order. Although the assumption that rate of bubble growth is proportional to the bubble surface area is a fair first approximation, it is clearly not a rigorous treatment of bubble growth. However, it is apparent from the results of this and the previous chapter that factors having a stronger influence on the bubble size distribution are the rate of nucleation, bubble coalescence, and the mass and energy balances. In addition, the objective of the present study is to model the extrudate puffing process in terms of the bubble size distribution. Unless Equation 8.7 is drastically unreasonable, it will have little effect on the results other than changing the

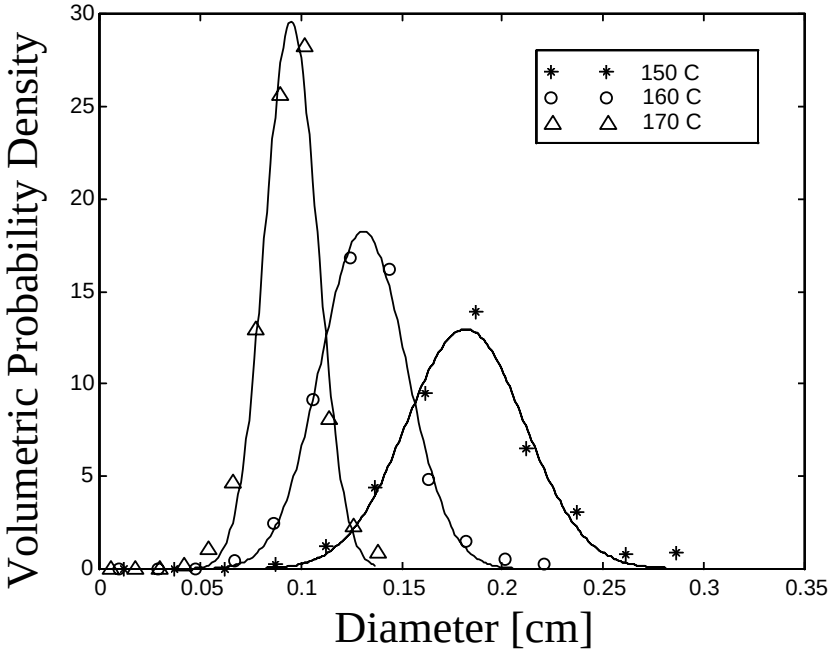

Figure 8.2: Simulated distributions when temperature is varied (with normal curves fitted).

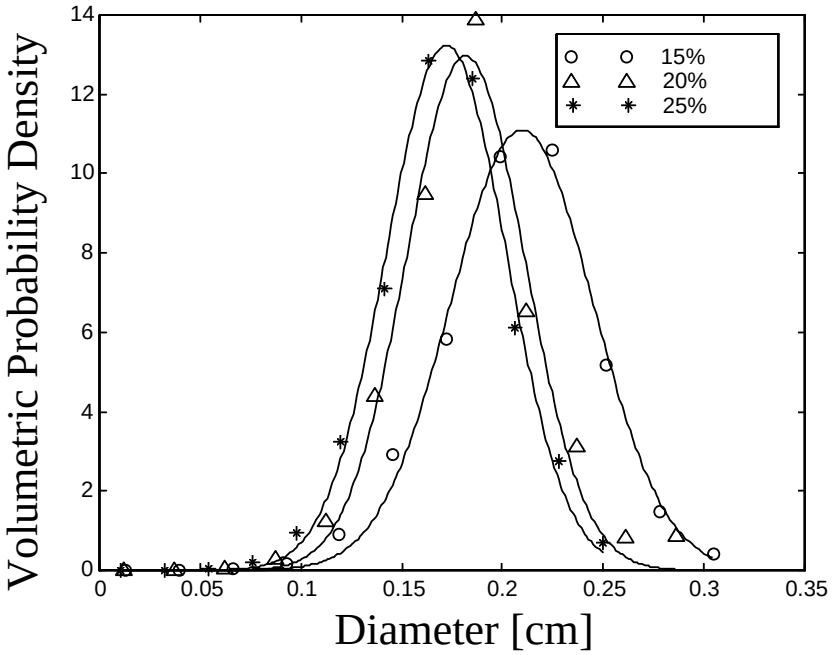

Figure 8.3: Simulated distributions when moisture content is varied (with normal curves fitted).

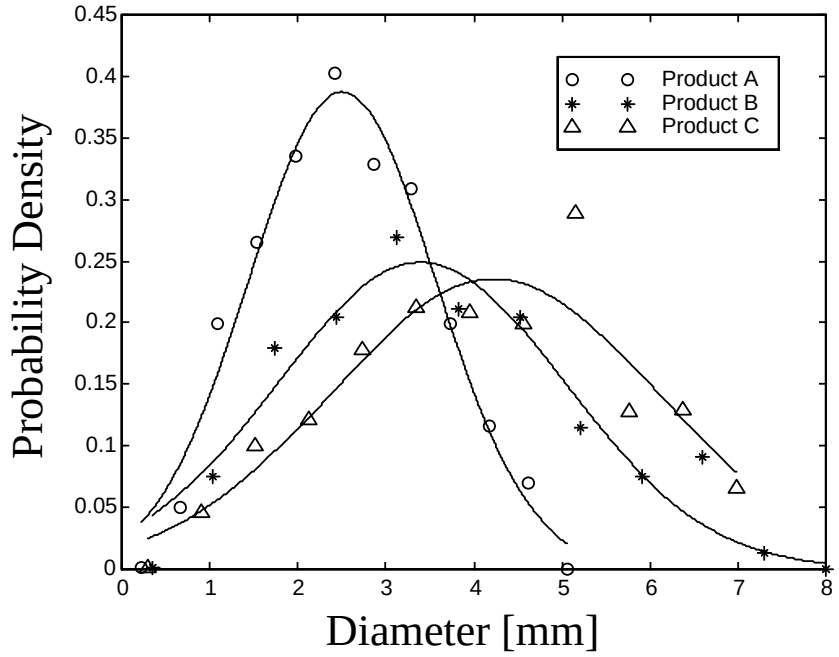

Figure 8.4: Experimentally observed void volume distributions for three different puffed corn products with normal distribution curves fitted (results from Chapter 7).

time-scale of the puffing process, which is not of interest here. The fact that the simulation trends are in close agreement with the experimentally measured bubble size distributions in Chapter 7 is evidence that the chosen model is not inappropriate.

8.4 Conclusions

It has been found using a simple bubble nucleation, growth and coalescence model that the total bubble volume in a puffed extruded product is fitted very well by a normal distribution over the bubble diameter range. This simulation result agrees qualitatively with the experimental results presented in Chapter 7. It was found that bubble coalescence is an important factor contributing to the development of a normal-shaped distribution. Without it, the predicted distribution is completely one-sided. It was also found that the mean bubble diameter on a volumetric basis is approximately the same as that of a single bubble grown in isolation under the prevailing conditions from the start of the simulation.

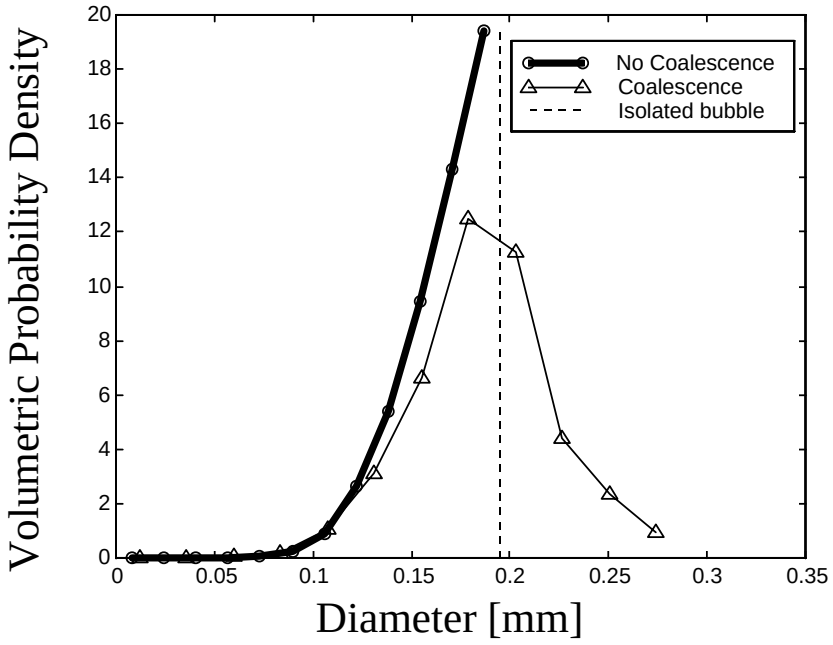

Figure 8.5: The effect of coalescence on the predicted volumetric diameter distribution.

Chapter 9

Acoustics Based Product Quality Estimation

Abstract: In this chapter an acoustic sensor for estimating the physical properties of puffed extruded cereal products is developed. The basis of the approach relies on the fact that as the extrudate leaves the die, the water content partially flashes causing the extrudate to puff with tiny steam bubbles. There are discernible differences in the sound the escaping steam makes when different products are being extruded. A set of experiments was performed to record the sounds made by the extrudate leaving the die under different operating conditions and to measure the subsequent physical properties of the product, specifically, bulk density and fracture force. The acoustic signals were analysed to extract both time domain and frequency domain information. It was found that by using non-linear regression techniques such as artificial neural networks or genetic programming, a model relating the acoustic variables to the corresponding experimentally measured physical properties could be developed. The resulting model was found to perform well on unseen experimental data, with correlation coefficients exceeding 0.96. Due to the low cost and accuracy of this approach, it may prove useful in industrial monitoring applications and feedback controllers.

9.1 Introduction

The food industry is one of the world's biggest industrial sectors. It is also an industry where the provision of consistently high-quality products is of paramount importance. Whilst many traditional food production processes are batch and craft-oriented, there has been an increasing drive in recent years to improve process efficiency by reducing wastage and improving product consistency. In regard to cooking extruders, particularly evident is the need for improved control of the process in order to achieve these efficiency goals. However, the product properties which are deemed important to control, such as bulk density, texture and degree of cook, are difficult to measure on-line to provide the feedback information for a control system.

The present study concerns the manufacture of a puffed extruded cereal product. Puffing occurs when the extrudate leaves the die at sufficiently high temperatures to cause the entrained water to flash, resulting in the growth of tiny steam bubbles. These steam bubbles can burst if they are close to the surface. There are discernible differences in the sound the escaping steam makes when different products are being extruded. Given that these sounds must be related to factors such as bubble size and number, material rheology, moisture content and surface tension, there is a good reason to suspect that they might be correlated with product properties of interest such as product bulk density and texture. The aim here was to examine the use of acoustic signals for predicting product quality attributes, the ultimate goal being the development of a fast, automatic acoustics based quality estimator.

Exploitation of acoustic information has been employed in many sensing problems in the literature. Booker and Doe (1994) used acoustic emissions to determine surface strain energy in drying timber while Kruft and Friedsch (1986) used such emissions to detect and control cavitation in pumps. Speech recognition (Rabiner and Juang, 1993) is also an obvious application of acoustic analysis techniques. There is no known precedent to the specific application presented here, although the signal processing and non-linear identification techniques used to solve this problem are known in the literature.

The approaches presented in this chapter use both time and frequency domain information in the development of models for product bulk density and texture (quantified here by the fracture force). Principal component analysis (PCA) (Manly, 1986) is used to reduce the dimensionality of the frequency domain data, while genetic programming (GP) (Koza, 1992) and artificial neural networks (Cybenko, 1989) are used to identify models for the quality variables.

9.2 Experimental Procedure and Apparatus

An APV-Baker MPF-40 twin-screw cooking extruder was operated at a range of conditions to give products with different physical properties. Feed rates of 15, 20, and 25 kg/h;

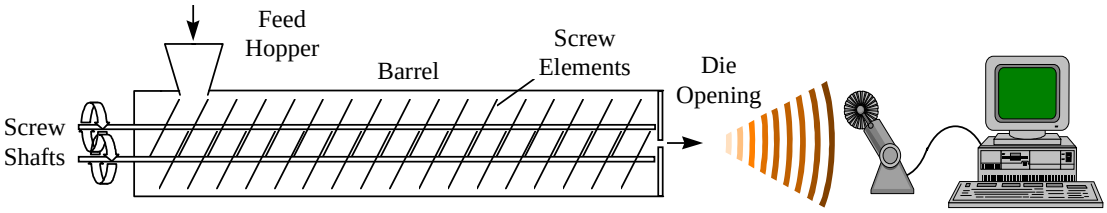

Figure 9.1: Schematic representation of experimental apparatus.

moisture contents of 0.14, 0.18 and 0.22 w/w; and screw speeds of 250, 350 and 450 RPM were used in all permutations, resulting in 27 different operating conditions, with two additional runs performed to check for consistency in the data. A microphone connected to a personal computer with a sound-card was used to digitally record the sounds emitted by the extruder. The experimental apparatus used in this investigation is illustrated in Figure 9.1. Equipment not shown in this figure includes the motor used to drive the screw shafts, its cooling fan and a cutter placed over the die to cut the product as it exits the extruder. Each of these contribute significant additional noise which is also detected by the microphone. A sound file of approximately 10 seconds recorded at 22kHz was taken when each run had reached steady-state. Product samples were collected and their bulk density ρ_B and fracture force F_F were measured off-line in a laboratory environment.

9.3 Data Analysis

To compensate for having a relatively small data set (29 separate sound measurements), 10 samples of 2^{14} points each were taken from each sound file to build a data set containing $N_S = 290$ sound samples. Sound files of 2^{14} points, equivalent to 0.74 seconds of continuous sound, proved to be sufficiently long to characterise each product, as taking longer sound samples did not significantly improve the modelling results. A power of two was selected to allow the use of the computationally efficient Fast Fourier Transform algorithm (Press et al., 1992).

Aural observations indicated that the acoustic features of importance were the rate at which popping noises were made by the bursting bubbles and also the pitch (i.e. frequency) of these sounds. Consequently, an attempt was made to extract both time domain and frequency domain variables from the acoustic data to construct a correlation model. It should be noted that there is a practical incentive to minimise the number of variables included in the final modelling data set, as the non-linear regression methods used here increase rapidly in computational complexity as the number of variables increases.

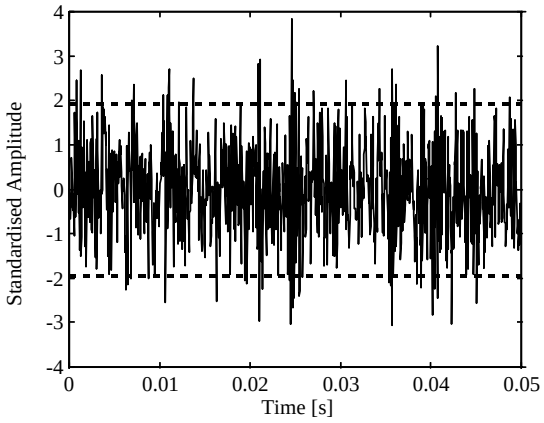

Figure 9.2: Time domain signal showing popping rate bounds. Points further than 1.9 standard deviations from the mean were counted to give a measure of the popping rate.

9.3.1 Time Domain Information

A measure of the popping rate for each sound sample was obtained by finding the number of points per second in the discrete time domain signal that were more than 1.9 standard deviations from the mean value of the signal, i.e.

$$R_P = \frac{1}{n_p T_s} \sum_{k=1}^{n_p} (y(k) > 1.9\sigma) \tag{9.1}$$

where R_P is the popping rate, n_p is the number of sample points being analysed, T_s is the sampling interval, $y(k)$ is the discrete time domain acoustic signal, σ is the standard deviation of the acoustic signal, and the bracked logical expression has a value of one when true and zero when false. A typical signal and bounds are shown in Figure 9.2. The value of 1.9 was arrived at by an optimisation procedure designed to give a value of the popping rate most highly correlated with the bulk density (the correlation coefficient here was 0.73). A measure of the average power of the signal was calculated by taking the root mean square (RMS) value of the signal, i.e.

$$P_{RMS} = \sqrt{\frac{\sum_{k=1}^{n_p} y(k)^2}{n_p}} \tag{9.2}$$

9.3.2 Frequency Domain Information

A Fourier transform was used to determine the frequency content of the acoustic signal. The acoustic power spectrum (i.e. the magnitude of the Fourier coefficients) for a typical sound sample taken from the extruder is shown in Figure 9.3(a). The power spectrum contains a large number ($\lfloor n_p/2 + 1 \rfloor$) of data points, so it is impractical to include each

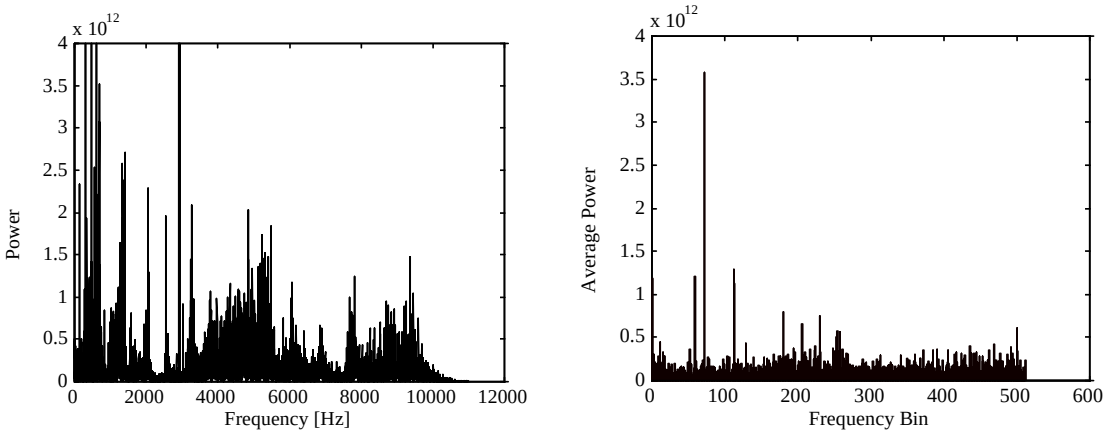

(a) (b)

Figure 9.3: (a) Power spectrum of a typical sound sample when extruding wheat flour; (b) same data grouped into bins and averaged.

datum as a modelling input variable. To reduce the number of data points comprising the power spectrum for each sound sample, the frequency range was divided into N_B bins and the average energy in each bin was taken. A value of $N_B = 512$ proved suitable, resulting in the power spectrum shown in Figure 9.3(b).

To further distill the power spectrum data, and to extract variables that more concisely described the variation in the data, the principal components of the binned power spectrum data were determined, as described in the following section.

Principal Component Analysis

The objective of principal component analysis is to take a set of data $\mathbf{X}$, in which the variables $(x_1, x_2, \ldots, x_q)$ may be highly correlated, and to map it onto a new set of uncorrelated variables $(\varepsilon_1, \varepsilon_2, \ldots, \varepsilon_q)$. These ε_i variables are made up of linear combinations of the original variables and are ordered so that

$$\text{var}(\varepsilon_1) \geq \text{var}(\varepsilon_2) \geq \ldots \geq \text{var}(\varepsilon_q) \tag{9.3}$$

where $\text{var}(\varepsilon_i)$ denotes the variance of ε_i in the data set being considered. The ε_i are called *principal components*. The first principal component is thus

$$\varepsilon_1 = \nu_{11}x_1 + \nu_{21}x_2 + \ldots + \nu_{q1}x_q \tag{9.4}$$

where the ν_{i1} are selected so that the variance of ε_1 is maximised subject to the constraint

$$\sum_{i=1}^{q} \nu_{i1}^2 = 1 \tag{9.5}$$

Similarly, the second principal component is given by maximising the variance of ε_2

$$\varepsilon_2 = \nu_{12}x_1 + \nu_{22}x_2 + \ldots + \nu_{q2}x_q \tag{9.6}$$

subject to two constraints, firstly that

$$\sum_{i=1}^{q} \nu_{i2}^2 = 1 \tag{9.7}$$

and secondly that ε_1 and ε_2 are uncorrelated. Further principal components are defined by continuing in the same way, with there being as many principal components as there were variables in the original data set. The equations for calculating the principal components can be summarised in matrix form as

$$\mathbf{E} = \mathbf{XV} \tag{9.8}$$

where each column of $\mathbf{V}$ (the 'loading matrix') contains the weights ν_{ij} for a different principal component ε_j. Each column of the matrix $\mathbf{E}$ (the 'score matrix') contains one of the principal components evaluated for all the observations in $\mathbf{X}$.

It can be shown that the eigenvectors of the covariance matrix of $\mathbf{X}$ form the matrix $\mathbf{V}$, while the corresponding eigenvalues show the variance of each principal component (Manly, 1986).

The acoustic power spectrum data were grouped into an $N_S \times N_B$ matrix of observations, i.e.

$$\mathbf{X} = \begin{bmatrix} x_{11} & \ldots & x_{1N_B} \\ \vdots & \ddots & \vdots \\ x_{N_S1} & \ldots & x_{N_SN_B} \end{bmatrix} \tag{9.9}$$

and the first 10 principal components were calculated for inclusion in the set of modelling variables. The first 10 principal components were found to account for about half of the total variance in the power spectrum data.

An important point to mention about PCA is its noise filtering property. Because each principal component is designed to account for the maximum amount of variation in the remaining data dimensions, the background noise, being reasonably consistent across all samples and therefore producing little variation, is effectively eliminated from the major principal components.

Table 9.1: Correlation coefficients between modelling inputs and outputs.

Outputs→ Inputs↓	*Bulk Density* ρ_B	*Fracture Force* F_F
R_P	0.73	0.65
P_{RMS}	0.21	0.21
ε_1	0.30	0.23
ε_2	-0.36	-0.21
ε_3	0.33	0.37
ε_4	-0.42	-0.58
ε_5	-0.04	0.11
ε_6	-0.14	-0.17
ε_7	-0.34	-0.23
ε_8	0.06	0.07
ε_9	0.18	0.11
ε_{10}	0.01	-0.04

9.4 Modelling Procedure

Both artificial neural networks (ANNs) and genetic programming (GP) were used to develop models for bulk density and fracture force as a function of the inputs 'popping rate' R_P, RMS power P_{RMS}, and the 10 most significant principal components from the frequency domain $\varepsilon_1, \ldots, \varepsilon_{10}$. ANNs are already well established in the field of data-based modelling, and the feedforward neural network used in this work is discussed by Cybenko (1989). GP (Koza, 1992; McKay et al., 1997) is a relatively new non-linear data-based modelling technique which offers a useful alternative to ANNs. Unlike conventional modelling procedures that seek the best set of parameters for a pre-specified model, the GP methodology performs symbolic regression to determine the structure and complexity of the required model simultaneously with model parameter estimation. While the apparent advantages and disadvantages of each of these techniques over the other are debatable, GP, while slower, has the particular advantage that it produces explicit equations relating the input and output variables, while also automatically including only the input variables which have an effect on the outputs.

The correlation coefficients between each of the inputs and the outputs to be modelled is shown in Table 9.1, from which it can be observed that principal components 5, 8 and 10 have a relatively low correlation with both bulk density and fracture force. Consequently, to reduce the number of modelling variables, these inputs were removed from the training data set prior to presenting the data to the ANN and GP identification algorithms.

9.5 Modelling Results

9.5.1 Genetic Programming Modelling

The best final expression obtained by the GP algorithm for predicting bulk density is as follows:

$$\rho_B = \frac{2.64\varepsilon_1\varepsilon_7 - 0.70\varepsilon_3 + \varepsilon_7^2 + 82.4\varepsilon_9 + 2R_P + 8.90\varepsilon_1 - 1466}{\varepsilon_1 + 1170\varepsilon_7 + 841\varepsilon_9 + 253\varepsilon_2 - 466\varepsilon_3 + 764\varepsilon_4\varepsilon_9 - 66.4\varepsilon_1\varepsilon_2 + 26790} \tag{9.10}$$

while the best expression for predicting fracture force is:

$$\begin{aligned} F_F &= 1251 - 63.5\varepsilon_6 + 23.5\varepsilon_1 + \left(\varepsilon_7\varepsilon_1 - 5.76\varepsilon_4 - 7.40\varepsilon_7 + 40.3 - \frac{5.87\times10^{-3}\varepsilon_1\varepsilon_3}{\varepsilon_2}\right)\times\ldots \\ &\quad \left(1.07\varepsilon_3 - 0.446\varepsilon_2 + 0.435\varepsilon_9 + 0.294\varepsilon_7^2 - 1.86\varepsilon_7 - 2.73\varepsilon_4\right) \end{aligned} \tag{9.11}$$

The performance of each of these models at fitting both the training and unseen data is shown in Figure 9.4. The model for bulk density provides a generally unsatisfactory fit to the experimental data, having a correlation coefficient of 0.93 on the training data and 0.91 on the verification data. The model for fracture force is slightly better, having a correlation coefficient of 0.94 on the training data and 0.92 on the verification data. It is interesting to note that the variable P_{RMS} from the training data set does not appear in either of Equations 9.10 or 9.11, demonstrating the input variable selectivity that is characteristic of the GP algorithm.

9.5.2 Artificial Neural Network Modelling

The same data set was used to train ANNs to predict bulk density and fracture force. A network structure of 8 inputs and 8 hidden neurons in a single layer was chosen, making a total of 81 internal weights which were determined using a Levenberg-Marquardt non-linear parameter fitting algorithm (Press et al., 1992). The performance of the ANNs at fitting the training and verification data for both the product bulk density and product fracture force is shown in Figure 9.5. The fit to the bulk density experimental data is quite good, having a correlation coefficient of 0.98 on the training data and 0.96 on the verification data. The fit to the fracture force experimental data is even better, with a correlation coefficient of 0.99 on the training data and 0.98 on the unseen verification data.

9.6 Conclusions

The ability to predict certain physical properties of a puffed extruded product based on acoustic information alone has been demonstrated. This novel result was achieved by using

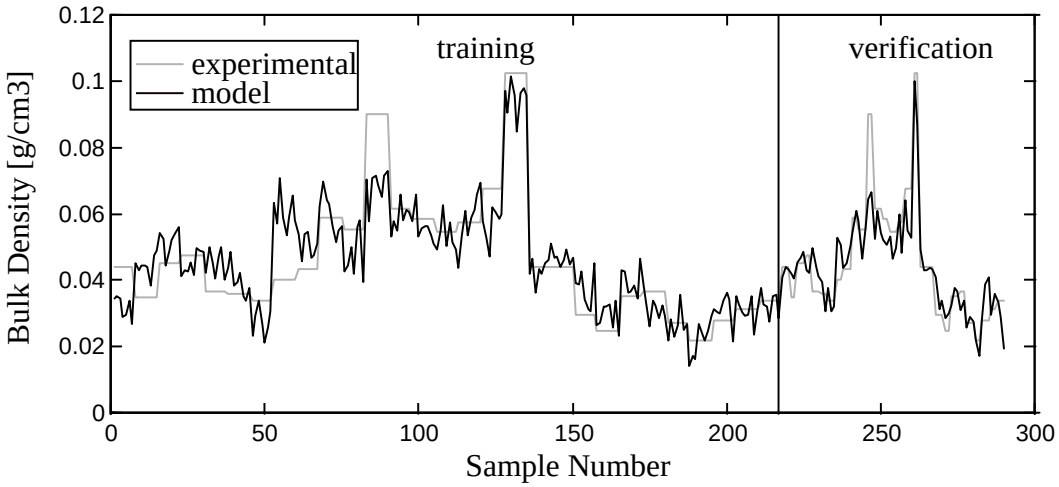

(a)

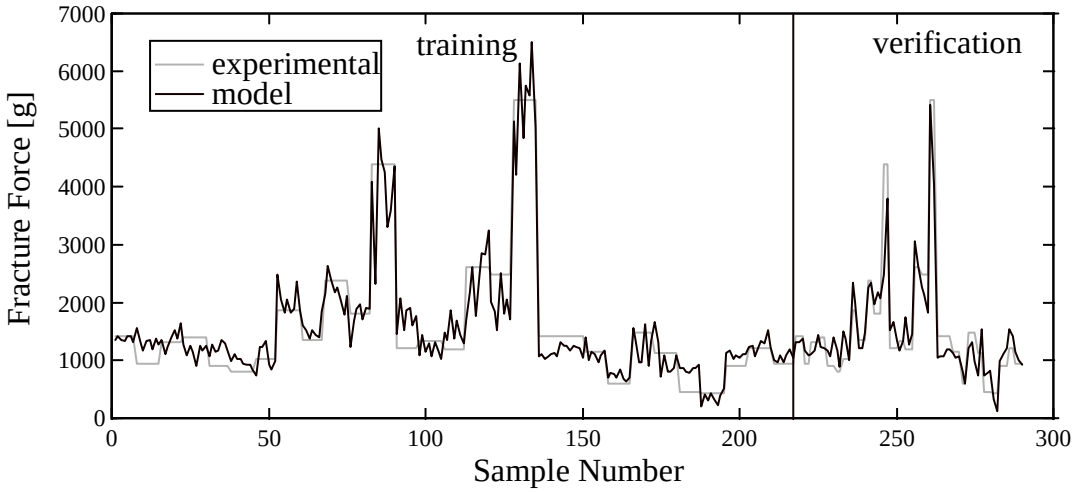

(b)

Figure 9.4: (a) GP generated model for bulk density, training data correlation coefficient 0.93, verification data correlation coefficient 0.91; (b) GP-generated model for fracture force, training data correlation coefficient 0.94, verification data correlation coefficient 0.92.

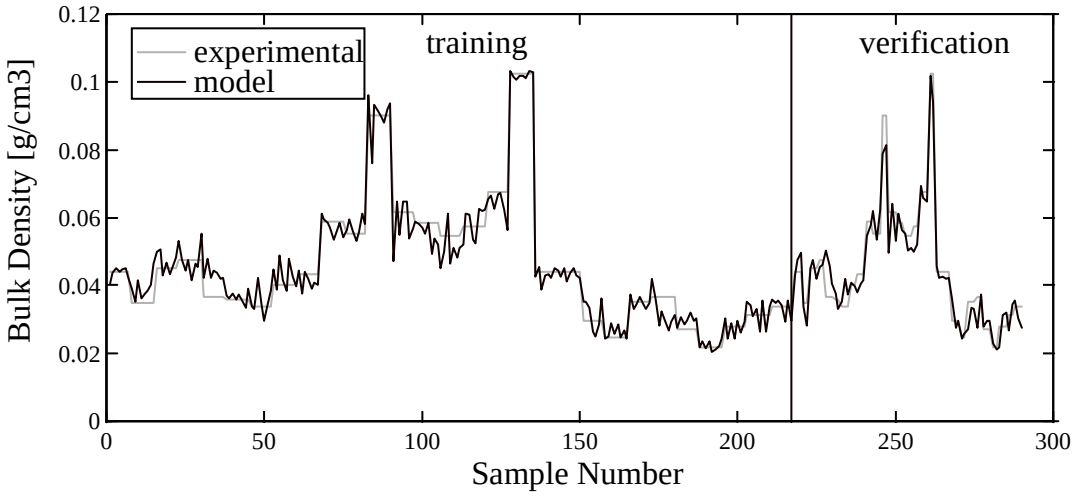

(a)

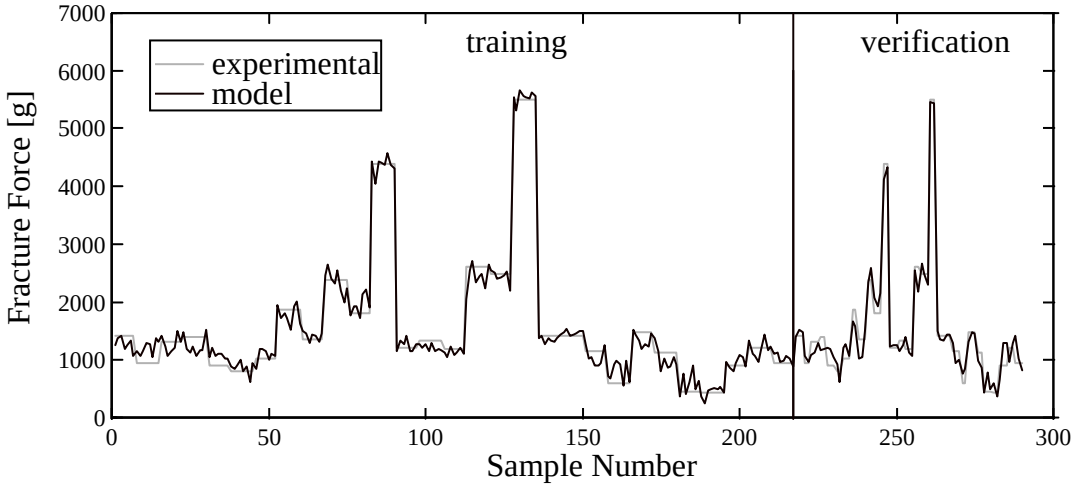

(b)

Figure 9.5: (a) ANN-model for bulk density, training data correlation coefficient 0.98, verification data correlation coefficient 0.96; (b) ANN-model for fracture force, training data correlation coefficient 0.99, verification data correlation coefficient 0.98.

non-linear regression techniques to identify correlations between acoustic variables and experimentally measured physical properties. While there is obvious scope for improvement, the present models, particularly those generated by the ANNs, performed well on unseen experimental data with correlation coefficients exceeding 0.96. The general drawback of the present method is that it requires calibration against experimental data, so applying it to new products would require a comprehensive experimental program and the fitting of new non-linear models. However, the advantage of the present approach lies in its low cost and reasonable accuracy, which may make it practical for industrial monitoring applications where high quality product controllers are deemed necessary. The potential utility of this technique is exemplified in the following chapter.

9.7 Recommendations

The method described in this chapter could benefit from additional experiments to further explore its potential. In the present example only acoustic data was used for model training, however, additional process measurements, such as temperatures and pressures, could easily be added to the set of input variables. This may allow for more accurate estimates of the product properties than those obtained using acoustic data alone.

Chapter 10

Model Predictive Control of Product Quality Attributes in an Extrusion Cooking Process

Abstract: Traditional control strategies for twin-screw cooking extruders often seek to regulate the process by maintaining constant die pressure, die temperature, and/or specific mechanical energy input. These variables are typically chosen as process indicators because the primary product quality attributes (PQAs) of interest, such as degree of cook or extent of puffing, are difficult to measure rapidly on-line for control purposes. In the present study, a dynamic model of the twin-screw extrusion cooking process is used to compare two model predictive control strategies for regulating the PQAs. The first uses a traditional indirect approach whereby the die pressure and temperature are controlled using the screw speed and the water injection rate as manipulated variables. The second approach uses the same manipulated variables to control the product gelatinisation fraction and product bulk density directly. The performance of each controller is assessed by simulating disturbances to the process. The principal disturbances of interest are changes in the rheological properties of the feed material, screw wear and variations in feedstock moisture content. Both controllers perform well at controlling their specified output variables. However, for effectiveness in maintaining constant values for the chosen PQAs when the process is subjected to disturbances, it is found that taking no control action at all is preferable to controlling the secondary process indicators temperature and pressure.

10.1 Introduction

Extrusion cooking is used extensively in the food industry as it provides an efficient means for the continuous processing of a wide range of foodstuffs (Harper, 1981). Intense competition amongst food companies in recent years has heightened pressures to reduce operating costs while at the same time improve product quality and diversity. Moreover, there is growing pubic concern over food safety issues and a demand for better standards. This has lead the food industries to place greater emphasis on improved and consistent product quality.

Product quality variability can be reduced through better process control. However, there are several challenges involved in controlling food extrusion processes. Firstly, the process is highly non-linear and displays a high degree of interaction between process variables. Both of these characteristics require special consideration in controller design. The second, and more problematic issue, concerns the difficulty in measuring the product quality attributes (PQAs) of interest in a manner suitable for feedback control. This is because the relevant PQAs are usually chemical or physical properties, such as the degree of cooking or product bulk density, which are difficult to measure rapidly on-line. This difficulty has led to the use of indirect control strategies based on regulating more easily measured variables. The common approach is to determine the operating conditions, such as the temperature and pressure profiles along the barrel, which give the desired product quality, and then to maintain these values as closely as possible using various control loops, if not manual control. The intention is that by controlling these secondary process variables, the product quality will also be maintained at the desired level. Clearly, while this may go some way towards regulating the PQAs in certain cases, it does not directly address the issue of product quality control.

That is not to say that certain PQAs cannot be measured on-line in a manner suitable for feedback control. Recent applications of near infrared spectroscopy (Evans et al., 1999) have demonstrated the ability to measure the degree of cook by measuring the absorbance of spectral lines associated with hydrogen bonding between starch molecules. Also, inferential estimators based on acoustics (see Chapter 9) or other process data (Wang et al., 2001) have demonstrated the ability to estimate product bulk density and surface hardness of puffed extruded products. It is recognised, however, that implementing such sensors or estimators requires a substantial capital outlay or modelling effort, so it is important to evaluate the extent to which these tools can improve control over PQAs.

The goal of this chapter is to compare the effectiveness of both direct and indirect control strategies for regulating the PQAs of an extrusion cooking process. Model predictive controllers (MPC) for each strategy are developed and tested in the presence of simulated process disturbances. The MPC approach is used here because of its inherent decoupling properties, as the extrusion process is known to be highly interactive (Singh and Mulvaney, 1994). Although the implementation hardware for MPC is more compli-

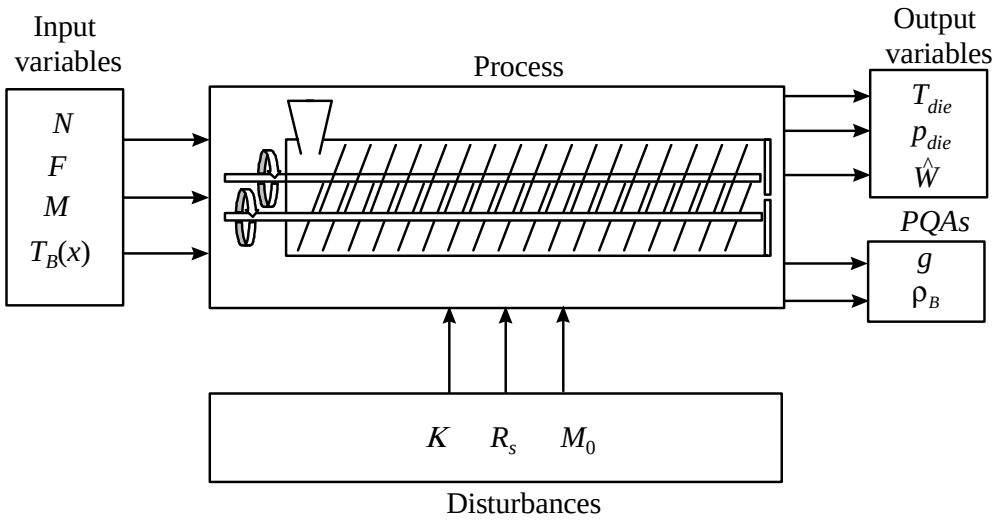

Figure 10.1: The extrusion cooking process showing inputs, outputs and disturbances.

cated than for three-term (PID) controllers, the objective here is to compare direct and indirect control strategies rather than compare different control algorithms for the same control task.

The chapter begins with a description of the extrusion cooking process, followed by a review of the literature pertaining to cooking extrusion process control. The process characteristics are then analysed from a controller design perspective, and the design and tuning of the model predictive controllers is discussed. Results of the control simulations are presented, followed by conclusions and recommendations for future work.

10.2 Extrusion Cooking Process Description

A typical extruder consists of a barrel inside which one or more helical screws rotate to propel the feed material towards a die opening at the discharge end of the extruder, as illustrated in Figure 10.1. Extrusion cooking of puffed snack foods generally involves the use of a starchy feed material, such as corn flour, mixed with a small amount of water. Screw configurations which promote shearing and viscous heat dissipation are used to effect gelatinisation and cooking of the starchy process material. The high pressure built up during this process forces the material to exit the extruder through the die. If the material leaving the extruder is of sufficiently high temperature then the entrained water will flash causing tiny bubbles of steam to develop, resulting in a puffed cellular structure.

Cooking extrusion is a multiple-input-multiple-output (MIMO) process. The process variables which are available for manipulation are the feed rate F, the moisture content M, the screw speed N, and the barrel temperature profile $T_B(x)$. The process outputs include the die temperature T_{die}, the die pressure p_{die}, the product specific mechanical energy $\hat{W}$,

the product bulk density ρ_B, and the product gelatinisation fraction g. Disturbances may be introduced into the process via a number of avenues, although the ones considered to be of the greatest importance here are the rheological consistency index K, the tip radius of the screw R_s, which is gradually affected by mechanical wear, and the inherent moisture content of the feed material M_0.

10.3 Literature Review

The extrusion cooking process is widely reported to be highly non-linear and interactive, making it difficult to control. The literature reports many different approaches for controlling the twin-screw extrusion cooking process, a number of which are reviewed in this section.

Several researchers have simulated the performance of various control schemes for co-rotating twin-screw extruders. Moreira et al. (1990) simulated the feedback control of die pressure using screw speed as the manipulated variable. Their simulations were based on experimentally determined transfer functions. In addition to the feedback control loop, they also recommended the use of feedforward control to minimise the transient error caused by measurable disturbances in feed rate and feed moisture. Linko et al. (1992a) used a neural network model to simulate control of specific mechanical energy input (SME) using feed rate, moisture content and screw speed as the manipulated variables. Singh and Mulvaney (1994) used transfer function models published in the literature to calculate the relative gain array (RGA) (Bristol, 1966) to determine the multivariable control loop pairings having the least interaction. They concluded that the extrusion process exhibited a high degree of interaction and predicted unstable controller operation for a 3×3 process involving screw speed, barrel temperature and moisture content as the manipulated variables and die pressure, die temperature and motor torque as the controlled variables. They also reported a 2×2 controller pairing which produced minimal interaction where the screw speed was used to control the motor torque and the barrel temperature setting was used to control the product temperature. A controller for this pairing was designed and simulated.

Kulshreshtha (1991b) developed a dynamic model of the extrusion process and used it to calculate the RGA. Based on this analysis it was concluded that the die temperature should be controlled with the feed moisture content, the die pressure with the feed rate, and the SME with the screw speed. This model was also used to investigate the non-linearity of the process. The gain non-linearity was assessed by measuring the process gain when step changes of different magnitudes were made in the manipulated variables. A moderate gain non-linearity was noted for the process. Non-linearity in the dynamics was assessed by measuring the settling time when both positive and negative step changes in the manipulated variables were made. The settling times were found to be similar in most

cases, except for the screw speed and die pressure pairing. Kulshreshtha concluded that process non-linearities would complicate the control of die pressure with feed moisture content and the control of SME with the screw speed. Alternatively, a model-based set-point adjustment control scheme was simulated for controlling die pressure with feed rate.

In regard to product quality control, the principal problem with food extrusion processes lies in measuring the desired process variables rapidly on-line. Onwulata et al. (1994) performed correlation analysis on experimental data from a cooking extruder and proposed an algorithm for controlling product bulk density using a correlation model to estimate the density from more easily measured process data. Elsey et al. (1997) proposed the use of an adaptive inferential estimation routine allowing slow off-line product quality measurements to be used to update a fast on-line inferential estimator for the PQAs. Haley and Mulvaney (2000) used a model-based predictive control law to regulate SME using screw speed. Here operating set-points were determined using an inferential model that correlated SME with product bulk density and melt moisture content. A ratio control strategy was also used to regulate feed moisture content. Wang et al. (2001) used an inferential control strategy to control product bulk density and product moisture content using the screw speed and water feed rate as the manipulated variables. Experiments were performed to identify a linear correlation model relating the PQAs to 21 measurable process variables including die pressure, various process temperatures, screw speed, feed rate and motor torque. The correlation model was used to infer values of the PQAs in a 2×2 model predictive control loop.

10.4 Process Characteristics

Controller design requires a thorough understanding of the process characteristics in order to select the most suitable manipulated variables and control strategy. This normally involves a thorough experimental investigation into the process dynamics, variable interactions, process non-linearity, and output sensitivity to the manipulated variables. In the present study these experiments will be carried out on the dynamic process model developed in Chapter 6. The following sections discuss the process characteristics from a controller design perspective.

10.4.1 Process Non-Linearity

Linear MPC algorithms require the process being controlled to behave approximately linearly over the controlled range. Non-linear behaviour manifests itself as different process gains and different process dynamics at different operating points. Before linear MPC can be applied to the extrusion cooking process with any confidence, the degree of process non-linearity needs to be assessed.

The extrusion cooking process step response behaviour was assessed at 27 operating

points corresponding to all permutations of screw speed (5, 6.5 and 8 s^{-1}); feed rate (20, 25 and 30 kg/hr); and moisture content (0.15, 0.20 and 0.25 w/w). At each operating point, a step change in each manipulated variable was made, and the steady-state gain and open-loop process settling times were measured.

Table 10.1 lists the minimum and maximum steady-state gain between each manipulated variable and process output over the 27 points in the studied operating range. The percentage variation over the range, calculated according to

$$\Delta\% = \frac{100\,|\max - \min|}{(\max + \min)/2} \tag{10.1}$$

is also listed in the table. A large variation in the gain over the operating range indicates strong gain non-linearity, whereas a small variation indicates approximately linear gain behaviour. It can be seen that the steady-state gains in general are moderately non-linear, with percentage variations up to around 100%, while the gains for bulk density exhibit variations of around 200%, indicating a strong gain non-linearity. This strong non-linearity is a result of the highly non-linear dependence of bulk density on both temperature and moisture fraction, particularly the latter. This can be seen in Figure 10.2, which shows the *reciprocal*[1] of the bulk density versus temperature and moisture fraction. There are two features of importance to note on this surface. Firstly, it can be seen that there is a stationary point with respect to moisture fraction at approximately 0.17 w/w at all temperatures. Clearly the gain $\Delta\rho_B/\Delta M$ changes sign on either side of this stationary point, resulting in strong gain non-linearities and likely control complications. Secondly, it can be seen that at high moisture contents (around 0.30 w/w), and also at low temperatures, the bulk density is nearly insensitive to changes in moisture content. These observations indicate that in order to avoid process control difficulties, the process should not be operated with a moisture fraction close to 0.17 w/w nor an especially high moisture fraction close to 0.30 w/w unless a non-linear controller is specifically designed for this task. Note that these specific values are a function of the parameters used in the bubble growth and puffing model described in Chapter 6. Real processes may exhibit these effects at different specific moisture fraction values.

Table 10.2 shows the minimum and maximum settling times when a small step change is made in each of the manipulated variables over the 27 points in the studied operating range. The settling time here is defined to be the time required for the output variable to reach 95% of its final value after the step change is made. A large variation in the settling times over the operating range indicates a strong non-linearity in the process dynamics. It can be seen that the process dynamics are moderately non-linear for most input-output variable pairings. Again, the bulk density settling times show a large variation, as does the die pressure versus feed rate pairing.

[1] For graphical clarity.

Table 10.1: Variation in steady-state gain over operating range.

	Screw Speed (s^{-1})			*Feed Rate* (kg/s)			*Moisture Fraction* (w/w)		
	min	*max*	$\Delta\%$	*min*	*max*	$\Delta\%$	*min*	*max*	$\Delta\%$
p_{die}(Pa)	-3.9E5	-1.9E5	69	6.6E8	10.0E8	43	-1.1E7	-6.1E6	59
T_{die}(°C)	5.7E0	9.0E0	44	-6.8E3	-3.6E3	61	-3.2E2	-1.9E2	51
$\hat{W}$($J\,m^{-3}$)	4.4E7	8.1E7	55	-8.7E10	-2.7E10	106	-2.9E9	-1.7E9	53
g (w/w)	3.1E-2	7.4E-2	82	-1.3E2	-3.7E1	110	-2.7E0	-1.1E0	85
ρ_B(kg/m^3)	-1.6E2	2.0E-9	200	1.2E-6	8.8E4	200	-2.9E2	5.2E4	202

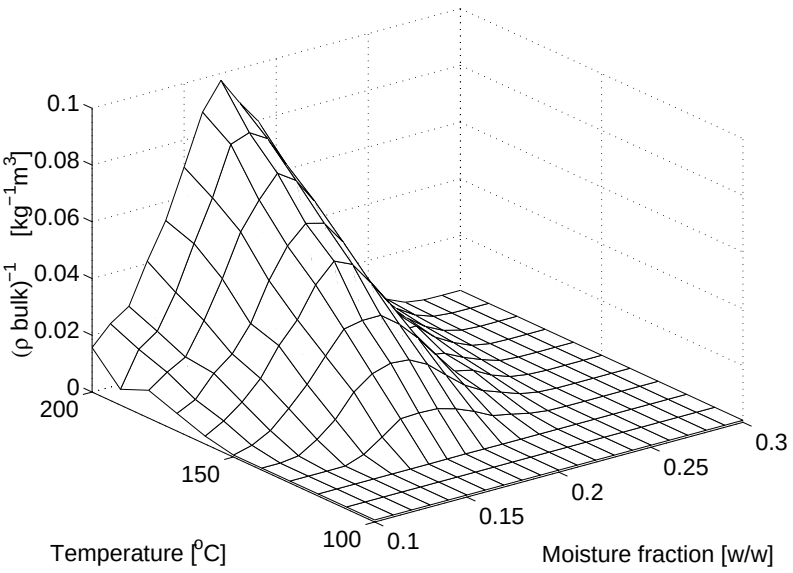

Figure 10.2: Reciprocal bulk density as a function of moisture content and temperature.

Table 10.2: Variation in settling times (in seconds) over operating range.

	Screw Speed			*Feed Rate*			*Moisture Fraction*		
	min	*max*	$\Delta\%$	*min*	*max*	$\Delta\%$	*min*	*max*	$\Delta\%$
p_{die}	220	400	58	25	120	131	40	65	48
T_{die}	370	595	47	315	590	61	350	610	54
$\hat{W}$	20	40	67	20	40	67	35	70	67
g	270	480	56	105	240	78	250	410	48
ρ_B	80	1175	176	315	1155	114	35	235	148

The strong non-linear dynamics of the bulk density responses are due to the insensitivity of bulk density to moisture fraction variations at around 0.30 w/w, as seen in Figure 10.2. With there being negligible change in the bulk density at these points, the settling time required is correspondingly low. However, at lower moisture contents, there are larger changes in the bulk density and the settling times are much greater. This accounts for the large range of observed settling times in product bulk density over the investigated operating range.

It can be concluded that the cooking extrusion process is moderately non-linear provided that the 0.17 w/w lower limit and 0.30 w/w upper limits in moisture fraction are avoided, at which the bulk density dependence on moisture content is highly non-linear. If the process is operated away from these points then a linear control algorithm is expected to provide satisfactory control.

10.4.2 Process Output Sensitivity

A choice has to be made as to which pair of manipulated variables (from the options N, F and M) will be used to control the output variables, die pressure and temperature for the first (indirect) controller, and gelatinisation fraction and bulk density for the second (direct) controller. For MIMO algebraic control loops, the selection of manipulated variables needs to be considered in light of minimising loop interactions, which may be diagnosed using the RGA method. The inherent decoupling property of the MPC algorithm used here, however, allows highly interactive processes to be controlled with ease, so minimising variable interactions is not a primary concern in the choice of manipulated variables in this study. Instead, the two manipulated variables that permit the greatest range of variation in the controlled output variables will be chosen.

Table 10.3 shows, for each possible pair of manipulated variables, the minimum and maximum values reached in the output variables over the studied operating range. The total change in the outputs (Δ) is also listed. It can be seen, in general, that a similar range of output values is spanned by all pairing combinations. Seeing that there is no great advantage in choosing one particular pairing over another, the N-M pairing was chosen for practical reasons, as it leaves the feed rate variable free to be maximised or fixed at a constant desired throughput.

10.4.3 Scaling Issues

It is necessary to scale the raw process data so that each variable is given a similar weighting in the MPC algorithm (see Section 10.5). If $\mathbf{K}$ is the steady-state gain matrix between the input and output vectors then the scaled gain matrix $\mathbf{K}'$ can be written

$$\mathbf{K}' = \mathbf{S}_y \mathbf{K} \mathbf{S}_u^{-1} \tag{10.2}$$

Table 10.3: Variation in outputs over studied operating range for different manipulated variable pairings.

	$F-M$			$N-M$			$N-F$		
	min	*max*	Δ	*min*	*max*	Δ	*min*	*max*	Δ
p_{die}	1.2E7	8.8E6	3.1E6	1.2E7	1.0E7	1.5E6	1.2E7	8.9E6	2.9E6
T_{die}	2.0E2	1.6E2	3.5E1	2.0E2	1.5E2	4.6E1	1.9E2	1.6E2	3.1E1
$\hat{W}$	9.7E8	6.7E8	3.0E8	9.5E8	5.9E8	3.6E8	9.4E8	6.8E8	2.7E8
g	5.9E-1	1.9E-1	4.1E-1	4.3E-1	1.5E-1	2.9E-1	5.5E-1	2.0E-1	3.5E-1
ρ_B	2.9E2	1.5E1	2.8E2	5.0E2	1.5E1	4.8E2	3.1E1	1.8E1	1.3E1

where $\mathbf{S}_u$ and $\mathbf{S}_y$ are diagonal scaling matrices having real positive entries corresponding to the plant inputs and outputs, respectively, and $\mathbf{S}_y\mathbf{K}\mathbf{S}_u^{-1}$ is the gain matrix corresponding physically to another choice of units for the plant inputs and outputs. The prime symbol ($'$) is used here to signify a scaled variable. It is advantageous to choose scaling matrices that result in a well-conditioned gain matrix $\mathbf{K}'$. An ill-conditioned gain matrix, indicated by a high condition number[2], is symptomatic of a system with strong directionality, meaning that the responses of the plant outputs depend strongly on how the inputs interact with each other. To minimise the directionality as much as possible, $\mathbf{S}_u$ and $\mathbf{S}_y$ are chosen to minimise the condition number of $\mathbf{K}'$.

10.4.4 System Identification

The linear MPC algorithm requires a causal linear time invariant process model that describes the transient effect of each of the manipulated variables on each of the controlled output variables. The model, expressed in terms of deviation variables around some chosen operating point, does not in practice need to be exceptionally accurate, as modelling errors are corrected in the control feedback loop. On a real process the controller model can be identified by performing step changes in each of the manipulated variables and recording the effect on each of the controlled output variables. A linear transfer function can then be fitted to the data, using the techniques described in Ljung (1987). In this study, the dynamic process model developed in Chapter 6 was used to generate step response data for model fitting. The MATLAB (Mathworks, 1998) software routine `arx` from the System Identification Toolbox was used to perform the identification and the resulting transfer

[2]The condition number of a matrix $\mathbf{A}$ is defined by

$$\text{cond}(\mathbf{A}) = ||\mathbf{A}||_\infty ||\mathbf{A}^{-1}||_\infty$$

where the infinity norm of a matrix $\mathbf{x}$ is defined by

$$||\mathbf{x}||_\infty = \max_{i = 1, 2, \ldots, n} |x_i|.$$

Table 10.4: Process transfer functions and scaling matrices, for the manipulated variables N and M.

	P_{die} and T_{die}	g and ρ_B
$\mathbf{G}(s)$	$\begin{bmatrix} \frac{-2.52\times10^5(0.296s+1)(-16.2s+1)}{(4.17s+1)^2(16.9s+1)} & \frac{-8.65\times10^6(17.5s+1)}{(39.1663s+1)^2} \\ \frac{6.99(8.28s+1)}{(31.4s+1)(127s+1)} & \frac{-239(-2.80s+1)}{(140s+1)^2} \end{bmatrix}$	$\begin{bmatrix} \frac{0.0521(-21.3s+1)}{(8.36s+1)(52.1s+1)} & \frac{-2.24(-5.88s+1)}{(70.9s+1)^2} \\ \frac{-2.22(8.22s+1)}{(31.0s+1)(127s+1)} & \frac{979.6258(-2.5876s+1)}{(52.0s+1)^2} \end{bmatrix}$
$\mathbf{S}_u^{-1}$	$\begin{bmatrix} 1.00 & 0 \\ 0 & 2.92\times10^{-2} \end{bmatrix}$	$\begin{bmatrix} 1.00 & 0 \\ 0 & 7.20\times10^{-3} \end{bmatrix}$
$\mathbf{S}_y$	$\begin{bmatrix} 3.97\times10^{-6} & 0 \\ 0 & 0.144 \end{bmatrix}$	$\begin{bmatrix} 19.19 & 0 \\ 0 & 0.141 \end{bmatrix}$
$\mathbf{K}'$	$\begin{bmatrix} -1 & -1.003 \\ 1.003 & -1 \end{bmatrix}$	$\begin{bmatrix} 1 & -0.31 \\ -0.31 & 1 \end{bmatrix}$

functions are listed in Table 10.4. A sampling interval of 5 seconds was used for the process. The process dead time was generally less than 5 seconds and could thus be ignored for control purposes.

10.5 Model Predictive Control

MPC uses a model of the process to calculate the future changes in the manipulated variables that will minimise some performance index. A variety of different MPC methods are in popular use, such as Dynamic Matrix Control (Cutler and Ramaker, 1979), Unified Predictive Control (Soeterboek, 1992), and Generalised Predictive Control (Clarke et al., 1987). In the present study, a MPC formulation known as Global Predictive Control (Desbiens et al., 2000), based on the internal model control scheme shown in Figure 10.3, is used. The observer model contains a discrete state-space representation of the extruder transfer functions listed in Table 10.4. The controller uses a separate model to make predictions about the future state of the process. This model is the same as the observer model, but with the unstable and oscillatory zeros removed.

The set-point tracking and disturbance rejection dynamics are obtained by minimising the quadratic cost function

$$J = \sum_{i=1}^{N_y}\sum_{j=1}^{H_p} W_{y_{ij}}\left[\hat{y}'_i(t+j) - r_i(t+j)\right]^2 + \sum_{k=1}^{N_u}\sum_{j=0}^{H_c-1} W_{u_{kj}}\left[u'_k(t+j) - u'_k(t+j-1)\right]^2 \tag{10.3}$$

subject to the constraint

$$u'_{\min} \le u' \le u'_{\max} \tag{10.4}$$

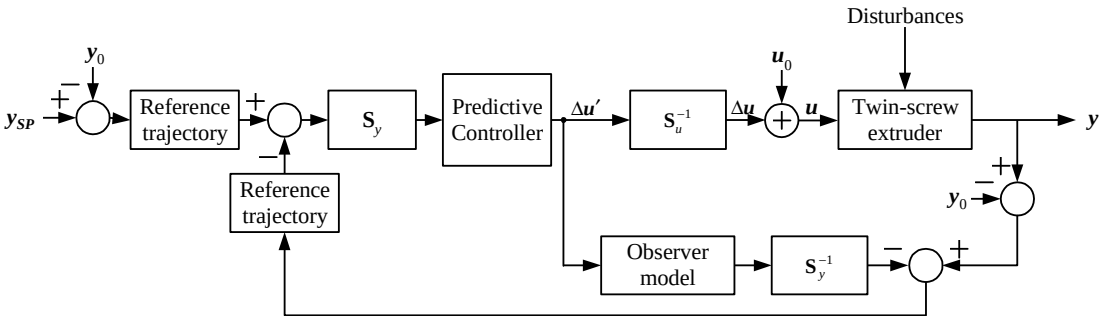

Figure 10.3: MPC structure.

where t is the time index, N_y the number of controlled variables, N_u the number of manipulated variables, i the process output index, k the manipulated variable index, H_p the prediction horizon (the number of time steps into the future over which the control performance is to be optimised), H_c the control horizon (the number of time steps into the future over which control actions are taken), r_i are the reference trajectories (the desired trajectories of the output variables), $\hat{y}'$ the scaled controller model outputs, u' the scaled manipulated variables, $\mathbf{W}_y$ the weighting matrix for the deviations between the outputs and the reference trajectories, and $\mathbf{W}_u$ the weighting matrix on the magnitude of the control actions. Inequality constraint Equation 10.4 is required to account for the physical limitations of the actuators.

10.5.1 MPC Controller Tuning

The tuning guidelines outlined in Desbiens et al. (2000) are followed here. The reference trajectories r_i define the desired paths to be tracked by the process outputs. When a set-point change or a disturbance related offset correction is required, a step change reference trajectory can result in abrupt changes in the control action, so it is better in practice to smooth the requested reference trajectory. Their guidelines recommend filtering the required step change through a double pole second-order filter (i.e. one exhibiting a critically damped response) having a similar settling time to the actual process. Consequently, for the present case, such filters having settling times of 100 seconds were used in all control loops.

The scaling matrices $\mathbf{S}_y$ and $\mathbf{S}_u$ effectively normalise the plant data, so the weighting matrices $\mathbf{W}_y$ and $\mathbf{W}_u$ can be used to fine-tune the controller response. A conservative tuning for $\mathbf{W}_y$ is to use a diagonal matrix whose entries are the squared inverse of the accepted deviations between $\hat{y}'(t)$ and $r(t)$. Similarly, for $\mathbf{W}_u$, a diagonal matrix of the squared inverse of an acceptable average variation in the control action amplitudes is used.

The prediction horizon H_p specifies how far into the future the process response to any control actions is considered. A prediction horizon close to the dominant time response

of the process is suitable. Here a value of $H_p = 120$ (600 seconds) was used. The control horizon H_c ($H_c \leq H_p$) specifies the number of future control action steps to be considered in the optimisation, with no additional control action taken after time $t + H_c - 1$ up to $t + H_p$. A value of $H_c = 50$ (250 seconds) was used in this study.

10.6 Results

In this section the results of three simulations are presented with the objective being to observe how well the process PQAs are maintained as a result of these different control strategies. The first simulation considers the open-loop response of the extruder to simulated disturbances to observe the effect of taking no control action. The second example considers the regulatory control of die pressure and die temperature using the screw speed and moisture content as manipulated variables. The third strategy considers the regulatory control of the PQAs gelatinisation fraction and product bulk density directly again using the screw speed and moisture content as manipulated variables. The same disturbances, described below, are introduced into the system in all simulations.

Figure 10.4 shows the open-loop response of the cooking extruder to the simulated disturbances. At time 1000 seconds, the consistency index parameter in the power-law rheology model is increased by 10%, a disturbance akin to a change of feed material. At time 2000 seconds, the screw tip diameter R_s is reduced by 1%, an abrupt and perhaps overly extreme simulation of screw wear. At time 3000 seconds, the moisture content of the feed material is increased by 1% on a total weight basis, a disturbance analogous to storing the feed stock under different humidity conditions. Each disturbance, once introduced, persists until time 4000 seconds, when all disturbed variables are returned to their original values.

Figure 10.5 shows the closed-loop response to the same simulated disturbances when die pressure and die temperature are the controlled variables. It can be seen that despite the die pressure and die temperature set-points being maintained effectively, the PQAs vary significantly, even more so than for the uncontrolled disturbances. This is perhaps not such an unexpected result, as the extrusion process is known to be highly interactive. Regulatory control of one variable, therefore, would not be expected to improve regulation of another variable unless the two were highly correlated, which is clearly not the case here.

Figure 10.6 shows the closed-loop response to the same simulated disturbances when gelatinisation fraction and product bulk density are the controlled variables. It can be seen that the controller successfully maintains close to constant gelatinisation and bulk density, despite the disturbances. The manipulated variables, shown in the bottom two plots, vary smoothly when rejecting these disturbances, indicating a good controller tuning that does not produce high frequency actuator responses. The same controller can be used

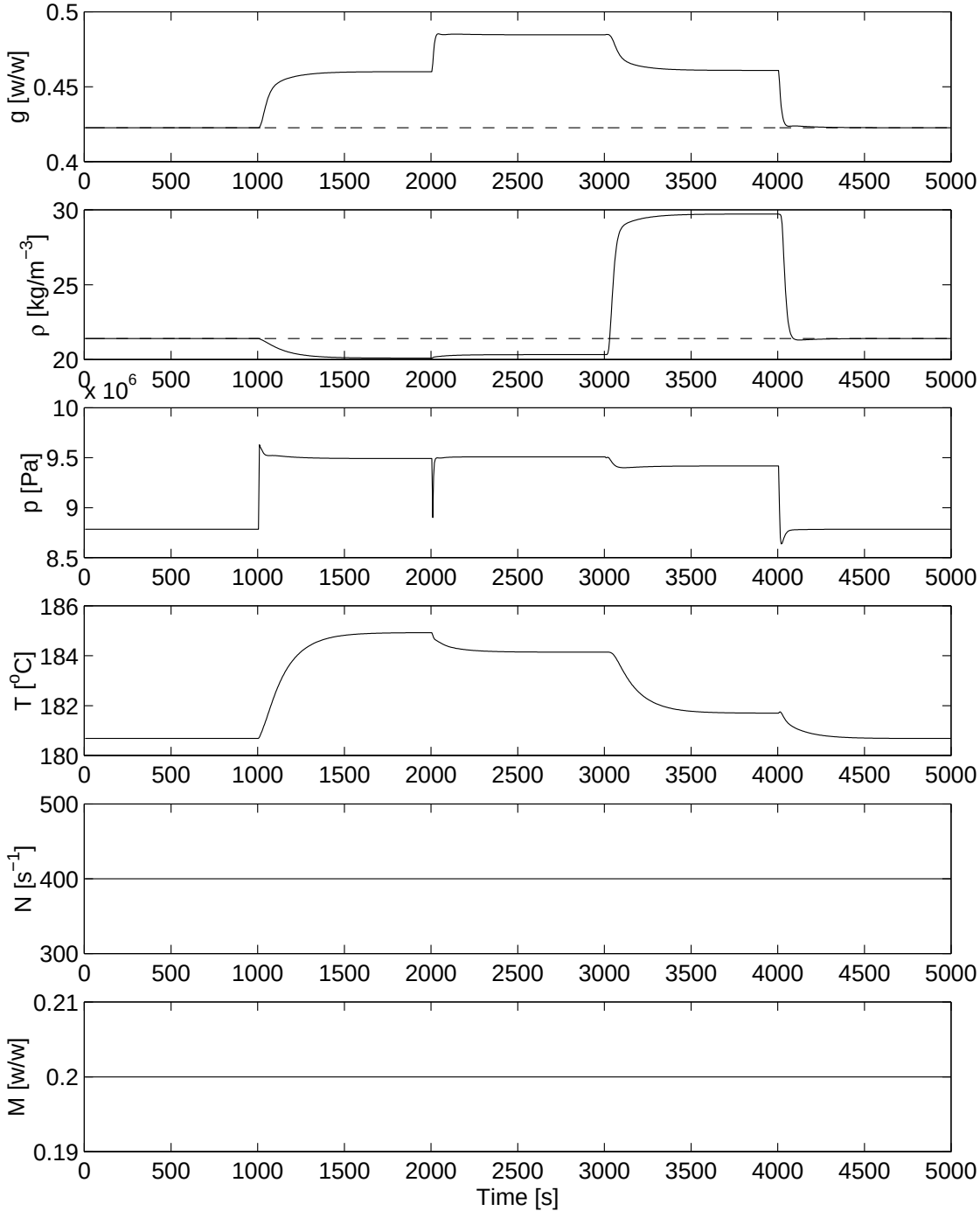

Figure 10.4: Open-loop response to simulated disturbances.

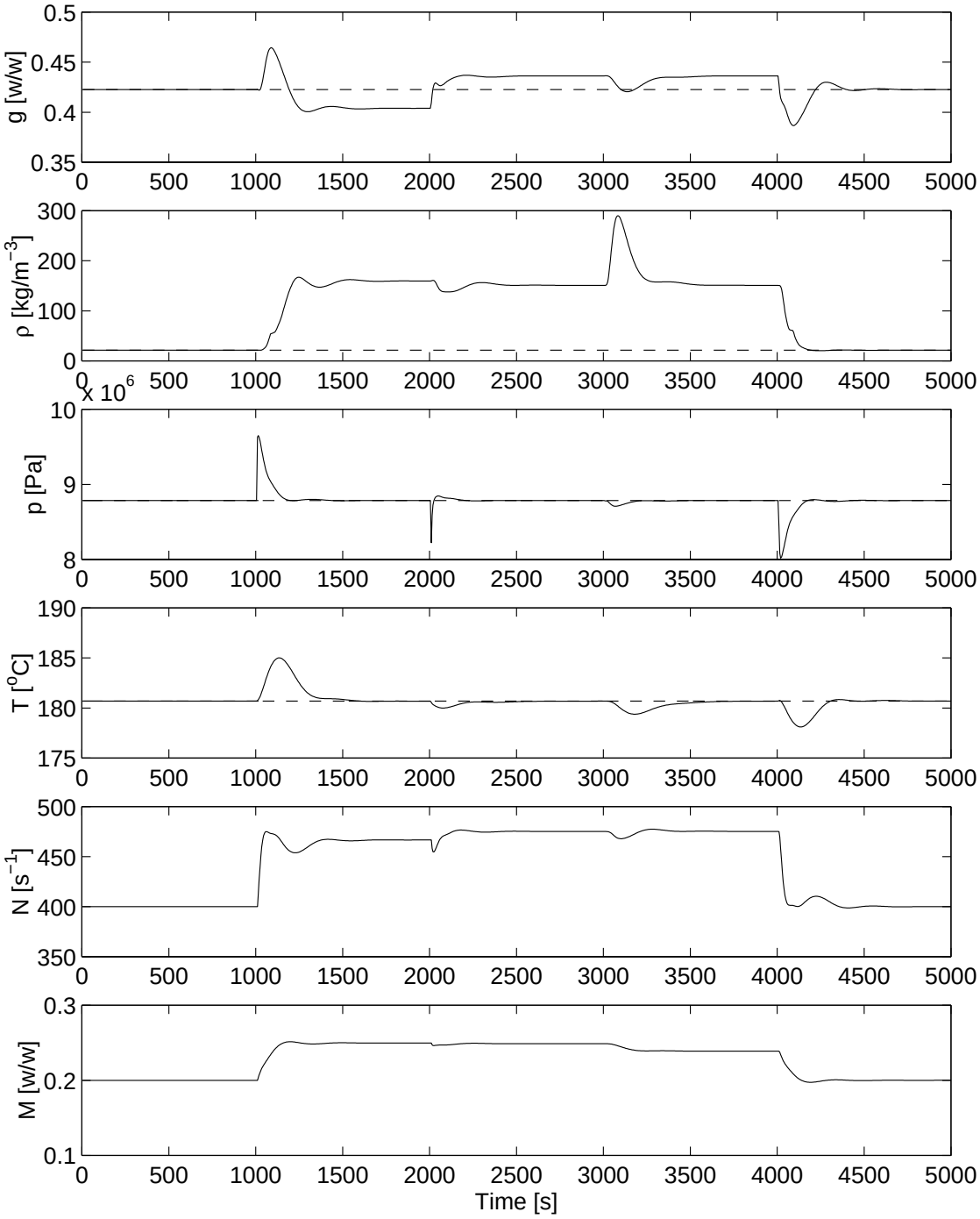

Figure 10.5: Closed-loop response to simulated disturbances when die pressure and die temperature are the controlled variables.

for set-point tracking (i.e. servo control), as shown in Figure 10.7. Again, good control performance is observed, and the settling times are in the order of 100 seconds, as specified in the controller design.

10.7 Conclusions

In this chapter both direct and indirect control strategies for regulating the product quality attributes (PQAs) of an extrusion cooking process were compared. The indirect controller was designed to regulate the die pressure and temperature, while the direct controller was designed to regulate the two PQAs product gelatinisation and bulk density. Both controllers were designed using a model predictive control approach with the screw speed and moisture feed rate being the manipulated variables. It was found that the indirect controller caused larger variations in the PQAs than taking no control action at all. On the other hand, good regulation of the PQAs could be achieved by controlling them directly. Physically realising such a controller would require the implementation of on-line product quality sensors or inferential estimators to provide feedback values of the PQAs. There is sufficient reporting in the literature and Chapter 9 to suggest that this is achievable.

This study also highlights the value of a detailed dynamic process model for rapidly evaluating the effect of various process disturbances and comparing alternative control strategies. Although the conclusions reached here are based on simulation results only, it would serve industrial extruder users well to review control strategies that do not control the PQAs of interest directly.

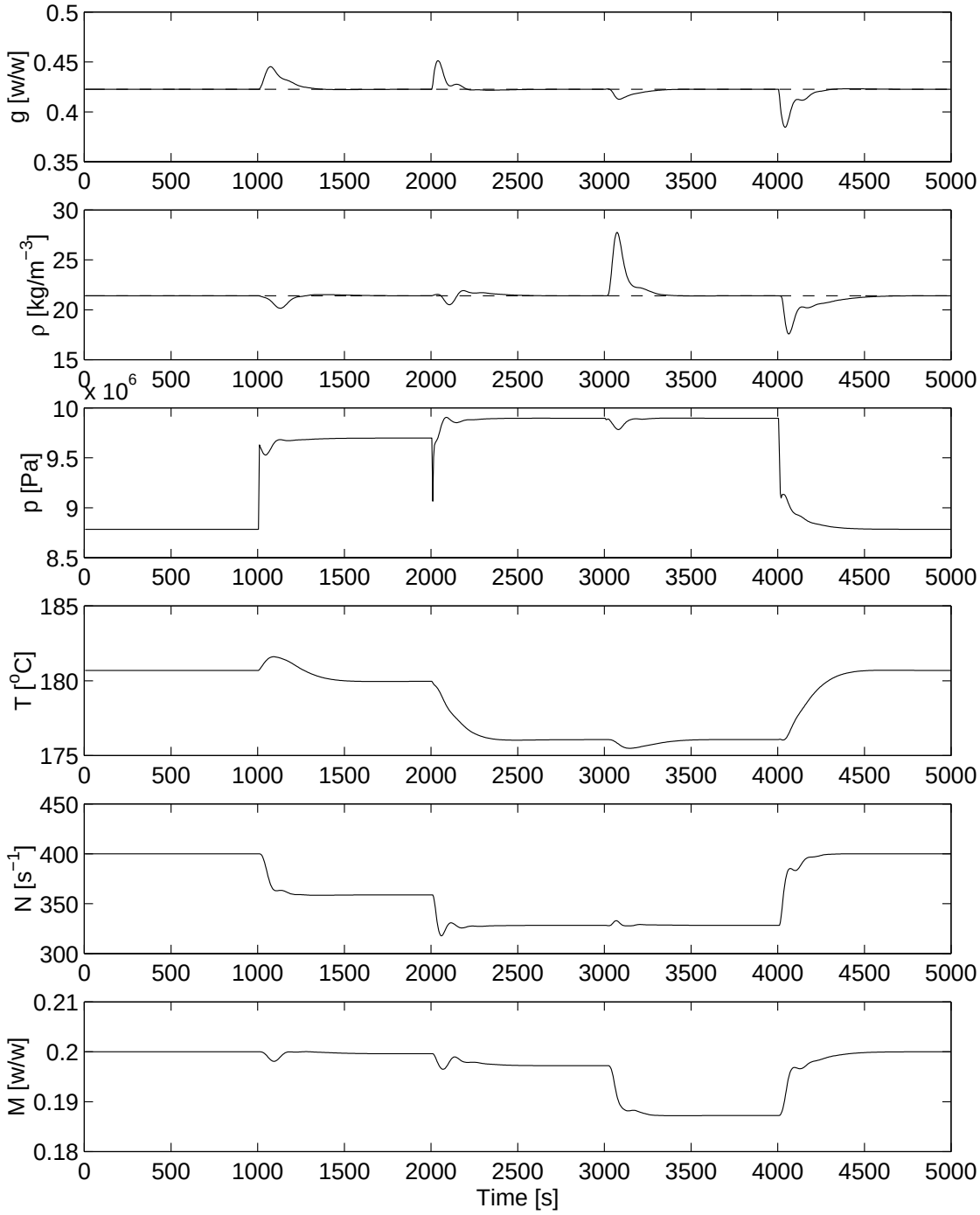

Figure 10.6: Closed-loop response to simulated disturbances when gelatinisation fraction and product bulk density are the controlled variables.

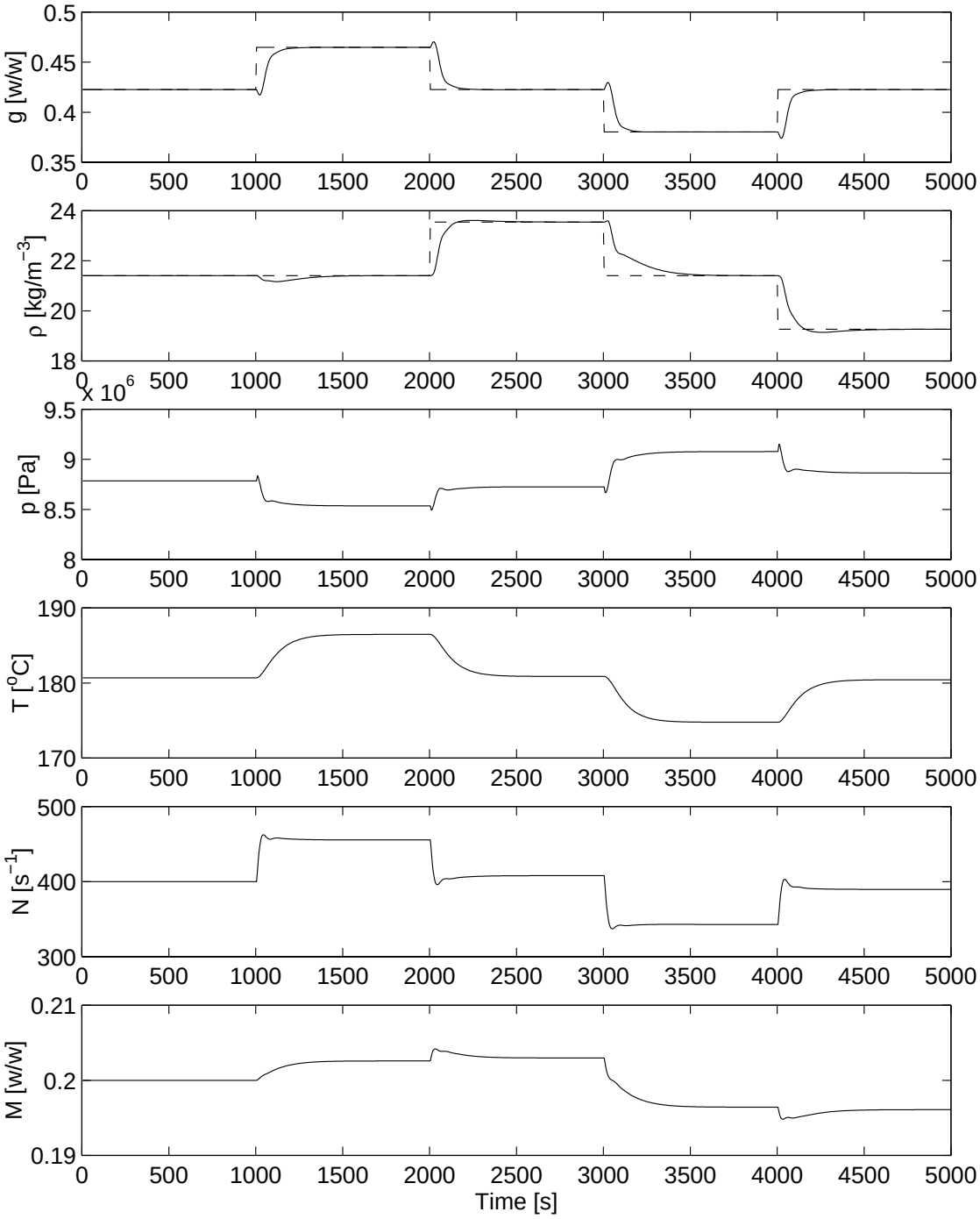

Figure 10.7: Closed-loop response for set-point tracking when gelatinisation fraction and product bulk density are the controlled variables.

Chapter 11

Conclusions

This thesis has been primarily concerned with improving the productivity and utilisation of co-rotating twin-screw extruders. Recognising that productivity gains in mature processes are typically gained though better process understanding and process control, this thesis has sought to develop a dynamic model of the co-rotating twin-screw extrusion process, to develop a product quality sensor suitable for feedback control, and to evaluate the performance of direct and indirect control strategies on the regulatory control of product quality attributes.

In regard to the dynamic modelling aspect of this thesis, it is noted that extrusion process models must make a trade-off between accuracy and computational expedience, as the exact representation of material and heat transport in a complete extruder is beyond present practical computing ability. Recognising that the accuracy of an extrusion process model is limited by the accuracy of the individual material transport models which constitute it, this thesis has undertaken to determine which fluid transport models offer the best accuracy for their computational effort for each common screw type.

This involved the development of a new fluid transport model for threaded screw types, whereby the screws' flow volume is divided for analysis along the natural flow bottlenecks and screw boundaries into a repeating sequence of six elements. To expedite the calculation of the flows in the screw channel and leakage gaps, a computationally efficient method for calculating the flow rate of non-Newtonian fluids through conduits of arbitrary shape was devised. The prediction capability of the resulting model was accurate to within 10% of a full 3D finite volume solution of the flow equations in the screws. A similar investigation into kneading discs determined that a flow analysis network (FAN) approach consisting of a single layer of elements extending in the rotation direction of the kneading discs could provide a computationally inexpensive and reasonably accurate estimate of the flow rate in such disc sections. Similar flow models for orifice discs and circular dies were also described.

In the past, the most serious challenge facing dynamic model development has been the problems associated with the moving interface between the partially filled and fully

filled sections of the extruder. All dynamic modelling approaches prior to this thesis have required the flow domain to be re-meshed after every time step in order to determine the new pressure distribution in the extruder. This is not only computationally expensive, but also tends to require a homogeneous 1D representation of the extruder which ignores local screw features and is therefore inherently unrealistic. The approach proposed here suggests using a fixed model grid and assuming a slight compressibility for the process material. This allows the local pressure in each model element to be calculated from the degree of over-fill using an equation of state, such as the material's bulk modulus of elasticity relationship. This allows the dynamic mass balance over each model element to be written in terms of the fill fraction only. Using this approach, the mass and energy balances over each model element have a simple form which can be solved in a straightforward manner using a stiff ordinary differential equation solver.

The resulting dynamic model can simulate dynamic step changes in a complete twin-screw extruder in approximately 30 seconds on a 600 MHz Pentium 3 personal computer. In addition to its obvious applications as a dynamic predictor, the presently developed process model is also expected to be of use as a steady-state predictor due to its low computational overhead, demonstrated accuracy and validated constituent transport models.

A related issue addressed by this thesis concerns the direct measurement of bubble size distributions in puffed extruded products using a digital image processing technique. Such measurements would be useful, for example, in calibrating puffing models to real-world data. The major challenges with this task lay in discriminating between the regions of the image corresponding to a bubble edge and those corresponding to a bubble cavity, and also in determining the size of individual bubbles which may be connected to others by small breaks in their walls. The first problem was overcome by using a mean filtering technique and the second by using an algorithm which "grows polygons" in potential bubbles to measure their areas. It was found that the distribution of the total void volume over the range of bubble diameters was fitted well by a normal distribution. A direct computer simulation based on simple models for bubble nucleation, growth and coalescence in a puffing medium also produced distributions that were fitted very well by normal distributions, suggesting that normal bubble size distributions on a volumetric basis may be characteristic of the puffing process. It is anticipated that this image analysis technique might be a useful tool in industry, as it offers the ability to rapidly measure a material property which is known to have an impact on product quality.

In regard to on-line product quality estimation, it is noted that process control of extruders is presently limited by the availability of fast, cheap and reliable product quality feedback sensors. Aural observations indicate that the extrudate makes different sounds as it leaves the extruder which appear to be correlated with the extent of puffing of the product. This led to the development of an acoustic estimator for product bulk density and hardness based on non-linear regression models between the experimentally measured

product characteristics and the principal components of the acoustic power spectrum. The non-linear models were developed using both genetic programming based symbolic regression and neural network based regression approaches, with the latter giving better correlations in a shorter time-frame. The resulting models performed well on unseen process data. Because of the low-cost and accuracy of this approach, it may prove useful in industrial applications. The drawback of the method is that it requires calibration to experimental data, so applying it to new products would require a reasonably involved experimental program and non-linear regression exercise.

The final investigation performed in this thesis compared direct and indirect control strategies for regulating the product quality attributes of an extrusion cooking process. It was found that indirect control, which aims to achieve consistency in the product quality attributes by regulating readily measured process variables such as die temperature and pressure, may in fact be worse than taking no control action at all in some situations. This is not overly surprising, as the regulatory control of one variable would not be expected to improve control over another unless they are significantly correlated. While this conclusion was reached based on a simulation study using the dynamic model developed herein, it may serve as a warning to industrial extruder users to consider this potential effect before implementing, or continuing to use, indirect control techniques.

In conclusion, it is anticipated that the dynamic modelling, measurement and sensing tools demonstrated here will be of use in improving the productivity of extrusion processes through better process understanding, computer aided process design and optimisation, product quality measurement and estimation suitable for feedback control, and off-line controller design and simulation.

Notation

Symbol	*Description*	*Units*
Roman uppercase		
A_b	Bubble area in cross-sectional image (Chapter 7)	m^2
A_{BX}	The cross-sectional area of a figure-eight shaped barrel bore	m^2
A_c	Conduit cross-sectional area	m^2
A_S	Total screw surface area	m^2
A_{SX}	The cross-sectional area of a screw	m^2
A_{cyl}	The area of a helical strip in deriving screw surface area (Chapter 2)	m^2
A_{flank}	The surface generated by one flank curve	m^2
A_k	The area of barrel surface in contact with flow network element k	m^2
A_w	The area of wall in contact with the melt	m^2
A	Constant (Chapter 3)	(–)
B	Constant (Chapter 3)	(–)
C	Concentration	w/w
C	Constant (Chapter 3)	(–)
C_1	Integration constant	s^{-1}
C_2	Integration constant	m/s
C_L	The distance between the screw axes	m
C_{p_m}	Heat capacity of the metal comprising the screws	$J\,kg^{-1}\,K^{-1}$
C_x	Grouped term	$m^{-1}\,s^{-1}$
C_y	Grouped term	$m^{-1}\,s^{-1}$
C_z	Grouped term	$m^{-1}\,s^{-1}$
D	True diameter of sphere (Chapter 7)	m
D	Constant (Chapter 3)	m/s
$\mathbf{E}$	The score matrix (Chapter 9)	(–)
E	Grouped term (Chapter 3)	m^2/s
E	Activation energy	J/kg-mol

Symbol	*Description*	*Units*
E_0	Activation energy in starch gelatinisation model	J/kg-mol
E_c	Coefficient in nucleation model (Chapter 8)	(–)
E_v	The bulk modulus of elasticity	$\mathrm{N/m^2}$
$E(t)$	The residence time distribution	(–)
$E(x, y)$	Binary edge map image	(–)
F	Grouped term (Chapter 3)	m/s
F	Feed rate to the extruder	kg/s
$\hat{\dot{F}}$	The irreversible specific rate of conversion of mechanical energy into heat energy due to friction between solids	$\mathrm{J\,s^{-1}\,m^{-3}}$
F_F	Fracture force	N
F_s	Coefficient of friction	(–)
$F_p(a, b)$	Function arising from the solution of flow in a rectangular conduit	$\mathrm{m^4}$
F_r	The ratio of the entire kneading disc flow cross-section to that of a single kneading disc chamber	(–)
$G_c(r)$	The screw channel width at a radial distance r from the screw axis	m
G_n	Calendar gap width	m
$G_s(x)$	The width of the side gap as a function of the distance x along the screw tip	m
$\mathbf{G}(s)$	Continuous transfer function matrix	(–)
$G_t(x)$	The width of the tetrahedron gap as a function of distance	m
$H^{(X,Y)}$	Average height in FAN element (X, Y)	m
H_c	Control horizon for model predictive controller	s
H_p	Prediction horizon for model predictive controller	s
$H(p, D)$	Probability that the observed diameter is less than a given diameter p in a slice through a sphere of diameter D (Chapter 7)	(–)
$I(x, y)$	Grayscale image	(–)
J	Model predictive control cost function	(–)
J_0	Grouped unknown terms in bubble nucleation model	$\mathrm{s^{-1}}$
J_N	Steady-state homogeneous nucleation rate in expanding viscoelastic media	$\mathrm{s^{-1}}$
$\mathbf{K}$	The steady-state gain matrix between the input and output vectors	(–)
$\mathbf{K}'$	The scaled gain matrix between the input and output vectors	(–)
K	Consistency index of the power-law rheology model	$\mathrm{Pa\,s^n}$

Symbol	*Description*	*Units*
K_B	Bubble growth rate constant	m/s
L	Characteristic length of fluid sytem	m
L_d	The length of the die	m
L_m	The thickness of the melt layer in the clearance gap between the screw flight and the barrel	m
L_p	Screw pitch length; disc thickness	m
L_x	Flight gap width; orifice gap width	m
L_y	Flight gap length; orifice disc gap length	m
M	Moisture fraction	w/w
M_0	Reference moisture fraction	w/w
M_0	The inherent moisture content of the feed material (Chapter 10)	w/w
M_e	Mass of material in the control volume	kg
$M_k(x, y)$	Mean filtered and thresholded binary image	(–)
N	Screw rotation rate	s^{-1}
N_0	Initial concentration of dissolved gas (Chapter 8)	w/w
N_B	Number of frequency bins in the acoustic power spectrum	(–)
N_S	Number of sound samples	(–)
N_Z	Number of elements in the z-direction of the 3D flow model grid	(–)
N_g	Dissolved gas concentration	w/w
N_p	Number of polygon sides (Chapter 7)	(–)
N_s	The number of nucleation sites per unit mass of extrudate	kg^{-1}
N_u	Number of manipulated variables	(–)
N_y	Number of controlled variables	(–)
$O(\cdot)$	Order of computational complexity	(–)
$\mathbf{P}$	Vector containing all the pressures in the FAN flow grid	Pa
$P(x)$	Frequency distribution function (Chapter 7)	(–)
P_B	Barrel perimeter	m
P_{RMS}	The root mean square power of the sound signal	(–)
Q	Volumetric flow rate	m^3/s
Q^+	Component of the flow rate in the forward direction	m^3/s
Q^-	Component of the flow rate in the reverse direction	m^3/s
Q_c	Flow rate in the screw channel	m^3/s
Q_d	Flow rate through the circular die	m^3/s
Q^{drag}	Drag induced flow rate	m^3/s
Q_f	Flow rate across the screw flights in the annular region between the flight tip and the barrel wall	m^3/s

Symbol	*Description*	*Units*
Q_m	Flow rate in the kneading disc section	m^3/s
Q_n	Flow rate through the calender gap between the tip of one screw and the root of the other	m^3/s
Q_o	Flow rate past a pair of orifice discs	m^3/s
Q_p	Flow rate from the positive displacement action of the screw	m^3/s
$Q^{pressure}$	Pressure induced flow rate	m^3/s
Q_s	Flow rate through the side gap between the tip edge of one screw flight and the flank of another	m^3/s
Q_t	Flow rate through the tetrahedron gap between adjacent screw channels	m^3/s
Q_x	Flow rate in the x-direction	m^3/s
Q_y	Flow rate in the y-direction	m^3/s
Q_z	Flow rate in the z-direction	m^3/s
$\mathbf{R}$	Ideal gas constant	$J\,kg\text{-}mol^{-1}\,K^{-1}$
R	Bubble radius (Chapter 7)	m
R_B	The barrel bore radius	m
R_P	The popping rate	s^{-1}
$R_D(\theta)$	Kneading disc radius as a function of angle θ about the screw axis	m
R_d	Die aperture radius	m
R_r	The radius of the screw root	m
R_s	The radius of the screw tip	m
$S(X,Y)$	Function in FAN model in element (X,Y)	$m^4\,Pa^{-1}\,s^{-1}$
$\mathbf{S}_u$	Diagonal scaling matrix of the inputs	(–)
$\mathbf{S}_y$	Diagonal scaling matrix of the outputs	(–)
T	Grouped term (Chapter 3)	Pa/m
T	Temperature	K
T_B	The axial temperature of the barrel surface	K
T_C	Temperature in Celsius	°C
T_K	Temperature in Kelvin	K
T_{K0}	Reference temperature	K
T_{die}	Die temperature	K
T_m	Initial temperature of the melt	K
T_s	Sampling interval	s
T_w	Wall surface temperature	K
T_0	Initial temperature of puffing media in puffing model (Chapter 8)	K

Symbol	*Description*	*Units*
U	Characteristic velocity of fluid sytem	m/s
$\hat{\dot{U}}$	The specific rate of conversion of mechanical energy into heat energy	$\mathrm{J\,s^{-1}\,m^{-3}}$
U_y	Barrel wall velocity	m/s
$\mathbf{V}$	The loading matrix (Chapter 9)	(–)
V	Volume of model element	$\mathrm{m^3}$
V	Total volume of steam evaporated (Chapter 8)	$\mathrm{m^3}$
V_S	The volume of the screw element	$\mathrm{m^3}$
V_d	The volume of the die cavity	$\mathrm{m^3}$
V_m	The volume of metal comprising the die block	$\mathrm{m^3}$
V_{m_k}	The volume of screw metal associated with element k	$\mathrm{m^3}$
V_s	Specific volume of steam at temperature T_0 (Chapter 8)	$\mathrm{m^3/kg}$
V_t	Total void volume if all moisture present in the control volume is evaporated	$\mathrm{m^3}$
$\hat{W}$	The specific mechanical energy input to the process material	$\mathrm{J/m^3}$
$\hat{W}_0$	Reference specific mechanical energy	$\mathrm{J/m^3}$
W_c	Critical work of bubble formation	J
$\mathbf{W}_u$	The weighting matrix on the magnitude of the control actions	(–)
$\mathbf{W}_y$	The weighting matrix for the deviations between the outputs and the reference trajectories	(–)
$\mathbf{X}$	The observations matrix (Chapter 9)	(–)
X	Mesh index in x-direction	(–)
$X(r)$	Helicity, $X(r) = \sqrt{1 + (r\varphi')^2}$ (Chapter 3)	(–)
Y	Mesh index in y-direction	(–)
Z	Mesh index in z-direction	(–)

Roman lowercase

$a(x)$	Conduit width in negative direction	m
$b(x)$	Conduit width in positive direction	m
d	Equivalent circular diameter of a bubble cavity (Chapter 7)	m
d_i	Distance of barrel temperature controlled zone i from the die ($i = 1, 2, \ldots, 9$ for the extruder used in the case studies)	m
$d(r)$	Screw flight thickness at a radius r from the axis	m

Symbol	*Description*	*Units*
$\vec{e}_r$	Unit vector in the r-direction of the helical coordinate system	(–)
$\vec{e}_\theta$	Unit vector in the θ-direction of the helical coordinate system	(–)
$\vec{e}_l$	Unit vector in the l-direction of the helical coordinate system	(–)
f	The fill fraction of a model element	(–)
$f(x)$	The true bubble size distribution in a material (Chapter 7)	(–)
g	The fraction of gelatinised starch	w/w
$g(s)$	The observed bubble size distribution in a slice through a material (Chapter 7)	(–)
g_s	The clearance gap between a self-wiping screw pair	m
h	The overall heat transfer coefficient between the process material and the barrel wall	$\mathrm{W\,m^{-2}\,K^{-1}}$
h_t	The heat transfer coefficient between the barrel and the stagnant melt layer	$\mathrm{W\,m^{-2}\,K^{-1}}$
h_k	The k-by-k two-dimensional averaging filter (Chapter 7)	(–)
$h(p, D)$	Probability density function, the derivative of the cumulative distribution function $H(p, D)$ (Chapter 7)	(–)
i	Integer index	(–)
$\vec{i}$	Cartesian x-direction unit vector	(–)
j	Integer index	(–)
$\vec{j}$	Cartesian y-direction unit vector	(–)
k	Integer index	(–)
$\vec{k}$	Cartesian z-direction unit vector	(–)
k_B	Boltzmann's constant	J/K
k_g	The gelatinisation rate constant	$\mathrm{s^{-1}}$
k_0	The Arrhenius pre-exponential factor	$\mathrm{s^{-1}}$
k_t	Grouped unknown terms in bubble nucleation model	$\mathrm{K^{-1}}$
k_v	Constant relating steam formation to temperature change	$\mathrm{K/m^3}$
l	Down-channel helical coordinate	m
m	Fraction multiplier indicating contribution to drag transport for a particular feed solid.	(–)
m_g	The mass of a gas molecule (Chapter 8)	kg
n	Pseudoplastic index of the power-law rheology model	(–)
n_p	The number of sample points in the sound signal being analysed	(–)

Symbol	*Description*	*Units*
n_t	The number of screw tips	(–)
p	Pressure	Pa
p_b	The pressure inside a bubble (Chapter 8)	Pa
p_{die}	Die pressure	Pa
p_m	The pressure of the melt (Chapter 8)	Pa
p_o	Observed diameter of a sphere (Chapter 7)	m
q	Volumetric flow rate in FAN element	m^3/s
$\dot{q}$	The rate of heat transfer	W
r	Radial coordinate	m
r_b	Bubble radius	m
r_i	Reference trajectory for controlled output i (Chapter 10)	(–)
s_i	Centres of the frequency histogram of the observed diameters (Chapter 7)	m
t	Time	s
t_f	The screw flight tip width	m
u'	Scaled manipulated variables (Chapter 10)	(–)
$\mathbf{v}$	Velocity vector	m/s
$v(x)$	Volume weighted bubble diameter distribution	(–)
$\mathrm{var}(\cdot)$	Variance	(–)
v_0	Velocity of conduit wall adjacent to first grid element	m/s
v_N	Velocity of conduit wall adjacent to last grid element	m/s
$v_a(x)$	Conduit wall velocity in the down stream direction at the negative bounding wall	m/s
$v_b(x)$	Conduit wall velocity in the down stream direction at the positive bounding wall	m/s
v^{obs}	Velocity of the observer's frame of reference	m/s
v_l	Velocity in the l-direction	m/s
v_r	Velocity in the r-direction	m/s
v_w	Velocity in the w-direction	m/s
v_x	Velocity in the x-direction	m/s
v_y	Velocity in the y-direction	m/s
v_z	Velocity in the z-direction	m/s
v_θ	Velocity in the θ-direction	m/s
w	Cross-channel helical coordinate	m
w_c	The screw channel width	m
w_u	Under-relaxation factor in 3D flow simulations	(–)
w/w	Fraction on a weight basis	(–)
x	Linear coordinate	m

Symbol	*Description*	*Units*
$\bar{x}$	Average bubble diameter	m
x_i	Centres of the frequency histogram for the true diameters (Chapter 7)	(–)
x_i	The value of the i-th bin in the power spectrum (Chapter 9)	(–)
x_o	Distance from sphere centre of slice (Chapter 7)	m
x_1	Minimum root of quadratic for fluid velocity field in the x-direction	m
x_2	Maximum root of quadratic for fluid velocity field in the x-direction	m
y	Linear coordinate	m
$\hat{y}'$	Scaled controller model outputs (Chapter 10)	(–)
y_{SP}	Controlled output set-point (Chapter 10)	(–)
y_1	Minimum root of quadratic for fluid velocity field in the y-direction	m
y_2	Maximum root of quadratic for fluid velocity field in the y-direction	m
$y(k)$	The discrete time domain acoustic signal	(–)
z	Linear coordinate	m

Greek

Δ	The rate of deformation tensor	s^{-1}
$\Theta_c(r)$	The angular distance about the screw axis between screw flanks at a radial distance r from the screw axis	rad
α	Parameter of the Rosin-Rammler distribution (Chapter 7)	(–)
α	The screw tip angle (equivalent to the screw root angle for self-wiping screws)	rad
α_m	Rheology model parameter	$(w/w)^{-1}$
α_w	Rheology model parameter	$m^3\,J^{-1}$
α_1	Rheology model parameter	K^{-1}
α_2	Rheology model parameter	$(w/w)^{-1}$
α_3	Rheology model parameter	$K^{-1}\,(w/w)^{-1}$
β	Angle (Chapter 2)	rad
β	Parameter of the Rosin-Rammler distribution (Chapter 7)	(–)
γ	Angle (Chapter 2)	rad
$\dot{\gamma}$	Shear rate	s^{-1}
ε_i	Principal component i	(–)

Symbol	*Description*	*Units*
θ	Angle coordinate	rad
θ_1	Angle parameter in side gap width derivation	rad
θ_2	Angle parameter in side gap width derivation	rad
ϑ	Activation volume in starch gelatinisation kinetics model (Chapter 6)	m^3/kg-mol
κ_1	Rheology model parameter	(–)
κ_2	Rheology model parameter	K^{-1}
κ_3	Rheology model parameter	$(w/w)^{-2}$
κ_4	Rheology model parameter	$K^{-1}\,(w/w)^{-1}$
κ_5	Rheology model parameter	$K^{-1}\,J^{-1}\,m^3$
λ	The thermal conductivity of the feed material	$W\,m^{-1}\,K^{-1}$
λ	The screw flank angle (Chapter 2)	rad
λ_m	Heat capacity of the metal comprising the screws	$W\,m^{-1}\,K^{-1}$
λ_s	The stagger angle between successive kneading discs	rad
λ_v	Latent heat of vaporisation of water	J/kg
μ	Viscosity	Pa s
$\bar{\mu}$	Average viscosity at cell face centre	Pa s
$\hat{\mu}$	Average viscosity at cell corner	Pa s
ν_{ij}	Coefficient of observation x_i in principal component ε_j (Chapter 9)	(–)
ρ	Feed material density	kg/m^3
ρ_B	Product bulk density	kg/m^3
ρ_m	The density of the metal comprising the screws	kg/m^3
σ	Standard deviation of bubble diameters (Chapter 7)	m
σ	Surface tension (Chapter 8)	N/m
σ	Standard deviation of the acoustic signal (Chapter 9)	(–)
$\boldsymbol{\tau}$	The stress tensor	N/m^2
τ	Shear stress	N/m^2
$\phi(r)$	Helix angle as a function of radius r	rad
ϕ_s	The rotational phase difference between screw pairs	rad
φ	Helical rotation angle	rad
φ'	l-derivative of the helical rotation angle	rad/m
ψ_B	Barrel overlap angle	rad
ψ_S	Screw overlap angle	rad

Abbreviations

1D	One-dimensional	(–)

Symbol	*Description*	*Units*
2D	Two-dimensional	(–)
3D	Three-dimensional	(–)
ANN	Artificial neural network	(–)
CPU	Central processor unit	(–)
CSTR	Continuously stirred tank reactor	(–)
FAN	Flow analysis network	(–)
GP	Genetic programming	(–)
KD	Kneading disc	(–)
MIMO	Multiple input multiple output	(–)
MPC	Model predictive control	(–)
OD	Orifice disc	(–)
ODE	Ordinary differential equation	(–)
PC	Personal computer	(–)
PQA	Product quality attribute	(–)
RMS	Root mean square	(–)
RPM	Revolutions per minute	min^{-1}
RTD	Residence time distribution	(–)
SWS	Self-wiping screw	(–)
TFS	Trapezoidal flight screw	(–)
TFSR	Reverse-threaded trapezoidal flight screw	(–)

Other

$\approx$	Is approximately equal to	(–)
$*$	Two-dimensional convolution operator	(–)

Bibliography

A. Albert. *Regression and the Moore-Penrose Pseudoinverse*. Academic Press, New York, NY, USA, 1972.

T. Allen. *Particle Size Measurement*. Kluwer Academic Publishers, Dordrecht, The Netherlands, 5th edition, 1999.

F.S. Anselmetti, S. Luthi, and G.P. Eberli. Quantitive characterization of carbonate pore systems by digital image analysis. *AAPG Bulletin*, 82(10):1815–1836, 1998.

C. Barrès, B. Vergnes, and J. Tayeb. An improved thermal model for the solid conveying section of a twin-screw extrusion cooker. *Journal of Food Engineering*, 15:167–185, 1991.

G.W. Barton, J. Elsey, C. Chessari, G. Francis, and J. Sellahewa. The application of genetic programming in extruder modelling and control. *Automatic Control of Food and Biological Processes, Goteborg, Sweden, 21-23 September*, 2:557–562, 1998.

G.W. Barton, J. Elsey, S. Jungk, G. Francis, J. Sellahewa, and C. Chessari. Acoustics based on-line quality estimation. *Australian MATLAB Conference, Sydney, 23-24 October*, 1997.

G.W. Barton, J. Elsey, B. McKay, and C. Sanderson. AI based hybrid modelling. *Australasia-Pacific Forum on Intelligent Processing and Manufacturing of Materials, Gold Coast, 14-17 July*, 1:356–362, 1997.

G.W. Barton, J. Elsey, B. McKay, and M. Willis. Modelling extrusion cooking: A comparison of neural networks and genetic programming. *7th International Congress on Engineering and Food, Part 2, Brighton, England, 13-17 April*, pages N9–N12, 1997.

S. Bawiskar and J.L. White. A composite model for solid conveying, melting, pressure and fill factor profiles in modular co-rotating twin screw extruders. *International Polymer Processing*, 12:331–340, 1997.

M. Bhattacharya and M.A. Hanna. Kinetics of starch gelatinization during extrusion cooking. *Journal of Food Science*, 52:764–766, 1987.

G.G. Birch and R.J. Priestley. Degree of gelatinization of cooked rice. *Starch*, 25:98–100, 1973.

R.B. Bird, W.E. Stewart, and E.N. Lightfoot. *Transport Phenomena*. John Wiley & Sons, Inc., New York, 1960.

J.D. Booker and P.E. Doe. Acoustic emission related to strain energy during drying of *eucalyptus regnans* boards. *Wood Science and Technology*, 28:249–254, 1994.

M.L. Booy. Geometry of fully wiped twin-screw equipment. *Polymer Engineering and Science*, 18(12):973–984, 1978.

M.L. Booy. Isothermal flow of viscous liquids in corotating twin screw devices. *Polymer Engineering and Science*, 20(18):1220–1228, 1980.

D. Bounie. Modelling of the flow pattern in a twin-screw extruder through residence-time distribution experiments. *Journal of Food Engineering*, 7:223–246, 1988.

E.H. Bristol. On a new measure of interactions for multivariable process control. *Trans. IEEE*, page 133, 1966.

B.C. Burros, L.A. Young, and P.A. Carroad. Kinetics of corn meal gelatinization at high temperature and low moisture. *Journal of Food Science*, 50:1697–1699, 1987.

W. Cai and L. L. Diosady. A model for gelatinization of wheat starch in a twin-screw extruder. *Journal of Food Science*, 58:872–875, 887, 1993.

M.E. Camire, A. Camire, and K. Krumhar. Chemical and nutritional changes in foods during extrusion. *Critical Reviews in Food Science and Nutrition*, 29(1):35–57, 1990.

G.M. Campbell, C.D. Rielly, P.J. Fryer, and P.A. Sadd. The measurement of bubble size distributions in an opaque food fluid. *Trans IChemE, Part C*, 69:67–76, 1991.

N. W. Cervone and J. P. Harper. Viscosity of an intermediate moisture dough. *Journal of Food Process Engineering*, 2:83–95, 1978.

H. Cheng and I. Manas-Zloczower. Chaotic features of flow in polymer processing equipment – relevance to distributive mixing. *International Polymer Processing*, 12(2):83–91, 1997.

H. Cheng and I. Manas-Zloczower. Distributive mixing in conveying elements of a ZSK-53 co-rotating twin screw extruder. *Polymer Engineering and Science*, 38(6):926–935, 1998.

R.V. Chiruvella, Y. Jaluria, M.V. Karwe, and V. Sernas. Transport in a twin-screw extruder for the processing of polymers. *Polymer Engineering and Science*, 36(11):1531–1540, 1996.

D.W. Clarke, C. Mohtadi, and P.S. Tuffs. Generalized predictive control – Part i. The basic algorithm. *Automatica*, 23(2):137–148, 1987.

L.M. Cruz-Orive. Distribution-free estimation of sphere size distributions from slabs showing overprojection and truncation, with a review of previous methods. *Journal of Microscopy*, 131(3):265–290, 1983.

C.R. Cutler and B.L. Ramaker. Dynamic matrix control: A computer control algorithm. *Proceedings of the 86th National AIChE Meeting*, 1979.

G. Cybenko. Approximation by superpositions of a sigmoidal function. *Mathematics of Control, Signals, and Systems*, 2:303–314, 1989.

V. J. Davidson, D. Paton, L. L. Diosady, and L. J. Rubin. A model for mechanical degradation of wheat starch in a single-screw extruder. *Journal of Food Science*, 49: 1154–1157, 1984.

H. De Ruyck. Modelling the residence time distribution in a twin screw extruder. *Journal of Food Engineering*, 32:375–390, 1997.

C.D. Denson and B.K Hwang. The influence of the axial pressure gradient on flow rate for Newtonian liquids in a self wiping, corotating twin screw extruder. *Polymer Engineering and Science*, 20(14):965–971, 1980.

A. Desbiens, D. Houdouin, and E. Plamondon. Global predictive control: A unified control structure for decoupling setpoint tracking, feedforward compensation and disturbance rejection dynamics. *IEE Proceedings: Control Theory and Applications.*, 147(4):465–475, 2000.

K. D. Dolan, J. F. Steffe, and R. G. Morgan. Back extrusion and simulation of viscosity development during starch gelatinization. *Journal of Food Process Engineering*, 11: 79–101, 1989.

T. Domschke and C. Justus. Heat transfer in single and twin screw extruders. *International Polymer Processing*, 8(4):294–307, 1993.

J. Elsey and G.W. Barton. Measurement of bubble size distributions in extruded food products. *CHEMECA'99, Newcastle, Australia, 26-29 September, Proceedings on CD-ROM*, 1999. Paper 122.

J. Elsey, G.W. Barton, S. Jungk, G. Francis, J. Sellahewa, and C. Chessari. Acoustics based on-line quality estimation. *Computers in Chemical Engineering Supplementary Series*, 22:S925–S928, 1998.

J. Elsey, B. McKay, M. Willis, and G.W. Barton. Extruder modelling using genetic programming. *MODSIM 95, Newcastle, Australia, 27-30 November*, 1:276–283, 1995.

J. Elsey, J. Riepenhausen, B. McKay, G.W. Barton, and M. Willis. Dynamic modelling of a cooking extruder. *CHEMECA'96 Sydney, Australia, 30 September - 2 October*, 2: 43–48, 1996.

J. Elsey, J. Riepenhausen, B. McKay, G.W. Barton, and M. Willis. Modelling and control of a food extrusion process. *Computers in Chemical Engineering Supplementary Series*, 21:S361–S366, 1997.

A.J. Evans, S. Huang, B.G. Osborne, Z. Kotwal, and I.J. Wesley. Near infrared on-line measurement of degree of cook in extrusion processing of wheat flour. *Journal of Near Infrared Spectroscopy*, 7(2):337–356, 1999.

J. Fan, J.R. Mitchell, and J.M.V. Blanshard. A computer simulation of the dynamics of bubble growth and shrinkage during extrudate expansion. *Journal of Food Engineering*, 23:337–356, 1994.

D. Goffart, D.J. van der Wal, E.M. Klomp, H.W. Hoogstraten, L.P.B.M. Janssen, L. Breysse, and Y. Trolez. Three-dimensional flow modeling of a self-wiping corotating twin-screw extruder. Part 1: The transporting section. *Polymer Engineering and Science*, 36(7):901–911, 1996.

P.L. Goldsmith. The calculation of true particle size distributions from the sizes observed in a thin slice. *British Journal of Applied Physics.*, 18:813–830, 1967.

M. H. Gomez and J. M. Aguilera. A physicochemical model of corn starch. *Journal of Food Science*, 49:40–43, 1984.

C. Gutfinger, E. Broyer, and Z. Tadmor. Analysis of a cross head die with the flow analysis network (FAN) method. *Polymer Engineering and Science*, 15(5):381–385, 1975.

T.A. Haley and S.J. Mulvaney. On-line system identification and control design of an extrusion cooking process: Part 2. Model predictive and inferential control design. *Food Control*, 11:121–129, 2000.

J. Happel and H. Brenner. *Low Reynolds Number Hydrodynamics.* Prentice Hall, Englewood Cliffs, N.J., U.S.A., 1965.

R.M. Haralick. Image segmentation survey. In O.D. Faugeras, editor, *Fundamentals in Computer Vision.*, pages 209–223. 1983.

J. M. Harper. *Extrusion of Foods.* CRC Press, Boca Raton, FL, 1981.

J.M Harper, T.P Rhodes, and L.A. Wanninger. Viscosity model for cooked cereal dough. *AIChE Symposium Series*, 67(108):40–43, 1971.

T. Jager, D. J. van Zuilichem, and W. Stolp. Residence time distribution, mass flow, and mixing in a corotating, twin-screw extruder. In J. L. Kokini, C. T. Ho, and M. V. Karwe, editors, *Food Extrusion Science and Technology*, pages 165–176. Marcel Decker, New York, 1992.

L. P. B. M. Janssen. *Twin Screw Extrusion.* Elsevier Scientific Publishing Co., Amsterdam, 1978.

C.H. Jepson. Future extrusion studies. *Industrial and Engineering Chemistry*, 45(5): 992–993, 1953.

K. Joshi, J.G. Lee, M.A. Shafi, and R.W. Flumerfelt. Prediction of cellular structure in free expansion of viscoelastic media. *Journal of Applied Polymer Science*, 67(8):1353–1368, 1998.

E.K. Kim and J.L. White. Isothermal transient startup of a starved flow modular co-rotating twin screw extruder. *Polymer Engineering and Science*, 40(3):543–553, 2000.

K. E. Kinnear. *Advances in Genetic Programming.* MIT Press, 1994.

J. R. Koza. *Genetic Programming: On the programming of computers by means of natural selection.* MIT Press, 1992.

R. Kruft and J. Friedsch. Cavitation as a means for control. *North European Dairy Journal*, 52(8):267–271, 1986.

M. K. Kulshreshtha, C. A. Zaror, D. J. Jukes, and D. L. Pyle. A generalised steady state model for twin screw extruders. *Trans IChemE, Part C, Food and Bioproducts Proc.*, 69(C4):189–199, 1991a.

M.K. Kulshreshtha. *Modelling and control of a twin screw food extruder.* PhD thesis, Department of Food Science and Technology, University of Reading, 1991b.

M.K. Kulshreshtha and C.A. Zaror. An unsteady state model for twin screw extruders. *Trans IChemE, Part C, Food and Bioproducts Proc.*, 70(C4):21–28, 1992.

J.G. Lee and R.W. Flumerfelt. A refined approach to bubble nucleation and polymer foaming process: Dissolved gas and cluster size effects. *Journal of Colloid and Interface Science*, 184(2):335–348, 1996.

L. Levine, S. Symes, and J. Wiemer. A simulation of the effect of formula and feed rate variations on the transient behaviour of starved extrusion screws. *Biotechnology Progress*, 3(4):221–230, 1987.

P. Linko, K. Uemura, and T. Eerikäinen. Neural networks in fuzzy extrusion control. *IChemE Symposium Series*, 126:401–410, 1992a.

L. Ljung. *System Identification – Theory for the User.* Prentice Hall, Englewood Cliffs, N.J., 1987.

B.F.J. Manly. *Multivariate Statistical Methods: A Primer.* Chapman and Hall, United Kingdom, 1986.

The Mathworks. *MATLAB software documentation.* 24 Prime Park Way, Natick, MA 01760-1500, USA, 1998.

B. McKay, J. Elsey, M.J. Willis, and G.W. Barton. Evolving input-output models of chemical process systems using genetic programming. *13th World Congress, International Federation of Automatic Control (IFAC'96), San Francisco, 30 June - 5 July*, M: 277–282, 1996.

B. McKay, M.J. Willis, and G.W. Barton. Steady-state modelling of chemical process systems using genetic programming. *Computers and Chemical Engineering*, 21:981–996, 1997.

H.E.H. Meijer and P.H.M. Elemans. The modeling of continuous mixers. Part 1: The corotating twin-screw extruder. *Polymer Engineering and Science*, 28(5):275–290, 1988.

J.J. Monaghan. Smoothed particle hydrodynamics. *Annual Review of Astronomy and Astrophysics*, 30:543–574, 1992.

R. G. Moreira, A. K. Srivastava, and J. B. Gerrish. Feedforward control model for a twin-screw food extruder. *Food Control*, pages 179–184, 1990.

C.I. Onwulata, S.J. Mulvaney, and F. Hsieh. System analysis as the basis for control of density of extruded cornmeal. *Food Control*, 5(1):39–48, 1994.

R. Pelton. A model for foam growth in the presence of antifoam emulsion. *Chemical Engineering Science*, 51(19):4437–4442, 1996.

D. Pomerleau, J. Elsey, and G.W. Barton. Model-predictive control of an extrusion cooking process. *APCChE/CHEMECA 2002, 29 September – 3 October 2002, Christchurch, New Zealand*, 2002. In press.

H. Potente, U. Melisch, and K.P. Palluch. A physico-mathematical model for solids conveying in co-rotating twin screw extruders. *International Polymer Processing*, 11(1): 29–41, 1996.

W.H. Press, S.A. Teukolsky, W.T. Vetterling, and B.P. Flannery. *Numerical recipes in C: the art of scientific computing.* Cambridge University Press, 2nd edition, 1992.

J.P. Puaux, G. Bozga, and A. Ainser. Residence time distribution in a corotating twin-screw extruder. *Chemical Engineering Science*, 55:1641–1651, 2000.

L. Rabiner and B.H. Juang. *Fundamentals of Speech Recognition.* Prentice Hall, USA, 1993.

C. Rauwendaal, T.A. Osswald, G. Tellez, and P.J. Gramann. Flow analysis in screw extruders—effect of kinematic conditions. *International Polymer Processing*, 13(4):327–333, 1998.

H.S. Rowell and D. Finlayson. Screw viscosity pumps. *Engineering (London)*, 114:606–607, 1922.

L.E. Scriven. On the dynamics of phase growth. *Chemical Engineering Science*, 10:1–13, 1959.

L.F. Shampine and M.W. Reichelt. The MATLAB ODE suite. *SIAM Journal on Scientific Computing*, 18:1–22, 1997.

B. Singh and S.J. Mulvaney. Modeling and process control of twin-screw cooking food extruders. *Journal of Food Engineering*, 23:403–428, 1994.

R. Soeterboek. *Predictive Control: A Unified Approach.* Prentice Hall, Englewood Cliffs, 1992.

W. Szydlowski, R. Brzoskowski, and J.L. White. Modelling flow in an intermeshing co-rotating twin screw extruder: Flow in kneading discs. *International Polymer Processing*, 1:207, 1987.

W. Szydlowski and J.L. White. An improved theory of metering in an intermeshing corotating twin-screw extruder. *Advances in Polymer Technology*, 7(2):177–183, 1987.

W. Szydlowski and J.L. White. An improved model of flow in the kneading disc region of an intermeshing co-rotating twin screw extruder. *International Polymer Processing*, 2: 142, 1988a.

W. Szydlowski and J.L. White. A non-Newtonian model of flow in a kneading disc region of a modular intermeshing co-rotating twin screw extruder. *Journal of Non-Newtonian Fluid Mechanics*, 28:29–46, 1988b.

Z. Tadmor, E. Broyer, and C. Gutfinger. Flow analysis network (FAN) – a method for solving flow problems in polymer processing. *Polymer Engineering and Science*, 14(9): 660–665, 1974.

Z. Tadmor and I Klein. *Engineering principles of plasticating extrusion.* Robert E. Krieger Publishing Company, Huntington, New York, 1970.

J. Tayeb, B. Vergnes, and G. Della Valle. A basic model for a twin-screw extruder. *Journal of Food Science*, 53(4):1047–1056, 1988b.

D.J. van der Wal, D. Goffart, E.M. Klomp, H.W. Hoogstraten, and L.P.B.M. Janssen. Three-dimensional flow modeling of a self-wiping corotating twin-screw extruder. Part 2: The kneading section. *Polymer Engineering and Science*, 36(7):912–924, 1996.

B. Vergnes, G. Della Valle, and L. Delamare. A global computer software for polymer flows in corotating twin screw extruders. *Polymer Engineering and Science*, 38(11): 1781–1792, 1998.

B. Vergnes and J.P. Villemaire. Rheological behaviour of low moisture molten maize starch. *Rheologica Acta*, 26:570–576, 1987.

L. Wang, C. Chessari, and E. Karpiel. Inferential control of product quality attributes — application to food cooking extrusion process. *Journal of Process Control*, 11:621–636, 2001.

S. S. Wang, W. C. Chiang, A. Yeh, B. Zhao, and I. Kim. Kinetics of phase transition of waxy corn starch at extrusion temperatures and moisture contents. *Journal of Food Science*, 54:1298–1326, 1989.

S. S. Wang, W. C. Chiang, X. Zheng, B. Zhao, M. H. Cho, and A. Yeh. Application of an energy equivalent concept to the study of the kinetics of starch conversion during extrusion. In J. L. Kokini, C. T. Ho, and M. V. Karwe, editors, *Food Extrusion Science and Technology*, pages 165–176. Marcel Decker, New York, 1992.

Y. Wang and C.C. Tsay. Non-Newtonian flow modeling in the mixing section of a single-screw extruder with flow analysis network method. *Polymer Engineering and Science*, 36(5):643–650, 1996.

Y. Wang and J.L. White. Non-Newtonian flow modelling in the screw regions of an intermeshing corotating twin screw extruder. *Journal of Non-Newtonian Fluid Mechanics*, 32:19–38, 1989.

R.C. Warren. *A model of 2 dimensional flow in a twin-screw mix-extruder kneading disc using a full 2 dimensional solution of the flow equations.* Department of Defence, DSTO Materials Research Laboratory, Maribyrnong Victoria, Australia, 1993. MRL-TN-636.

H. Werner and K. Eise. An analysis of the conveying characteristics of twin-screw co-rotating extruders. *SPE Antec Technical Papers*, 37:181–187, 1979.

J.L. White, E.K. Kim, J.M. Keum, and H.C. Jung. Modelling heat transfer in screw extrusion with special application to modular self-wiping co-rotating twin-screw extrusion. *Polymer Engineering and Science*, 41(8):1448–1455, 2001.

S.D. Wicksell. The corpuscle problem: A mathematical study of a biometric problem. *Biometrika*, 17(1):84–99, 1925.

W. A. Yacu. Modelling a twin screw co-rotating extruder. *Journal of Food Process Engineering*, 8:1–21, 1985.

H.H. Yang and I. Manas-Zloczower. Flow field analysis of the kneading disc region in a co-rotating twin screw extruder. *Polymer Engineering and Science*, 32(19):1411–1417, 1992.

A.L. Yarin, D. Lastochkin, Y. Talmon, and Z. Tadmor. Bubble nucleation during devolatilization of polymer melts. *AIChE Journal*, 45(12):2590–2605, 1999.

Q. Yu and G.H. Hu. Development of a helical coordinate system and its application to analysis of polymer flow in screw extruders Part I. The balance equations in a helical coordinate system. *Journal of Non-Newtonian Fluid Mechanics.*, 69:155–167, 1997.